

REPORT DOCUMENTATION PAGE

Form Approved OMB NO. 0704-0188

The public reporting burden for this collection of information is estimated to average 1 hour per response, including the time for reviewing instructions, searching existing data sources, gathering and maintaining the data needed, and completing and reviewing the collection of information. Send comments regarding this burden estimate or any other aspect of this collection of information, including suggestions for reducing this burden, to Washington Headquarters Services, Directorate for Information Operations and Reports, 1215 Jefferson Davis Highway, Suite 1204, Arlington VA, 22202-4302. Respondents should be aware that notwithstanding any other provision of law, no person shall be subject to any penalty for failing to comply with a collection of information if it does not display a currently valid OMB control number.

PLEASE DO NOT RETURN YOUR FORM TO THE ABOVE ADDRESS.

1. REPORT DATE (DD-MM-YYYY) 05-04-2013	2. REPORT TYPE Final Report	3. DATES COVERED (From - To) 15-Sep-2006 - 14-Sep-2012		
4. TITLE AND SUBTITLE Final Report		5a. CONTRACT NUMBER W911NF-06-1-0446		
		5b. GRANT NUMBER		
		5c. PROGRAM ELEMENT NUMBER 611103		
6. AUTHORS Martin Richardson, Michael Sigman, Matthieu Baudelet, Candice Bridge, Santiago Palanco, Matthew Fisher, Christopher Brown, Yuan Liu, Matthew Weidman, Cheonha Jeon, Khan Lim, Caitlin Rinke, Lionel		5d. PROJECT NUMBER		
		5e. TASK NUMBER		
		5f. WORK UNIT NUMBER		
7. PERFORMING ORGANIZATION NAMES AND ADDRESSES University of Central Florida Office of Research 12201 Research Parkway, Suite 501 Orlando, FL		8. PERFORMING ORGANIZATION REPORT NUMBER		
32826 -0150				
9. SPONSORING/MONITORING AGENCY NAME(S) AND ADDRESS(ES) U.S. Army Research Office P.O. Box 12211 Research Triangle Park, NC 27709-2211		10. SPONSOR/MONITOR'S ACRONYM(S) ARO		
		11. SPONSOR/MONITOR'S REPORT NUMBER(S) 50351-EG-MUR.33		
12. DISTRIBUTION AVAILABILITY STATEMENT Approved for Public Release; Distribution Unlimited				
13. SUPPLEMENTARY NOTES The views, opinions and/or findings contained in this report are those of the author(s) and should not be construed as an official Department of the Army position, policy or decision, unless so designated by other documentation.				
14. ABSTRACT The overall objective of this MURI program is to obtain a comprehensive understanding of the interaction of ultrafast femtosecond laser pulses with matter, with specific reference to the detection of trace elements of materials by techniques such as LIBS and Raman spectroscopy. Ultrafast Laser Interaction Processes for Lips and Other				
15. SUBJECT TERMS spectroscopy, laser induced spectroscopy, chemical physics, filamentation, atomic modeling, plasma modeling, chemometrics, explosives, energetic materials				
16. SECURITY CLASSIFICATION OF: a. REPORT UU		17. LIMITATION OF ABSTRACT UU	15. NUMBER OF PAGES	19a. NAME OF RESPONSIBLE PERSON Martin Richardson
b. ABSTRACT UU				19b. TELEPHONE NUMBER 407-823-6819
c. THIS PAGE UU				

Report Title

Final Report

ABSTRACT

The overall objective of this MURI program is to obtain a comprehensive understanding of the interaction of ultrafast femtosecond laser pulses with matter, with specific reference to the detection of trace elements of materials by techniques such as LIBS and Raman spectroscopy.

Enter List of papers submitted or published that acknowledge ARO support from the start of the project to the date of this printing. List the papers, including journal references, in the following categories:

(a) Papers published in peer-reviewed journals (N/A for none)

03/30/2010 30.00 M. Baudelet, C. Willis, L. Shah, M. Richardson. Laser-induced breakdown spectroscopy of copper with a 2 μ m thulium fiber laser, , (03 2010): . doi:

03/30/2010 29.00 P. Dagdigian, A. Khachatrian, V. Babushok. Kinetic model of C/H/N/O emissions in laser-induced breakdown spectroscopy of organic compounds, *Applied Optics*, (02 2010): . doi:

08/30/2010 32.00 Yuan Liu, Matthieu Baudelet, Martin Richardson. Elemental analysis by microwave-assisted laser-induced breakdown spectroscopy: Evaluation on ceramics , *Journal of Analytical Atomic Spectrometry*, (05 2010): . doi:

09/22/2010 26.00 A. Khachatrian, P. J. Dagdigian. Laser-induced breakdown spectroscopy with laser irradiation resonant with vibrational transitions, *Applied Optics*, (05 2010): . doi:

10/02/2009 1.00 V.I. Babushok, F. DeLucia Jr, P.J. Dagdigian, J. Gottfried, C.A. Munson, M.J. Nusca, A.W. Mizolek. Kinetic modeling study of the laser-induced plasma plume of cyclotrimethylenitramine (RDX), *Spectrochimica Acta*, (10 2007): . doi:

10/06/2009 2.00 J. Li, D. Alexander, H. Zhang, U. Parali, D. Doerr, J. Bruce III, H. Wang. Propagation of ultrashort pulses through water, *Optics Express*, (02 2007): . doi:

12/02/2009 8.00 Z. Chen, S. Mao. Femtosecond laser-induced electronic plasma at metal surface, *Applied Physics Letters*, (08 2008): . doi:

12/02/2009 17.00 M. Weidman, S. Palanco, M. Baudelet, M. Richardson. Thermodynamic and spectroscopic properties of Nd:YAG-CO₂ Double-Pulse Laser-Induced Iron Plasmas, *Spectrochimica Acta*, (08 2009): . doi:

12/02/2009 16.00 M. Baudelet, M. Boueri, J. Yu, S. Mao, X. Mao, R. Russo. Correlation between early-stage expansion and spectral emission of a nanosecond laser-induced plasma from organic material, *Proceedings of SPIE*, (12 2009): . doi:

12/02/2009 15.00 V. Babushok, F. DeLucia, P. Dagdigian, J. Gottfried, C. Munson, M. Nusca, A. Mizolek. Kinetic modeling study of the laser-induced plasma plume of cyclotrimethylenetrinitramine (RDX), *Spectrochimica Acta*, (10 2007): . doi:

12/02/2009 14.00 D. Wong, P. Dagdigian. Comparison of laser-induced breakdown spectra of organic compounds with irradiation at 1.5 and 1:064 μ m at 1.5 and 1:064 μ m, *Applied Optics*, (11 2008): . doi:

12/02/2009 13.00 M. baudelet, M. Sigman. Self-channeling of Femtosecond Laser Pulses for Rapid and Efficient Standoff Detection of Energetic Materials, , (08 2009): . doi:

12/02/2009 12.00 M. Baudelet, M. Boueri, J. Yu, S. Mao, V. Piscitelli, X. Mao, R. Russo. Time-resolved ultraviolet laser-induced breakdown spectroscopy for organic material analysis, *Spectrochimica Acta*, (10 2007): . doi:

12/02/2009 11.00 Q. Lu, S. Mao, X. Mao, R. Russo. Theory analysis of wavelength dependence of laser-induced phase explosion of silicon, *Journal of Applied Physics*, (10 2008): . doi:

12/02/2009 10.00 M. Boueri, M. Baudelet, J. Yu, X. Mao, S. Mao, R. russo. Early stage expansion and time-resolved spectral emission of laser-induced plasma from polymer, *Applied Surface Science*, (12 2009): . doi:

12/02/2009 9.00 M. Rogers, C. Grigoropoulos, A. Minor, S. Mao. Absence of amorphous phase in high power femtosecond laser-ablated silicon, *Applied Physics Letters*, (01 2009): . doi:

12/03/2009 19.00 . Atmosphere Issues in Detection of Explosives and Organic Residues, *Proceedings of SPIE*, (11 2009): . doi:

12/03/2009 24.00 R. Bernath, C. Brown, J. Aspiotis, M. Fisher, M. Richardson. Shock-wave generation in transparent media from ultra-fast lasers, *Proceedings of SPIE*, (12 2001): . doi:

12/03/2009 23.00 J. Martin, M. Baudelet, M. Weidman, M. Fisher, C. Bridge, C. Brown, M. Sigman, P. Dagdigian, M. Richardson. Stand-off detection of organic samples using filament-induced breakdown spectroscopy, *Proceedings of SPIE*, (12 2009): . doi:

12/03/2009 22.00 C. Brown, R. Bernath, M. Fisher, M. Richardson, M. Sigman, R. Walters, A. Mizolek, H. Bereket, L. Johnson. Remote Femtosecond Laser Induced Breakdown Spectroscopy (LIBS)in a Standoff Detection Regime, *Proceedings of SPIE*, (12 2009): . doi:

12/03/2009 20.00 J. Aspiotis, N. Barbieri, R. Bernath, C. Brown, M. Richardson, B. Cooper. Detection and analysis of RF emission generated by laser-matter interactions, *Proceedings of SPIE*, (12 2009): . doi:

12/03/2009 21.00 M. Weidman, M. Baudelet, M. Fisher, C. Bridge, C. Brown, M. Sigman, P. Dagdigian, M. Richardson. Molecular signal as a signature for detection of energetic materials in filament-induced breakdown spectroscopy, *Proceedings of SPIE*, (12 2009): . doi:

12/03/2009 18.00 M. Fisher, C. Siders, E. Johnson, O. Andrusyak, C. Brown, M. Richardson. Control of Filamentation for Enhancing Remote Detection with Laser Induced Breakdown Spectroscopy, *Proceedings of SPIE*, (11 2009): . doi:

12/23/2009 25.00 M. Weidman, M. Baudelet, S. Palanco, M. Sigman, P. Dagdigian, M. Richardson. Nd:YAG-CO₂ double-pulse laser induced breakdown spectroscopy of organic films, , (01 2010): . doi:

TOTAL: 24

Number of Papers published in peer-reviewed journals:

(b) Papers published in non-peer-reviewed journals (N/A for none)

Received Paper

TOTAL:

(c) Presentations

Matthew Weidman, Khan Lim, Nicholas Barbieri, Erik McKee, Magali Durand, Matthieu Baudelet, Martin Richardson, "Quantitative studies of filament interaction with matter for spectroscopic applications", seminar at GAP Biophotonics group, University of Geneva; Geneva, Switzerland; 11/30, 2012. Seminar

7. Yuan Liu, Matthew Weidman, Christopher Brown, Corey Butler, Marie Vangheluwe, Shima Fardad, Andreas Knebl, Lionel Gigant, Martin Richardson, Matthieu Baudelet, "New Perspectives in Laser Spectroscopy as a Science for Sensing, Monitoring and Diagnostics", seminar at Center of Excellence "Laser & Photonique en Aquitaine", University of Bordeaux; Bordeaux, France; 11/13, 2012. Seminar

8. Martin Richardson, Matthieu Baudelet, Michael Sigman and Andrzej Miziolek, "Stand-off chemical and biological sensing", Frontiers in Optics 2012, Laser Science XXVIII; Rochester, NY, USA; 10/14-18, 2012; Invited talk

9. Martin Richardson, Matthieu Baudelet, Michael Sigman and Andrzej Miziolek, "Stand-off LIBS – The status today and the future", LIBS 2012; Luxor, Egypt; 09/29 – 10/04, 2012; Invited talk

10. Yuan Liu, Matthieu Baudelet, Martin Richardson, "Microwave-assisted LIBS: Signal enhancement and beyond", SciX 2012; Kansas City, MO, USA; 10/02, 2012. Invited talk

11. Matthieu Baudelet, "Fifty years of LIBS and no limits for analysis", SciX 2012; Kansas City, MO, USA; 10/02, 2012. Invited talk

12. Yuan Liu, Matthieu Baudelet, Martin Richardson, "Laser-Induced Breakdown Spectroscopy for Moisture Monitoring in Food"; Pittcon 2012, Orlando, FL, USA; 03/11, 2012

13. Yuan Liu, Mark Koehler, Matthieu Baudelet, Martin Richardson, "Fusion of infrared and Raman spectroscopy for carotenoid analysis"; Pittcon 2012, Orlando, FL, USA; 03/11, 2012.

14. Yuan Liu, Matthieu Baudelet, Martin Richardson, "Advanced LIBS Methodology for Food and Environment Monitoring"; 2012 Winter Conference on Plasma Spectrochemistry; Tucson, AZ, USA; 01/10, 2012. Poster presentation

15. Cheonha Jeon, Matthieu Baudelet, Martin Richardson, "Fundamental Time-Resolved Mass Spectrometry of Laser-Induced Plasmas for Organic Analysis"; 2012 Winter Conference on Plasma Spectrochemistry; Tucson, AZ, USA; 01/10, 2012.

16. Matthieu Baudelet, Michael Sigman, Martin Richardson, "Laser-induced breakdown spectroscopy in complex situations"; FACSS 2011; Reno, NV, USA; 10/06, 2011. Invited talk

17. Yuan Liu, Matthieu Baudelet, Martin Richardson, Richard Russo "Advanced LIBS Methodologies for Food and Environment Monitoring"; Euro-Mediterranean Symposium on Laser-Induced Breakdown Spectroscopy 2011; Izmir, Turkey; 09/13, 2011

18. Matthieu Baudelet, Martin Richardson, Michael Sigman, "Laser spectroscopy and sensing at the Townes Laser Institute"; ATLANTIS-MILMI Summer School; Orlando, FL, USA; 07/21, 2011. Invited talk

19. Yuan Liu, Lionel Gigant, Matthieu Baudelet, Martin Richardson, "Combination of LIBS and Raman for Food Quality Monitoring"; North-American Symposium on Laser-Induced Breakdown Spectroscopy 2011; Clearwater, FL, USA; 07/20, 2011.

20. Yuan Liu, Matthieu Baudelet, Martin Richardson, "Laser Material Analysis using Calibration Free Laser-Induced Breakdown Spectroscopy"; North-American Symposium on Laser-Induced Breakdown Spectroscopy 2011; Clearwater, FL, USA; 07/19, 2011. Poster presentation

21. Matthew Weidman, Matthieu Baudelet, Martin Richardson, "Time-Resolved Goniometric Measurement of the Filament-Induced Plasma Emission for Stand-Off LIBS Applications"; North-American Symposium on Laser-Induced Breakdown Spectroscopy 2011; Clearwater, FL, USA; 07/19, 2011. Poster presentation

22. Santiago Palanco, Jose Ramos-Barrado, Matthew Weidman, Matthieu Baudelet, Martin Richardson, "Correlation Between Spectral Emission and Nanoparticle Generation During Nano- and Femtosecond Laser-induced Breakdown"; North-American Symposium on Laser-Induced Breakdown Spectroscopy 2011; Clearwater, FL, USA; 07/18, 2011.

23. Caitlin Rinke, Christopher Brown, Martin Richardson, Matthieu Baudelet, Michael Sigman, "LIBS signature recognition of trace materials in complex background environments"; North-American Symposium on Laser-Induced Breakdown Spectroscopy 2011; Clearwater, FL, USA; 07/18, 2011. Invited talk

24. Yuan Liu, Lionel Gigant, Matthieu Baudelet, Martin C. Richardson, "Combination of LIBS and Raman for food quality monitoring"; SPIE Defense, Security, Sensing; Orlando, FL, USA; 04/26, 2011.

25. Khan Lim, Jason M. Eichenholz, Matthieu Baudelet, Martin C. Richardson, "Far-UV LIBS for biological and organic samples"; SPIE Defense, Security, Sensing; Orlando, FL, USA; 04/25, 2011.

26. Khan Lim, Yuan Liu, Matthieu Baudelet, Evgeni Slobodtchikov, Peter Moulton, Andrzej W. Miziolek, Martin C. Richardson, "New generation of compact femtosecond system for laser-based detection and identification of biological materials"; SPIE Defense, Security, Sensing; Orlando, FL, USA; 04/25, 2011.

27. Matthew Weidman, Matthieu Baudelet, Christina C. C. Willis, Lawrence Shah, Martin C. Richardson, "Novel laser sources for LIBS: From fiber lasers, self-channeled laser to dual pulse configuration"; Pacificchem 2010; Honolulu, HI, USA; 12/18, 2010.

28. Yuan Liu, Matthieu Baudelet, Martin C. Richardson, "Microwave-assisted LIBS: Extending the laser induced plasma lifetime for trace detection" Pacificchem 2010; Honolulu, HI, USA; 12/18, 2010. Poster presentation

29. Matthew Weidman, Matthieu Baudelet, Martin C. Richardson, Paul J Dagdigian, "Spatial and temporal spectral imaging of self-channeled laser-induced breakdown spectroscopy on carbon-based samples: Molecular chemistry in air"; Pacificchem 2010; Honolulu, HI, USA; 12/18, 2010. Poster presentation

30. Martin Richardson, Michael Sigman, Matthieu Baudelet, "Standoff Detection of Trace Radio-Nuclides using New Laser Spectroscopy

Techniques"; NNSA, University and Industry Technical Interchange (UITI2010) Review Meeting; Knoxville, TN, USA; 12/08, 2010

31. Matthew Weidman, Matthew Fisher, Khan Lim, Christopher Brown, Caitlin Rinke, Matthieu Baudelet, Michael Sigman, Martin Richardson, "Advanced LIBS Modalities for Stand-Off Detection of Explosive and Biological Threats"; 27th Army Science Conference; Orlando, FL, USA; 11/30, 2010.

32. Caitlin Rinke, Christopher G. Brown, Matthieu Baudelet, Martin C. Richardson, Michael Sigman, "A New Paradigm for Substrate Independent Discrimination of Organic and Explosive Materials by Target Factor Analysis of Molecular Optical Signatures"; 2010 Chemical and Biological Defense Science and Technology Conference; Orlando, FL, USA; 11/16, 2010. Poster Presentation

33. Yuan Liu, Matthieu Baudelet, Martin C. Richardson, "Compact Laser-based Spectroscopic Systems for Biological Analysis"; 2010 Chemical and Biological Defense Science and Technology Conference; Orlando, FL, USA; 11/16, 2010. Poster Presentation

34. Matthew Weidman, Matthieu Baudelet, Martin C. Richardson, "Stand-off Laser Sensing for Chemical and Biological Traces Detection"; 2010 Chemical and Biological Defense Science and Technology Conference; Orlando, FL, USA; 11/16, 2010. Poster Presentation

35. Danielle Simmons, Nathan Bodnar, Matthieu Baudelet, Martin Richardson, "Fourier Transform Infrared Spectroscopy"; Symposium on undergraduate research, Division of Laser Science of A.P.S - LS XXVI; Rochester, NY, USA; 10/25, 2010. Poster Presentation

36. Khan Lim, Matthieu Baudelet, Jason Eichenholz, Martin C. Richardson, "Far-UV LIBS for Biological and Organic Samples"; 6th International Conference on Laser-Induced Breakdown Spectroscopy; Memphis, TN, USA; 09/16, 2010.

37. Yuan Liu, Matthieu Baudelet, Martin C. Richardson, "Elemental Analysis on Ceramic and Soil Samples Using Microwave-Assisted Laser-Induced Breakdown Spectroscopy"; 6th International Conference on Laser-Induced Breakdown Spectroscopy; Memphis, TN, USA; 09/16, 2010. Poster Presentation

38. Matthew Weidman, Matthieu Baudelet, Paul J Dagdigan, Martin C. Richardson, "Temporally and Spatially Resolved Filament Induced Breakdown Spectroscopy of Carbon Based Samples"; 6th International Conference on Laser-Induced Breakdown Spectroscopy; Memphis, TN, USA; 09/15, 2010. Poster Presentation

39. Khan Lim, Yuan Liu, Matthieu Baudelet, Evgueni Slobodtchikov, Peter Moulton, A Mizolek, Martin C. Richardson, "LIBS of Biological Materials with a Compact Femtosecond System"; 6th International Conference on Laser-Induced Breakdown Spectroscopy; Memphis, TN, USA; 09/15, 2010. Poster Presentation

40. Yuan Liu, Matthieu Baudelet, Paul J Dagdigan, Martin C. Richardson, "Molecular Emission Enhancement from Microwave-Assisted Laser-Induced Breakdown Spectroscopy"; 6th International Conference on Laser-Induced Breakdown Spectroscopy; Memphis, TN, USA; 09/15, 2010. Poster Presentation

41. Christopher G. Brown, Reuvani Devi Kamtaprasad, Matthieu Baudelet, Michael Sigman, Martin C. Richardson, "Stoichiometric Study of Organic Mass Limited Droplets"; 6th International Conference on Laser-Induced Breakdown Spectroscopy; Memphis, TN, USA; 09/15, 2010. Poster Presentation

42. Martin C. Richardson, Matthieu Baudelet, Michael Sigman, "Fundamental Considerations for an Efficient Application of LIBS in Forensics and Security"; 6th International Conference on Laser-Induced Breakdown Spectroscopy; Memphis, TN, USA; 09/14, 2010. Invited paper

43. Matthew Weidman, Matthieu Baudelet, Michael Sigman, Martin C. Richardson, "Nd:YAG-CO₂ double-pulse laser-induced breakdown spectroscopy for explosive residues detection"; SPIE Defense, Security, Sensing; Orlando, FL, USA; 04/07, 2010.

44. Matthew Weidman, Matthieu Baudelet, Paul J Dagdigan, Michael Sigman, Martin C. Richardson, "Self-channeled laser-induced breakdown spectroscopy for detection of organic compounds in atmosphere via their molecular signature"; SPIE Defense, Security, Sensing; Orlando, FL, USA; 04/07, 2010.

45. Yuan Liu, Matthieu Baudelet, Martin C. Richardson, "Microwave-assisted laser-induced breakdown spectroscopy for trace detection in soil and food"; SPIE Defense, Security, Sensing; Orlando, FL, USA; 04/06, 2010.

46. Matthieu Baudelet, Christina C. C. Willis, Lawrence Shah, Martin Richardson, "Mid-IR Tm-fiber laser for laser-induced plasma spectroscopy of organic and biological materials"; SPIE Defense, Security, Sensing; Orlando, FL, USA; 04/05, 2010.

47. Yuan Liu, Matthieu Baudelet, Martin C. Richardson, "Trace Detection in Ceramics, Organic and Biological Samples by Microwave-assisted Laser-induced Plasma Spectroscopy"; 2010 Pittsburgh Conference on Analytical Chemistry and Applied Spectroscopy; Orlando, FL, USA; 03/04, 2010.

48. Matthieu Baudelet, Christina C. Willis, Pankaj Kadwani, Lawrence Shah, Martin C. Richardson, "Laser-induced Breakdown Spectroscopy of Organic Materials with a Mid-IR Thulium-fiber-laser Nanosecond Pulse at 2 μ m"; 2010 Pittsburgh Conference on Analytical Chemistry and Applied Spectroscopy; Orlando, FL, USA; 03/04, 2010. Poster presentation

49. Caitlin Rinke, Christopher G. Brown, Douglas Clark, Matthieu Baudelet, Martin C. Richardson, Michael Sigman, "Substrate Independent Discrimination of Organic and Explosive Materials Via Target Factor Analysis of Their Molecular Optical Signature"; 2010 Pittsburgh Conference on Analytical Chemistry and Applied Spectroscopy; Orlando, FL, USA; 03/04, 2010. Poster presentation

50. Matthew Weidman, Matthieu Baudelet, Michael Sigman, Paul J Dagdigan, Martin C. Richardson, "Nd:YAG-CO₂ Double-Pulse Laser Induced Breakdown Spectroscopy for Explosive Detection"; OSA Laser Application to Chemical Security and Environmental Analysis; San Diego, CA, USA; 02/03, 2010.

51. Matthieu Baudelet, Yuan Liu, Martin C. Richardson, "Microwave-Assisted LIBS: Towards a New Tool for Trace Element Detection

and Molecular Plasma Spectrochemistry"; OSA Laser Application to Chemical Security and Environmental Analysis; San Diego, CA, USA; 02/03, 2010.

52. Matthieu Baudelot, Christina C. C. Willis, Lawrence Shah, Martin C. Richardson, "Tm-Fiber 2 μ m Laser for Laser-Induced Plasma Spectroscopy of Organic and Biological Materials"; OSA Laser Application to Chemical Security and Environmental Analysis; San Diego, CA, USA; 02/03, 2010.

53. Matthieu Baudelot, Yuan Liu, Martin Richardson, "Trace Detection in Ceramics, Organics, and Biological Samples by Microwave-Assisted Laser-Induced Breakdown Spectrometry"; 2010 Winter Conference on Plasma Spectrochemistry; Fort Myers, FL, USA; 01/05, 2010.

54. Matthieu Baudelot, Yuan Liu, Paul J. Dagdigian, Martin Richardson, "Molecular Emission Enhancement From Microwave-Assisted Laser-Induced Breakdown Spectroscopy on Alumina"; 2010 Winter Conference on Plasma Spectrochemistry; Fort Myers, FL, USA; 01/05, 2010. Poster presentation.

55. Matthew Weidman, Matthieu Baudelot, Paul J. Dagdigian, Martin Richardson, "Spatial and temporal spectral imaging of self-channeled laser-induced breakdown spectroscopy on carbon-based samples: Thermochemistry leading to molecular formation in air"; 2010 Winter Conference on Plasma Spectrochemistry; Fort Myers, FL, USA; 01/05, 2010. Poster presentation.

56. Matthieu Baudelot, Matthew Weidman, Christopher G. Brown, Michael Sigman, Paul J. Dagdigian, Martin Richardson, "Enhancement of LIBS signal from metallic, ceramic and organic samples by a Nd:YAG-CO₂ double-pulse scheme"; North-American Symposium on Laser-Induced Breakdown Spectroscopy 2009; New Orleans, LA, USA; 07/15, 2009.

57. Martin Richardson, Dennis Alexander, Matthieu Baudelot, Paul J. Dagdigian, Lewis E. Johnson, Samuel S. Mao, Michael Sigman, "Femtosecond LIBS – Light at the end of the end of the channel: The ARO MURI program on femtosecond LIBS"; North-American Symposium on Laser-Induced Breakdown Spectroscopy 2009; New Orleans, LA, USA; 07/15, 2009.

58. Matthieu Baudelot, Christina Willis Lawrence Shah, Martin Richardson, "Laser-induced breakdown spectroscopy of organic materials with a mid-IR Thulium fiber-laser nanosecond pulse at 2 μ m"; North-American Symposium on Laser-Induced Breakdown Spectroscopy 2009; New Orleans, LA, USA; 07/14, 2009. Poster presentation.

59. Yuan Liu, Nicholas Barbieri, Matthew Weidman, Matthieu Baudelot, Martin Richardson, "Plasma heating by microwave radiation: thermodynamic processes and analytical applications"; North-American Symposium on Laser-Induced Breakdown Spectroscopy 2009; New Orleans, LA, USA; 07/14, 2009. Poster presentation.

60. Matthew Weidman, Matthieu Baudelot, Christopher G. Brown, Michael Sigman, Paul J. Dagdigian, Martin C. Richardson, "Self-channeled femtosecond LIBS: Molecular processes between the atmosphere and the plasma and their analytical use for detection of organic samples"; North-American Symposium on Laser-Induced Breakdown Spectroscopy 2009; New Orleans, LA, USA; 07/14, 2009. Poster presentation.

61. Christopher G. Brown, Caitlin Rinke, Matthieu Baudelot, Martin C. Richardson, Michael Sigman, "Substrate Independent Identification of Organic Analytes with LIBS"; North-American Symposium on Laser-Induced Breakdown Spectroscopy 2009; New Orleans, LA, USA; 07/14 2009. Poster presentation.

62. Martin C. Richardson, Matthieu Baudelot, Michael Sigman, Matthew Weidman, Christopher G. Brown, "Ultra-fast lasers for stand-off detection", Ultrashort Pulse Laser Workshop, Directed Energy Professional Society; Newton, MA, USA; 06/29, 2009.

63. Martin C. Richardson, Michael Sigman, Matthieu Baudelot, "Self-channeling of Femtosecond Laser Pulses as an Efficient and Rapid Tool for standoff detection of energetic materials", IEEE 2009 International Conference on Technologies for Homeland Security; Waltham, MA, USA; 05/12, 2009.

64. Christopher G. Brown, Matthieu Baudelot, Candice Bridge, Matthew Fisher, Michael Sigman, Martin Richardson, Paul J Dagdigian, "Atmosphere issues in detection of explosives and organic residues"; SPIE Defense, Security, and Sensing; Orlando, FL, USA; 04/16, 2009.

65. Matthieu Baudelot, Matthew Weidman, Matthew Fisher, Christopher G. Brown, Michael Sigman, Martin Richardson, Paul J Dagdigian, "Molecular signal as a signature for detection of energetic materials in filament-induced breakdown spectroscopy"; SPIE Defense, Security, and Sensing; Orlando, FL, USA; 04/16, 2009.

66. James Martin, Matthieu Baudelot, Matthew Weidman, Matthew Fisher, Candice Bridge, Christopher G. Brown, Michael Sigman, Martin C. Richardson, Paul J Dagdigian, "Stand-off detection of organic samples using filament-induced breakdown spectroscopy"; SPIE Defense, Security, and Sensing; Orlando, FL, USA; 04/15, 2009.

67. Matthieu Baudelot, Christopher G. Brown, Candice Bridge, Matthew Weidman, Matthew Fisher, Michael Sigman, Martin C. Richardson, Paul J Dagdigian, "Influence of atmosphere and laser parameters on LIBS detection and analysis of explosives and organic thin films"; SPIE Defense, Security, and Sensing; Orlando, FL, USA; 04/13, 2009.

68. Matthieu Baudelot, Matthew Fisher, Matthew Weidman, Candice Bridge, Christopher G. Brown, Michael Sigman, Martin C. Richardson, Paul J Dagdigian, "LIBS Detection of Explosives with Self-Channeled Laser Light"; GOMACTech Conference; Orlando, FL, USA; 03/19, 2009.

69. Christopher G. Brown, Matthieu Baudelot, Candice Bridge, Matthew Fisher, Michael Sigman, Martin Richardson, Paul J Dagdigian, "Femtosecond LIBS: a better regime to analyze organic samples"; Southeast Ultrafast Conference; Orlando, FL, USA; 01/16, 2009. Poster presentation.

70. Matthieu Baudelet, Matthew Weidman, Matthew Fisher, Candice Bridge, Christopher G. Brown, Michael Sigman, Martin C. Richardson, Paul J Dagdigian, "Filament-Induced Breakdown Spectroscopy on Organic Thin Films: Towards an Efficient Detection of Energetic Materials"; Southeast Ultrafast Conference; Orlando, FL, USA; 01/16, 2009. Poster presentation.

71. James Martin, Matthew Weidman, Christopher Brown, Candice Bridge, Matthieu Baudelet, Martin Richardson, "Light Detection for Laser Induced Breakdown Spectroscopy"; Symposium on undergraduate research, Division of Laser Science of A.P.S; Rochester, NY, USA; 10/28, 2008. Poster presentation.

72. James Martin, Matthew Weidman, Matthieu Baudelet, Matthew Fisher, Martin C. Richardson, Paul J. Dagdigian, "Towards an efficient remote LIBS detection of organic materials"; 5th International Conference on Laser-Induced Breakdown Spectroscopy; Berlin, Germany; 09/25, 2008. Poster presentation.

73. Christopher G. Brown, Candice Bridge, Matthew Fisher, Matthieu Baudelet, Michael Sigman, Martin Richardson, Paul J Dagdigian, "Comparison of nanosecond and femtosecond Laser Regimes for LIBS Analysis of Organic Thin Films"; 5th International Conference on Laser-Induced Breakdown Spectroscopy; Berlin, Germany; 09/24, 2008. Poster presentation.

74. Matthew Weidman, Santiago Palanco, Matthieu Baudelet, Michael Sigman, Martin Richardson, "Thermodynamic properties of Nd:YAG-CO₂ Double-Pulse Laser-Induced Plasma: Applications Under Stand-Off Conditions,"; 5th International Conference on Laser-Induced Breakdown Spectroscopy; Berlin, Germany; 09/24, 2008. Poster presentation.

75. Matthew Weidman, Matthieu Baudelet, Matthew Fisher, Candice Bridge, Christopher G. Brown, Michael Sigman, Martin C. Richardson, Paul J Dagdigian, "Filament-Induced Breakdown Spectroscopy on Organic Thin Films: Towards an Efficient Detection of Energetic Materials"; 5th International Conference on Laser-Induced Breakdown Spectroscopy; Berlin, Germany; 09/24, 2008.

76. "Laser-Induced Breakdown Spectroscopy and Related Stand-off Detection"; Santiago Palanco, Martin Richardson; Laser Application to Chemical Security and Environmental Analysis, OSA (St. Petersburg, FL, USA) 17-20 March 2008

77. "Thermodynamic Properties of a Nd:YAG-CO₂ Double Pulse Laser-Induced Plasma and Its Applications Under Stand-off Conditions"; Matthew Weidman, Santiago Palanco, Martin Richardson; Laser Application to Chemical Security and Environmental Analysis, OSA (St. Petersburg, FL, USA) 17-20 March 2008

78. "Experimental and Kinetic Modeling Study of the Emission Spectrum from Laser-Induced Plasma in Air"; Paul Dagdigian, Valeri Babushok, Christopher Brown, Matthew Fisher, Santiago Palanco, Martin Richardson; North American Symposium on Laser Induced Breakdown Spectroscopy 2007 (New Orleans, LA, USA, 2007) 8-10 October 2007

79. "Modeling of the Development of Carbon and Polyethylene LIBS Plasmas- Study of Chemical Processing in the Plume"; Christopher Brown, Valeri Babushok, Paul Dagdigian, Santiago Palanco, Martin Richardson; North American Symposium on Laser Induced Breakdown Spectroscopy 2007 (New Orleans, LA, USA, 2007) 8-10 October 2007

80. "Stand-off Detection Technologies"; Santiago Palanco; North American Symposium on Laser Induced Breakdown Spectroscopy 2007 (New Orleans, LA, USA, 2007) 8-10 October 2007Invited paper.

81. "Use of a Hyper Michelson Interferometer for Multiple Pulse Femtosecond Laser-Induced Breakdown Spectroscopy in the Self-Channeled Mode"; Matthew Fisher, Santiago Palanco, Martin Richardson; North American Symposium on Laser Induced Breakdown Spectroscopy 2007 (New Orleans, LA, USA, 2007) 8-10 October 2007

82. "A Spectroscopic Analysis Study of Graphite Using LIBS and Semiempirical Calculations"; Ahmed Khalil, M. Ibrahim, Martin Richardson, Lewis Johnson; Laser Induced Breakdown Spectroscopy 2006 (Montreal, Canada, 2006) 5-8 September 2006

83. "Control of Filamentation for Enhancing Remote Detection with Laser Induced Breakdown Spectroscopy "; Matthew Fisher, Craig Siders, Eric Johnson, Oleksiy Andrusyak, Christopher Brown, Martin Richardson; SPIE Defense and Security Symposium , SPIE (Orlando, FL, USA, 2006) May 2006

84. "Femtosecond Interaction Studies for Stand-off LIBS"; Martin Richardson, Christopher Brown, Matthew Fisher, Robert Bernath; Laser Induced Breakdown Spectroscopy 2006 (Montreal, PQ, Canada) 5-8 September 2006

85. "New plasma regimes for stand-off LIBS"; Martin Richardson, Christopher Brown, Matthew Fisher, Robert Bernath, Simi George, Michael Sigman, Cleon Barnett, H. Bereket, Lewis Johnson, A Mizolek, Frank DeLucia; Laser Application to Chemical Security and Environmental Analysis, OSA (Incline Village, UT, USA) (2006)

86. "Remote Femtosecond Laser Induced Breakdown Spectroscopy (LIBS) in a Standoff Detection Regime."; Christopher Brown, Robert Bernath, Matthew Fisher, Martin Richardson, Michael Sigman, R.A. Walters, A Mizolek, H. Bereket, Lewis Johnson;SPIE Defense and Security Symposium , SPIE (Orlando, FL, USA) May 2006

87. "UV-Visible Spectra of Double pulse LIBS in Metals"; Ahmed Khalil, Martin Richardson, C. Barnett, Lewis Johnson; Laser Induced Breakdown Spectroscopy 2006 (Montreal, Canada, 2006) 5-8 September 2006

N. Batta, Y. F. Lu, X. W. Wang, J. Shi, D. W. Thompson, D. W. Doerr, D. R. Alexander, "Monitoring of steam laser cleaning using optical-probe techniques", The Sixth International Symposium on Laser Precision Microfabrication (LPM 2005, 4-8 April 2005, Radisson Fort Magruder Hotel and Conference Center Williamsburg, Virginia, USA)

ζ H. Wang, K. K. Mendu, Y. F. Lu, J. Shi, D. R. Alexander, D. W. Doerr, "Laser-assisted fabrication of 3-D structures on polymer film", The Sixth International Symposium on Laser Precision Microfabrication (LPM 2005, 4-8 April 2005, Radisson Fort Magruder Hotel and Conference Center Williamsburg, Virginia, USA)

ζ D. Alexander, D. Doerr, N. Singh, Q. Peng, J. Schiffen, "Femtosecond Laser Production of Silicon Nanoparticles and Metal Surfaces

having Nanostructures that are Broadband Absorbers." INVITED PAPER,(ICCE-12) Tenerife, Spain, August 1-6, 2005

↳ D. Alexander, J.S. Deogun, H.S. Hamza, J. Bruce III, C. Zulke, B. Koch, P. Le, "Quantum Dots Based Technology for multiple wavelength conversion" LEOS IEEE 18th, October 23-27, Sydney, Australia

↳ Jian Chao Li, Hai Feng Zhang, Dennis R. Alexander, David W. Doerr, "Characteristics of Ultrashort Laser Pulses Illumination of a Fresnel Zone Plate," Conference on Lasers and Electro-Optics Quantum Electronics and Laser Science Conference, Long Beach Convention Center, Long Beach, California, USA, May 22-25, 2006.

↳ Dennis Alexander, Jitender S. Deogun2, Haitham S. Hamza2, John Bruce III, Craig Zuhlke1, Brandon Koch, Pong Le "Quantum Dots Based Technology for Multiple Wavelength Conversion", IEEE, LEOS conference, Oct. 23., Sydney Australia, 2005

↳ Dennis R. Alexander, John Bruce III, "Femtosecond LIBS for Detection of Biological/Chemical Agents Nanomorphing/Stratigraphy ", Pacificchem 2005 Congress, INVITED, Honolulu, Hawaii, December, 2005.

↳ Jian Chao Li, HaiFeng Zhang, Dennis R. Alexander, David W. Doerr, "Characteristics of Ultrashort Laser Pulses Illumination of a Fresnel Zone Plate," Conference on Lasers and Electro-Optics Quantum Electronics and Laser Science Conference, Long Beach Convention Center, Long Beach, California, USA, May 22-25, 2006.

↳ D. Alexander, S. Mao, R. Russo, M. Richardson and R. Fedosejev, "Particle Generation in FS Laser Interactions," MURI Kickoff Meeting, August 8, 2006.

↳ D. Alexander, John Schiffern, David Doerr, "Dual Pulse Femtosecond Laser Fundamentals for the Detection of Biological, Chemical, and Explosives," LIBS 2006, September 4-9, Montreal Canada.

↳ D.R. Alexander, Jianchao Li, Haifeng Zhang, David W. Doerr, "Optical Communications with Femtosecond Lasers", SPIE INVITED Paper, Stockholm, Sweden, September 13, 2006.

↳ D. Alexander, John Schiffern, David Doerr, "Optimization of Collinear Dual Pulse Femtosecond Laser Induced Breakdown Spectroscopy of Silicon, EMLIBS Conference, Paris France, September 11, 2007.

↳ D. Alexander, John Schiffern, David Doerr, "Optimization of Collinear Dual Pulse Femtosecond Laser Induced Breakdown Spectroscopy of Silicon," NASLIBS, New Orleans, October 8-11, 2007.

↳ D. Alexander, "All Optical Multicast Devices and Switches Based on Nanotechnology and Micro Ring Cavities," Verizon, Invited, November 14, 2007.

↳ Dennis R. Alexadner, John Schiffern, and Victor A. Rivas, "Femtosecond laser Modified Surfaces for Enhanced Broadband Absorbers," Southeast Ultrafast Conference (SEUFC), January 10th and 11th 2008, University of Arkansas.

↳ Dennis R. Alexander, "Dual Pulse Femtosecond Spectroscopy for FLIBS and Issues Related to Femtosecond Pulse Propagation," DARPA working group meeting on Femtosecond Spectroscopy, Dr. Devanand Shenoy, Program Manager DARPA/MTO, February 28, 2008, Washington, DC.

↳ Dennis R. Alexander and John Bruce, "Collinear Dual Pulse-Dual Focus Enhancement of Femtosecond LIBS," LIBS 2008, International Conference on Laser Induce Breakdown Spectroscopy, September 22-26, Adlershof, Berlin, Germany, September 23, 2008.

↳ J. Bruce III, D. R. Alexander, "Fundamentals Associated with Collinear Dual Beam Dual Focus Femtosecond LIBS," LIBS 2009, New Orleans, July 13-15, 2009.

↳ E. Jackson, D. Admiraal, D. Alexander, J. Stansbury, J. Guo, D. Rundquist, and M. Drain. "Thermal Imaging for Discharge and Velocity Measurements in Open Channels," Proceedings 33rd Congress of the International Association of Hydraulic Research, Vancouver, Canada, 2009.

↳ J. Bruce III, D. R. Alexander, "Fundamentals Associated with Collinear Dual Beam Dual Focus Femtosecond LIBS," LIBS 2009, New Orleans, July 13-15, 2009.

↳ Troy Anderson, John Bruce III, and Dennis Alexander, "The Use of A "Bulls eye" Focal Distribution in a Dual-Pulse Arrangement for Efficient Interaction with Ejected Nanoparticles for Analytical LIBS," LIBS 2010, Memphis, Tennessee, August, 2010.

↳ John Bruce III, Troy Anderson, and Dennis Alexander, "Spatial Distribution of LIBS Plasma Emission Using A Dual Pulse Arrangement," LIBS 2010, Memphis, Tennessee, August, 2010.

↳ Troy Anderson, John Bruce III, and Dennis Alexander, "The Role of Nanoparticles and Dual Pulse Dual Focus in the Enhancement of LIBS Sensors for Detection ECBN, 27th Army Science Conference, November 28-December 2, Orlando, Florida, 2010.

↳ Craig Zuhlke, and John Bruce III, "Femtosecond Laser Production of Nanoparticles and Their Subsequent Layered Aggregate Growth Using a Line Focused Beam," 18th International Conference on Composites or Nano Engineering, Anchorage Alaska, ICCE July 4-10, 2010.

↳ Dennis R. Alexander, and John Bruce III, "Fundamentals of femtosecond laser induced breakdown spectroscopy: effects of focus location and short time emissions on the entrainment of atmospheric species," 2010 International Chemical Congress of Pacific Basin Societies, Honolulu, Hawaii, Sept. 15, 20, 2010.

↳ Dennis R. Alexander, "Modeling the Single-Cycle Laser Pulse Interaction with Matter," Invited Lecture, University of Tennessee Space Institute, March 24, 2011.

↳ Dennis R. Alexander, "Femtosecond Laser Surface Modification Processes for Producing Super-Hydrophobic/Super-Hydrophilic Material Properties" Invited Lecture, University of South Dakota, Chemistry Department, Smart Grid Presentation to All South Dakota Schools, November, 2011.

↳ T. Anderson, C. Zuhlke, J. Bruce III, D. Alexander, C. Parigger, "Evidence of near-field filaments and how sample location affects femtosecond LIBS," NASLIBS 2011: 3rd North American Symposium on Laser-Induced Breakdown Spectroscopy, Clearwater, USA, July 18-20, 2011.

↳ J. Bruce III, T. Anderson, D. Alexander, "An investigation of dual pulse femtosecond LIBS on aluminum", NASLIBS 2011: 3rd North American Symposium on Laser-Induced Breakdown Spectroscopy. Clearwater, USA. July 18-20, 2011.

• In the current report period, the UCB PI gave invited presentations in the following international conferences:

2010 Society of Engineering Science (SES) Technology Conference, invited

2010 NSF-MEXT Symposium on the Future of Nanotechnology, invited

2010 Julius Springer Applied Physics Forum, invited

2011 NSF Workshop on Laser Processing and Energy Applications, invited

2011 7th International Conference on Low Dimensional Structures and Devices, invited

2011 9th International Meeting of Pacific Rim Ceramic Societies, invited

2011 International Workshop on Nanomaterials for Clean Energy Conversion, invited

2011 1st Joint Workshop on Advanced Materials for Energy Conversion, invited/keynote

2011 2nd International Workshop on Renewable Energy, invited/keynote

2011 SPIE Optics and Photonics Conference, invited

Number of Presentations: 121.00

Non Peer-Reviewed Conference Proceeding publications (other than abstracts):

Received

Paper

03/29/2013 38.00 Yuan Liu, Matthieu Baudelet, Martin Richardson. Microwave-Assisted LIBS: Towards a New Tool for Trace Element Detection and Molecular Plasma Spectrochemistry, OSA LACSEA 2010. 2010/02/03 00:00:00, . . . ,

03/29/2013 39.00 Matthieu Baudelet, Christina Willis, Lawrence Shah, Martin Richardson. Tm-Fiber 2 ?m Laser for Laser-Induced Plasma Spectroscopy of Organic and Biological Materials, OSA Advances Solid State Photonics (ASSP). 2010/01/31 00:00:00, . . . ,

03/29/2013 40.00 Matthew Weidman, Matthieu Baudelet, Michael Sigman, Paul Dagdigan, Martin Richardson. Nd:YAG-CO2 Double-Pulse Laser Induced Breakdown Spectroscopy for Explosive Detection, OSA Advanced Solid-State Photonics (ASSP). 2010/01/31 00:00:00, . . . ,

03/29/2013 42.00 James Martin, Matthieu Baudelet, Matthew Weidman, Matthew Fisher, Candice Bridge, Christopher Brown, Michael Sigman, Paul Dagdigan, Martin Richardson. Stand-off detection of organic samples using filament-induced breakdown spectroscopy, SPIE Optics & Photonics. 2009/08/02 00:00:00, . . . ,

TOTAL:

4

Number of Non Peer-Reviewed Conference Proceeding publications (other than abstracts):

Peer-Reviewed Conference Proceeding publications (other than abstracts):

Received

Paper

TOTAL:

Number of Peer-Reviewed Conference Proceeding publications (other than abstracts):

(d) Manuscripts

03/29/2013 35.00 Yuan Liu, Matthieu baudelet, Martin Richardson. Moisture Measurement Using LIBS, *Laboratory Journal Europe* (06 2012)

03/29/2013 34.00 Yuan Liu, Bruno Bousquet, Matthieu Baudelet, Martin Richardson. Improvement of the sensitivity for the measurement of copper concentrations in soil by Microwave-Assisted Laser-Induced Breakdown Spectroscopy, *Spectrochimica Acta Part B: Atomic Spectroscopy* (02 2012)

03/29/2013 36.00 Caitlin Rinke, Mary Williams, Christopher Brown, Matthieu Baudelet, Martin Richardson, Michael Sigman. Discriminant analysis in the presence of interferences: Combined application of target factor analysis and a Bayesian soft-classifier, *Analytica Chimica Acta* (06 2012)

03/29/2013 37.00 Yuan Liu, Lionel Gigant, Matthieu Baudelet, Martin Richardson. Correlation between laser-induced breakdown spectroscopy signal and moisture content, *Spectrochimica Acta Part B: Atomic Spectroscopy* (03 2012)

03/29/2013 43.00 A.A.I. Khalil, M. Richardson, C. Barnett, L. Johnson. Double pulse UV laser induced breakdown spectroscopy of stainless steel, *Journal of Applied Spectroscopy* (03 2006)

04/05/2013 44.00 V.I. Babushok, F.C. DeLucia Jr., P.J. Dagdigian, J.L. Gottfried, C.A. Munson, M.J. Nusca, A.W. Mizolek. Kinetic modeling study of the laser-induced plasma plume of the explosive cyclotrimethylenetrinitramine (RDX), *Spectrochimica Acta Part B: Atomic Spectroscopy* (12 2006)

04/05/2013 45.00 A. Khachatrian, PJ Dagdigian. Laser-induced breakdown spectroscopy with laser irradiation on mid-infrared hydride stretch transitions: polystyrene, *Applied Physics B* (04 2009)

04/05/2013 46.00 Qianli Ma, Paul J Dagdigian. Kinetic model of atomic and molecular emissions in laser-induced breakdown spectroscopy of organic compounds, *Analytical and Bioanalytical Chemistry* (11 2010)

04/05/2013 47.00 John T. Schiffers, David W. Doerr, Dennis R. Alexander. Optimization of collinear double-pulse femtosecond laser-induced breakdown spectroscopy of silicon, *Spectrochimica Acta Part B: Atomic Spectroscopy* (12 2006)

04/05/2013 48.00 Ufuk Parali, Dennis R. Alexander. Interaction of a single-cycle laser pulse with a bound electron without ionization, *Optics Express* (05 2010)

04/05/2013 50.00 Craig Zuhlike, Dennis Alexander, John Bruce III, Natale Ianno, Chad Kamler, Weiqing Yang. Self Assembled nanoparticle aggregates from line focused femtosecond laser ablation, *Optics Express* (12 2009)

04/05/2013 51.00 Eric Manley, Jitender Deogun, Lisong Xu, Dennis Alexander. All-optical network coding, *Journal of Optical Communications and Networking* (04 2010)

04/05/2013 54.00 Junjie Li, Xuan Wang, Zhaoyang Chen, Jun Zhou, Samuel Mao, Jianming Cao. Real-time probing of ultrafast residual charge dynamics, *Applied Physics Letters* (08 2010)

04/05/2013 52.00 Cody Raml, Xiangnan He, Ming Han, Dennis Alexander, Yongfeng Lu. Raman Spectroscopy based on a Single-Crystal Sapphire Fiber, *Optics Letters* (04 2011)

04/05/2013 53.00 Amelie Veillere, Thomas Guillemet, Zhi Qiang Xie, Craig Zuhlke, Dennis Alexander, Jean-Francois Silvain, Jean-Marc Heintz, Namas Chandra, Yong Feng Lu. Influence of WC-Co Substrate Pretreatment on Diamond Film Deposition by Laser-Assisted Combustion Synthesis, Applied Materials and Interfaces (03 2011)

04/05/2013 55.00 Travis Owens, Samuel Mao, Erin Canfield, Costas Grigoropoulos, Xianglei Mao, Richard Russo. Ultrafast thin-film laser-induced breakdown spectroscopy of doped oxides, Applied Optics (05 2010)

04/05/2013 56.00 Junjie Li, Xuan Wang, Zhaoyang Chen, Richard Clinite, Samuel Mao, Pengfei Zhu, Zhengming Sheng, Jie Zhang, Jianming Cao. Ultrafast electron beam imaging of femosecond laser-induced plasma dynamics, Journal of Applied Physics (10 2009)

TOTAL: 17

Number of Manuscripts:

Books

Received Paper

04/05/2013 49.00 Ufuk Parali, Dennis R. Alexander. Modeling the interaction of a single-cycle laser pulse with a bound electron without ionization, Europe: Intech, (11 2010)

TOTAL: 1

Patents Submitted

LIBS Moisture Monitoring System

Wireless Laparoscopy

Femtosecond surface Modification Method for Increasing Surface Area and the release of small bubble

Enhanced Signal to Noise Ration Laser Induced Breakdown Spectroscopy (LIBS)

Femtosecond Nanomachines High Surface Electrodes for Super Capacitors and other Applications.

Patents Awarded

Laser Machining of Materials

~~Nano-particle/quantum dot based optical diode~~

Remote Chemical and Elemental Analysis by Ultra Fast Spectroscopy

Laser Scribing and Machining of Materials

Awards

Graduate Students

<u>NAME</u>	<u>PERCENT SUPPORTED</u>	Discipline
Diane Wong	0.75	
Qianli Ma	0.75	
Matthew Fisher	0.90	
Christopher Brown	0.75	
Matthew Weidmen	0.90	
Yuan Liu	0.75	
Caitlin Rinke	0.05	
Cheonha Jeon	0.75	
Khan Lim	0.10	
Gregory Katona	0.90	
Julien Cheiroux	0.60	
Marie Vangheluwe	0.10	
Shima Fardad	0.75	
David Doeer	0.75	
John Schiffern	0.60	
John Bruce III	0.90	
Craig Zuhlke	0.00	
Ufuk Parali	0.00	
Kimberly Bay	0.00	
Travis Owens	0.75	
Jorge Martinez	0.60	
FTE Equivalent:	11.65	
Total Number:	21	

Names of Post Doctorates

<u>NAME</u>	<u>PERCENT_SUPPORTED</u>
Ani Khachatrian	0.75
Santiago Palanco	0.90
Candice Bridge	0.00
Matthieu Baudelet	0.90
Troy Anderson	0.90
FTE Equivalent:	3.45
Total Number:	5

Names of Faculty Supported

<u>NAME</u>	<u>PERCENT_SUPPORTED</u>	National Academy Member
Paul Dagdigian	0.03	No
Martin Richardson	0.08	
Michael Sigman	0.00	
Dennis Alexander	0.08	
Samuel Mao	0.08	
Lewis Johnson	0.08	
FTE Equivalent:	0.35	
Total Number:	6	

Names of Under Graduate students supported

<u>NAME</u>	<u>PERCENT SUPPORTED</u>	Discipline
Lionel Gigant	0.10	Physics
Danielle Simmons	0.10	Physics
Mark Koehler	0.10	Physics
James Martin	0.90	Physics
Alex Sincore	0.10	Physics
Dorian Gomez	0.10	Physics
Craig Zhulke	0.00	Electrical Engineering
John Bruce	0.90	Electrical Engineering
Cody Raml	0.00	Electrical Engineering
Christopher Wilson	0.00	Electrical Engineering
Nick Roth	0.00	Electrical Engineering
FTE Equivalent:	2.30	
Total Number:	11	

Student Metrics

This section only applies to graduating undergraduates supported by this agreement in this reporting period

The number of undergraduates funded by this agreement who graduated during this period: 11.00

The number of undergraduates funded by this agreement who graduated during this period with a degree in science, mathematics, engineering, or technology fields:..... 11.00

The number of undergraduates funded by your agreement who graduated during this period and will continue to pursue a graduate or Ph.D. degree in science, mathematics, engineering, or technology fields:..... 10.00

Number of graduating undergraduates who achieved a 3.5 GPA to 4.0 (4.0 max scale):..... 6.00

Number of graduating undergraduates funded by a DoD funded Center of Excellence grant for Education, Research and Engineering:..... 0.00

The number of undergraduates funded by your agreement who graduated during this period and intend to work for the Department of Defense 5.00

The number of undergraduates funded by your agreement who graduated during this period and will receive scholarships or fellowships for further studies in science, mathematics, engineering or technology fields: 4.00

Names of Personnel receiving masters degrees

<u>NAME</u>
Matthew Fisher
Total Number:

1

Names of personnel receiving PHDs

<u>NAME</u>
Diane Wong
Christopher Brown
Matthew Weidman
Caitlin Rinke
John Bruce III
John Schiffen
Craig Zuhlke
Total Number:

7

Names of other research staff

<u>NAME</u>	<u>PERCENT SUPPORTED</u>
FTE Equivalent:	
Total Number:	

1 a. University of California - Berkeley

1 b. Sponsored Projects Office

The Regents of the University of Califor

Berkeley

CA

947045940

Sub Contractor Numbers (c):

Patent Clause Number (d-1):

Patent Date (d-2):

Work Description (e):

Sub Contract Award Date (f-1):

Sub Contract Est Completion Date(f-2):

1 a. University of Nebraska

1 b. Research Grants and Contracts

303 Administration Building

Lincoln

NE

658880430

Sub Contractor Numbers (c):

Patent Clause Number (d-1):

Patent Date (d-2):

Work Description (e):

Sub Contract Award Date (f-1):

Sub Contract Est Completion Date(f-2):

1 a. University of Nebraska

1 b. Board of Regents, Univ of Nebraska, Un

312 N 14th Street

Lincoln

NE

685880430

Sub Contractor Numbers (c):

Patent Clause Number (d-1):

Patent Date (d-2):

Work Description (e):

Sub Contract Award Date (f-1):

Sub Contract Est Completion Date(f-2):

Inventions (DD882)

Scientific Progress

Technology Transfer

US Army Research Office Grant # W911NF-06-1-0446
(Reporting Period: August 1, 2006 – July 31, 2012)

Ultrafast Laser Interaction Processes for LIBS and other sensing technologies.

Martin Richardson, Michael Sigman,
Matthieu Baudelet, Candice Bridge, Santiago Palanco,
Matthew Fisher, Christopher Brown, Yuan Liu, Matthew Weidman,
Cheonha Jeon, Khan Lim, Caitlin Rinke,
Lionel Gigant, Danielle Simmons, Mark Koehler, James Martin,
Matthew Chun

Townes Laser Institute, CREOL – The College of Optics & Photonics,
University of Central Florida, Orlando, FL 32816

REPORT

OBJECTIVE OF THE PROJECT

The overall objective of this MURI program is to obtain a comprehensive understanding of the interaction of ultrafast femtosecond laser pulses with matter, with specific reference to the detection of trace elements of materials by techniques such as LIBS and Raman spectroscopy. The UCF team forms the core effort for this MURI, and is concentrating on femtosecond (and nanosecond) LIBS interaction science, self-channeling of femtosecond laser radiation and stand-off detection techniques, trace explosives detection, chemometrics and plasma modeling. The other members of the MURI bring key areas of expertise to the program. University of Nebraska, Lincoln (UNL- Dennis Alexander) in femtosecond LIBS, nanoparticles and fundamental interactions, University of California, Berkeley (UCB – Samuel Mao) in theory and experiments in the early stages of femtosecond laser materials interaction, Johns Hopkins University (JHU – Paul Daggigian) in kinetics theory and LIBS spectroscopy, and Florida A&M University (FAMU- Lewis Johnson) in femtosecond and ns LIBS.

APPROACH

1. Plasma modeling with a 1-D hydrodynamic code of plasmas from organic mass limited droplets
2. High-resolution plasma diagnostics
3. Enhancement of LIBS signals
4. Use of laser filaments towards very large distance sensing
5. Quantification of LIBS in all its analysis from line assignment to decision making

ACCOMPLISHMENTS

PLASMA MODELING WITH A 1-D HYDRODYNAMIC CODE OF PLASMAS FROM ORGANIC MASS LIMITED DROPLETS

Comparison between plasma modeling and organic mass limited plasmas

Motivation

Optimizing parameters such as the shot-to-shot stability, signal-to-noise ratio, and the gate delay and gate width are not enough to fully explain all of the processes involved in the plasma generation on organics. A greater understanding of the fundamental LIBS interaction with organics would serve to improve detection methods thus improving the sensing technique. As such, fundamental LIBS experiments that explored the plasma emission of simple organics were conducted. These experiments were designed with the intended purpose of exploring the ambiguity in the resulting spectral emission of LIBS plasmas from both the sample and the surrounding ambient atmosphere of organics. With this goal in mind, it was necessary to create samples with well-known constitutions that could be explored under a variety of controlled atmospheric conditions.

The Laser & Plasma Laboratory has become adept at designing and modeling mass-limited droplets for the purpose of Extreme Ultraviolet Lithography source development and the

technology was adapted for use with LIBS. Utilizing the mass-limited target concept allowed for liquid droplets of known size and a known quantity of organic material to be constructed. In addition, the known spherical geometry of the droplet allows for an isotropic expansion of the LIBS plasma plume, which in theory would make observation of the plasma similar from all collection angles. The expansion in the experimental regime could be considered as a pseudo 1D expansion, and thus can be modeled using a 1-dimensional theoretical code.

The investigation of the behavior of complex physical systems has traditionally been carried out through both experiments and theory. With the advent of the laser, both approaches have been used to study, analyze and predict the results of laser-induced plasmas. Laser fusion plasmas have been extensively studied. However, LIBS plasmas, (which have lower densities and lower temperatures in comparison with fusion plasmas) have not been studied as significantly, due to the numerous physical and chemical processes that cannot be neglected. The idea of using computer simulations to study and analyze plasmas is over fifty years old. As a result it has become a very large and extensive subject, employing a wide range of techniques and attacking a vast array of physical problems¹. In fact, every experimental technique that is currently accepted by the analytical community has a modeling effort behind it. Computer simulations of plasmas can be divided into many categories with the equilibrium models being the most prevalent in this case. Equilibrium models consist of thermodynamic equilibrium (TE), local thermodynamic equilibrium (LTE), partial local thermal equilibrium (PLTE), model of coronal equilibrium (MCE), and collisional-radiative model (CRM)². While these codes are often used to describe the LIBS plasma, they often have to be modified in order to be accurate. The LIBS plasma does not begin in equilibrium; in fact due to the small momentum transfer in collisions between bodies of very different masses, time scales for equilibrium between electrons and atoms can be very long³.

Modeling a LIBS plasma is a very difficult task in which complex problems such as determining the equilibrium rate may arise. Many models focus on the physics of the propagation and expansion of the plasma, frequently opting to concentrate on a particular aspect. For instance, there are three models that are often used to model the expansion and propagation of the plasma: the laser-supported combustion (LSC), the laser-supported detonation (LSD), and the laser-supported radiation (LSR). They differ in their predictions of the opacity and energy transfer properties of the plasma to the ambient atmosphere. At the low irradiances used in LIBS experiments, the models that most closely match experiment are LSC and LSD. This is due to the relatively low temperature and density of the plasma⁴.

¹ A. R. Bell, *Astrophysics and Space Science* 256, (1998), 13.

² V. Ochkin, *Spectroscopy of Low Temperature Plasma*, (WILEY-VCH Verlag GmbH & Co. KGaA, Weinheim, 2009).

³ V. I. Babushok, "Processes Induced by the LIBS Technique," (2005).

⁴ A. W. Mizolek, V. Palleschi, and I. Schechter, eds., *Laser-Induced Breakdown Spectroscopy (LIBS) Fundamentals and Applications* (Cambridge University Press, Cambridge, 2006).

More recently, models for laser-induced plasmas have become more sophisticated and have started to incorporate both chemistry and physics. One code, NEQAIR96, has been used to compute the emission and absorption spectra for atomic and diatomic molecules, as well as the transport of radiation through a non-uniform gas mixture to a surface⁵. In another code (which has been developed as a computational model by Dors and Parigger⁶) plasma equilibrium kinetics are implemented in ionized regions, and non-equilibrium, multi-step, finite-rate reactions are implemented in non-ionized regions. The computational fluid dynamics model predicts species concentrations, free electron number density decay, blast wave formation and dynamics, and flow field interactions of the laser spark decay as a function of time⁴. While codes have started to implement chemistry and physics, the incorporation of both is just rudimentary, meaning that neither of the two is allowed to fully evolve. The LIBS plasma is unique in that both chemistry and physics play an active role, and the augmentation of either role can lead to a misinterpretation of experimental results.

rate reactions are implemented in non-ionized regions. The computational fluid dynamics model predicts species concentrations, free electron number density decay, blast wave formation and dynamics, and flow field interactions of the laser spark decay as a function of time⁴. While codes have started to implement chemistry and physics, the incorporation of both is just rudimentary, meaning that neither of the two is allowed to fully evolve. The LIBS plasma is unique in that both chemistry and physics play an active role, and the augmentation of either role can lead to a misinterpretation of experimental results.

MEDUSA Code

Med103⁷ or Medusa is a one dimensional Lagrangian hydrodynamic code that contains models of most laser-plasma coupling physics, electron, and radiation transport. It was initially developed for the application of inertial confinement fusion, however it can be adapted for lower temperature plasmas. In the code, the electrons and ions are treated as interpenetrating fluids, and Maxwell's Equations along with fluid mechanics is used to describe the plasma state. Propagation of the plasma is conducted using a Lagrangian hydrodynamics code in order to allow for longer simulation times however, the longer simulation time does not come without a cost. The gain of modeling a much larger system for a significant length of time forces the reduction of the information content for the simulation. Only, the crudest velocity space information is kept such as the root mean square particle velocity (the temperature), the mean particle mass drift velocity (the fluid velocity), and the electron drift velocity relative to the ions (the electric current)⁸. The electron and ion densities and temperatures, average ion state, and

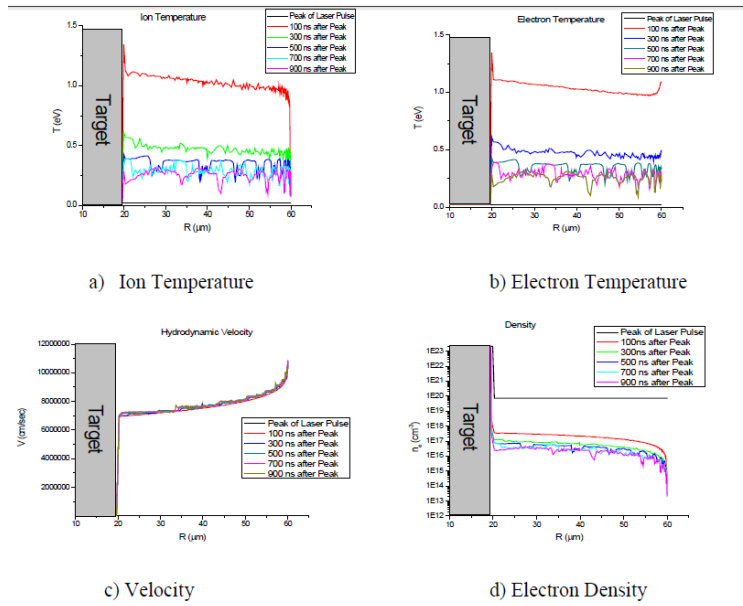


Figure 1. Figure 1 (a-d): MED103 calculations of T_i , T_e , v , n_e , respectively, at various times of a 5 ns laser pulse for a graphite target.

⁵ E. E. Whiting, C. Park, Y. Liu, J. O. Arnold, and J. A. Paterson, NASA Reference Publication 1389, (1996).
⁶ I. Dors, and C. Parigger, Appl. Optic 42, (2003), 5978
⁷ J. P. Christiansen, D. E. T. F. Ashby, and K. V. Roberts, Comp. Phys. Comm. 7, (1974), 271.
⁸ A. R. Bell, Astrophysics and Space Science 256, (1998), 13

plasma parameters such as the viscosity, velocity, and pressure are determined in each individual cell.

Medusa solves the group of equations in a moving frame numerically for the simple case in one dimension. The equations are solved using the Crank-Nicholson scheme and the Gauss elimination method and several iterations are performed at each time-step. As a result the Medusa code yields four dependent variables: the electron and ion, the density, and the velocity at each position as a function of time. From these four variables, other plasma properties such as the plasma expansion, plasma radiation, etc. can be determined. Examples of Medusa results can be found below. The code uses cells as means to calculate energy balance transport in a self-consistent manner over a number of time steps. The ion and electron temperatures are solved using the Navier-Stokes equation and are supplemented.

Strategy

Alternative techniques and methods are necessary to characterize LIBS plasmas on nonmetallic and organic samples as traditional methods cannot be successfully utilized, due to the limited number of emitters in the visible range. Without atomic emitters of different upper energy levels, the necessary conditions to construct a Saha-Boltzmann plot are unmet and thus temperature calculations become nontrivial. The interdependency between the density and temperature result in arduous calculations for the density, and thus the characterization of the plasma becomes problematic. For these reasons we have employed an alternative strategy for characterizing the plasma emission from organics that includes the use of a theoretical code to model the plasma expansion and predict the plasma parameters such as the electron and ion densities and temperatures. In this new strategy for examining organics organic signatures, LIBS was conducted on mass-limited droplets doped with simple molecules. Initial studies were first conducted with water droplets doped with copper-sulfate in order to characterize the plasma in a vacuum environment. The vacuum environment was selected as a method of minimizing the skewing effects caused by the radical recombination with the nitrogen and oxygen molecules present in an ambient air atmosphere. In this environment it was first assumed that the spectroscopic signatures obtained are characteristic of the samples alone. The copper lines from $\text{CuSO}_4 + \text{H}_2\text{O}$ were utilized to characterize the plasma through the traditional method of calculating the plasma temperature and electronic density from a Saha-Boltzmann plot and the hydrogen alpha line broadening, respectively. The experiment was then modeled using the Medusa code, and the theoretical results were compared with the experimental. If the theoretical results could be shown to accurately model the experimental results then the code could be used as a method of characterizing plasma emission from samples in which traditional techniques could not be used. Lastly, organic molecules were qualitatively compared and examined to determine if a distinction between the molecules could be made based on contributions from the CN emission. Spectroscopic signatures taken under both an argon and air environment were compared against spectra taken under vacuum. The use of mass limited droplets may give insight into distinguishing molecules that have a CN bond, and molecules that exhibit CN emission due to atmospheric recombination.

Experimental setup

The major components in the organic mass-droplet system were the laser and the vacuum chamber for the LIBS plasma generation. The instrumentation included an Echelle spectrometer

(spectrometer port), an energy detector (energy meter) for energy measurements, and a webcam (the imaging port) which was used to observe droplet flow consistency. A picture of the 12-port- $\frac{1}{4}$ cylindrical vacuum chamber and the setup within the chamber is shown below in Figure 2. Further details of the experimental setup, target droplet generation, analytical and theoretical methods used in the experiment are described in the following sections.

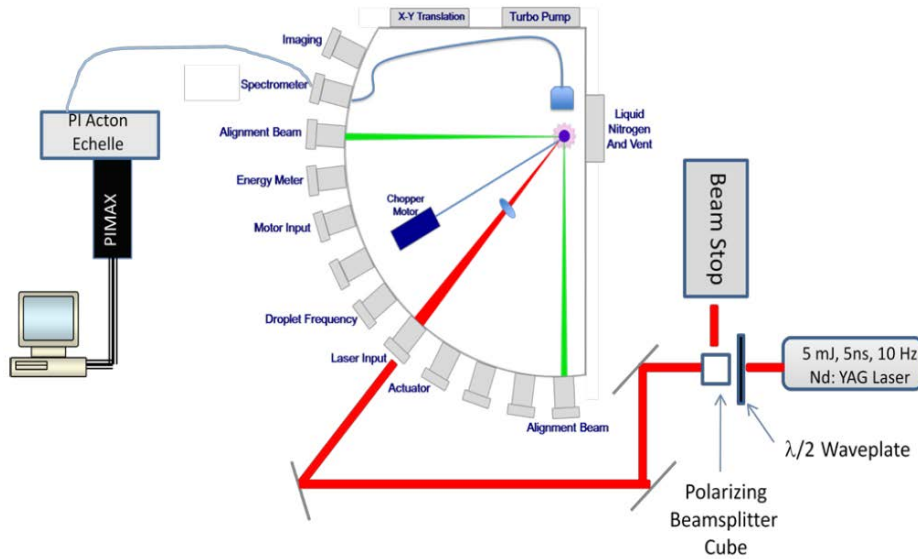


Figure 2. The vacuum chamber and important ports.

The laser (Brilliant, Quantel) was operated at its fundamental wavelength of 1064 nm and a repetition rate of 10 Hz. After passing through a light valve the laser produced a p-polarized pulse of 11.7 mJ per pulse and pulse duration (FWHM) of 6 ns. Other laser parameters are shown in the table below

Table 1. Laser statistics for 1064 nm over 500 shots at 10 Hz

Maximum Value (mJ)	11.9
Minimum Value (mJ)	11.7
Average Value (mJ)	11.7
Standard Deviation (μ J)	87
RMS Stability (%)	0.7447
Point-to-Point Stability (%)	4.306

Following the light valve, the beam was directed into the vacuum chamber and the target droplets were placed near the rear of the chamber. The laser beam was focused onto the target droplets using a 25.4 mm diameter, anti-reflection coated 50 mm focal length plano-convex lens, as illustrated in Figure 3.

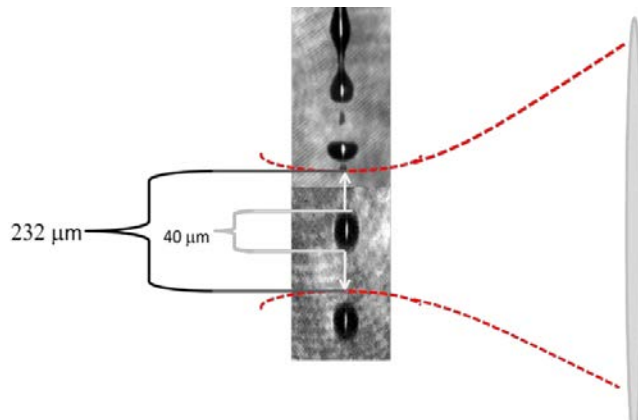


Figure 3. Laser being focused on 40 μm droplets

A knife-edge scan⁹, was conducted to measure the beam size and the focus through the 50 mm focal lens. The knife-edge scan yielded a beam waist of 232 μm , a focus of 51 mm, and a Rayleigh range of 3 mm. This resulted in an irradiance of 3.85 GW/cm². The laser's focus was aligned using green alignment Helium-Neon lasers, and the droplets and the observation optics were focused on this point.

Droplet target

LPL has become adept at designing and modeling mass-limited droplets for EUV source technology²¹⁶⁻²¹⁹. Unlike the high Z tin-chloride droplets constructed for EUV purposes, the materials selected for droplets in these studies were copper-sulfate pentahydrate ($\text{CuSO}_4 \cdot 5\text{H}_2\text{O}$), dimethylamine ($(\text{CH}_3)_2\text{NH}$), methanol (CH_3OH), and water (H_2O). The copper-sulfate pentahydrate was selected for its copper component which could be used to characterize the plasma. Water was selected due to its simplicity in chemical structure. The dimethylamine and methanol were selected in order to explore the CN band structure which is inherent in one sample and may occur in both due to recombination. It was necessary to dope 100 mL of water with 32 g of copper-sulfate pentahydrate, which came in crystal form, to yield a copper-sulfate-water solution. The dimethylamine came in an aqueous solution with 0.89 g of dimethylamine per mL of water. Calculations were done in order to determine the number of atoms present in each of the 40 μm droplets. The results are shown in Table 2.

Table 2. Number of atoms for each of the elements in the respective liquids

Copper Sulfate Pentahydrate Solution		Methanol	
Element	Number of Atoms	Element	Number of Atoms
Cu	$2.27 * 10^{13}$	C	$4.98 * 10^{14}$
S	$2.27 * 10^{13}$	H	$2.00 * 10^{15}$
H	$2.82 * 10^{15}$	O	$4.98 * 10^{14}$
O	$1.50 * 10^{15}$		

Dimethylamine Solution		Water	
Element	Number of Atoms	Element	Number of Atoms
N	$3.55 * 10^{13}$	H	$2.23 * 10^{15}$
C	$7.10 * 10^{13}$	O	$1.12 * 10^{15}$
H	$4.03 * 10^{15}$		
O	$1.02 * 10^{15}$		

Time-resolved spectral measurements were made in the same spectral range as a function of the detection delay. Spectral data was acquired by integrating the individual spectra from 15 to 25

⁹ CREOL, "Experiment I: The HeNE Laser," in *OSE 6525 L*, (University of Central Florida, Orlando, 2006).

shots (dependent on the sample and the environment) in order to acquire a signal-to-noise of at least 1:1.20, which was focused on the hydrogen alpha line as it was necessary for the electron density calculations. The number of integrated spectra ranged from. It was assumed that the mass-limited droplets were homogenous, and thus each droplet was equal in constitution to the next.

For each delay, twenty-five spectra were taken with a gate width of 20, 30, or 40 ns depending on the lifetime of the plasma. The twenty-five spectra were divided into groups of five, where each group was summed to yield a total of five spectra for each delay. The five spectra allowed for calculation of mean line intensities and associated relative standard deviations. The table below displays the specifics for each sample.

Table 3. Number of integrated spectra and gate width for each sample in each environment.

Sample	Environment	Gate Width (ns)	Number of Integrated Spectra
Copper- Sulfate Pentahydrate	Vacuum	20	35
	Argon	20	20
	Air	20	20
Water	Vacuum	20	25
	Argon	40	15
	Air	30	15
Methanol	Vacuum	20	50
	Argon	30	15
	Air	20	15
Dimethylamine	Vacuum	20	50
	Argon	40	30
	Air	20	30

It should be noted that the vacuum regime required the most number of integrated spectra due to the lower emission intensity. Additionally, the long lifetime of the plasma in the argon regime requires a larger gate width in order to cover the temporal range.

Droplet generation

Capillaries were used to generate liquid droplets of approximately 40 μm in diameter. The liquids were placed in a pressurized reservoir which using compressed nitrogen and maintained at a fluid backpressure of 1000 kPa. The pressurization of the reservoir served to help force the liquid through the capillary. The capillaries that were used in this study had a 10 μm diameter and were made of glass. A square wave voltage signal was used to drive a piezo-crystal, which in turn resonantly drove the glass capillary allowing droplets to be formed. While frequencies ranging from 10 kHz – 200 kHz could be obtained, a typical frequency of 20 kHz was used for the droplet generation in these studies. To synchronize the laser with the droplets, a portion of the capillary driving signal was directed into a phase-locked loop electronics that triggered the flash-lamps of the Brilliant laser. Inherent delays between the flash-lamps, the Q-switch, and the emission of the laser light had to be accounted for in the synchronization system. Full synchronization was accomplished by adjusting the delay between the droplet formation and the flash-lamp trigger. A web-camera monitored the laser interaction with the droplets in order to verify that the laser was ionizing the droplets. The substantial difference between the laser repetition rate and the droplet repetition rate required that unused droplets be collected in order

to preserve the vacuum levels in the chamber. In this study the laser irradiated one droplet in every two thousand droplets leaving 1,999 droplets to be collected by a cryogenic trap. The trap was cooled by liquid nitrogen, and was equipped with an electronic chopper to prevent the formation of ice crystals as shown in Figure 4. Water droplets have been characterized in the study conducted by Keyser¹⁰. Once the 40 μm droplet had been achieved, an image was recorded by a Logitech web-camera. The droplets were then measured in diameter against the water droplet for consistency of droplet size. The web camera also served as a method of determining when the droplet had strayed from the laser focus.

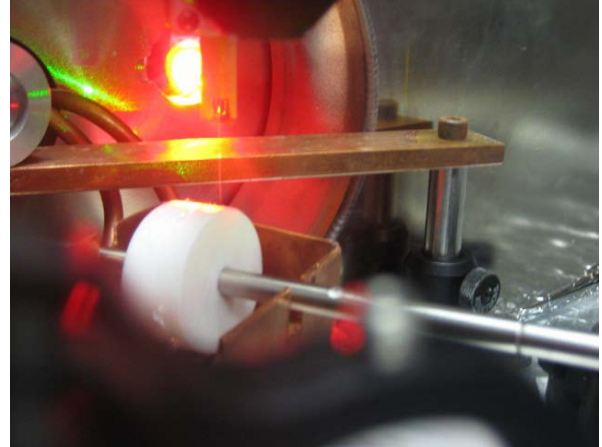


Figure 4. Cryogenic cooled droplet trap with the electric chopper (white wheel).

Medusa Code Assumptions

The MEDUSA code was selected to model the hydrodynamic expansion of the plasma. In order to do so however, the code had to make some assumptions that would cause the results to differ from the experimental. The initial assumption of the code begins with a two stream fluid that has free electrons and ions, which as discussed in Chapter 2 is not the initial point of a laser-induced plasma. The plasma is treated as a two component fluid in which one subsystem or fluid describes the electrons and the other the ions.

The laser-plasma coupling physics, electron, and radiation transport as shown above are incorporated and treated in the code.

Medusa assumes that there is charge neutrality between the two fluids which requires that both systems share the same velocity. This allows for a single equation of motion to describe both systems:

$$\rho \frac{du}{dt} = - \frac{dp}{dx}$$

where ρ is the mass density, u is the fluid velocity and $p = p_e + p_i$ is the hydrodynamic pressure. The electrons and ion fluids are further governed by an energy equation in which the absorbed laser energy is partitioned into both hydrodynamic and kinetic states. The energy equation is described as:

$$C_v \frac{dT}{dt} + B_T \frac{dp}{dt} + p \frac{dv}{dt} = S_{e,i}$$

where $C_v = (\partial U / \partial T) \rho$ is the specific heat per unit volume, $B_T = (\partial U / \partial \rho)_T$ describes the variation of internal energy due to the interaction between particles within the same subsystem, and $U = pV/(\gamma-1)$ is the internal energy per unit mass, and $S_{e,i}$ is the rate of energy input per unit mass for either the electrons or ions respectively¹¹. The S_e term represents the electron energy source and is composed of electron-ion energy exchange, Bremsstrahlung, laser absorption, and

¹⁰ C. Keyser, "Optical and spectral characterization of the water droplet laser plasma EUV source," in *Physics*, (University of Central Florida, Orlando, 1994).

¹¹ J. P. Christiansen, D. E. T. F. Ashby, and K. V. Roberts, *Comp. Phys. Comm.* 7, (1974), 271.s

thermal conduction terms. As only the electrons absorb the laser light they exchange energy with the ions through electron-ion collisions making the electron-ion energy exchange term common to both S_e and S_i . In addition to the electron-ion energy exchange, the ion energy source S_i is comprised of thermal conduction, and shock heating terms.

In most laser-produced plasmas or unmagnetized plasmas the major energy transport mechanism is diffusive conduction from cold electrons²²¹. The thermal electron energy flux is given by:

$$q_e = -\frac{1}{3} \lambda_e v_e k \nabla T_e = -K \nabla T_e$$

where λ_e is the average mean free path for electrons in multiple Coulomb collisions with ions which are deflected off at 90° angle and is expressed as:

$$\lambda_e = 1.12 \times 10^7 \frac{T_e^2}{z n_e \ln \Lambda}$$

And K is the classical Spitzer-Harm conductivity which is defined as:

$$K = 2 \times 10^{-4} \frac{T_e^{5/2}}{z \ln \Lambda}$$

The Spitzer-Harm conductivity is only valid if $\lambda_e/L \leq 10^{-2}$, where $L = T/(dT/dx)$ is the temperature scale length¹². In terms of heat flow (q), the Spitzer-Harm conductivity is valid only when $q/q_f \leq 2.4 \times 10^{-2}$, where q_f is associated with all electrons streaming in the same direction and is known as the free streaming limit of the heat flow and is defined as¹¹:

$$q_f = n_e k T_e \left(\frac{k T_e}{m_e} \right)^{1/2}$$

The Spitzer-Harm conductivity does not properly describe laser plasmas, as most laser produced plasmas have steep temperature and density gradients, and has been shown from numerical solutions to the Fokker-Planck equation to overestimate the heat flow¹¹. Medusa accounts for this multiplying the free streaming limit (q_f) by an adjustable parameter f , known as the flux limiter. This circumvents the overestimation by restricting the heat flux to the harmonic mean:

$$\frac{1}{q'_e} = \frac{1}{q_e} + \frac{1}{f \cdot q_f}$$

As a flexible parameter f is usually adjusted to match experimental results and is typically given a value of 0.1¹³

Experimental Results Compared to Theoretical Results

For the purpose of these studies MEDUSA will be used as a diagnostic tool for acquiring plasma parameters that cannot be calculated by traditional methods such as Stark broadening and Boltzman plots for the electronic density and the plasma temperature under the assumption of LTE respectively. The assumed environment in MEDUSA is a vacuum atmosphere and as such to accurately model and represent the LIBS studies, the experiments were also conducted in

¹² C. Keyser, "Optical and spectral characterization of the water droplet laser plasma EUV source," in *Physics*, (University of Central Florida, Orlando, 1994).

¹³ A. Djaoui, "A User Guide for the Laser-Plasma Simulation Code: MED103," (The Central Laboratory of the Research Councils, Rutherford Appleton Laboratory, Oxfordshire, 1996).

vacuum. Copper-sulfate pentahydrate was explored as the initial sample, as the copper lines could be used to characterize the plasma, and compare the electron density and electron temperature against those predicted by MEDUSA.

The collection of the LIBS signal began immediately as soon as the laser interacted with the target. However line emission was not detectable in the first 10 ns as shown below, due to the broad continuum emission.

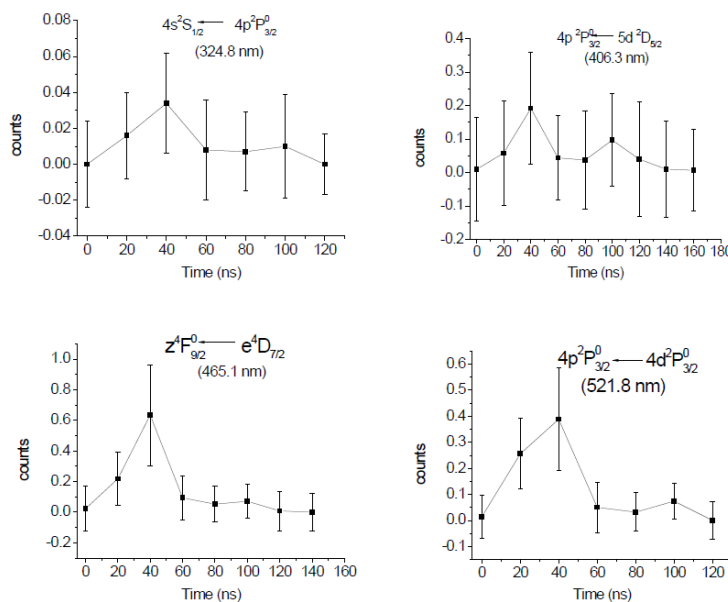


Figure 6. Cu I line emissions as a function of time under vacuum.

temporal window of detection of 20 ns. The temperature was calculated based on these copper line transitions and are shown below in Figure 95.

The temperature from the copper-sulfate pentahydrate reaches peak of 0.81 eV ($\pm 3\%$) throughout the emission of the copper lines. The copper lines which prevent further temperature calculations are the transitions of 521.8 nm and 324.8 nm lines, as their emission is indistinguishable from the background. As there was no emission from any of the lines at time 0, the graph starts at 20 ns. Exploration of the plasma closer to its initialization should be studied in order to assess the early plasma constituents, but is prevented due to the emission from the continuum (bremsstrahlung and recombination radiation), and the finite gate width of the iCCD camera due to various electronic limitations. As discussed in Chapter 4, in order to calculate the electron density it was necessary to measure the Stark Broadening of the H_a line (656.6 nm). Using the temperatures and Equation 4.4.3, the electron densities were approximated with the fractional intensity width of hydrogen which had to be determined from the tables listed in

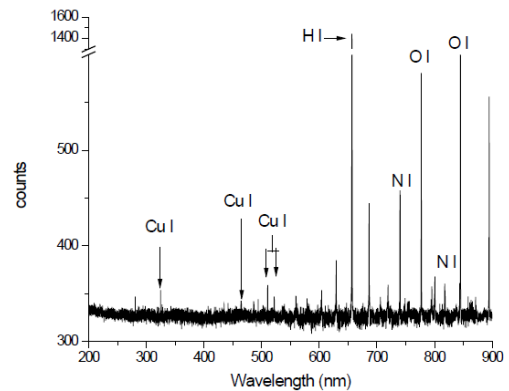


Figure 5 Copper-sulfate pentahydrate taken under a vacuum environment.

The copper lines peak at approximately 40 ns after the laser pulse has interacted with the sample. The 465 nm copper line had the strongest emission while the 324 nm had the lowest emission. The absence of intensities before the 40 ns can be attributed to the free-free transitions and free-bound transitions that precede the bound-bound transitions which do not emit specific line emissions that can be used for temperature measurements. The rapid decay after the peak indicates may be attributed to the free expansion of the plasma in the vacuum. The expansion may have been too rapid for measurements in

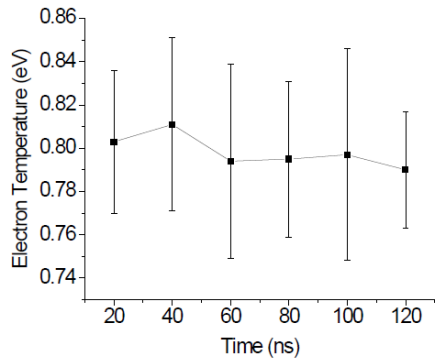


Figure 8. Copper-sulfate pentahydrate temperature under vacuum taken at various times.

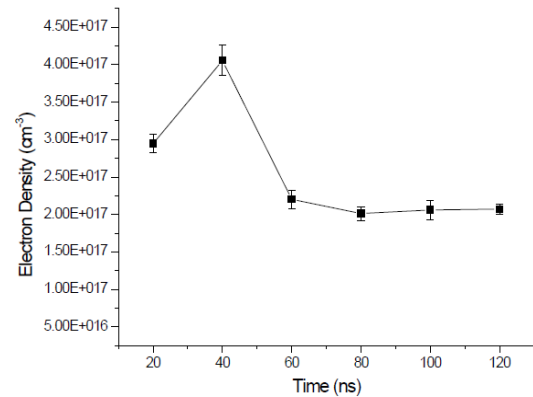


Figure 7. Experimental electron density for a copper-sulfate pentahydrate plasma

Appendix III of Griem's, *Spectral Line Broadening by Plasmas*¹⁸⁸. The parameters for determining the electron densities and the densities themselves are displayed in Table 4 and Figure 95, respectively.

Table 4. Electron densities and the parameters necessary for their calculation

Time (ns)	Temp (eV)	Temp Error (eV)	H α Stark Broadening (nm)	Balmer Alpha (2, 3) alpha (1/2)	Electron Density (cm ⁻³)	Density error (cm ⁻³)
20	0.803	0.033	0.4428	0.0186	2.946E+17	1.211E+16
40	0.811	0.04	0.5481	0.0186	4.057E+17	2.001E+16
60	0.794	0.045	0.3648	0.0186	2.203E+17	1.255E+16
80	0.795	0.036	0.3435	0.0186	2.013E+17	9.116E+15
100	0.797	0.049	0.3491	0.0186	2.062E+17	1.268E+16
120	0.79	0.027	0.3504	0.0186	2.073E+17	7.086E+15

The maximum density of $4.06 \times 10^{17} \text{ cm}^{-3}$ occurs at 40 ns and rapidly decays after this point to a density of $2.07 \times 10^{17} \text{ cm}^{-3}$.

MEDUSA was used to model the experimental conditions and the expansion of the plasma in terms of the electron density is shown below in Figure 10.

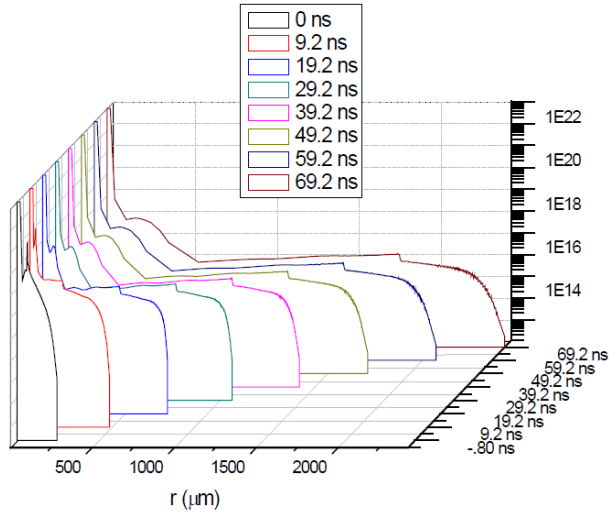


Figure 9. Electron density evolution as the plasma expands away from the center of $\text{CuSO}_4+5\text{H}_2\text{O}$ doped water droplet.

The timescale on the right-hand side of the figure represents the time relative to the peak of the laser pulse. The peak electron temperature of 0.81 eV and density of $4.06 \times 10^{17} \text{ cm}^{-3}$ which occur at 40 ns were used to match conditions for the MEDUSA predictions. These parameters allowed for the temporal and spatial location of the emission from the plasma to be identified.

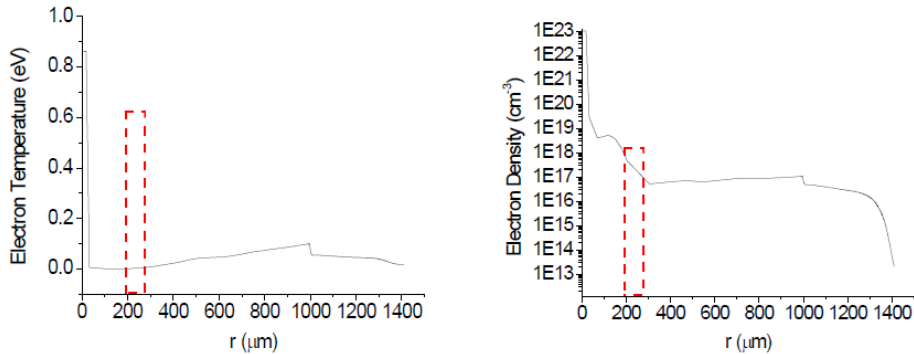


Figure 10. Predicted results for the electron temperature and density at 40 ns using MEDUSA. The red lines show the location of the experimental measurements

From the MEDUSA predictions the emissions from the copper lines occur in the corona of the plasma. The electron density range of 10^{17} cm^{-3} occurs at a distance approximately 190 - 280 μm away from the center of the $\text{CuSO}_4+5\text{H}_2\text{O}$ doped water droplet. The electron temperature was observed in the same interval and the temperatures range between 0.001 to 0.007 eV. In order to achieve an electron temperature of 0.81 eV MEDUSA predicts that the emission would occur at approximately 25 μm from the center of the droplet.

The discrepancy between the electron temperature and electron density location is attributed to the lower LIBS plasma temperature, as MEDUSA was designed to model fusion plasma temperatures which can range from 200 – 300 eV. Fusion temperature and densities are often achieved with intensities of approximately 10^{14} W/cm^2 whereas plasmas used for LIBS studies on

average range from 10^8 - 10^9 W/cm². In addition the experimental temperature was calculated by fitting a Boltzmann distribution to the emission lines that occur after the Planckian emission has ceased to dominate the spectrum. The MEDUSA code alternatively uses a Planckian model to calculate the temperature and does not include a subroutine which handles ionization temperatures.

Discussion

Comparison of the experimental and the theoretical results show that it may be possible to utilize the MEDUSA code as a diagnostic tool if appropriate assumptions are made. The hydrodynamic expansion calculations tend to follow the same patterns as the experimental results, but fine tuning the simulation may yield more accurate results, as the code was designed to model higher temperature and higher density plasmas. There will be a limit to the accuracy of the code as it does not include important chemical reactions that can extend the lifetime of the plasma emission via recombination.

Another modification that can improve the accuracy of MEDUSA includes either adding a laser ablation component to the code, or feeding in appropriate initial conditions calculated from an ablation code. As discussed in Chapter 2, laser ablation plays a critical role in the formation and expansion of plasma. While MEDUSA does allow for the user to suitably model the laser parameters and target composition, the initial free electrons and ions temperature make it difficult to pinpoint an agreement in the time domain where the simulations complement the experimental results. Additional knowledge and understanding also needs to be gained on the experimental side as to the initial plasma temperatures.

The continuum emission has classically been attributed to the combined effects of Bremsstrahlung (free-free transitions) and radiative recombination (free-bound) transitions^{124, 224}. Studies have linked the observed spectral continuum directly to both the electron and ion density and the electron temperature²²⁴⁻²²⁶. However, in using this approach towards non-hydrogenic plasmas this approach is non-trivial due to the lack of cross section data and the approximations necessary to determine correction factors. De Giacomo *et al.*²²⁷ have suggested fitting the continuum emission to a Planck-like distribution which does not necessitate theoretical data (cross-sections and correction factors) but does require spectral calibration of the continuum.

As an estimation method for determining initial temperatures Di Giacomo *et al.* point out that the fitting of a blackbody radiation curve does not imply that the photons produced by the continuum obey the black body theory. The number of photons generated from the Planck-like distribution corresponds to the photons contributing to the real experimental Planck-like curve. A Planck-like curve, defined as the irradiance (I_λ) of a blackbody in a spectral range ($d\lambda$) is represented by the following equation:

$$I_\lambda = W_\lambda d\lambda = G \frac{8hc_0^2}{\lambda^5} \frac{1}{\exp(hc_0/\lambda kT) - 1} d\lambda \approx G \frac{8hc_0^2}{\lambda^5} \exp\left(-hc_0/\lambda kT\right) d\lambda$$

where h is Planck's constant, k is Boltzmann's constant, c_0 is the speed of light, and G includes the instrumental response coefficient. This equation holds in vacuum, and if another gas replaces the vacuum, the right-hand side of the equation is multiplied by the square of the refractive index of the gas. This estimation of the earlier temperatures may give better initialization temperatures for the electrons and ions. Similar to constructing a Boltzmann plot, the logarithmic form of the Planck curve equation is necessary to form a linear relationship:

$$\ln \frac{I_\lambda \lambda^5}{8\pi h c^2} = Q - \frac{hc}{\lambda kT}$$

where the constant Q contains both the G factor and the spectrometer's spectral range ($d\lambda$). The inversion of the slope of the line yields the temperature of the photons produced from recombination, and the experimental photon number density can be obtained from:

$$N_{\lambda,exp} = \frac{4I_\lambda \lambda}{hc^2}$$

This method of determining the electron temperature and density has a few caveats, the first being that the Bremsstrahlung contribution to the continuum is neglected, and thus the electron temperature and density is due to the radiative recombination. This was due to the necessity of having to calculate the Biberman and Gaunt correction factor. De Giacomo *et al.*¹⁴ illuminate on other important reasons for neglecting the Bremsstrahlung from the Planck technique in their study. Another big caveat to using the Planck method to determine the plasma characteristics from the continuum lies in the limited amount of data and selected elements that have been studied. Currently, this method has only been applied to pure elements including Ti, Si, C, and Al, and has not been expanded to molecules. In addition, studies on these elements have only been conducted in an ambient air atmosphere. While not covered in this study, it is hypothesized that the MEDUSA code may be able to give an estimate of the plasma behavior over a wide range of atmospheres with a modifications and additional input data. The code is built around a three shell model, and currently the second and third shells could be filled with different gases including argon and air. The hydrodynamic expansion into these regions would be very beneficial as there are more interactions that occur, and without free expansion the lifetime of the plasma is increased as the plasma cannot expand as rapidly. In an effort to observe how the atmosphere affects the lifetime of the plasma, copper sulfate pentahydrate droplets were explored using LIBS under argon and air atmospheres. The emission from the copper lines lasted approximately 2.5 times longer in argon than that of the vacuum as discussed in Chapter 5. The temperature peaks at the same point as in the vacuum at 40 ns which corresponds a temperature of 0.87 eV. The electron density calculations for the argon atmosphere show a slight difference in the

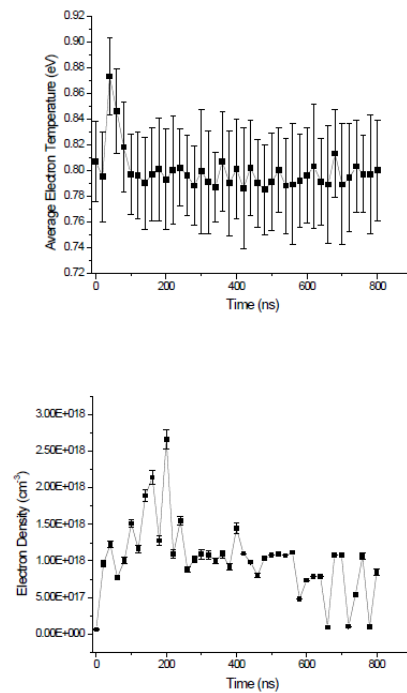


Figure 11. Temperature and density of plasmas for copper-sulfate pentahydrate doped droplets under an ambient argon environment.

¹⁴ A. D. Giacomo, R. Gaudio, M. Dell'Aglio, and A. Santagata, Spectrochim. Acta Part B 65, (2010), 385.

profile in comparison with the vacuum. The temperature peak at 40 ns does not correspond to the electron density peak, which occurs at approximately 200 ns and corresponds to density of $2.67 \times 10^{18} \text{ cm}^{-3}$. After this point there is a decay that, while not as rapid as in the vacuum, is still fairly quick. The earlier densities do not have a smooth increasing trend, which was accredited to the rough estimation that was done due to lack of information in the density tables provided by Griem. The tables only have information for temperature in increments of 5,000 K.

The temperatures measured were closer to 9,000 K, therefore the densities have some estimation error. The erratic behavior at later times was attributed to the drift in the droplet position as the data showed increasing amounts of droplets which had strayed from the focal point. Correction to the droplet position was necessary and had to be done manually adding to the error.

The air atmosphere has the longest plasma emission relative to the other atmospheres. Similar to the other atmospheres the temperatures remains constant around 0.8 eV, with the maximum temperature of 0.83 eV occurring at 40 ns. Again, however, it is the electron density that distinguishes the air atmosphere from the others. The air regime does not have as rapid a decay as the vacuum or argon, but has more of an exponential decay that occurs over a period of approximately of 400 ns. At 140 ns the electron density in the air reaches a peak value of $5.0 \times 10^{18} \text{ cm}^{-3}$, and 440 ns later decreases to an approximate value of $1.0 \times 10^{18} \text{ cm}^{-3}$ where it remains constant within the error.

Water plasma

Water is a simple molecule consisting of only two hydrogen atoms and a single oxygen atom, making it an ideal molecule to study and characterize using LIBS. In addition, by comparing the results of the copper sulfate solution to water, an understanding of how the copper-sulfate affects the plasma parameters of the water can be obtained. A LIBS spectrum of water in vacuum is shown below.

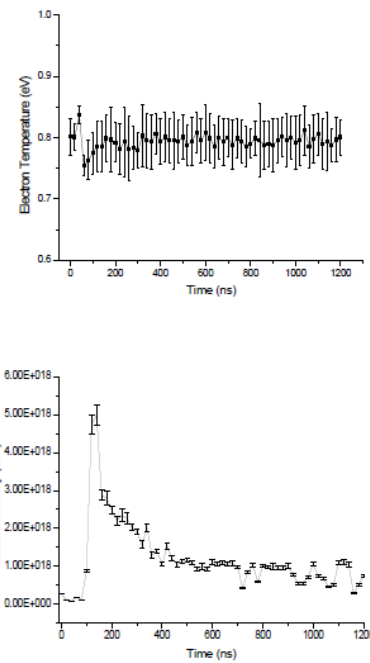


Figure 12. Electron temperature and electron density of plasmas for copper-sulfate pentahydrate doped droplets under an air environment.

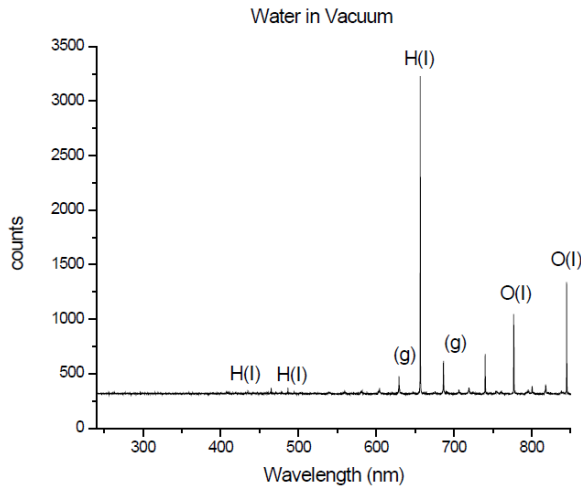


Figure 13. LIBS spectrum of water in vacuum.

The spectrum of water shows very strong hydrogen and oxygen transitions that are identified below in Table 40.

Table 5. Atomic transitions for hydrogen and oxygen

Atom	Configuration	Terms	Emission Line (nm)
H	$n=2 - n=3$		656 nm
	$n=2 - n=4$		486 nm
	$n=2 - n=5$		434 nm
O	$2s^2 2p^3(^4S^0)3s - 2s^2 2p^3(^4S^0)3p$	$^5S^0 - ^5P$	777 nm
	$2s^2 2p^3(^4S^0)3s - 2s^2 2p^3(^4S^0)3p$	$^3S^0 - ^3P$	844 nm

Other peaks that appear in the spectrum are artifacts due to the higher orders from the grating in the Echelle spectrometer. From the spectrum, the hydrogen alpha line dominates the spectrum, so much so that the other two hydrogen lines were barely visible. The emission peaks of the hydrogen and oxygen lines were collected over the lifetime of the plasma in order to determine their individual lifetimes.

The hydrogen beta (486 nm) and the hydrogen gamma (434 nm) have a similar trend in the rise and fall over the span of after 100 ns. The hydrogen alpha line (656 nm) had a sharp rise and a slow decay which lasts over the lifetime of the plasma. It was possible to calculate an electron temperature and density for the hydrogen peak at 40 ns and both are shown below in Table 41.

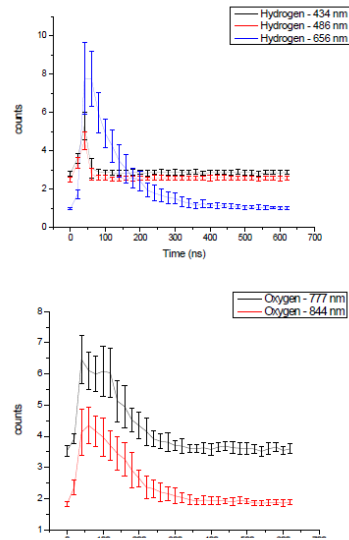


Figure 14. Lifetimes of the hydrogen and oxygen transition lines respectively

Table 6. Electron temperature, density, and the parameters necessary for their calculation for H₂O at 40 ns.

Temp (eV)	Temp Error (eV)	Temp (K)	Hydrogen alpha Stark Broadening (Å)	alpha (1/2)	Electron Density (cm ⁻³)	Density Error (cm ⁻³)
1.041	0.5832	12075.6	8.044710345	0.0186	7.214E+17	4.041E+17

The fluctuation in the error for the hydrogen was found to be higher in comparison with the copper-sulfate pentahydrate as hydrogen is a lighter element and is very sensitive to any perturbations. The oxygen lines follow a similar behavior to that of the hydrogen alpha line with a sharp rise time and slow decay, and while not as strong as the hydrogen transition they are still relatively prominent.

The results from MEDUSA are shown below in Figure 16.

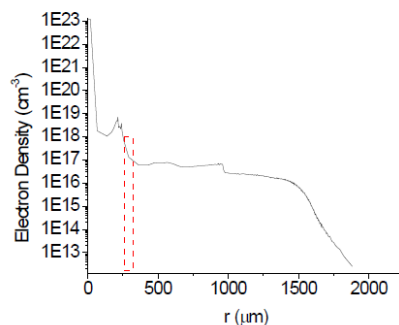


Figure 15. Electron density of water in vacuum as predicted by MEDUSA.

Similar to the CuSO₄+5H₂O the emission region from the water plasma occurs in the corona of the plasma. It spatially located between 258– 320 μm which is further away from the core in comparison with CuSO₄+5H₂O. In order to verify the MEDUSA predictions it is necessary to experimentally probe the plasma in a series of time-resolved studies and spatially resolve the temperatures regions of the plasma. However most plasmas are assumed to be in local thermodynamic equilibrium conditions but verification is necessary.

Applications to organics

The organic samples, methanol and dimethylamine, were studied in order to understand how the spectroscopic signature varies with an atmosphere. In LIBS when a target containing carbon is excited the carbon can react with the nitrogen in the atmosphere and emit characteristic CN line emission. The question of the origin of the CN emission becomes more complex in regards to identifying organics when samples which include inherent CN bonds or just carbon and nitrogen in the sample are explored as well. There are three main routes that have been cited: i) the original compound is fragmented to directly release carbon dimers and CN molecules, ii) the atomic and ionic constituents in the plume of the original compound reacts with the surrounding atmosphere leading to the production of CN, and iii) the C and N atoms from the original compound recombine in the plasma to produce both C₂ and CN¹⁵. While not solved here, an attempt is made to identify whether a sample containing a CN band can be distinguished from a

¹⁵ P. Lucena, A. Dona, L. M. Tobarria, and J. J. Laserna, Spectrochim. Acta Part B SAB 4222, (2010), 1.

sample which has CN emission due to radical recombination using these mass limited droplets at low irradiance.

From the previous sections if improvements to the MEDUSA code could be made to improve the accuracy of the theoretical calculations, then the calculated electron density and temperature may be used to better quantitatively characterize the organic samples. However, without MEDUSA calculations, it should still be possible to gain a better understanding of the differences in the samples based on their spectra, and their C, CN, and N emissions. In general, the C₂ emission would be used, however the band falls in-between two orders of the Echelle spectrometer making it difficult to accurately detect in our case.

Vacuum

The dimethylamine (C₂H₇N+H₂O) and methanol (CH₃OH) samples were first studied under a vacuum environment of approximately 5*10⁻¹ Torr. Studies have shown that an enhanced spectrum can be obtained from performing LIBS on a surface at pressures below atmosphere; more specifically, these enhancements can include an increase in the spectra signal-to-noise^{16,17,18}. While the LIBS spectrum taken under vacuum has a lower FWHM line width in comparison with that of atmospheric conditions is often less intense¹⁹. Dreyer *et al.*²⁰ confirmed that the lower FWHM line width was a result of the decreased electron density as observed by reduced Stark broadening. LIBS spectra of dimethylamine and methanol are shown in Figures 17 and 18.

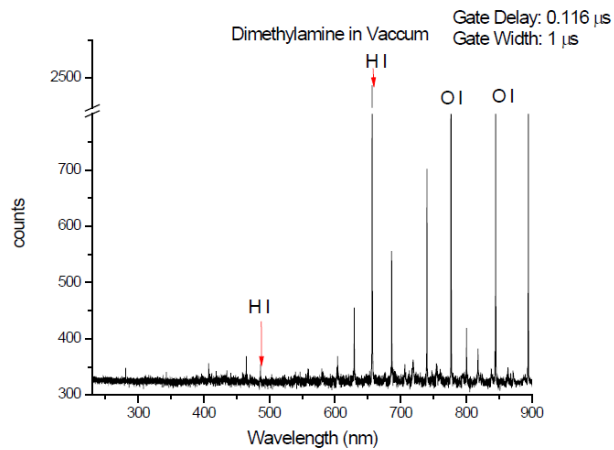


Figure 16. LIBS spectra from dimethylamine in vacuum

¹⁶ J. S. Cowpe, J. S. Astin, R. D. Pilkington, and A. E. Hill, Proc. of. 4th Euro Med. Symp. on LIBS, (2007), 1066

¹⁷ J. S. Cowpe, J. S. Astin, R. D. Pilkington, and A. E. Hill, Spectrochim. Acta Part B 62, (2007), 1335.

¹⁸ J. S. Cowpe, and R. D. Pilkington, Vacuum 82, (2008), 1341.

¹⁹ R. Shu, H. X. Qi, G. Lu, D. M. Ma, Z. P. He, and Y. Q. Xue, Chin. Opt. Lett. 5, (2007), 58.

²⁰ C. B. Dreyer, G. S. Mungas, P. Thanh, and J. G. Radziszewski, Spectrochim. Acta Part B 62, (2007), 1448.

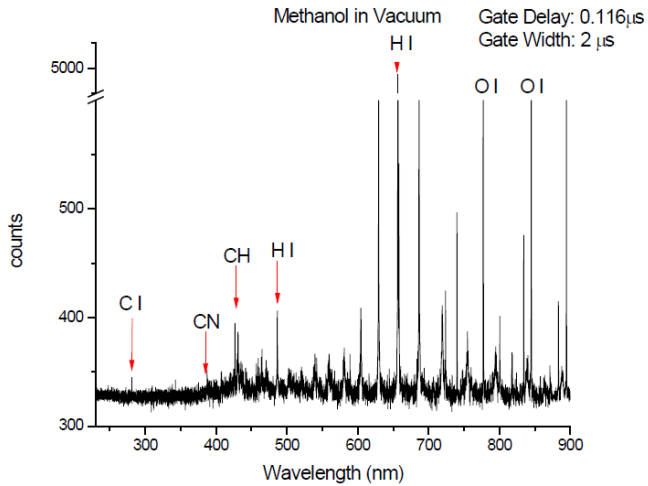


Figure 17. LIBS spectra from methanol in vacuum

While time-resolved studies were conducted, it was necessary to take an integrated spectrum in order to verify that the emissions were present in a high signal-to-noise spectrum. The samples are different in their respective spectra, as the methanol appears to have more carbon emission than the dimethylamine. The carbon emission may be due to the fact that the methanol was a pure sample and was not doped into water. While the dimethylamine as molecule has twice the mole fraction of carbon in comparison with methanol, the number of carbon atoms in the methanol was 4.98×10^{14} in comparison with the 7.10×10^{13} carbon atoms in the dimethylamine as shown in Table 2. There is an order of magnitude difference between the samples and the methanol has more possible carbon emitters. The oxygen in the dimethylamine is not native to the sample but instead is a result from the water, into which the dimethylamine was diluted. The spectra gave some insight into the differences between the two samples, specifically with the emission of atomic and molecular carbon molecules.

The carbon emission was monitored over the emission of the plasma in order to determine if there was any emission for the dimethylamine. There was a weak carbon emission present in the methanol, but not in the dimethylamine sample. The data was visually inspected to verify the presence of the carbon peaks. The plasma emission times are very different with the methanol lasting approximately a full microsecond longer, however the carbon emission only lasts for approximately 120 ns, after which the emission is indistinguishable from noise. In comparison with the pure water sample the lifetime of the dimethylamine solution is even shorter by approximately 200 ns. The decrease in the lifetime may be attributed to the droplet placement stability, which seemed to have more variance with the dimethylamine droplets than with the methanol droplets. Improvements to the positioning system could be made by automating the process, as manual adjustments had to be made in this study.

Due to the CN signature in the methanol but not in the dimethylamine, the nitrogen and CN emission signatures were studied for both samples. The CN signature was expected for the dimethylamine sample as it has nitrogen atoms in the molecule.

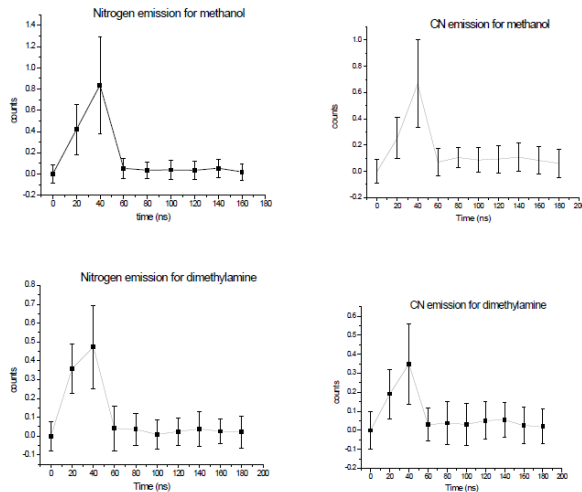


Figure 18. Nitrogen (left) and CN (right) emissions for methanol and dimethylamine over time in a vacuum environment

Both samples have N and CN emissions that last for approximately 160 ns. The CN emission follows the same trend as the nitrogen with the strongest emission occurring at 40 ns consistent with peaks in the carbon and nitrogen. The peaks were weak indicating that the CN emission was not very strong. The observance of the nitrogen emission could be interpreted as nitrogen remaining in the vacuum atmosphere. In order to truly remove the nitrogen from the vacuum, a higher vacuum pressure is necessary.

Argon

A study conducted by Aguilera *et al.* found that a higher plasma temperature and electron density could be achieved over a slower decay in an argon environment in comparison with air²¹. In comparison with the vacuum, more emission from the plasma should be captured as the shortened mean free path should retard the plasma expansion velocities. A LIBS spectrum of both the dimethylamine and methanol is shown below.

Similar to the vacuum regime, the methanol showed a weak atomic carbon emission, while the dimethylamine did not exhibit any atomic carbon. However, in the argon there did not appear to be any other molecular carbon emission. Also both samples appear not to show the H β line which was present in the vacuum atmosphere. The argon lines are very prominent in both spectra and tend to overshadow the signal from the sample. Due to the high argon signal, it was necessary to observe the hydrogen line and measure the relative standard deviation (RSD) in order to determine when the emission from the sample had ended. The oxygen lines were observed as well but the proximity of the oxygen line to the broad argon line made it difficult to accurately monitor.

²¹ J. A. Aguilera, and C. Aragon, Appl. Phys. A 69 [supp], (1999), S475.

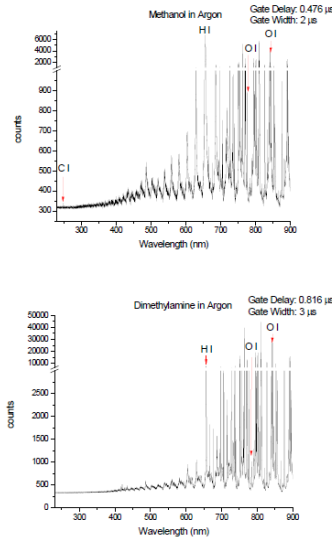


Figure 19. Methanol and dimethylamine spectra taken under argon.

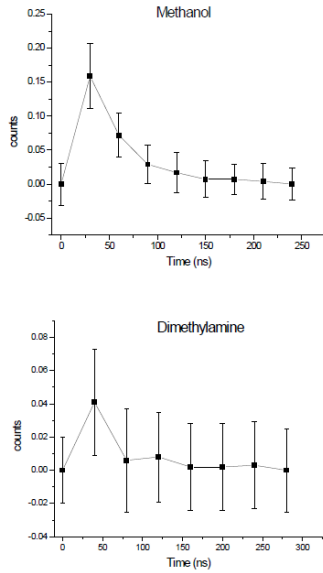


Figure 20. Carbon emission over time for methanol and dimethylamine in an argon environment

The dimethylamine spectra had a small atomic carbon emission of 250 ns during the lifetime of the plasma emission. The methanol conversely has a strong atomic carbon emission that lasted approximately 220 ns, but from the spectrum there does not appear to be any recombination with other atoms for any radical formation. It is interesting to note that the lifetime of the dimethylamine plasma appeared to last longer than the methanol based of the H_α line emission. According to the hydrogen RSD the plasma emission from the methanol sample did not die out until approximately 1900 ns, while the dimethylamine has plasma emission out to 3000 ns approximately 1 μs longer than the methanol. This may have been a consequence of the reliance on the hydrogen emission to determine when the plasma emission from the sample was completed, as there may have been a bias towards the dimethylamine. This bias would be due to the dimethylamine solution having approximately twice the amount of hydrogen atoms (4.03×10^{15} atoms) relative to the methanol (2.00×10^{15} atoms).

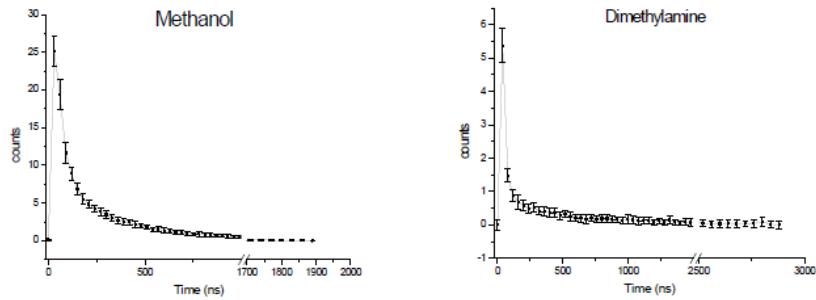


Figure 21. Hydrogen alpha emission representative of the sample plasma emission lifetime for methanol and dimethylamine in an argon environment.

The CN and N emissions for the methanol and dimethylamine are shown in the Figure 22.

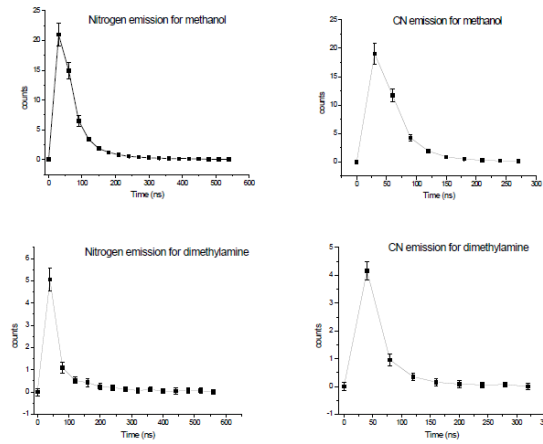


Figure 22. Nitrogen (left) and CN (right) emissions for methanol and dimethylamine over time in an argon environment

The CN emission for the methanol had a sharp rise time and reaches its peak at 30 ns, the subsequent decay lasts until 250 ns where it then becomes indiscernible from the noise. In the dimethylamine case, the CN emission reaches its peak at 40 ns and decays until 320 ns where it can no longer be distinguished from the noise. The nitrogen in both cases followed the same rise as the CN emission, however the nitrogen in the methanol lasted until 540 ns and in the dimethylamine the nitrogen remained until 560 ns. The nitrogen emission however, needs to be monitored with a high resolution spectrometer as the nitrogen emission was very close to the argon lines in the NIR region.

Air atmosphere

The air atmosphere is the most complex of the three regimes in terms of spectral signature and the radical recombination. A study conducted by Arp *et al*²² indicated that as the pressure is increased the LIBS signal intensity and signal-to-noise ratio is decreased. In addition, the spectra from LIBS show a significant peak broadening, and unlike in the argon atmosphere self-

²² Z. A. Arp, D. A. Cremers, R. C. Wiens, D. M. Wayne, B. A. Salle, and S. Maurice, *Appl. Spectrosc.* 58, (2004), 897.

absorption of the emission lines may occur. Also with the introduction of air, comes nitrogen which is inherent to the atmosphere making it difficult to distinguish if the CN band emission is due to atmospheric recombination.

Spectra for the methanol and dimethylamine in air are shown below in Figure 23.

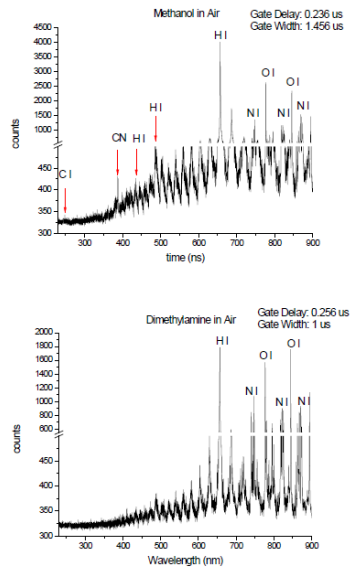


Figure 23. Methanol and dimethylamine spectrums taken under an air atmosphere

From the spectra of the samples, the dimethylamine does not exhibit any carbon emissions atomic or molecular recombination. This was attributed to the early gate delay as the methanol taken under at a slightly earlier delay does show carbon emissions. This behavior has been constant throughout all of the atmospheres explored. To verify that there was no atomic carbon present throughout the plasma emission the atomic carbon emission was inspected.

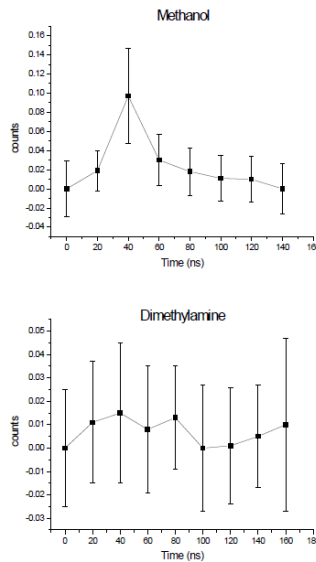


Figure 24. Carbon emission over time for methanol and dimethylamine in an ambient air atmosphere.

Figure 25 shows similar results to the vacuum environment in that there is no atomic carbon emission for the dimethylamine whose plasma emission lasts for approximately 760 ns. In

contrast, the methanol does have a strong atomic carbon emission that lasts for approximately 140 ns, in comparison with the emission of the plasma which lasts for 1200 ns. The behavior of the carbon emission is very similar to that of the argon atmosphere, although the initial intensity count was higher in the argon by approximately 10%. While the atomic carbon may not have been detected for the dimethylamine, there still may have been molecular recombination occurring as was evident in the vacuum and argon environments.

The nitrogen lines were inspected along with the CN band emission in order to determine if there was any molecular structure emission

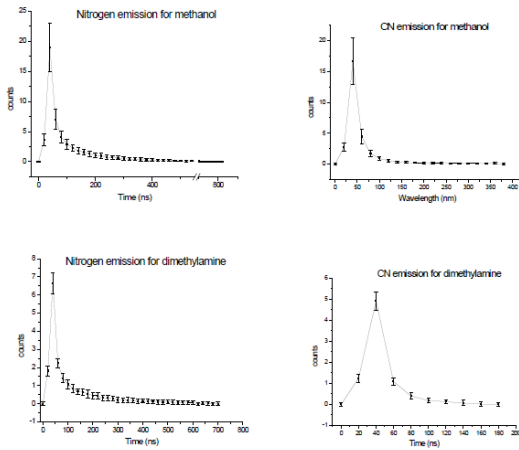


Figure 25. Nitrogen (left) and CN (right) emissions for methanol and dimethylamine over time in an ambient air atmosphere

In the air regime the nitrogen emissions have a longer time of emission in comparison with the argon and vacuum regime. Both the dimethylamine had nitrogen signatures that lasted out until 700 ns before falling into the noise range. The methanol had signatures of nitrogen that lasted out to approximately 800 ns before the emission was indiscernible from noise. The CN emission from the methanol sample lasted out 360 ns, whereas the dimethylamine only had CN emission out to 180 ns.

Discussion

While not all these experiments were optimized, there are some general trends that warrant further studies. The vacuum regime, proved to have the shortest emission times attributed to the rapid free expansion of the plasma. In terms of spectra, the vacuum may have had the least intense spectrum in comparison with air and argon, but it had the least noise influenced spectra as shown below in Figure 27.

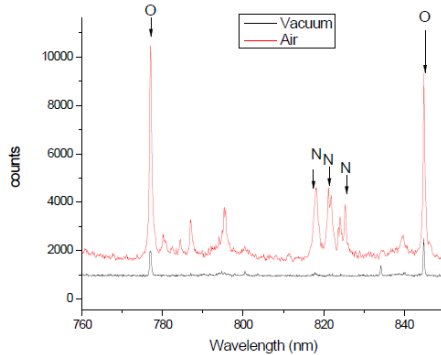


Figure 26. Comparison of methanol spectrum taken in an air and vacuum environment

A higher signal-to-noise is obtained from the droplets in the vacuum environment in agreement with Cowpe and Pilkington²³. If CN formation is to be studied in the vacuum, a higher vacuum than 10⁻¹ Torr is necessary in order to remove the remaining nitrogen. However as the pressure is lowered the expansion of the plasma will be faster, and faster diagnostics will be necessary to characterize the emission. While not as clear a signal as the vacuum the argon environment may offer an alternative to vacuum if longer emission times are necessary to study the CN formation. In agreement, with Aguilera²⁴ the argon environment does appear to have the longest plasma emission. It was also the only environment in which there was an atomic carbon emission in the dimethylamine. However droplet stability proved to be difficult to maintain in this environment. The stability challenge can be solved by adding an automated system that tracks the droplet position and instructs motorized stages in order to maintain this position. This reduces the amount of missed shots, and automatically corrects for the drift from the focal position. In addition a more efficient manner of determining the end of the plasma emission is necessary. The dominant argon lines make it difficult to determine whether emission from the sample is still present as the argon lines dominate the spectrum while trying to monitor various lines such as hydrogen, nitrogen, oxygen simultaneously. This may be solved by having a high resolution focusing on these elements in a window which excludes the argon emission.

The air environment as expected had longer nitrogen emission over the plasma emission as atomic nitrogen emission due to the ambient air contributed to the total emission. If adequate suppression of the nitrogen (or careful characterization of the nitrogen) could be obtained in the other environments then an accurate estimation of the role of the atmospheric nitrogen could be gained from using the mass-limited droplets as targets. Better characterization of the droplets using a fully calibrated LIBS setup would allow for stoichiometric measurements to be made. However this would mean monitoring the environmental conditions in addition to the laser conditions for each laser shot. Such monitoring would also help increase the understanding of the CN emission as well.

In the air environment, the atomic carbon had a longer emission lasting approximately 20 ns longer in the air, and the CN emission was comparable to that of the argon environment. There have been many hypothesis put forth as to formation of the CN structure in air whether it be from the C or C₂ molecule. With additional equipment it may be possible to answer this question with the use of the mass limited droplets. In order to do this however the C, C₂, CN, and N lines must all be monitored. Unfortunately, in this experiment due to the Echelle spectrometer, it was

²³ J. S. Cowpe, and R. D. Pilkington, Vacuum 82, (2008), 1341.

²⁴ J. A. Aguilera, and C. Aragon, Appl. Phys. A 69 [supp], (1999), S475.

difficult to monitor the C₂ emission as it fell between a spectral region in which different orders overlapped. The C₂ emission may have explained why although there was no atomic C emission for the dimethylamine in the vacuum and argon atmospheres but there was still a CN signature. Another possible change that may be necessary if organics are to be studied is the wavelength of the laser. Baudelet *et al.*²⁵ suggested the use of the 266 nm wavelength as an appropriate ablation source. From their study, they concluded that the infrared regime is not a suitable regime in which to study the analysis of organics with molecular emission using LIBS. This was due to high rate of recombination with the atmosphere, and the low efficiency rate producing native molecular fragments that is characteristic of the nanosecond IR ablation regime. Whereas, for the UV laser ablation even at low energy (1-5 mJ) efficient molecular ablation occurs and in addition there is low interference due to atmospheric recombination.

Conclusions

This was the first attempt by the Laser Plasma Lab to characterize the low temperature and density (in comparison with an EUV plasma) LIBS plasma. In addition, to studying the plasma under a low irradiance regime, the samples studied were constructed from low Z materials. A copper-sulfate pentahydrate solution as well as de-ionized water was utilized to try and establish a link between theoretical results predicted from MEDUSA to the experimental. The successful linking of the results allows for MEDUSA to be used as a diagnostic tool to characterize non-metallic and organic samples which cannot be done using current plasma characterization techniques.

In its current form MEDUSA was used to identify the region in the plasma from which the emission occurs. Supplementary improvements to the theoretical code, such as the addition of an ablation module, would further help to refine simulations of the hydrodynamic plasma expansion. The ablation module would not only help to better model the laser absorption and heating of the material, but would also serve to give better input temperatures for the free electrons and ions characteristic of a two fluid stream code. The addition of chemical kinetic processes would help to better simulate the plasma cooling yielding times that should better compliment the experimental results.

In the experimental regime, additional diagnostic equipment such as a mass spectrometer and a high resolution spectrometer are necessary in order to improve and better characterize the experiments. A mass spectrometer would be extremely useful at the initialization of the plasma where we are limited in spectral data until the formation of well-defined lines. If the mass spectrometer has time resolution capabilities then a more accurate understanding of the constituent particles (atoms and molecules) generated from the laser ablation can be obtained. In addition, knowledge of the molecular recombination indicative of the sample itself can be gained in an argon and vacuum environment. Insight from the mass spectrometer would help shed light onto any molecular fragments which could be generated from the low irradiance ablation.

While an Echelle can be used to simultaneously monitor line emissions, the amount of light collected is sacrificed for resolution. With a high-resolution spectrometer the amount of light collected is increased and we are able to focus specifically on regions of interest thus increasing the effectiveness of the time resolved study. An added advantage of the high resolution spectrometer is that gratings with high quantum efficiencies for specific wavelength regimes (UV, VIS, IR, etc) can be utilized to increase the signal-to-noise ratio.

²⁵ M. Baudelet, M. Boueri, J. Yu, X. Mao, S. Mao, and R. Russo, Proc. of SPIE 7214, (2009), 72140J-1.

Implementation of these improvements to both theoretical and experimental studies will help to provide a better understanding of the fundamental LIBS processes in a low irradiance regime. This could lead to further development of plasma codes specifically for the LIBS plasma regime, as physical and chemical processes can be incorporated into the models. The development of a comprehensive model for LIBS plasma is essential if LIBS is to become a main stream diagnostic technique

With the use of mass-limited droplets the quantitative ability of LIBS can be further improved. Known concentrations make it possible to do very accurate stoichiometric studies, and with the characterization of more samples the limits of detection for LIBS can be further refined. Another advantage to using the mass-limited droplets is the homogeneity of the sample studied, which is ideal for exploring non-metallic and organic samples.

FUNDAMENTAL PLASMA DIAGNOSTICS

Spectral imaging for filament-induced plasma chemistry and hydrodynamics

Spectral imaging experiments were performed using the MTFL femtosecond laser system operated at a repetition rate of 10 Hz and with pulse energy of 14 mJ per pulse. The sample was a 2 x 3 x 0.25 inch graphite block with RMS surface roughness less than 0.4 μm , measured using an interferometric microscope (*New View 6300*, Zyglo), with a purity grade of EC-17 and purchased from the GraphiteStore.com.

A negative lens combined with a positive lens provided an adjustable focal length that was used to initiate filamentation (Fig. 28). The geometrical focus of this lens combination was near the sample, approximately 4 meters from the lenses. Filamentation was initiated approximately 1 meter in front of the sample. Although the sample was positioned with a sample chamber, these experiments were performed at normal atmospheric pressure and room temperature. Plasma emission was collected at 90 degrees from the laser axis using an f/2 triplet objective (*NT47-613*, Edmund Optics). The collected light was transmitted through a fused silica chamber window and dispersed with a 0.5 m Czerny-Turner spectrometer (*2500i*, Princeton Instruments) with 600 line/mm grating and detected using a 256 x 1024 ICCD camera (*iStar 720*, Andor). In this configuration each grating position provided a spectral window of approximately 80 nm, and at 400 nm the resolution was 0.08 nm.

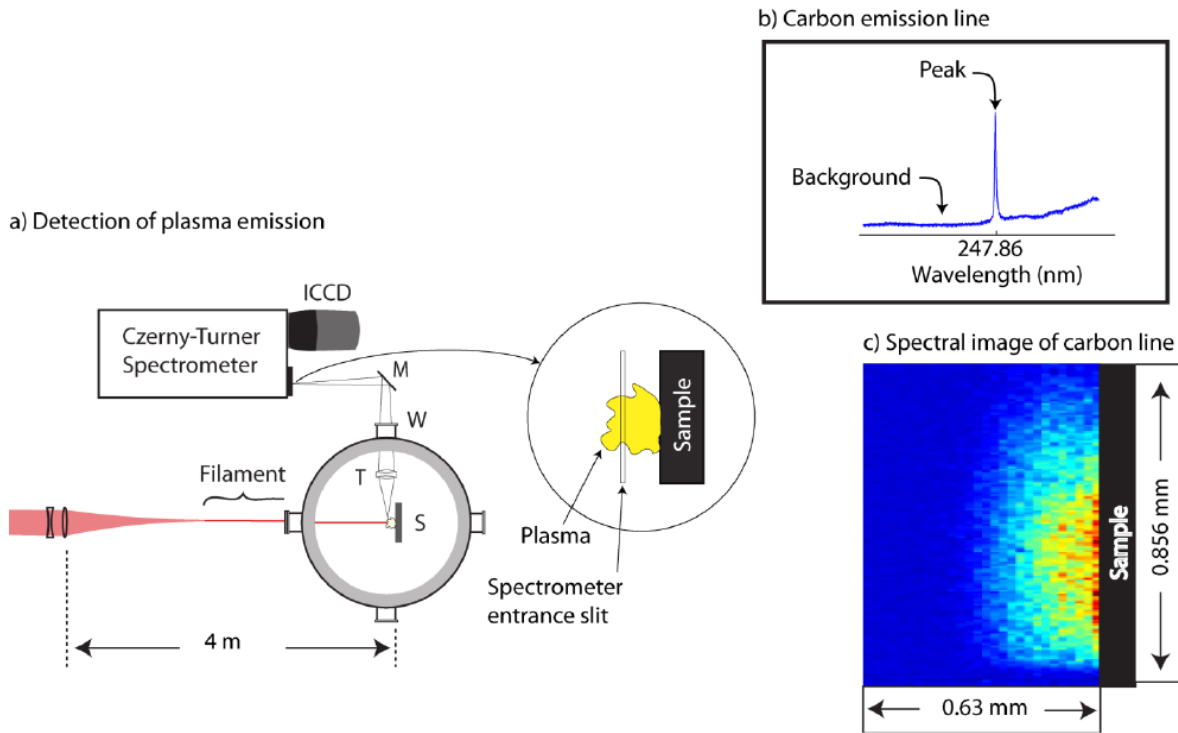


Figure 27. Experimental setup for measuring the filament-induced plasma as a function of time, space and spectrum. In a) the plasma was imaged onto the entrance slit of the imaging spectrometer with a triplet objective (T) and by translating the mirror (M), the image was scanned across the spectrometer slit. The signal and background are shown in b) and the reconstructed image is shown in c).

Spectrally resolved images (Figure 28c) were obtained by translating the projected plasma image across the entrance slit of the spectrometer (by translating mirror M in Figure 28a) and thus provided the spectrum for a slice of the plasma—a line parallel to the sample surface. Full spectral images were obtained by stitching these image-slices together. For each image slice (mirror position) 100 shots were acquired after 10 ‘cleaning shots’. This method of reconstructing a spectrally resolved image by scanning the image across the spectrometer entrance slit provided several advantages over simply using a band-pass filter in front of an array detector. The use of a grating spectrometer provided sufficient resolution and adequate throughput while also providing wavelength flexibility. The scanning nature of this method, however, restricted its use to multi-shot analysis.

From the standpoint of analytical spectroscopy, the validity of spectroscopic plasma temperature calculation as well as other plasma diagnostics relies upon the assumption of local thermodynamic equilibrium (LTE). The 1-dimensional expansion of the filament-induced shockwave was characteristic of a plasma with higher kinetic energy yet lower excitation energy and therefore fewer collisions between atoms and ions. These plasma conditions suggest that, for early times, LTE was not established^{26,27,28}.

²⁶ X. Zeng, et al., "Experimental investigation of ablation efficiency and plasma expansion during femtosecond and nanosecond laser ablation of silicon," *Applied Physics A: Materials Science & Processing*, vol. 80, pp. 237-241, 2005.

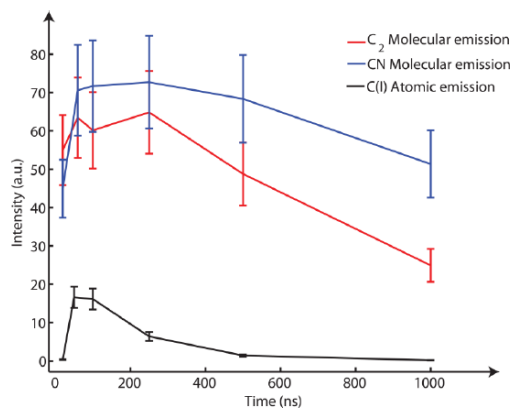


Figure 28. Spatially integrated temporal emission profile from atomic and molecular plasma species resulting from filament-induced ablation of graphite.

graphite sample provided both atomic and molecular carbon emission following filament-induced ablation as well as emission from CN radicals. Molecular CN emission from samples not containing nitrogen results from a plasma phase reaction that likely occurs between atmospheric nitrogen and ablated carbon species within the plasma^{30,31,32}. The plasma phase chemistry that leads to molecular formation within filament induced plasma is not yet well understood.

Correlation between atomic carbon and CN molecular emission was found during the initial 100 ns of plasma expansion. Following the decay of atomic carbon emission within the first couple hundred nanoseconds, C_2 and CN molecular emission was correlated. After the initial expansion, this longer lived molecular emission, as compared with atomic emission, had a spatial profile that expanded predominately along the sample surface. This preferential lateral extension (Figure 30) of the plasma up to 1 μ s after the laser pulse was consistent with the type of expansion that was observed using shadowgraph imaging of GaAs, Ge and Ti. In contrast to this lateral expansion observed using filament irradiation, the shape of the plasma resulting from external focusing of the beam using a 5 \times microscope objective was spherical.

In contrast to focused laser-induced-plasmas the emission from filament-induced-plasmas was characteristic of a lower electron plasma temperature²⁹, as seen by a lower degree of ionization among emission species as well as increased molecular emission. Atomic emission decays more rapidly in time as compared with the molecular emission, and in the case of filament-induced plasmas, the decay of atomic emission occurred in the first couple hundred nanosecond (Figure 29). A similar decay profile was observed for focused femtosecond irradiation, The molecular emission from organic materials that follows filament-induced plasma formation is often stronger than atomic or ionic emission. For analytical purposes, this molecular emission is not necessarily representative of the sample composition; however, for the characterization of plasma dynamics, it provided a marker for monitoring the dynamics over a longer time period. A

²⁷ X. Zeng, *et al.*, "Laser-induced plasmas in micromachined fused silica cavities," *Applied Physics Letters*, vol. 83, p. 240, 2003

²⁸ X. Zeng, *et al.*, "Laser–plasma interactions in fused silica cavities," *Journal of Applied Physics*, vol. 95, p. 816, 2004.

²⁹ H. L. Xu, *et al.*, "Understanding the advantage of remote femtosecond laser-induced breakdown spectroscopy of metallic targets," *Journal of Applied Physics*, vol. 101, p. 033124, 2007.

³⁰ M. Weidman, *et al.*, "Nd: YAG-CO₂ double-pulse laser induced breakdown spectroscopy of organic films," *Optics Express*, vol. 18, pp. 259-266.

³¹ L. St-Onge, *et al.*, "Carbon emissions following 1.064 μ m laser ablation of graphite and organic samples in ambient air," *Applied Physics A: Materials Science & Processing*, vol. 69, pp. 913-916, 1999.

³² M. Baudelet, *et al.*, "Time-resolved ultraviolet laser-induced breakdown spectroscopy for organic material analysis," *Spectrochimica Acta Part B: Atomic Spectroscopy*, 2007.

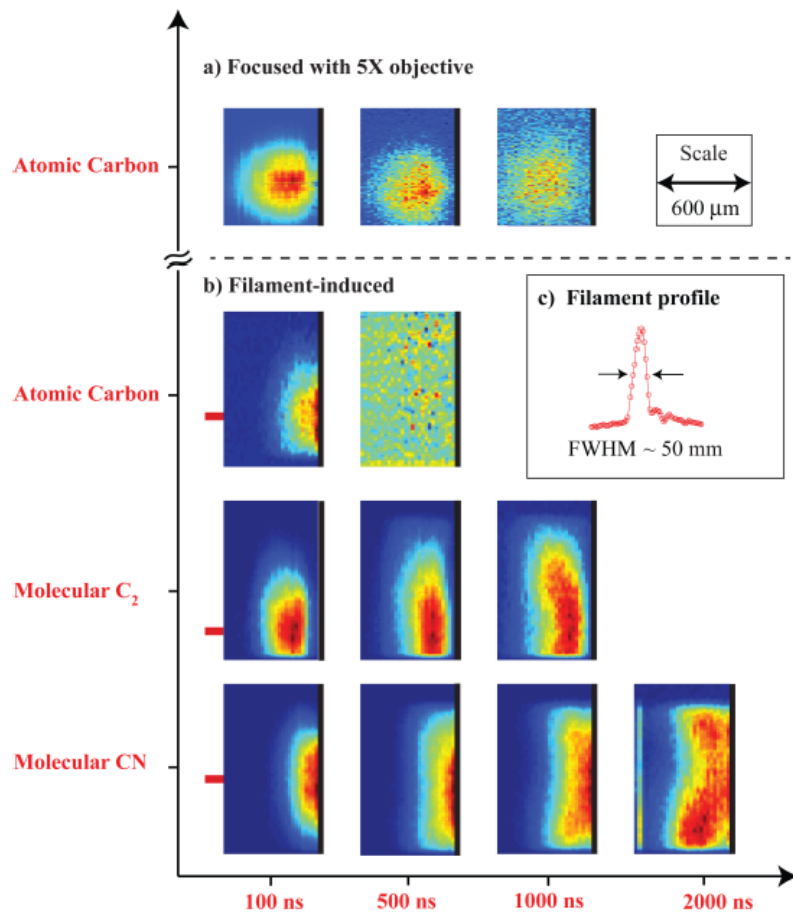


Figure 29. Spectrally resolved plasma emission: from a) focused laser induced carbon plasma and b) filament-induced plasma emission from atomic and molecular species (C, C₂ and CN). The target material was graphite and in the case of filament irradiation, a 5 m focusing optic was used and the resulting profile is shown in c).

External focusing optics were used to help stabilize the filament and the resulting profile was, therefore, characteristic of the 5 m focus that was used. The position of the filament relative to the resulting plasma image was depicted by the red boxes immediately to the left of the images for 100 ns delay in Figure 30.

The expansion characteristics of filament-induced plasmas—non-spherical in nature—raised the question, ‘is there a preferential emission direction relative to the sample surface?’ For application of filament-induced plasmas for stand-off spectroscopy, the detection of signal emitted in the backward direction becomes essential.

Thomson scattering of LIP from solid samples in air at atmospheric pressure

Thomson scattering is an alternative approach for general LIP Te and Ne measurements^{33,34}. Thomson scattering is based on the elastic scattering of light by free charges,

³³ Ross, J.S., et al., *Thomson-scattering measurements in the collective and noncollective regimes in laser produced plasmas (invited)*. Review of Scientific Instruments, 2010. 81(10): p. 10D523-6.

and here particularly free electrons. Both Te and Ne can be measured simultaneously from the electron feature of the Thomson scattering spectra, and no assumption of LTE or other specific equilibrium condition is needed. Meanwhile Thomson scattering measurements provide good spatial (determined by the probe beam size) and temporal (determined by the pulse duration) resolution. Therefore Thomson scattering is considered the most accurate and reliable method for Te and Ne measurements of a plasma³⁵. These properties make Thomson scattering a powerful tool in the diagnostics of fusion plasma^{36,37} and many other types of plasmas^{38,39,40} as well.

LIP diagnostics by Thomson scattering is rarely reported, but a few excellent experiments can still be found in recent publications. Delserieys et al. studied the LIP from magnesium samples in a vacuum chamber, and the results provided insights into the plasma cooling and expansion processes^{41,42}. Similar work can also be found in some early days experiments on aluminum sample in vacuum chambers⁴³. At atmospheric pressure, Thomson scattering measurements were performed on air⁴⁴, argon⁴⁵, and helium⁴⁶ plasmas. These studies managed to tackle different problems, which range from characterizing plasma heating by the probe laser to validating a new method for electron density measurements. However, for LIP from solid samples at atmospheric pressure, which is the most common plasma investigated by LIBS, almost no study has been reported yet. The difficulty in performing Thomson scattering experiments on such plasmas are related to the pressure and reflection from sample surfaces. Compared with Thomson scattering experiments in vacuum, the size of the plasma at 1 atm is much smaller, so the probe laser has to be extremely close to the sample surface (1 mm or less, depending on the size of the plasma). The small distance dramatically increases the probe signal on the detector due to surface reflection. As a result the weak Thomson signal is washed out. In

³⁴ Froula, D., et al., *Plasma scattering of electromagnetic radiation: theory and measurement techniques* 2010: Academic Press.

³⁵ Meulenbroeks, R.F.G., et al., *Four ways to determine the electron density in low-temperature plasmas*. Physical Review E, 1994. 49(3): p. 2272-2275.

³⁶ Glenzer, S.H., et al., *Thomson Scattering from Inertial-Confinement-Fusion Hohlraum Plasmas*. Physical Review Letters, 1997. 79(7): p. 1277-1280.

³⁷ Schaeffer, D.B., et al., *Thomson Scattering Measurements of Temperature and Density in a Low-Density, Laser-Driven Magnetized Plasma*. Journal of Instrumentation, 2012. 7(02): p. P02002.

³⁸ Sande, M.J.v.d. and J.J.A.M.v.d. Mullen, *Thomson scattering on a low-pressure, inductively-coupled gas discharge lamp*. Journal of Physics D: Applied Physics, 2002. 35(12): p. 1381.

³⁹ van der Mullen, J., G. Boidin, and M. van de Sandea, *High-resolution electron density and temperature maps of a microwave plasma torch measured with a 2-D Thomson scattering system*. Spectrochimica Acta Part B: Atomic Spectroscopy, 2004. 59(7): p. 929-940.

⁴⁰ Gessel, A.F.H.v., et al., *Laser scattering on an atmospheric pressure plasma jet: disentangling Rayleigh, Raman and Thomson scattering*. Plasma Sources Science and Technology, 2012. 21(1): p. 015003

⁴¹ Delserieys, A., et al., *Optical Thomson scatter from laser-ablated plumes*. Applied Physics Letters, 2008. 92(1): p. 011502-3.

⁴² Delserieys, A., et al., *Optical Thomson scatter from a laser-ablated magnesium plume*. Journal of Applied Physics, 2009. 106(8): p. 083304-8.

⁴³ George, T.V., A.G. Engelhardt, and C. DeMichelis, *THOMSON SCATTERING DIAGNOSTICS OF LASER-PRODUCED ALUMINUM PLASMAS*. Applied Physics Letters, 1970. 16(6): p. 248-251

⁴⁴ Dzierżęga, K., et al., *Thomson scattering from laser induced plasma in air*. Journal of Physics: Conference Series, 2010. 227(1): p. 012029.

⁴⁵ Mendys, A., et al., *Investigations of laser-induced plasma in argon by Thomson scattering*. Spectrochimica Acta Part B: Atomic Spectroscopy, 2011. 66(9-10): p. 691-697.

⁴⁶ Nedanovska, E., et al., *Comparison of the electron density measurements using Thomson scattering and emission spectroscopy for laser induced breakdown in one atmosphere of helium*. Applied Physics Letters, 2011. 99(26): p. 261504-3.

the case of the air plasmas, since there is no solid surfaces, reflection is not an issue. Due to these differences, diagnostics of atmospheric pressure LIP from a solid target is even more complicated than other types of plasmas.

In this study, the feasibility of using Thomson scattering for Te and Ne measurements on air and aluminum plasma at atmosphere pressure was investigated. Both collective and non-collective Thomson scattering spectra from air plasmas were analyzed for Te and Ne estimation. Time resolved Te and Ne estimates of the Al plasma from a solid aluminum target at atmosphere pressure were presented with delay time from 400 ns to 2.5 μ s for the first time. A discussion on the McWhirter criterion and LTE is given based on the data obtained.

Experimental setup

The schematic diagram of our experiment is shown in Figure 3.1. Air and aluminum plasmas were created by 35 mJ and 20 mJ 4 ns pulses respectively at 1064 nm from an Nd:YAG laser (Brillant, Quantel) running at 10 Hz. The combination of a half wave plate and a polarization beam splitter adjusts the energy that goes to the sample. The 10 cm focal length lens (L1) generates a 100 μ m diameter focal spot. For air plasma studies, the air plasma was created at the focal point. For on the aluminum plasma studies, the reduced energy was used to ensure no air plasma was created before the laser pulse hit the aluminum target. A frequency doubled Nd:YAG laser (Quanta Ray, Spectra Physics) produced 20 mJ probe pulses with a pulse duration around 10 ns at 532 nm. This second laser has a repetition rate of 100 Hz. A mechanical shutter (Thorlabs SH05) was used to block the unwanted laser pulses and only pass the ones that showed up at the time of interest. The half wave plate adjusted the polarization of the probe beam and maximized the Thomson scattering signal. A 2 m lens (L2) was used to focus the probe laser beam. As a result the beam size was small in a long range around the plasma location, and the scattering from the sample surface could be reduced. This is particularly useful for the Al plasma diagnostics since unwanted surface reflection of the probe laser can be very harmful. Limited by our specific experimental condition irrelevant to this particular study, a mirror had to be at the position about 30 cm away from the plasma. A negative lens (L3, $f = -10$ cm) was placed in front of the mirror to avoid mirror surface damage by the focused probe laser. A positive lens (L4, $f = 10$ cm) was used to refocus the diverging beam, and its location was optimized to make sure the waist was at the plasma location. The final beam size was around the 220 μ m in diameter. In addition, an iris reduced stray light and limited the size of the beam.

The scattering light was collected in the direction perpendicular to the paper surface as shown in the inset plot on top in Figure 3.1. An F/2.4 lens collimated the light, and a second lens (F/4) focused the light onto the slit of a spectrometer (Acton 2300i, 1800 l/mm grating). In addition, dark tubes were used after lens L5 till the entrance slit to reduce stray light, which were not shown in the schematic plot. The slit was 100 μ m when the Thomson scattering spectra were taken. An ICCD camera (PI-Max 2, Princeton Instruments) was equipped with the spectrometer for spectrum recording. The exposure time was 20 ns centered at the laser pulse. Each spectrum accumulated 500 shots. Background emission from the plasma was removed by subtracting the spectra taken without the probe laser.

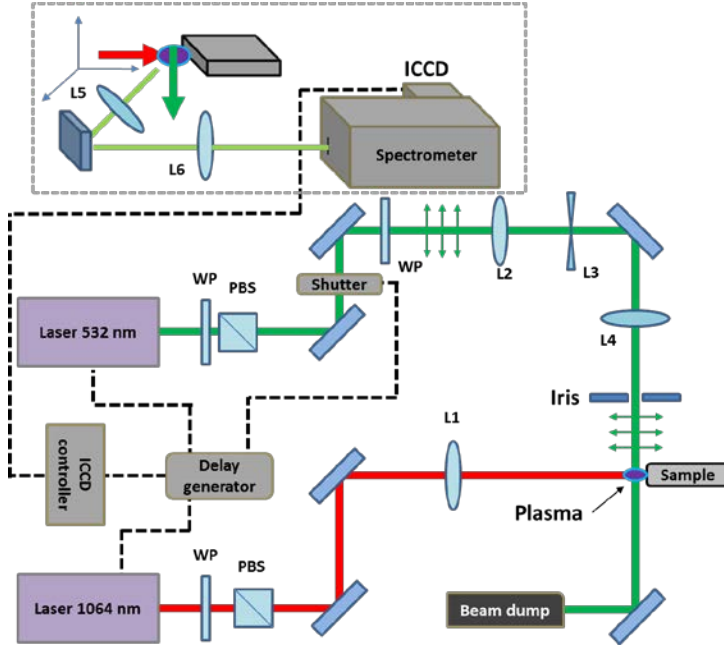


Figure 30. Schematics of the experimental setup. In the figure, WP = wave plate, PBS = polarization beam splitter, L1-6 = Lens 1-6.

Synchronization

Synchronizing different instruments is critical to perform Thomson scattering measurement due to the short lifetime of the plasma and fast varying plasma conditions. Since different equipment has its own trigger timing, the synchronization of two Q-switch lasers, an ICCD camera, a mechanical shutter, and a microwave generator (for future experiments) becomes a challenging problem. Here are some special requirements for the different equipment as shown in Figure 3.2. For the two Q-switch lasers, both of them have two inputs: the flash lamp trigger and the Q-switch trigger. For both lasers, the optimized Q-switch delay (the delay time between the flash lamp and the Q-switch trigger signals) is 190 μ s. However, their repetition rates are different as mentioned earlier. In addition, the Q-switch of the probe laser must be triggered at 100 Hz to have reproducible pulse energy, while the Quantel laser used for sample ablation and plasma creation can be triggered at any multiplication of 100 ms, as long as the flash lamp trigger remains at 10 Hz. The minimum period of time for which the mechanical shutter keeps open is 10 ms. This time slot can ensure only one probe pulse passes through the shutter. However, to open the shutter, the trigger signal must be received about 8 ms before the arrival of the probe pulse due to internal electronic delay. Additional time (1 ms or longer according to the manual) is needed to fully open the shutter. The maximum operation repetition rate for the shutter is 25 Hz. However, to protect the shutter and also to make the whole system compatible with the MA-LIBS system for future experiments, the Thomson scattering facility has to work at 1 Hz. The microwave plasma can last for 20 ms which will be described in the next chapter. Therefore the probe pulse should be able to probe any time from the beginning of the plasma to 20 ms after the plasma is created. In addition, the ICCD camera must be precisely synchronized with the probe laser pulse, since Thomson scattering signal can be detected only during the probe laser pulse duration.

To satisfy all the requirements, a synchronization scheme was designed. A schematic diagram is shown in Figure 31. The whole system was synchronized by three delay generators

(two DG645 and one DG535 from Stanford Research Systems). To ensure long term timing accuracy, a DG645 delay generator was used as the master clock, which triggers the flash lamp and the Q-switch of the probe laser at 100 Hz. Additional output from this delay generator was connected to the external trigger input of another DG645 delay generator. Using the trigger prescaler in the second DG645, 10 Hz and 1 Hz signal can be generated based on the 100 Hz clock. The AB output from the second DG645 triggers flash lamp at 10 Hz, and 20 ms delay was applied to make sure there is enough time to open the shutter. Signal from GH output was sent to the ICCD camera external trigger input, and the repetition rate was further reduced to 1 Hz. Since the delay between the Q-switch and the flash lamp is fixed at 190 μ s, the delay time for the ICCD camera was set as 20.190 ms so that the intensifier turns on when the laser pulse is fired. The T0 output on the ICCD controller produces a duplicate of the external trigger, but only send out signals when the software start to accumulate data. The T0 output signals then trigger the DG535 delay generator. The AB output of the DG535 controls the shutter. The delay time of AB was set as 6 ms which compensate the electronic delay and the time to open the shutter. The 10 ms pulse duration determines how long the shutter is kept open.

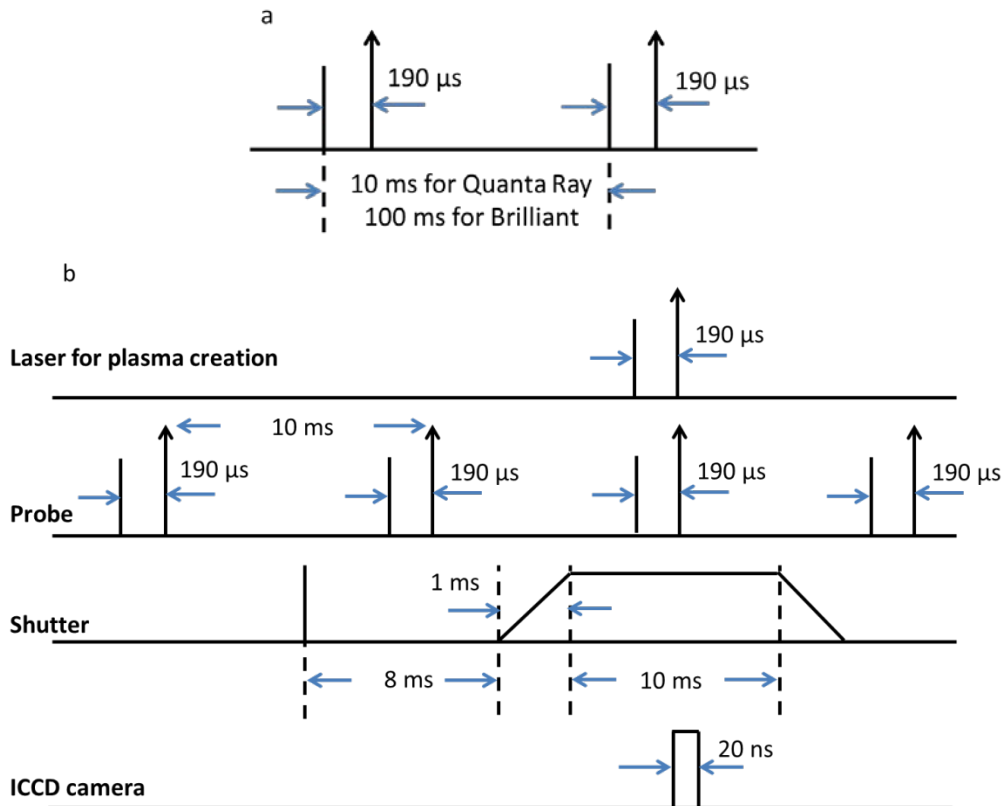


Figure 31. Timing sequence for synchronization. (a) Flash lamp and Q-switch; (b) Synchronization of the two lasers the shutter, and the camera.

All the delay time is under the assumption that there is negligible electronic delay caused by the equipment and cables except the shutter. The CD output of the DG535 triggers the Q-switch of the ablation laser. With the help of an oscilloscope, the delay time can be further adjusted to compensate the electronic delay, and the probe laser pulse, the ablation laser pulse, and the ICCD gate can be precisely synchronized with undetectable jitter (less than 1 ns for the

oscilloscope used in the experiment). Furthermore, to introduce a delay between the probe and ablation pulses, one only needs to subtract the delay time from all the “20 ms” shown in Figure 32.

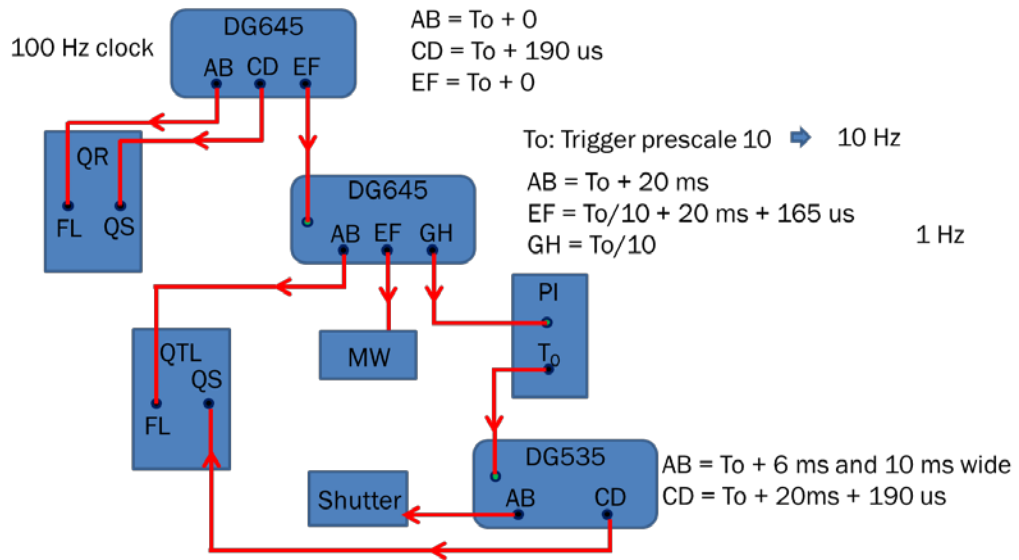


Figure 32. Synchronization for Thomson scattering experiment

Air plasma

To collect Thomson scattering spectra, air plasmas are good candidates to start with. By optimizing the laser energy, air plasma can be created at the focus of the lens and is relatively stable from one shot to another. With the air plasma, the range of Ne and Te that Thomson scattering can measure was determined. As the plasma evolves over time, the Ne and Te decrease. Depending on the spectral features, methods for treating both collective and non-collective Thomson scattering were applied.

Collective Thomson scattering spectra

During the early time of plasma evolution, both T_e and N_e are high. The satellite peaks are the dominating feature of the TS spectra as shown in Figure 33. As the electron temperature and density increases, the satellite peak tends to move farther away from the original probe wavelength, and peak becomes broader. The spectrum shape is determined by the shape factor, which can be simulated numerically.

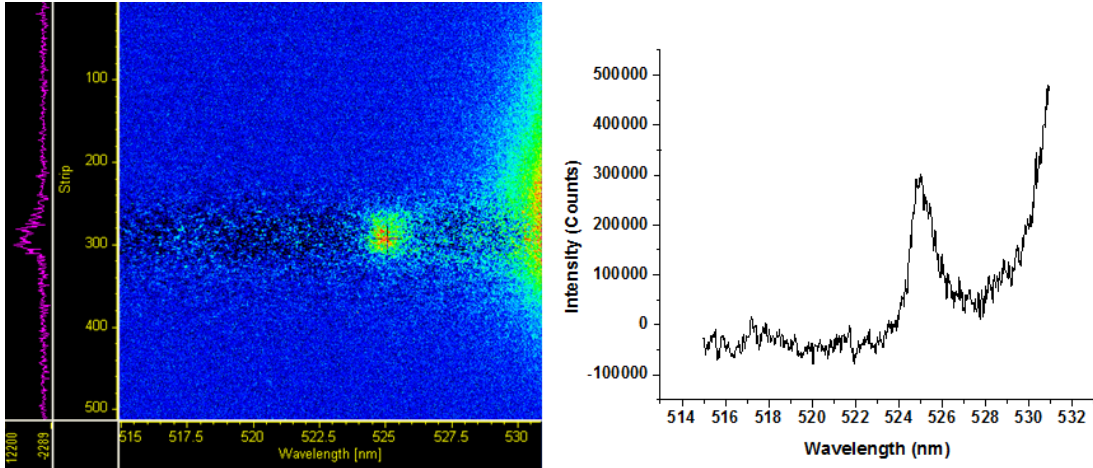


Figure 33. Typical collective Thomson scattering signal: ICCD image of the spectrum (left) and spectrum after binning (right).

The numerical simulation can be used to retrieve the Te and Ne values from the TS spectrum. The pixels, i.e. vertical axis of the CCD, where Thomson scattering signals can be observed were binned to generate a raw spectrum. This is how the spectrum on the right in Figure 3.4 was obtained from the image on the left. The baseline of this raw spectrum close to 532 nm was then corrected by subtracting a scaled spectrum of the probe laser without the plasma. The fitting algorithm was thoroughly discussed in early publications^{47,48}. Using the fitting MATLAB program, the Te and Ne can be estimated. Figure 34 shows the fitting result of the spectrum shown in Figure 33. The estimated Te and Ne are 66800 K and $3.94 \times 10^{17} \text{ cm}^{-3}$ respectively. One advantage of the collective Thomson scattering spectra is its unambiguity. One pair of Te and Ne always produces a unique spectrum⁴⁹. In most spectra, both the blue- and red-shifted peaks produce very similar fitting results. For consistency, the fitting was mainly based on the blue-shifted peak, unless severe distortion or noise was observed.

⁴⁷ Froula, D., et al., *Plasma scattering of electromagnetic radiation: theory and measurement techniques* 2010: Academic Press.

⁴⁸ Palastro, J.P., et al., *Erratum: Fully relativistic form factor for Thomson scattering [Phys. Rev. E 81, 036411 (2010)]*. Physical Review E, 2011. **83**(5): p. 059905.

⁴⁹ Ross, J.S., et al., *Thomson-scattering measurements in the collective and noncollective regimes in laser produced plasmas (invited)*. Review of Scientific Instruments, 2010. **81**(10): p. 10D523-6.

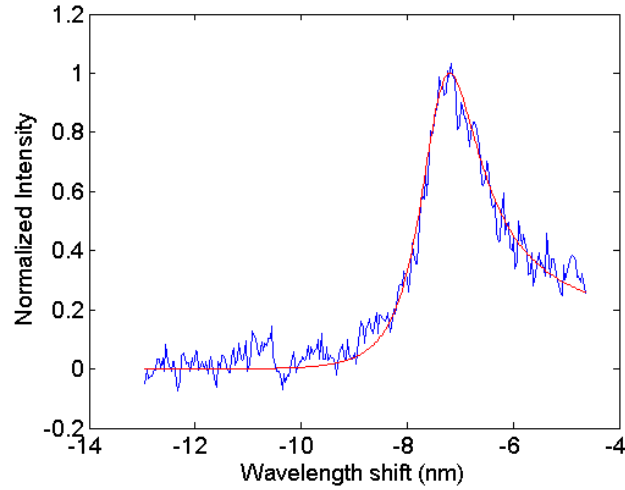


Figure 34 Fitting of the spectrum in Figure 3.4. Te was found to be 58500 K and Ne was $4.39 \times 10^{17} \text{ cm}^{-3}$.

Collective Thomson scattering spectra were collected at different time after the plasma was created. The minimum delay time needed to obtain a clear TS spectrum was 300 ns for the air plasma. For smaller delay time, the continuum emission of the plasma was so intense that the TS signal could not be separated from the background. Two microseconds after the plasma formation, TS peaks were located close to the central peak at 532 nm as shown in Figure 35. The two satellites are no longer distinct as in the early time spectra. This feature indicates the transition from collective to non-collective Thomson scattering. From the fitting result of the spectrum in Figure 3.6, the Te and Ne are estimated as 21000 K and $1.69 \times 10^{16} \text{ cm}^{-3}$ respectively. This pair of Te and Ne indicates an α parameter of 0.78.

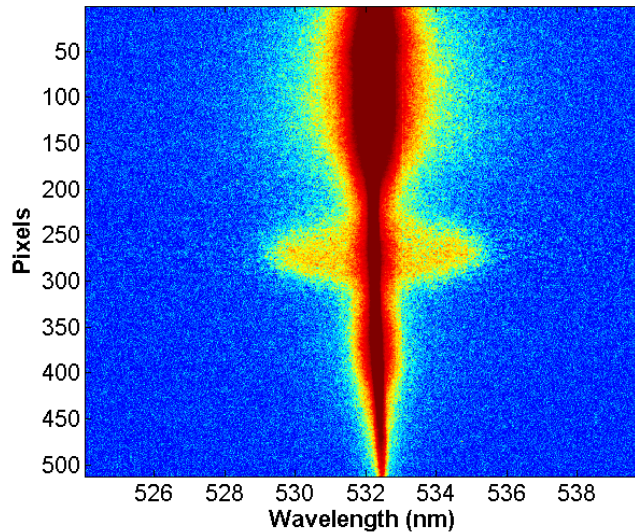


Figure 35. Thomson scattering spectrum image taken at 2 μs after plasma creation.

Non-collective Thomson scattering spectra

As the temperature and density decrease, the satellite features are gone. Compared with the Rayleigh scattering spectrum which does not exhibit wavelength shift, the non-collective TS

spectra are distinguished by the broader line width. Figure 36 illustrates the shape difference between two Rayleigh scattering spectra from air and the difference between TS spectrum from air plasma 4 μ s after plasma creation and Rayleigh scattering spectrum from air. Both the Rayleigh scattering spectra and the Thomson scattering spectra were first normalized within the scale 0 to 1. The red curve in Figure 36 is the difference between two normalized Rayleigh scattering spectra. Extremely small difference can be observed. The blue curve in the same figure is the difference between the normalized TS spectrum and the Rayleigh scattering spectrum. The broadening caused by the Thomson scattering can be observed from this comparison.

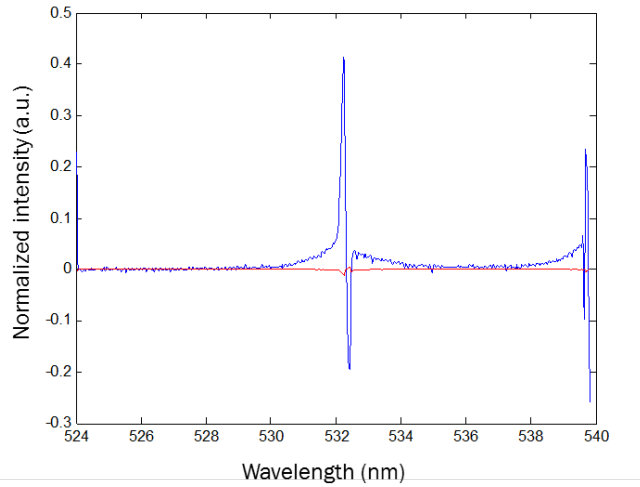


Figure 36. The difference between two normalized Rayleigh scattering spectra from air (red) and the difference between the normalized TS spectrum from an air plasma 4 μ s after the plasma creation and the normalized Rayleigh scattering spectrum (blue).

In Figure 36, although most of the Rayleigh scattering signal is removed in the blue curve, the central part of the peak is still strongly influenced by the Rayleigh scattering signal. As a result, the central region is blocked during the fitting process, and only the wings of the peak are used for a Gaussian fit. Before the Thomson scattering peak is fit, the spectrum is scaled back to the original unit, so that the integrated area can still represent the peak intensity. The fitting result is demonstrated in Figure 37. After the fitting process, the width of the peak $\Delta\lambda$ and the integrated peak area of the Thomson scattering signal I_{TS} can be obtained.

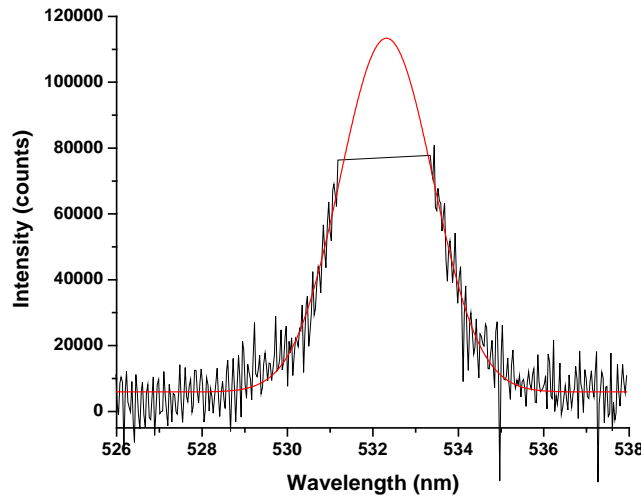


Figure 37. Gaussian fit of the Thomson scattering spectrum from air plasma at 4 μ s after plasma creation.

Once the $\Delta\lambda$ and I_{TS} are obtained, Te and Ne can be calculated. According to Equation 2.13, under the geometry used in our experiment ($\theta=\pi/2$), Te can be expressed as:

$$T_e = \frac{m_e}{2k_B} \left(\frac{c}{\sqrt{2}} \frac{\Delta\lambda}{\lambda_0} \right)^2$$

If the fitting result does not provide 1/e width but FWHM, the 1/e width $\Delta\lambda$ can be found by

$$\Delta\lambda = w / (2\sqrt{\ln 2})$$

In this expression, w is the FWHM of the Gaussian fit. To obtain Ne, the integrated area of the Rayleigh scattering peak must be obtained. The Rayleigh scattering spectrum from normal air can be simply collected by turning the ablation laser off. Once the integrated area is obtained, Ne can be calculated based on the equation:

$$n_e = n_g \frac{\sigma_{Ray,g}}{\sigma_{TS}} \frac{I_{TS}}{I_{Ray}}$$

3.3.3 Time resolved Te and Ne measurements for air plasma

The Te and Ne values of the air plasma are plotted as a function of the delay time in Figure 38. The minimum delay that TS spectra can be resolved is 300 ns. The Te and Ne are estimated to be 91000 K and $6.13 \times 10^{17} \text{ cm}^{-3}$. Within less than 2 μ s, the temperature dropped to about 21000 K, and the density decreased to $1.69 \times 10^{16} \text{ cm}^{-3}$. Between 2 and 3 μ s, the Te and Ne are difficult to estimate since Thomson scattering is in the transition process from the collective regime to the non-collective regime. Three microseconds after the plasma creation, a broad Gaussian spectrum can be observed. Hence Te and Ne can be calculated using the non-collective TS treatment. The minimum electron temperature and density measured by this TS method are 12800 K and $1.86 \times 10^{15} \text{ cm}^{-3}$. After 4 μ s, the wings of the TS spectrum become less clear, and a reasonable fitting result could not be obtained. This indicates that the temperature and density become so low that the TS spectrum feature shrinks into the region where Rayleigh scattering is

dominating. However as a method that can measure the electron density of plasma, Thomson scattering can obtain 1 to 2 order of magnitude lower density compared with Stark broadening method without using very high resolution spectrometers.

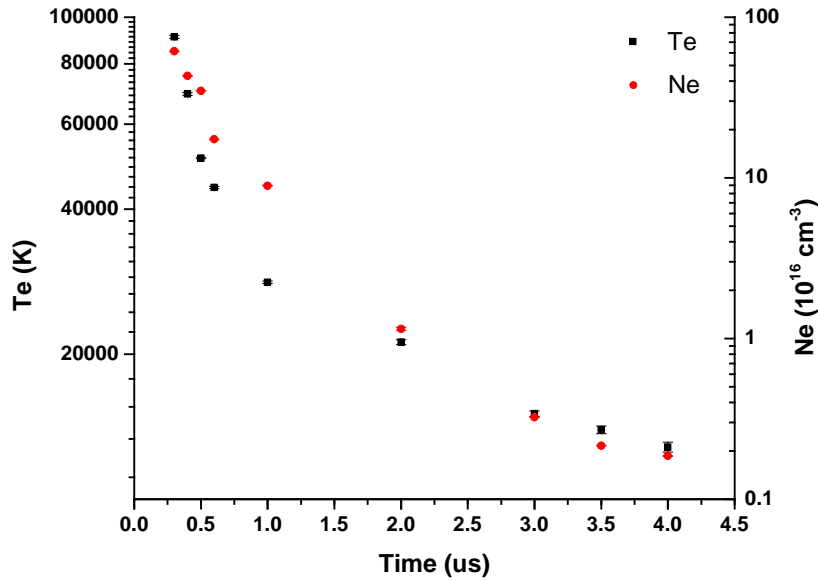


Figure 38. *Te and Ne of air plasma as a function of the delay time.*

From the study of air plasma using Thomson scattering method, the capability of Thomson scattering in Te and Ne measurements become clear. Typical laser plasmas that have Te in the range between 90000 K and 20000 K with Ne in the range of 10^{18} to 10^{16} cm^{-3} can be investigated with the help of collective Thomson scattering spectra. For lower density plasma, the non-collective TS method can be used. Although gas samples are often studied and used in LIBS or other laser plasma applications, more experiments are investigating solid samples. Whether similar results can be found in plasma from solid samples becomes the next question. With this question in mind, a Thomson scattering study of aluminum plasma was conducted after the air plasma experiment.

Aluminum plasma

Plasma imaging and probe position

To measure the electron temperature and density, the probe laser must pass through the Al plasma. At atmosphere condition, the plasma plume was about 1-2 mm along the direction of the laser propagation. Therefore the gap between the probe laser and the surface of the Al sample has to be 1 mm or less to probe the core of the plasma. Although special treatment was applied to make sure the surface reflection is minimized, the probe laser still cannot get infinitely close to the sample surface. Before taking TS spectra, it is good to know how far away the probe is from the sample surface and whether the probe can pass through the dense region of the plasma. Hence the images of the probe and the plasma were taken.

By opening the slit on the spectrometer set at the zero-order, the image of the plasma and the probe laser could be recorded. Figure 39 shows the relative position between the plasma and

the probe laser. The distance between the probe and the sample surface was around 700 μm estimated with the help of an air force resolution test chart [24]. During the expansion the probe was close to the core of the plasma. The size of the aluminum sample was 23.4x16.8x1.6 mm. Clear reduction of surface reflection was observed when the plasma was created at the edges due to the decrease of surface area along the laser path. The flare on the right in the first image of Figure 3.10 was caused by the surface reflection. Further reducing the sample-probe distance could significantly increase the reflection and lower the signal-to-noise ratio to an unacceptable level.

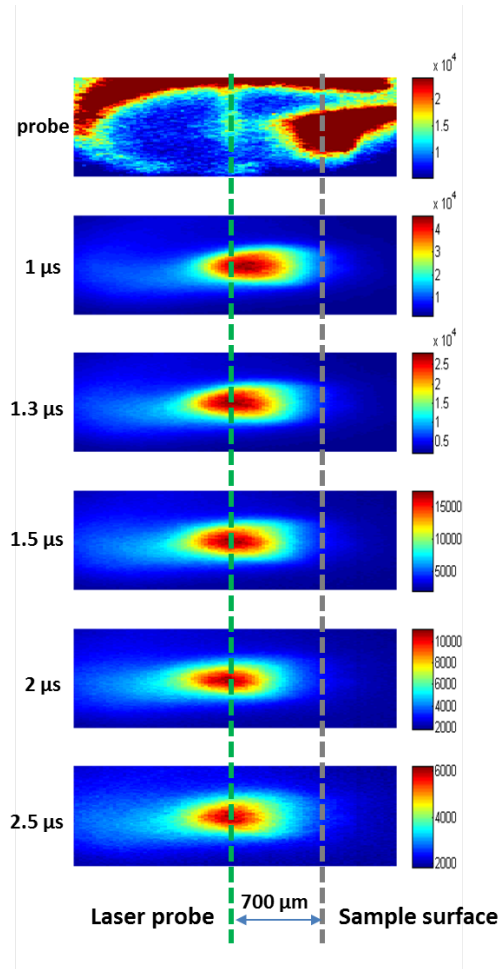


Figure 39. Probe laser and plasma images at different delay time.

Plasma heating

Plasma heating by the probe laser in Thomson scattering was discussed in early literatures^{50,51}. A portion of the probe laser energy can be absorbed by the plasma and result in increased Te and Ne values. Such situation is similar to the dual-pulse LIBS experiment in the

⁵⁰ Mendys, A., et al., Investigations of laser-induced plasma in argon by Thomson scattering. Spectrochimica Acta Part B: Atomic Spectroscopy, 2011. 66(9–10): p. 691-697.

⁵¹ Dzierżęga, K., et al., Experimental investigations of plasma perturbation in Thomson scattering applied to thermal plasma diagnostics. Physical Review E, 2006. 74(2): p. 026404.

reheating configuration^{52,53}. If significant reheating happens, the emission lines are expected to show higher intensity. Since LIBS analysis is based on the plasma emission, the measured Te and Ne is no longer representing the original plasma conditions once the plasma emission changes. In our experiment, 20 mJ laser pulses were used, which are lower than most of works mentioned earlier. According to existing studies, lower laser energy leads to weaker heating effect. Hence the heating effect in our experiment is expected to be insignificant. This expectation is confirmed by the indirect measurement below.

To confirm, the intensity of the 396.2 nm Al line was recorded at four different delay times after the plasma formation. The gate width was 100 ns instead of 20 ns in the previous discussion. This longer gate width ensured the heating effect could be observed even if there was a delay between the heating process and the increase of the plasma emission. At several different delay times, the peak intensities with and without the probe laser were shown in Figure 40. The average intensities are comparable and their differences are within the signal fluctuation. Such comparison cannot completely eliminate the existence of the heating effect, but at least it shows there is no significant heating that can affect the plasma emission.

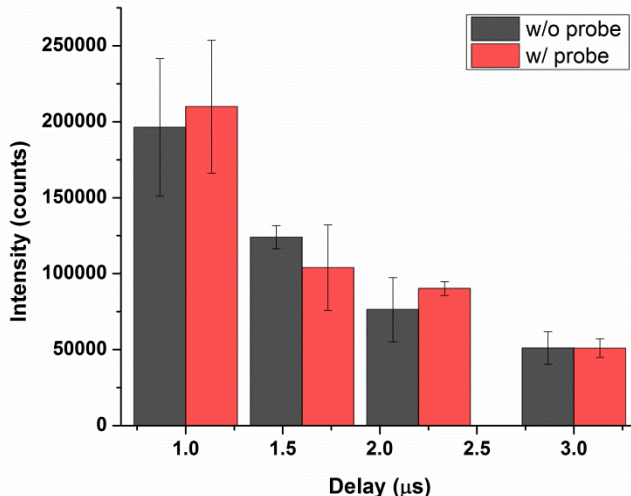


Figure 40. Intensities comparison of the 396.2 nm with and without the probe laser at 1, 1.6, 2.2, and 3 μ s after the plasma formation.

Thomson scattering spectrum

Similar to the early time air plasma Thomson scattering experiments, the collective Thomson scattering spectrum featured with two symmetric satellite peaks were observed and shown in Figure 41-a. The vertical binning of the CCD, from 330 to 355, where Thomson scattering signals can be observed, generated a raw spectrum. For consistency with the air plasma study, the fitting was mainly based on the blue-shifted peak (Figure 41-b), unless severe distortion or noise was observed.

⁵² Scaffidi, J., S.M. Angel, and D.A. Cremers, Emission Enhancement Mechanisms in Dual-Pulse LIBS. *Analytical Chemistry*, 2006. 78(1): p. 24-32.

⁵³ Weidman, M., et al., Thermodynamic and spectroscopic properties of Nd:YAG-CO₂ Double-Pulse Laser-Induced Iron Plasmas. *Spectrochimica Acta Part B: Atomic Spectroscopy*, 2009. 64(10): p. 961-967.

The higher Te and Ne, the more distinct and separated these two satellite peaks become. Compared with the Rayleigh scattering signal from the air molecules at 1 atm, the intensity of the two peaks are hundreds times weaker. However, as long as the features of the satellite peaks are resolved, Te and Ne can be obtained by fitting the spectra. Due to the low intensity of the Thomson scattering signals, accumulation of a large number of shots (500 shots in our case) are usually needed for better SNR.

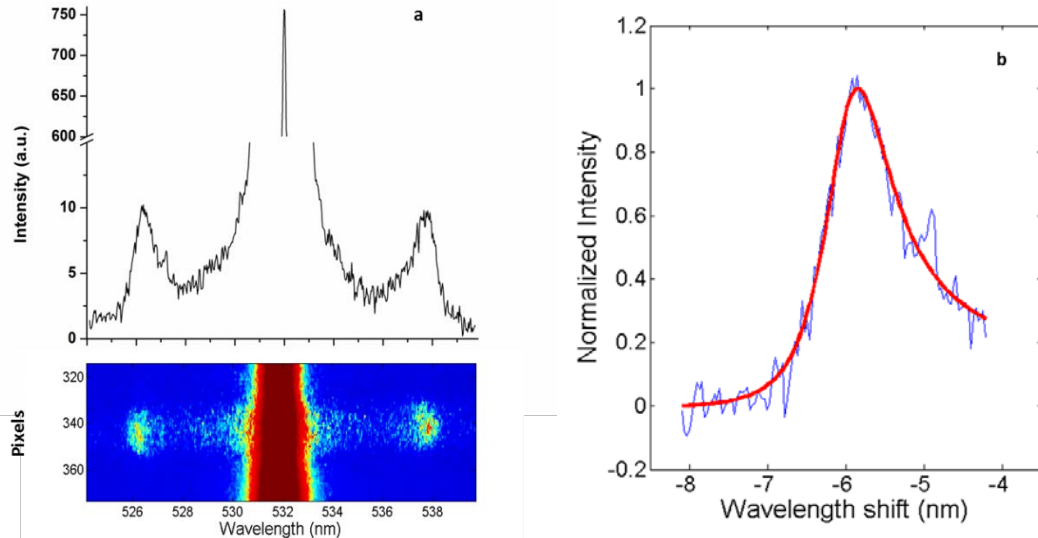


Figure 41. a) Raw Thomson scattering spectrum and b) Fitting of the blue-shifted satellite peak of the spectrum for the Al plasma 800 ns after plasma creation at 1 atm pressure.

Time resolved Te and Ne measurements

Time resolved Thomson scattering spectra of the Al plasma were recorded. By fitting the spectra, Te and Ne values were obtained and are shown in Figure 42. The highest Te and Ne detected were 96000 ± 1400 K and $6.10 \pm 0.07 \times 10^{17}$ cm $^{-3}$ at 400 ns after plasma creation. Then both Te and Ne quickly decrease to less than 40000 K and 2×10^{17} cm $^{-3}$ within the next 600 ns. The lowest Te and Ne detected were around 19000 K and 5.5×10^{16} cm $^{-3}$ at 2.5 μ s after plasma creation. The minimum delay time at which Thomson scattering signal could be resolved was 400 ns in this study. For delay time less than 400 ns, the continuum emission of the plasma was so strong that the SNR of the Thomson scattering signal was too low to be considered acceptable. For delay time of 3 μ s or more, the separation between the satellite peak and the central Rayleigh scattering peak was so small that only the rising part of the peak can be resolved. The fitting algorithm was not able to generate a reasonable estimate of Te and Ne without the falling edge of the peak. Unfortunately in the study of the Al plasma, the non-collective TS spectra could not be successfully taken, because the peak at 532 nm was distorted due to the surface reflection. Hence all the measurements were restricted in the collective Thomson scattering regime. The error bars in Figure 42 are the 3σ errors of the fitting parameters. Larger error bars at early time of the plasma are due to the higher noise level caused by the continuum emission.

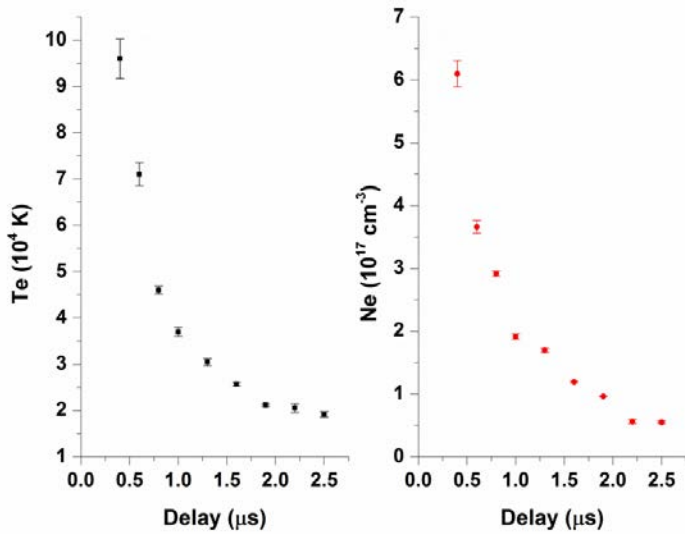


Figure 42. Time evolution of the Te and Ne of the Al plasma at 1 atm pressure.

In LIBS experiments, gated detection is often used. A gate delay is used to reduce the early time continuum emission so that the SNR of the ionic and atomic peaks is improved. Furthermore, in Te and Ne sensitive studies, a short gate width from hundreds of ns to a few μ s is often used to avoid significant changes of the plasma condition. Fortunately, the effective time window for Thomson scattering measurements matches very well with the detection window for many LIBS experiments. This overlap in time indicates great potential of Thomson scattering measurements in LIBS plasma characterization.

McWhirter criterion and LTE

The McWhirter criterion is often used to check if LTE condition is violated. A simple form of the criterion can be expressed as

$$N_e \geq 1.6 \times 10^{12} T_e^{1/2} (\Delta E)^3.$$

In this expression, ΔE is the highest energy transition in eV for which the condition holds, Ne is in cm^{-3} and Te is in K. Although the McWhirter criterion does not guarantee LTE if the inequality is satisfied⁵⁴, once the above relation is violated, LTE no longer holds. According to the above expression, one can easily find the maximum transition energy that breaks the criterion at a given plasma condition. Using the Te and Ne measured from Thomson scattering, the highest ΔE that satisfies the McWhirter criterion as a function of the delay time is plotted in Figure 43. The ΔE values are spread between 6 and 11 eV, and can be fitted by a linear model $\Delta E = -2t_d + 11$, where t_d is the delay time. The shortest wavelength recorded in many LIBS experiments is 200 nm, corresponding to 6.2 eV. Therefore until 2.5 μ s after plasma initiation, all transitions which show up as an emission line in the LIBS spectrum satisfy the McWhirter criterion.

⁵⁴ Cristoforetti, G., et al., *Local Thermodynamic Equilibrium in Laser-Induced Breakdown Spectroscopy: Beyond the McWhirter criterion*. Spectrochimica Acta Part B: Atomic Spectroscopy, 2010. 65(1): p. 86-95.

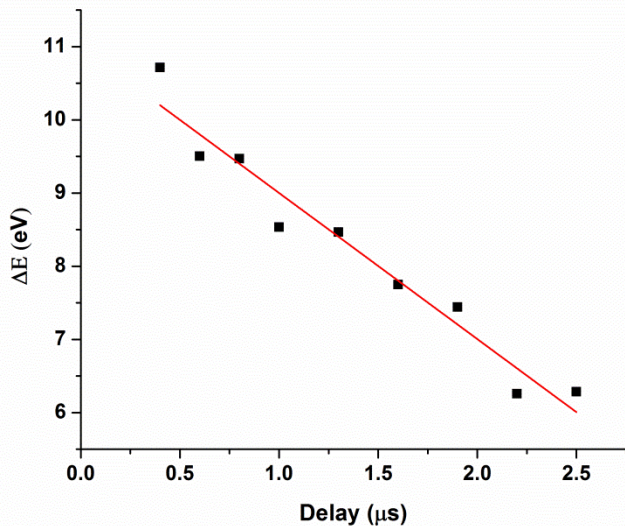


Figure 43. The maximum transition energy that satisfies the McWhirter criterion as a function of delay time between the creation of plasma and the detection.

In addition, Figure 42 still provides some insights to the selection of the detection window of a LIBS experiment. Due to the transient nature of LIP, the larger Te and Ne change during the detection window, the farther away the plasma status deviates from LTE. Clearly the decay rate was faster during the first 1 μ s than in the later time. To minimize the temporal variation of Te and Ne, the gate delay is preferred to be later than 1 μ s, and the gate width should be as short as possible if SNR is acceptable. Further examination of the LTE condition requires additional analysis, such as the comparisons between the decay rate of the plasma and the relaxation rate (or time) of different species, and between the variation length of the plasma and the diffusion length.

ENHANCEMENT OF LIBS SIGNALS

Enhancement of LIBS signal by double-pulse Nd:YAG-CO₂ LIBS

A suggested approach to improve sensitivity (by increasing the signal-to-continuum-background ratio) is the use of a dual-pulse configuration (DP-LIBS). The aim of DP-LIBS is to improve the coupling of the laser energy to the target and to the ablated material, leading to a higher number of emitters from the analyzed sample in the plasma.

Since the first demonstration of dual-pulse LIBS in 1969 by Piepmeier and Malmstadt⁵⁵, it has been demonstrated that two laser pulses for LIBS lead to enhanced emission intensities, longer plasma lifetime and higher plasma temperature. To optimize these effects, several combinations have been proposed involving various geometries (angle between the laser beams), different laser wavelengths and/or pulse durations and interpulse delay, as well as different pulse energies.

⁵⁵ E.H. Piepmeier, H.V. Malmstadt, Q-Switched laser energy absorption in the plume of an aluminum alloy, *Anal. Chem.* 41 (1969) 700–707.

A collinear approach combines two pulses following the same path and focused upon the same point of the sample. The orthogonal configuration uses multiple optics to focus at different locations (double-focus collinear configuration has also been demonstrated⁵⁶). Two configurations are possible with an orthogonal geometry: a pre-ablation spark to produce plasma above the sample prior to the ablation or a reheating spark focused upon the expanding plasma created by the first pulse.

In Babushok et al.⁵⁷ and Scaffidi et al.⁵⁸, overviews of the different mechanisms leading to emission enhancement in DP-LIBS experiments are given. Depending on the delay time between the pulses, several explanations to the enhancement can be given. From zero-delay to tens of ms, the physics behind the phenomenon changes. In Scaffidi et al., three mechanisms are mainly detailed: Pulse-plasma coupling (re-exciting or exciting of the plasma components), sample heating (heating by the hot plasma close to the surface resulting in increased ablation) and atmospheric effects (creation of a hot region with low density above the sample). In Babushok et al., an extensive list of possible effects is given from the preparation of the sample by the first pulse (smoothing, first crater, onset of melt) to the energy coupling with the plasma (ion yield, plasma re-heating, electron density).

In this study, we present the results of a dual-pulse LIBS experiment where a nanosecond NIR pulse is combined with a MIR CO₂ laser pulse and focused on an iron sample. An 8-fold enhancement is reached by irradiating the sample first with the CO₂ laser pulse and then ablating it with the Nd:YAG laser. The effect of interpulse delay allows us to advance a combination of mechanisms leading to the enhancement of the LIBS signal compared to that obtained with a single Nd:YAG laser pulse.

Experimental Setup

The experimental configuration is shown in Figure 1. Two lasers are fired onto the same spot of a sample and the light emitted by the plasma is collected and guided to a spectrometer.

Laser sources

The first laser is a Q-switched Nd:YAG (Quantel Brilliant) at the fundamental wavelength of 1064 nm. It is externally triggered at 0.33 Hz. A thin-film polarizer is used in conjunction with a $\lambda/2$ plate to provide continuous control of the laser energy from 5 mJ up to 340 mJ without changing the flashlamp voltage or the Q-switch delay time. The pulse energy is measured with a calibrated pyroelectric joulemeter (Gentec SOLO 2 with a QE-25 head). The peak-to-peak and RMS fluctuations in pulse energy are 1.51 % and 0.44 % respectively. The full width half maximum (FWHM) pulse duration is 5 ns as measured with a fast photodiode (Thorlabs) placed behind a dielectric turning mirror. The laser is focused with a 13.5 cm focal length lens at normal incidence, and the lens-to-sample distance is 13 cm. The beam radius at the sample location, determined by the knife-edge scan technique, is approximately 230 μ m.

⁵⁶ J. Bruce III, Alexander Dennis, Collinear dual pulse-dual focus enhancement of femtosecond LIBS, 5th International Conference on Laser-Induced Breakdown Spectroscopy (Berlin, Germany, 2008), 2008, 22–26 September

⁵⁷ V.I. Babushok, F.C. DeLucia Jr., J.L. Gottfried, C.A. Munson, A.W. Mizolek, Double pulse laser ablation and plasma: laser induced breakdown spectroscopy signal enhancement, Spectrochim. Acta Part B 61 (2006) 999–1014.

⁵⁸ J. Scaffidi, S.M. Angel, D.A. Cremers, Emission enhancementmechanismsin dual-pulse LIBS, Anal. Chem. 78 (1969) 24–32.

The second laser is a transversely excited atmospheric (TEA) CO₂ laser with components made by Lumonics. It utilizes an external 1 m half-symmetric resonator and emits at 10.6 μ m. An intra-cavity iris is used to limit the number of higher order transverse modes and provide a circularly symmetric beam profile as viewed using an IR pyroelectric beam camera (Spiricon Pyrocam III). The laser energy is continuously tunable between 70 μ J and 80 mJ by using a set of crossed polarizers. The pulse energy is measured using the same pyroelectric joulemeter

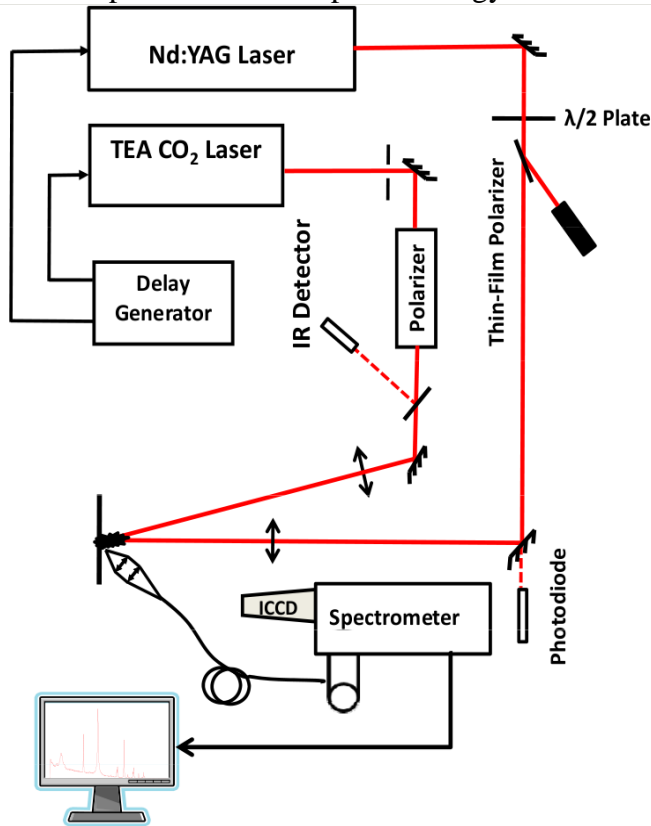


Figure 44. Experimental setup

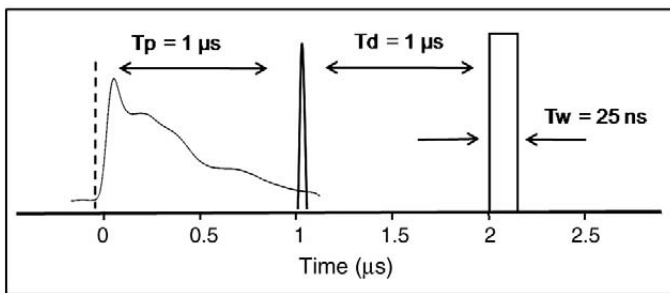


Figure 45. Timing configuration of the experiment. The interpulse delay T_p is set as positive when the Nd:YAG laser precedes the CO₂ laser pulse and negative in the opposite order. The acquisition delay T_d is set to 1 μ s after the second pulse and the duration of acquisition T_w to 25 ns.

described above. The peak-to-peak and RMS fluctuations in pulse energy are 3.5 % and 0.98 %, respectively. The temporal profile is measured with a multiple junction photovoltaic detector (Vigo Systems PVM-10.6) with nanosecond response time. The temporal profile is composed of a 100 ns pulse followed by a 1 μ s tail (Fig. 51). The laser is focused with a 26 cm focal length lens at 13 degrees from normal, and the lens-to-sample distance is 25.5 cm. The beam radius at the sample location is approximately 280 μ m as determined using a knife-edge scan.

Collection optics and spectrometer

The plasma emission is collected using an f/1 quartz lens and is coupled to a 1 m round-to-line UV-grade fiber bundle using a second (f/2) lens. The collection optics are at 40 degrees from the surface normal. The fiber bundle is f-matched to a 0.5 m Czerny-Turner imaging spectrometer (Acton 2500i, Princeton Instruments) with a 1800 lines/mm grating. The light is detected using an intensified charge coupled device (Andor iStar DH720-25F-03) with 1024 x 256 pixels and a 25 mm Gen II intensifier. The intensifier delay is measured from the rising edge of the second pulse. Each spectrum is the average of 30 single acquisitions.

Timing

The timing of the experiment is controlled using two digital delay generators (Stanford Research Models DG-645 and DG-535). The DG-645 triggers the flashlamp of the Nd:YAG laser and also triggers the DG-535 at 10 Hz. The DG-535 divides the frequency

to 0.33 Hz and triggers the Q-switch of the Nd:YAG laser, the CO₂ laser and the ICCD camera. Timing uncertainty between Nd:YAG and CO₂ pulses is primarily limited by the CO₂ laser and has peak-to-peak fluctuations of approximately 42 ns and a standard deviation of 9 ns.

Samples

The sample is a 100 μm -thick foil of 99.9+% pure iron (Product #: 356808, Sigma-Aldrich, St. Louis, MO, USA). The foil is cleaned with acetone and mounted so that it remains flat and vertical to minimize any deposition of material after the ablation. The sample is translated between each acquisition in order to have a fresh location for each shot.

Results and discussion

The original intention of the present dual-pulse LIBS study was to use 10.6 μm radiation from a CO₂ laser to raise the temperature of the plasma created using an Nd:YAG laser. The reason to use a CO₂ laser instead of another Nd:YAG laser is that the critical electron density scales with the square of the plasma frequency and thus, longer wavelength laser pulses are more easily absorbed by the relatively low density regions of the plasma. The use of multiple wavelengths for dual pulse LIBS has been reported⁵⁹ using both UV and NIR pulses, and a correlation was found between signal enhancement and plasma temperature.

A comparison between single-pulse and double-pulse LIBS spectra is shown in Figure 46. Each spectrum represents the average of 30 acquisitions with 1 μs delay and 25 ns integration. Spectra for the single-pulse case of Nd:YAG and CO₂ are shown in a) and b) respectively, and the double-pulse case for Nd:YAG preceding the CO₂ pulse and Nd:YAG following the CO₂ pulse are shown in c) and d) respectively. In all cases, the energy of Nd:YAG and CO₂ lasers were 39 mJ and 75 mJ respectively.

The spectral lines in Fig. 46a are singly-ionized iron lines. The weak signal in Fig. 46b can be attributed to minimal ablated mass during the relatively long interaction time of the CO₂ pulse and consequently low irradiance on the sample. For dual pulse case, with the CO₂ laser pulse reheating the plasma (Fig. 46c), there is no signal enhancement relative to the Nd:YAG only. This can be partially attributed to the acquisition delay of 1 μs measured from the second laser pulse; therefore, 2 μs after the Nd:YAG pulse. This behavior is not representative of significant plasma heating by the CO₂ pulse. However, the effects of plasma reheating using a CO₂ laser pulse (increased line intensities) have been demonstrated previously.

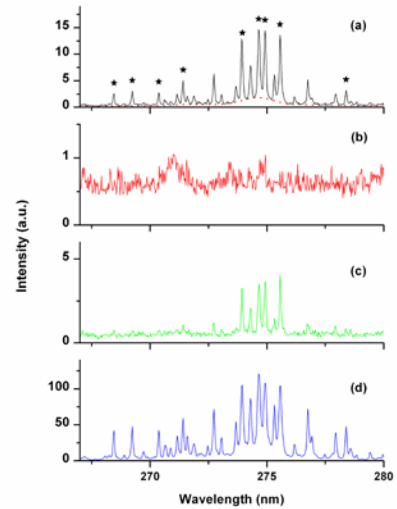


Figure 46. LIBS spectra of iron from a) a single Nd:YAG pulse, b) a single CO₂ laser pulse, c) double pulse spectra with CO₂ following Nd:YAG by 1 μs compared with Nd:YAG alone LIBS spectrum and d) double pulse spectra with CO₂ preceding Nd:YAG by 1 μs . (Acquisition delay: 1 μs , duration of acquisition: 25 ns). In a), the dotted line shows a background spline interpolation and the stars indicate the lines used for plasma temperature calculation. Baseline correction is applied for all spectra.

⁵⁹ L. St-Onge, V. Detalle, M. Sabsabi, Enhanced laser-induced breakdown spectroscopy using the combination of fourth-harmonic and fundamental Nd:YAG laser pulses, Spectrochim. Acta Part B 57 (2002) 121–135

Table 7. Parameters of the spectral lines used in the plasma temperature calculations⁶⁰ [12].

Wavelength λ_{ul} (nm)	Upper level energy E_u (eV)	Degeneracy g_u	Transition probability A_{ul} (s ⁻¹)
268.48	8.43	10	$1.4 \cdot 10^8$
269.26	8.37	12	$1.2 \cdot 10^8$
270.40	7.97	8	$1.2 \cdot 10^8$
271.44	5.55	6	$5.5 \cdot 10^7$
273.96	5.51	8	$1.9 \cdot 10^8$
274.65	5.59	6	$1.9 \cdot 10^8$
274.93	5.55	8	$2.1 \cdot 10^8$
275.57	5.49	10	$2.1 \cdot 10^8$
278.37	7.70	10	$7.0 \cdot 10^7$

Table 8. Physical and numerical parameters used in our 1D heat equation model. The value corresponding to the solid form is given by the literature.⁶¹

Parameters	Values
Thermal conductivity, κ (W.cm ⁻¹ .K ⁻¹)	0.802
Specific heat, C_p (J.g ⁻¹ .K ⁻¹)	0.449
Mass density, ρ (g.cm ⁻³)	7.87
Absorption coefficient, α (m ⁻¹) ($\lambda=10.6$ μ m)	$3.3 \cdot 10^7$
Reflectivity, R ($\lambda=10.6$ μ m)	0.967
Melting point, T_m (K)	1811
Space range	[$x_0=0$ μ m ; $x_f=10$ μ m]
Space sampling	701 points
Time range	[$t_0= -650$ ns ; $t_f = 1849$ ns]

⁶⁰ Y. Ralchenko, A.E. Kramida, J. Reader andNIST ASDTeam(2008). NIST Atomic Spectra Database (version 3.1.5), [Online]. Available: <http://physics.nist.gov/asd3> [2008, December 2]. National Institute of Standards and Technology, Gaithersburg, MD

⁶¹ E.N. Sobol, Phase transformations and ablation in laser-treated solids, John Wiley & Sons, New York, 1995.

Time sampling	2500 points
Initial condition	$T(x, t = 0) = 300K$
Boundary conditions on x_0 and x_f	$\frac{\partial T(x = x_0, t)}{\partial x} = 0, \frac{\partial T(x = x_f, t)}{\partial x} = 0$

In a previous work by Killinger et al.⁶², an enhancement of both atomic (up to a factor of 60) and ionic (up to a factor of 300) aluminum lines for a high purity alumina sample was observed when a Nd:YAG pulse (5 ns, 50 mJ mm⁻²) was followed by a CO₂ pulse (100 ns peak and 5 μs tail, 70 mJ.mm⁻²). This difference in behavior as compared to our results can be attributed to both energy density and sample properties, a metal in our case and an insulator in their case. To understand the effect of the CO₂ pulse in dual-pulse LIBS, the time delay between pulses has been varied from the CO₂ pulse preceding the Nd:YAG pulse by 5 ms to the CO₂ pulse following Nd:YAG pulse by 10 μs. For clarity, Fig. 47 shows the intensity of the Fe II 274.65 nm ionic line for a delay between -10 μs and +10 μs. A negative delay means the CO₂ pulse reaches the sample before the Nd:YAG pulse. Although there is minimal plasma reheating by the CO₂ pulse, a signal enhancement of approximately 8 times occurs for an interpulse delay of -1 μs. This signal enhancement is closely correlated to an enhancement in plasma temperature, as calculated using a Boltzmann plot with the parameters listed in Table 7. The temperature for a single-pulse Nd:YAG plasma is 15 000 ± 2000 K and 23 000 ± 2000 K for dual pulse with -1 μs interpulse delay.

When the CO₂ pulse is fired before the Nd:YAG, two mechanisms may occur: (i) the CO₂ pulse heats the sample before the arrival of the Nd:YAG pulse, (ii) the Nd:YAG interacts with the weak plasma created by the CO₂ pulse, ablating the sample softly and extracting non excited particles from the sample with size distribution ranging from atomic to clusters.

Heating of the sample by the CO₂ pulse

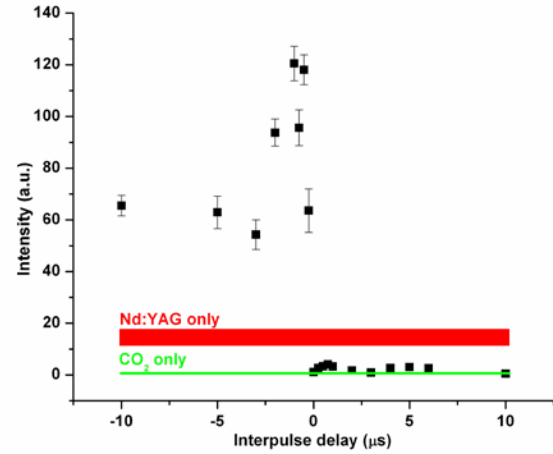


Figure 47. Background-corrected peak intensity of the Fe II 274.65 nm line as a function of the interpulse delay. A negative delay means the CO₂ pulse reaches the samples before the Nd:YAG pulse. A positive delay is for the opposite timing configuration. Comparison is made with the single-pulse cases. The error bars represent the standard deviation over 30 single acquisitions. The inset in the upper right corner is a zoom between -3 μs and 0 μs showing the maximum enhancement at -1 μs.

⁶² D.K. Killinger, S.D. Allen, R.D. Waterbury, C. Stefano, E.L. Dottery, Enhancement of Nd:YAG LIBS emission of a remote target using a simultaneous CO₂ laser pulse, Opt. Express 15 (2007) 12905–12915.

Several studies have shown a positive correlation between the intensity of the LIBS signal intensity and the sample temperature^{63,64}. This phenomenon is explained by less energy being required to melt or vaporize of the sample — the important parameters in long-pulse ablation above room temperature. Furthermore, the reflectivity of metals decreases when the surface temperature increases⁶⁵. These two factors could lead to a better energy coupling between the Nd:YAG pulse and the sample if previously heated by the CO₂ pulse. To understand the importance of this phenomenon, a simple model of heat conduction is used.

The model is one-dimensional (1D) since the absorption length of a radiation with a 10.6 μm-wavelength at 298K in the target is approximately 30 nm ($l_a=1/\alpha$, with $\alpha=3.3 \cdot 10^7 \text{ m}^{-1}$), which is much smaller than either laser beam diameter. The 1D heat equation has the following form:

$$\frac{\partial T(x,t)}{\partial t} = \frac{\partial}{\partial x} \left[\left(\frac{\kappa}{C_p \rho} \right) \frac{\partial T(x,t)}{\partial x} \right] + \frac{\alpha}{C_p \rho} S(x,t)$$

with $S(x,t) = I_0(t) e^{-\alpha x} (1 - R)$. $I_0(t)$ is the laser irradiance (in W cm⁻²) and the other parameters are listed in Table 2. This calculation is done via a matricial implicit algorithm for solving parabolic partial differential equations⁶⁶. The conditions of the algorithm are also given in Table 8. The temporal profile of the heat source $I_0(t)$ is an experimental profile acquired from a 75 mJ CO₂ pulse. The model yields an estimate of the temperature on the sample surface. However, no conclusions on the ablation products or the plasma characteristics can be extracted.

The calculated temperature distribution in the target is plotted as a function of time as shown in Fig. 48. The first conclusion is that the melting point T_m (1811 K for iron) is not reached with the irradiance of the CO₂ laser pulse used. The maximum temperature at the surface is approximately 860 K and occurs at 550 ns. This is supported by the microscope images of the sample irradiated by only the CO₂ laser (Fig. 50b) where small degradation of the material by the CO₂ pulse is observed after 30 shots on the same spot. The crater depth after 30 shots (using a Zygo NewView 6300 3D optical profiler) is not discernible within the roughness of the sample and is most likely

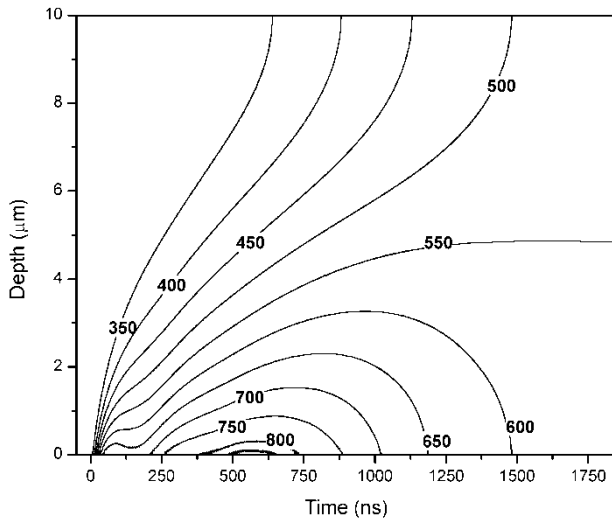


Figure 48. Calculated temperature distribution in the target as a function of time for an iron

⁶³ S. Palanco, L.M. Cabalín, D. Romero, J.J. Laserna, Infrared laser ablation and atomic emission spectrometry of stainless steel at high temperatures, *J. Anal. At. Spectrom.* 14 (1999) 1883–1887.

⁶⁴ S.H. Tavassoli, A. Gragossian, Effect of sample temperature on laser-induced breakdown spectroscopy, *Opt. Laser Technol.* 41 (2009) 481–485.

⁶⁵ M. von Allmen, A. Blatter, *Laser-beam interactions with materials — physical principles and applications*, 2nd edition, Springer, Berlin, 1998.

⁶⁶ J.P. Nougier, *Méthodes de calcul numérique*, 3rd edition, Masson, Paris, 1985.

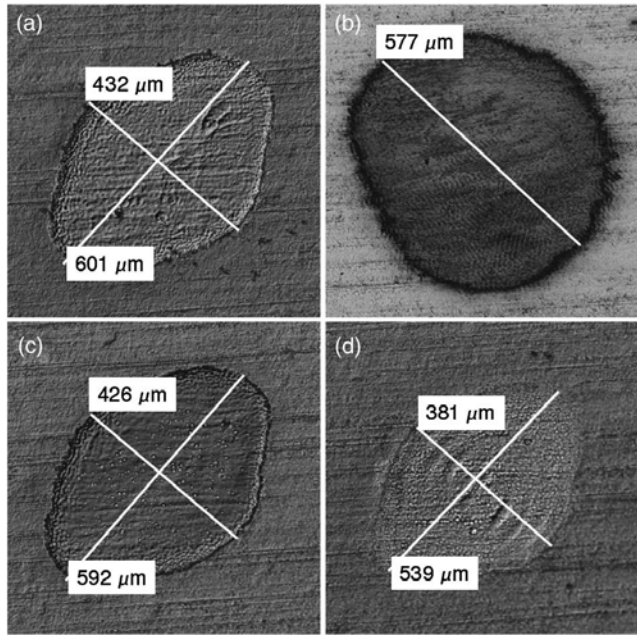


Figure 49. Microscope pictures of the iron sample after a) a single Nd:YAG laser shot, b) an accumulation of 30 CO₂ laser shots, c) a combination of a Nd:YAG laser shot followed by a CO₂ laser shot 1 μ s later and d) a combination of a CO₂ laser shot followed by a Nd:YAG laser shot 1 μ s later.

size distribution of particles is limited by the absorption depth $1/\alpha$ ⁶⁷. Two types of emitters are localized in time-integrated pictures of the plasma shown in Fig. 6b (using a manually triggered Nikon D40x DSLR with 300 mm 1:1 macro zoom lens at f/8 with 1 to 2 second exposure time to integrate the entire plasma lifetime). Light emission is observed at two different locations: one component along the normal and the other close to the surface. The paraxial emission is often attributed to small emitters, ejected with high speed from the sample (tens of $\text{km} \cdot \text{s}^{-1}$)⁶⁸, whereas the marginal emission is due to slow heavy emitters (hundreds of $\text{m} \cdot \text{s}^{-1}$).

The spatially integrated temporal trace of the visible emission is shown in Fig. 49c. The first peak is due to bremsstrahlung from electronic collisions with fast emitters, and is shown by the paraxial emission in Fig. 49b. During the course of the CO₂ laser pulse, there is a second emission increase peaking at 800 ns. This is attributed to heavy particles extracted from the surface during the relatively long CO₂ pulse evolution. The low velocity of these emitters restricts their position to within hundreds of microns of the sample, as seen in Fig. 49b.

smaller than the absorption length (30 nm) which is indicative of nanometric layers being ablated by each CO₂ pulse. Given minimal material removal by melting and vaporization, the Nd:YAG pulse following the CO₂ ablation is not influenced by significant sample deformation.

Given the maximum temperature occurs at t=550 ns, a maximum signal enhancement at an interpulse delay of 1 μ s is not completely explained by sample temperature effects.

Interaction of the Nd:YAG laser pulse with CO₂ laser induced plasma

With little apparent sample degradation as a result of the CO₂ laser, a continuum-like emission is detected as shown in Fig. 46b. This continuum can be attributed to bremsstrahlung and/or polyatomic clusters. These emitters are extracted by the CO₂ laser pulse during the interaction with the surface, when a nanometric layer is ablated. When the laser removes material from the surface, the

⁶⁷ E.N. Sobol, Phase transformations and ablation in laser-treated solids, John Wiley & Sons, New York, 1995.

⁶⁸ S. Noel, J. Hermann, T.E. Itina, Nanoparticle generation in plasmas produced by ultra-short laser pulses, *Appl. Surf. Sci.* 253 (2007) 6310–6315

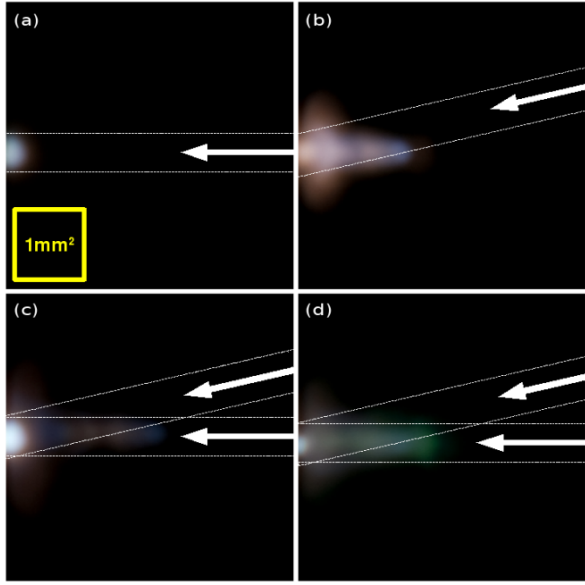


Figure 50. Time-integrated pictures of the plasma produced by a) a single Nd:YAG laser shot, b) a single CO₂ laser shot, c) a combination of an Nd:YAG laser shot followed by a CO₂ laser shot 1 μ s later and d) a combination of a CO₂ laser shot followed by a Nd:YAG laser shot 1 μ s later. The arrows represent the direction of the incoming laser and the dotted lines the laser beam diameter $2w_0$.

When the Nd:YAG pulse arrives 1 μ s after the CO₂ pulse, a maximum coupling with the CO₂ induced plasma occurs because the maximum number of particles has been extracted from the sample. Particle ablation by the Nd:YAG laser is efficient because of their high surface-to-mass ratio, and at this time an enhanced ionic LIBS spectrum is observed (Fig. 46d) compare to the surface ablation by the Nd:YAG only (Fig. 46a). There is a significant difference in the visible emission for the case of CO₂ pulse preceding the Nd:YAG pulse by 1 μ s and the CO₂ pulse following the Nd:YAG pulse by 1 μ s as reflected in Figs. 49c and 49d. These images show a less intense surface plasma in the second case suggesting the absorption of the Nd:YAG above the surface. This is also observed in the crater images shown in Fig. 50. The edges of the crater induced by the Nd:YAG in the dual pulse case of CO₂ first are smoother than in the case when a single Nd:YAG pulse reaches the sample first (Fig. 50a and c).

Combination of mechanisms for LIBS signal enhancement

Maximum signal enhancement occurs when the CO₂ pulse precedes the Nd:YAG pulse by 1 μ s. This condition is shown in Fig. 51 along with the normalized plasma emission and calculated surface temperature. We can divide the timescale in two stages:

The first 700 ns

During the first 700 ns, there is a strong correlation between the surface temperature and the plasma emission. The 100 ns peak of the CO₂ laser pulse quickly heats the sample from approximately 300 K to 650 K. The tail of the pulse reaches a hot surface and heats the sample to 860 K. The signal follows the same trend until approximately 700 ns. This enhances the production of emitting products. These products are mainly heavy emitters rather than ions or

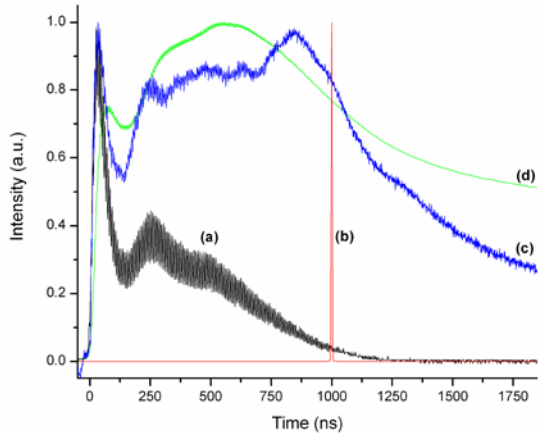


Figure 51. Optimal timing for the maximum of LIBS signal enhancement: a) CO₂ laser pulse intensity, b) Nd:YAG laser intensity, c) the plasma emission from the CO₂ pulse only and d) the calculated surface temperature of the sample.

atoms common to most LIBS plasmas and there is little surface modification. When the Nd:YAG pulse reaches a hot surface, less energy is needed for ablation resulting in increased mass ablation and LIBS signal.

Between 700 ns and 500 μ s

The extraction of particles from the surface increases until approximately 0.7 to 1 μ s. At this time, the coupling between the CO₂ induced plasma and the Nd:YAG pulse is maximum. Emission from the ablation of particles with a distribution of velocity around 500 meters per second will remain within the field of view (approximately 2 mm) for approximately 4 μ s. However, noticeable 2-fold enhancement of the LIBS signal occurs until 500 μ s. Further experiments are in progress to further explain the mechanisms of such a long enhancement.

Conclusion

The optical emission from laser-induced plasma in a dual-pulse LIBS experiment (Nd:YAG at 1064 nm and CO₂ laser at 10.6 μ m) on iron has been studied to understand which mechanisms are responsible for signal enhancement in this configuration. The CO₂ laser pulse heats the sample before the arrival of the Nd:YAG laser pulse during the first 700 ns, without melting the sample or creating noticeable surface deformation. Nevertheless, a nano-layer of heavy and slow particles are extracted and ejected during the CO₂ laser interaction with the iron sample. These particles act as fuel for the second pulse, and lead to greatest signal enhancement approximately one microsecond after the beginning of the CO₂ laser pulse.

Extension of Nd:YAG/CO₂ double pulse LIBS to organics

A potential advantage to using a second pulse at 10.6 μ m (rather than 1.064 μ m) is that longer wavelengths are more easily absorbed at lower electron densities by inverse Bremsstrahlung process. Laser absorption by inverse Bremsstrahlung processes has been described in the form of a simple model by Mora et al.⁶⁹. An increase in plasma temperature can also result in greater excitation of the surrounding gaseous environment or enrichment of the plasma by new chemically formed compounds in the hot medium⁷⁰. For analysis of organic compounds, sample identification can be complicated by a surrounding atmosphere of nitrogen, oxygen, water vapor, and dust. This intrusion of the surrounding atmosphere during sample analysis can be manifested by excited nitrogen and oxygen ions and atoms, as well as the formation of molecular species resulting from reactions between the native carbon from the analyte and the nitrogen of the air^{71,72}. In this study, we were interested in using this (1.064 μ m/10.6 μ m) multi-wavelength dual-pulse LIBS approach for examining the signal from a polystyrene film in an ambient air atmosphere. To evaluate the analytical usefulness of this technique for detecting trace amounts of explosive compounds, we have applied it to analyze 2,4,6-trinitrotoluene (TNT) residues

⁶⁹ P. Mora, "Theoretical model of absorption of laser light by a plasma," *Phys. Fluids* 25(6), 1051 (1982).

⁷⁰ Y. B. Zel'Dovich, *Physics of shock waves and high-temperature hydrodynamic phenomena* (Dover Publications, 2002).

⁷¹ L. St-Onge, R. Sing, S. Bechard, and M. Sabsabi, "Carbon emissions following 1.064 μ m laser ablation of graphite and organic samples in ambient air," *Appl. Phys., A Mater. Sci. Process.* 69, 913–916 (1999).

⁷² M. Baudelet, M. Boueri, J. Yu, S. S. Mao, V. Piscitelli, X. Mao, and R. E. Russo, "Time-resolved ultraviolet laser-induced breakdown spectroscopy for organic material analysis," *Spectrochimica Acta Part B: Atomic Spectroscopy* (2007).

The experimental setup for dual-pulse LIBS was similar to the one above. The polystyrene sample (Mw 280000, dilution of 100 mg/ml in toluene — Sigma Aldrich) was spin coated on a silicon wafer to provide a $3 \pm 0.3 \mu\text{m}$ thick uniform layer and approximate surface concentration of $30 \mu\text{g}/\text{cm}^2$. The thickness was determined using a profilometer (Veeco—Dektak 150). The TNT sample was dissolved in acetonitrile (1 mg/ml) and deposited on a silicon wafer. The solvent was allowed to evaporate leaving an approximate surface concentration of TNT corresponding to $7 \mu\text{g}/\text{cm}^2$. After each laser event (one shot for single pulse or two shots for double pulse), the spectrum was acquired and the sample was translated. To compute the statistical variation, this process was repeated 30 times.

Results and discussion

Polystyrene

A typical double-pulse LIBS spectrum of polystyrene spin coated on silicon (Fig. 3) contains atomic emission lines from carbon at 247.9 nm, nitrogen 742.4 nm, 744.2 nm and 746.8 nm and oxygen at 777.2 nm, 777.4 nm, and 777.5 nm as well as molecular emission from CN and C₂ molecules at 388.3 nm (violet (0-0) band head) and 516.5 nm (Swan (0-0) band head), respectively. The 2nd order of the CN violet (0-0) band head emission appears at 776.6 nm. The other spectral lines are mainly due to silicon emission resulting from the substrate. The thickness of the polystyrene film is much less than the 1/e penetration depth due to absorption by polystyrene; therefore, the laser pulse can be absorbed by the substrate⁷³. This spectrum was obtained using double-pulse excitation with the CO₂ laser pulse following the Nd:YAG pulse by 500 ns (Fig. 52). To reduce the background radiation, the signal was acquired after a 50 ns gate delay. In all cases, this delay was measured with respect to the rising edge (half maximum) of the second pulse. To acquire maximum signal, a 100 μs acquisition window was used to integrate over the complete decay time of the emitting species.

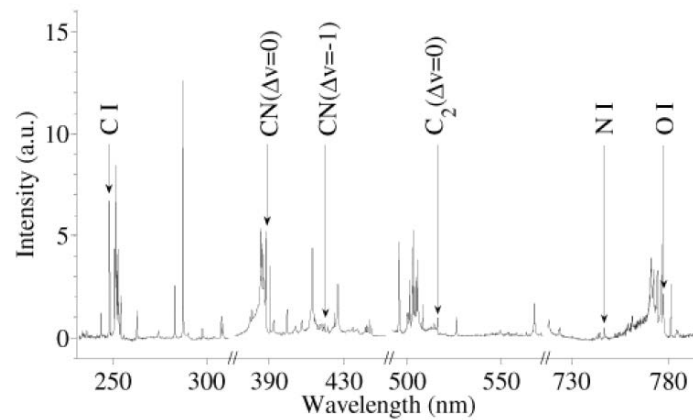


Figure 52. Double-pulse LIBS spectrum for polystyrene on silicon. The second order of the CN violet band system appears at 776.6 nm. There are silicon lines present as a result of the substrate. The CO₂ pulse followed the Nd:YAG pulse by 500 ns, gate delay of 50 ns and 100 μs acquisition.

⁷³ A. Khachatrian, and P. J. Dagdigian, “Laser-induced breakdown spectroscopy with laser irradiation on mid-infrared hydride stretch transitions: polystyrene,” *Appl. Phys. B* 97(1), 243–248 (2009).

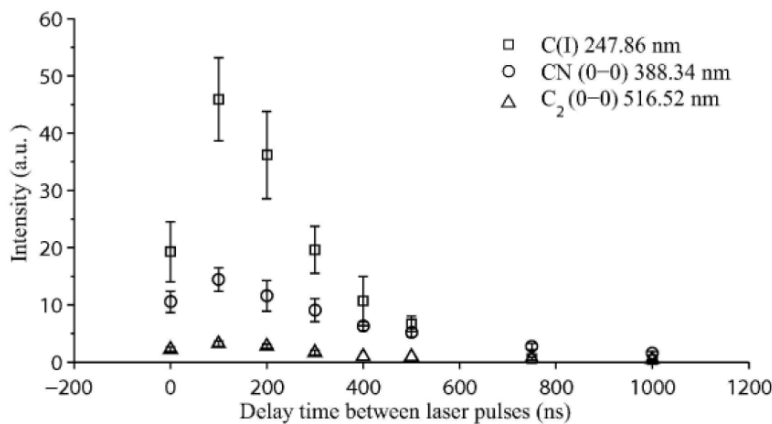


Figure 53. LIBS emission from polystyrene as a function of the delay between laser pulses—Nd:YAG preceding CO₂. Triggering the CO₂ laser before the Nd:YAG resulted in less signal from these three emitters

with respect to the Nd:YAG pulse), a gradual decrease in signal was observed until the two pulses were no longer overlapped in time, in which case, emission similar to that for Nd:YAG-alone was observed. Emission from the CN violet band system was likely resulting from a plasma reaction between atmospheric nitrogen and carbon species from the sample since neither polystyrene nor toluene contains nitrogen in their composition. Similarly, molecular CN formation has been reported from graphite plasmas^{74,75,76,77} as well as from polymers⁷⁸.

A comparison between single-pulse (Nd:YAG only) and double-pulse (Nd:YAG followed by CO₂) LIBS on polystyrene (Fig. 54) was made using the optimal interpulse delay of 100 ns (Fig. 53). The acquisition delay of 50 ns and gate width of 100 μ s was not changed. Excitation with only the CO₂ laser resulted in no observed spectral lines.

An increase in signal was observed for double-pulse compared to single-pulse excitation. The ratio of line intensities between double- and single-pulse excitation was approximately 230 for atomic carbon, 20 for CN and 7 for C₂. Since the sample was a uniform film and the crater diameter was \sim 300 μ m for both single- and double-pulse irradiation, as determined using an optical microscope (BX52—Olympus), the calculated amount of ablated polystyrene remained constant (within the shot-to-shot fluctuations) to approximately 20 ng.

This study has focused mainly on carbon emission: atomic carbon line at 247.9 nm, CN violet band system (with (0-0) band head at 388.3 nm) and C₂ Swan band system (with (0-0) band head at 516.5 nm). The optimal signal from these emitters resulted from a separation time between laser pulses of approximately 100 ns (Fig. 53). Triggering the CO₂ laser before the Nd:YAG resulted in less signal from these three emitters. When the Nd:YAG pulse was delayed with respect to the CO₂ pulse (detector gate is now delayed

⁷⁴ L. St-Onge, R. Sing, S. Bechard, and M. Sabsabi, “Carbon emissions following 1.064 μ m laser ablation of graphite and organic samples in ambient air,” *Appl. Phys., A Mater. Sci. Process.* 69, 913–916 (1999).

⁷⁵ S. S. Harilal, R. C. Issac, C. V. Bindhu, P. Gopinath, V. P. N. Nampoori, and C. P. G. Vallabhan, “Time resolved study of CN band emission from plasma generated by laser irradiation of graphite,” *Spectrochim. Acta A Mol. Biomol. Spectrosc.* 53(10), 1527–1536 (1997).

⁷⁶ C. Vivien, J. Hermann, A. Pertone, C. Boulmer-Leborgne, and A. Luches, “A study of molecule formation during laser ablation of graphite in low-pressure nitrogen,” *J. Phys. D Appl. Phys.* 31(10), 1263–1272 (1998).

⁷⁷ A. A. Voevodin, J. G. Jones, J. S. Zabinski, and L. Hultman, “Plasma characterization during laser ablation of graphite in nitrogen for the growth of fullerene-like CN_x films,” *J. Appl. Phys.* 92(2), 724 (2002).

⁷⁸ A. Portnov, S. Rosenwaks, and I. Bar, “Emission following laser-induced breakdown spectroscopy of organic compounds in ambient air,” *Appl. Opt.* 42(15), 2835–2842 (2003).

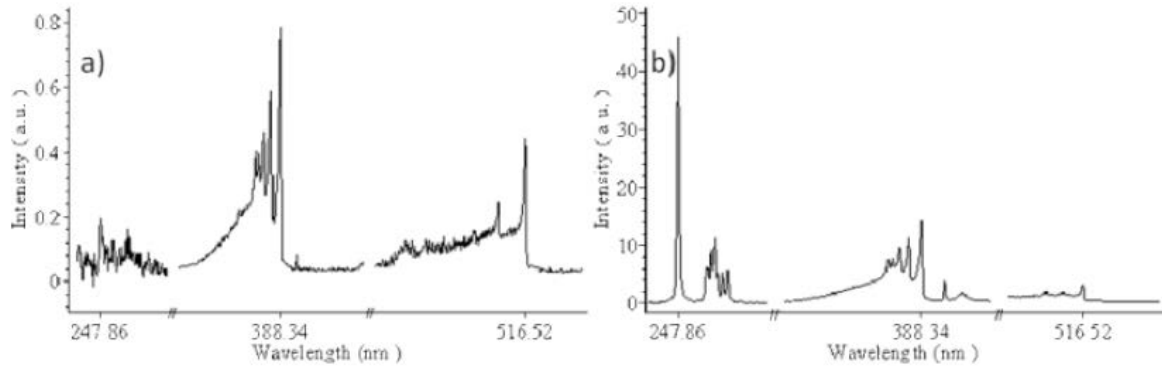


Figure 54. Polystyrene on silicon: a) Nd:YAG single pulse, b) Nd:YAG/CO₂ double-pulse

Therefore, the observed increase in signal suggests that the plasma is heated by the CO₂ laser, which is consistent with the greater atomic emission enhancement compared to molecular emission enhancement. An increase in the temperature will lead to an increased rate of molecular dissociation and hence to a lower molecular mole fraction. For graphite plasmas, atomic carbon emission was reported as having an I^{2.8} dependence on irradiance⁷⁴ while molecular emission remained roughly constant. The figure-of-merit used for evaluating the analytical usefulness of this double-pulse technique was the signal-to-noise ratio (SNR), defined as the background subtracted peak intensity divided by the standard deviation of this peak value. Double-pulse excitation improved the SNR: an increase from 1 to 11 for atomic carbon emission, from 7 to 15 for CN and an increase from 5.6 to 9.3 for C₂ molecular emission. The uniformity in both thickness and concentration of the polystyrene film allowed the SNR to be calculated based on spectra obtained at different locations on the sample without considering sampling heterogeneity. Statistics were based on spectra obtained from 30 independent locations on the sample —30 single-pulses or 30 double-pulses. Single pulse Nd:YAG irradiation using greater energy also resulted in more signal. For example, an Nd:YAG pulse with an energy of 330 mJ resulted in atomic carbon emission approximately half of that obtained with double-pulse. For this more energetic Nd:YAG pulse, the signal-to-noise ratio was 2.6. Therefore, simply increasing the energy of the Nd:YAG pulse yields a SNR of approximately one-quarter of that obtained for double-pulse. This interesting characteristic of double-pulse LIBS led to its evaluation on an explosive residue.

Application to 2,4,6-trinitrotoluene residues

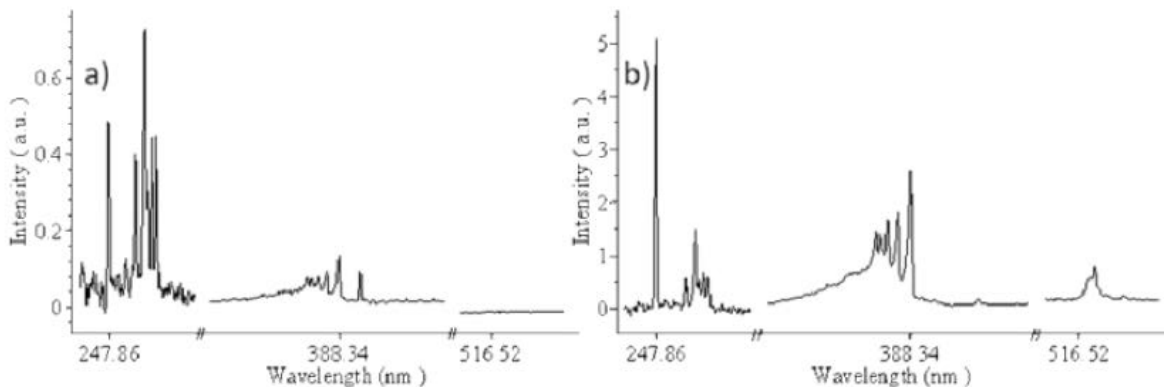


Figure 55. Fig. 6. TNT on silicon: a) Nd:YAG single pulse, b) Nd:YAG/CO₂ double-pulse

An enhanced emission spectra of 2,4,6-trinitrotoluene (2,4,6-TNT) was obtained (Fig. 55) using the same optimal acquisition parameters used for polystyrene. However, there was no C₂ emission (Swan system) observed for either single or double-pulse excitation. The atomic carbon emission is enhanced by a factor of 10 while CN emission is enhanced by a factor of 30. For atomic carbon, the signal-to-noise ratio is 1.5 and 2, and for CN the signal-to-noise ratio is 1.9 and 3.2 for single and double-pulse respectively. The evaporative deposition of TNT resulted in non-uniformity, as observed with an optical microscope (BX52—Olympus), and likely caused sampling heterogeneity that led to a reduced SNR. Molecular C₂ emission has been detected from polystyrene (Fig. 54); however, no C₂ molecular emission was observed from 2,4,6-TNT (Fig. 55). At first glance, the surface concentration of TNT was significantly less than the surface concentration of polystyrene. The 7 $\mu\text{g}\cdot\text{cm}^{-2}$ surface concentration of TNT over the 240 μm diameter crater (measured with the optical microscope) yields $\sim 98 \times 10^{-12}$ moles of carbon atoms in the plume if all TNT was ablated and atomized. Likewise, complete ablation and atomization of the polystyrene would produce $\sim 1.8 \times 10^{-9}$ moles of carbon atoms — two orders of magnitude greater than for TNT. Moreover, the oscillator strength of the C₂ Swan band (0-0) transition (0.005) is 6 times weaker than the CN violet band (0-0) transition (0.032)^{79,80}.

Furthermore, there is different chemistry within the plasma for TNT and polystyrene. A molecule of 2,4,6-TNT is formed of toluene with three attached nitro-groups. The necessary elements to form CN are present in the original molecular structure; yet, at temperatures of 3500 K and above, the most favorable path for thermal decomposition is the detachment of the -NO₂ groups around the aromatic ring, producing a 2,4,6-tolyl triradical⁸¹. The lack of C₂ emission observed in the case of TNT suggests that the presence of the extra nitrogen in the NO₂ groups provided an additional mechanism for consumption/removal of carbon which would otherwise be available to form C₂.

Conclusion

This preliminary study evaluated 1.064 μm /10.6 μm dual-pulse LIBS as a possible method of improving the signal-to-noise ratio (with respect to a single Nd:YAG pulse) from organic materials. For a film of polystyrene on silicon, ~10-fold improvement in SNR were observed for atomic carbon emission and ~2-fold improvements for molecular C₂ and CN emissions. This technique was further applied to the analysis of 2,4,6-TNT residue on silicon; however, there was less than a 2-fold SNR improvement for atomic carbon and molecular CN, and no C₂ emission was observed for single or double-pulse excitation. The lack of observed C₂ emission could be attributed to the low surface concentration of TNT (residue), as well as the chemistry in the plasma that provides additional mechanisms for consumption/removal of carbon which would otherwise be available to form C₂. For polystyrene, the enhanced SNR for the atomic carbon signal is noteworthy; however, the small SNR improvement seen from TNT residue is exceeded by the increased experimental complexity of this double pulse approach. Further experiments must be performed to fully characterize this approach for a more diverse set of

⁷⁹ J. E. Mentall, and R. W. Nicholls, “Absolute band strengths for the C₂ Swan system,” Proc. Phys. Soc. 86(4), 873–876 (1965).

⁸⁰ L. L. Danylewych, and R. W. Nicholls, “Intensity Measurements and Transition Probabilities for Bands of the CN Violet (B₂ Σ + - X₂ Σ +) Band System,” Proceedings of the Royal Society of London. Series A, Mathematical and Physical Sciences, 557–573 (1978).

⁸¹ R. Cohen, Y. Zeiri, E. Wurzberg, and R. Kosloff, “Mechanism of thermal unimolecular decomposition of TNT (2,4,6-trinitrotoluene): a DFT study,” J. Phys. Chem. A 111(43), 11074–11083 (2007).

organic samples, and to fully characterize the effects of changing the laser pulse parameters, such as pulse energy and duration.

Enhancement of LIBS signal by Microwave-Assisted LIBS

Motivation

The emission of plasma created by a nanosecond laser usually lasts for a few seconds to a few tens of seconds. This transit plasma does not produce strong emission especially when the emitter concentration is low. The weak signal generally leads to low sensitivity and makes it difficult to detect low concentration elements. If the lifetime of the useful line emission can be extended, the signal level will increase, and improved performance can be expected.

Since the LIBS plasma is a collision driven plasma, methods that can keep collision happening may be able to extend the plasma emission lifetime. One way to increase collision is applying an oscillating electric field to the plasma. When there is an E field, electrons will accelerate according to the E field direction and absorb energy from the field. Such energetic electrons can excite atoms through collisions. As a result, the atoms will keep emitting as long as the collisional excitation does not stop.

With this idea in mind, the Microwave-Assisted LIBS (MA-LIBS) was developed and studied. In several different experiments, the capability of signal enhancement and sensitivity improvement of MA-LIBS were demonstrated. Meanwhile, special properties such as selective enhancement of lines and enhanced molecular emission lead to new advantages as well as potential problems in spectroscopy applications. Best enhancement was observed with relatively low laser irradiance in normal air condition. The advantage and disadvantage of such operational conditions will be discussed in the end of the chapter.

4.2 Experimental

This section describes the basic components in MA-LIBS experiments. As a brand new addition to the LIBS system, the microwave system is illustrated first. The main features of the microwave system are discussed. For the rest of the system (ablation and detection), general experimental parameters are given. However, for specific experiments, those parameters are optimized for the best results.

4.2.1 Microwave system

To introduce an oscillating E field to the plasma, a specially designed microwave cavity manufactured by Envimetrics was added to a conventional LIBS setup. Microwave at 2.45 GHz was generated by a 1 kW magnetron. After passing through metallic waveguides and an isolator, the microwave enters a resonant cavity. A schematic illustration of the cavity is shown in Figure 4.1. The cylindrical cavity has a 3-inch (7.7 cm) diameter and 1.61-inch (4.1 cm) depth. The sample is placed close to the cover plate, on which a half inch (1.3 cm) aperture is designed to let the laser plasma expand into the cavity. This aperture also locates at the position where the E field has the highest field strength. The laser beam enters the cavity from an opening on the entrance side and creates plasmas on the sample surface on the other side of the cavity. The initial laser plasma expands into the cavity so that it can couple with the microwave. Without the initial laser plasma, the microwave does not generate any plasma by itself. A power supply

controls the microwave pulse duration with maximum value 28 ms, and minimum 1 ms. The generation of the microwave pulses must be synchronized with external trigger sources. The maximum repetition rate for safe microwave pulse generation is 1 Hz.

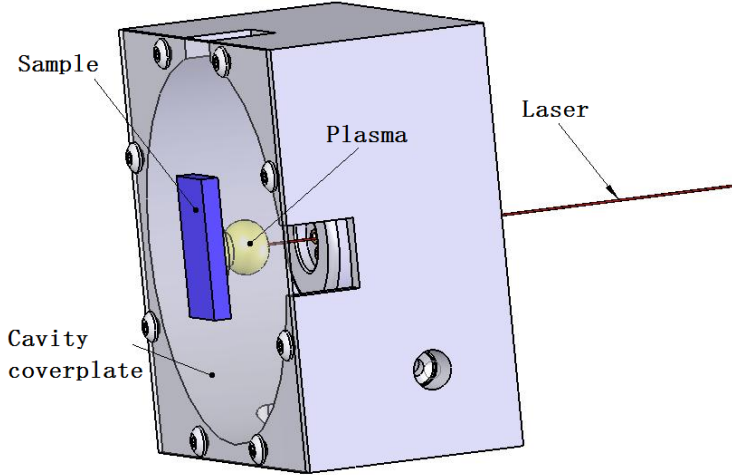


Figure 56. Schematic illustration of the microwave cavity.

4.2.2 Ablation system

A Nd:YAG laser (Brilliant, Quantel) with 5 ns pulse duration at 1064 nm was used with a 10 cm focal length lens with anti-reflection coating as the ablation source. The maximum pulse energy of the laser was 300 mJ, but the combination of a half-wave plate and a polarizer cube controlled the actual laser energy on the sample. As an additional degree of freedom, a translation stage could adjust the lens-to-sample distance around the focal position, controlling the area of the focusing spot, and as a consequence, the irradiance of the laser. The beam diameter, which is obtained from a knife-edge scan measurement, varies from about 100 μm near focal point to 1200 μm at the maximum defocusing available.

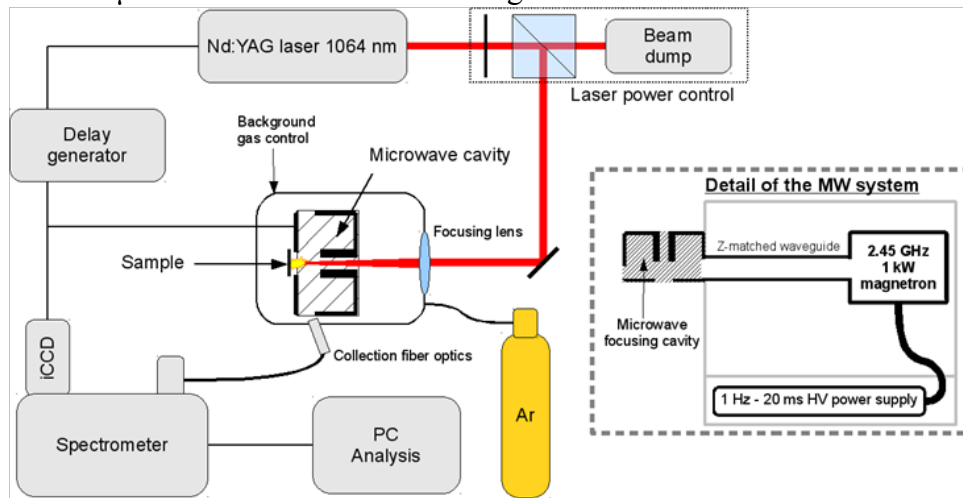


Figure 57. Experimental setup of the MA-LIBS system.

The samples were placed outside the microwave cavity but close to its bottom aperture where the electromagnetic field was the strongest. An X-Y translation stage was used in order to

provide a pristine surface for each laser shot during the analysis. The cavity and the sample could be enclosed by a plastic bag for the control of the atmosphere above the sample, allowing the plasma to expand either in normal atmosphere or in argon, both at room temperature and atmospheric pressure.

4.2.3 Detection system

The plasma emission was collected directly with a UV-transmissive multi-mode optical fiber with a numerical aperture of 0.22. Then it was transferred into a 0.3 m Czerny-Turner spectrometer (2300i, Princeton Instruments – Acton) equipped with two gratings (1800 l/mm and 150 l/mm) to satisfy different resolution requirements. A 512x512 pixels ICCD camera (PI-MAX 2, Princeton Instruments) was used for spectrum recording, providing a resolution from 0.02 to 0.04 nm/pixel with the 1800 l/mm grating depending on the central wavelength.

The whole timing configuration of the setup was driven by a delay generator (DG645, Stanford Research Systems) controlled the firing of the laser (via the Q-switch), and the injection of the microwave cavity. The inter pulse delay between the microwave and the laser did not show a noticeable effect on the spectral intensity or stability as long as the microwave and the plasma have enough overlap in time. 20 μ s were needed to stabilize the microwave signal, so the microwave pulse was triggered 25 μ s before the laser pulse.

Several different studies were conducted to evaluate the performance of the MA-LIBS, and results were compared with traditional LIBS. All comparisons were done with the same experimental parameters in each individual experiment, such as the laser ablation condition, collection geometry, delay time, detector gain and so on, except the gate width. When the microwave was on, the gate width was 20 ms for most studies. It was reduced to a few tens of microseconds in some studies when traditional LIBS signal was taken. The specific acquisition parameters will be given in the discussion of individual experiments.

4.3 MA-LIBS Plasma Characterization

Studies on metallic samples such as lead (Pb) and aluminum (Al) and air were conducted to understand and characterize the MA-LIBS plasma. Most emission and temperature features about MA-LIBS plasma were revealed by the study on Pb samples. In this particular study, 20 mJ of 1064 nm laser pulses were loosely focused onto the sample surface forming a spot with 1 mm diameter, corresponding to about 0.5 GW/cm². The detection was delay for 1 μ s which eliminated the broad continuum emission.

4.3.1 Plasma Emission

In the analysis of Pb with MA-LIBS, spectra of the lead plasma were taken the ICCD camera with 20 ms gate width. The spectra with and without the microwave were shown in Figure 58. One can clearly see the signal enhancement by comparing the two spectra. The 405.8 nm emission line is often used in the detection and quantification of Pb in samples. If we define the enhancement as the ratio between the MA-LIBS intensity and LIBS intensity after baseline removal, 17-fold signal enhancement of the 405.8 nm line was obtained.

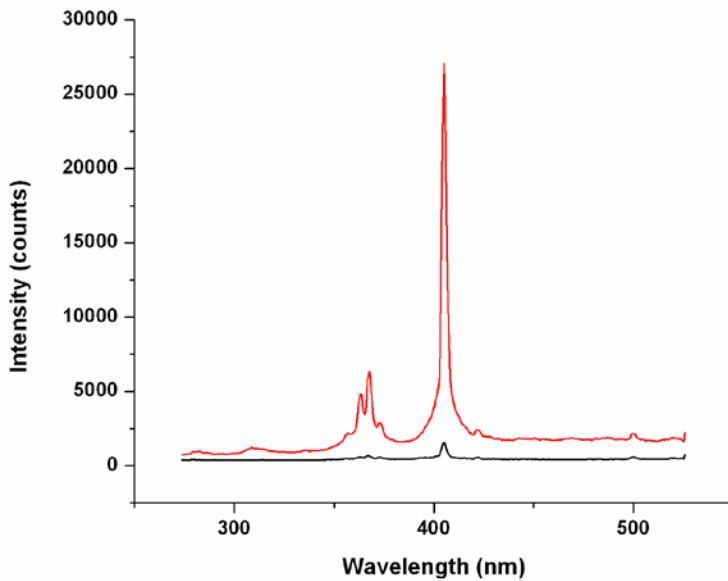


Figure 58. Comparison between LIBS (black) and MA-LIBS (red) spectrum of Pb samples.

The principal of microwave enhancement is considered to be the extended plasma lifetime. To confirm the enhancement mechanism, the intensity of the 405.8 nm line was measured as a function of time. The early time plasma often changes rapidly. In order to capture the fast dynamics, short gate width was used. During the first 10 μ s, the gate width was 50 ns. The short gate width was enough to cover the entire emission evolution of the traditional LIBS plasma. However, for MA-LIBS plasma, the plasma still produce detectable amount of emission after 10 μ s. Due to the reduction of emission in the later time of the MA-LIBS plasma evolution, longer gate width was necessary. As a result, 10 μ s gate width was used after the initial 10 μ s of plasma evolution. In order to make a reasonable comparison between the early time emission and the later time emission, the intensity after 10 μ s was then divided by 200 (the scaling ratio between 50 ns and 10 μ s), so that all the intensity values characterize the emission within 50 ns. The result is shown in Figure 59. Without the microwave, the LIBS plasma has a lifetime about 7 μ s. During the whole lifetime, the plasma emission with and without the microwave behaved similarly. After 7 μ s, the LIBS plasma emission became so weak that it was not detected by the camera. On contrary, the MA-LIBS plasma emission could still be detected and lasts much longer. Even after 18 ms, significant amount of emission could still be detected if a large gate width was applied. Figure 60 shows the spectrum after 18 ms after the laser pulse, and 2 ms gate width was applied.

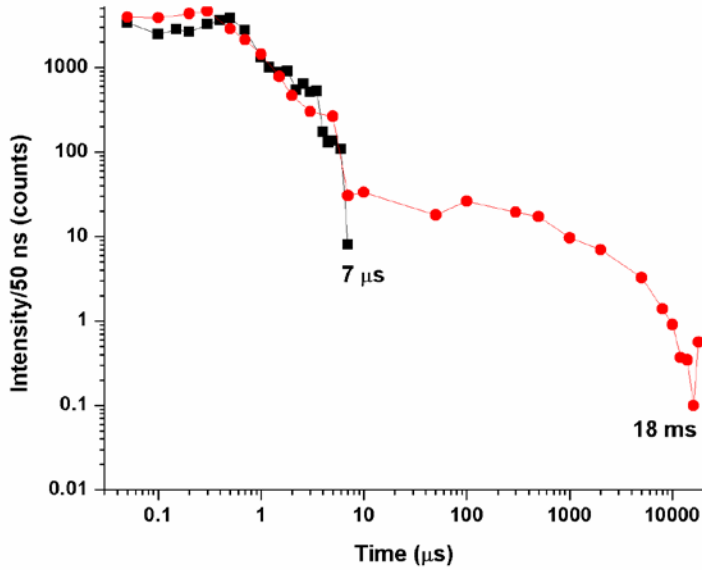


Figure 59. Comparison between the plasma emission at 405.8 nm with (red dot) and without (black square) the microwave. Plasma emission was normalized to characterize the emission per 50 ns.

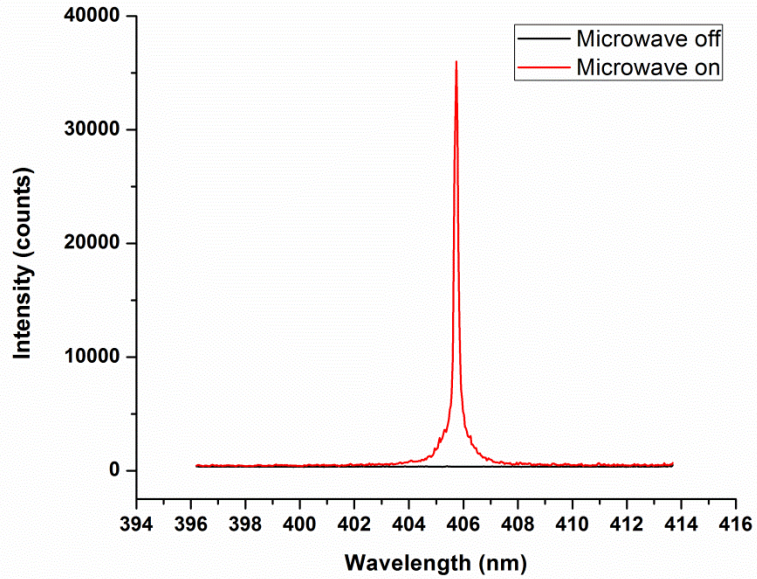


Figure 60. Spectra of Pb plasma with (red) and without (black) microwave 18 ms after the laser pulse with gate width 2 ms. Comparing with Figure 4.3, the high intensity in this spectrum is mainly due to much higher gain from the ICCD camera.

From these results, one can see the MA-LIBS plasma evolution can be characterized as three steps. In the first few microseconds, the plasma emission is dominated by the laser plasma

emission, and the microwave does not affect the plasma properties too much due the high electron density of the LIBS plasma. This step can be called the **LIBS regime**. Main features of the LIBS regime are intense plasma emission and fast decay of intensity. After tens of microseconds, normal LIBS plasma is no longer emitting. All the plasma emission is due to the microwave enhancement effect. The plasma emission per unit time can be thousand times weaker than in the LIBS regime, but it can last tens of thousand times longer. This step can be called the **microwave plasma regime**. Most signal enhancement of MA-LIBS is from this regime. In between these two regimes, there is a transition step from LIBS plasma to microwave plasma, which can be called the **transition regime**. Normal LIBS plasma dies in this regime, but with the help of microwave the plasma emission process can continue. This is the period of time that microwave begins to become effective. In this regime, the plasma emission is slightly stronger than the normal LIBS plasma emission but not much. The decrease of the plasma intensity is also slower than normal LIBS plasma at the same delay time. From this one can expect the plasma temperature and electron density should be higher than the LIBS plasma at the same delay time. There are no hard boundaries between different regimes. Such a classification is for the convenience of future discussions.

4.3.2 Plasma temperature estimation

The plasma temperature of the MA-LIBS plasma was estimated via the Boltzmann plot method based on the Pb spectra. The lines used in the estimation were listed in Table 9. All the three lines could be captured within one spectral window, so emission from the same plasma was evaluated. However, compared with the 405.8 nm line, these three lines had lower intensity. Therefore longer acquisition time was used. For the first 3 μ s, 500 ns gate width was used, while for larger delay time, the gate width increased to 10 μ s. As a result, the temperature is a time averaged estimate of the temperature.

Table 9. Lines used in Boltzmann plots for Pb plasma temperature estimation

λ (nm)	$A_{ij}g_i$ (s^{-1})	E_i (eV)
357.3	3.00E+08	6.13
364.0	1.00E+08	3.38
368.3	1.50E+08	3.33

The temperature as a function of time is shown in Figure 61. The plasma begins with a temperature that did not differ too much with and without the microwave. Slight deviation was observed when the plasma evolved over time, which indicates the entrance of the transition regime. After 3 μ s, the 357.3 nm line from the LIBS plasma became too weak to be used in the Boltzmann plot. However, for the MA-LIBS plasma, thanks to the long-lasting emission, the SNR of the lines was improved by increase the gate width. Therefore the plasma temperature could be investigated even after a very large delay time (500 μ s or longer). As shown in Figure 61, after 500 μ s the plasma temperature of the MA-LIBS plasma was much lower than the initial laser plasma, but it decayed at a much slower rate. Even after 10 ms, the measurement showed a temperature above 5000 K. These findings indicate the microwave can sustain low temperature plasma and keep it emitting for much longer time than the normal LIBS plasma

lifetime. These low temperature measurements agree with plasma temperature measurements for microwave plasmas^{82,83,84}.

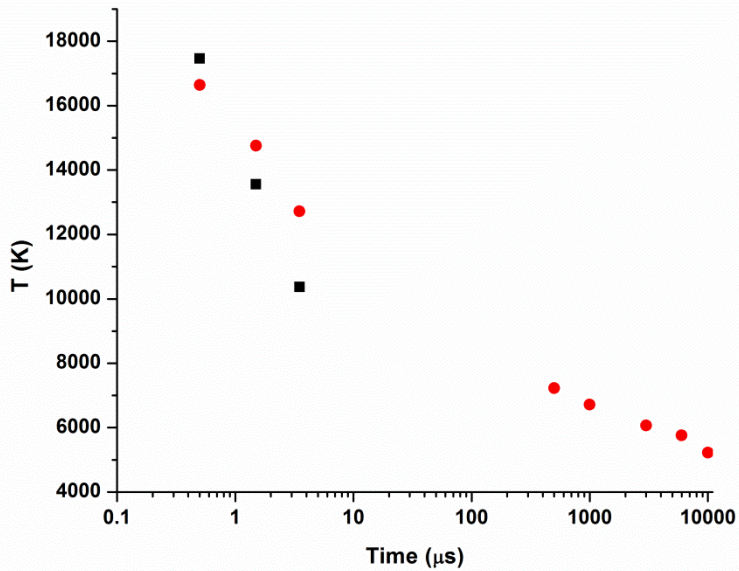


Figure 61. Plasma temperature of Pb plasma with (red dot) and without (black square) microwave.

4.3.3 Electron density

Knowing the electron density of plasma is beneficial to the understanding of the plasma conditions. For the MA-LIBS plasma it is especially interesting to know the electron density in the microwave plasma regime, since the microwave enhancement is due to the extended plasma emission lifetime. As discussed in Chapter 3, electron density within the first three microseconds of typical LIBS plasma is usually larger than 10^{16} cm^{-3} . According to the critical electron density of the 2.45 GHz microwave, which is around $7 \times 10^{10} \text{ cm}^{-3}$, the microwave sustained plasma should have a much lower electron density than the LIBS plasma. Therefore experiments were conducted to determine if the electron density of the MA-LIBS plasma remains as high as normal LIBS plasma (expect to be 10^{16} to 10^{17} cm^{-3}) even after a long delay (hundreds of microseconds or even milliseconds).

To measure the electron density, Thomson scattering experiments on both air and aluminum plasma were conducted with the microwave system turned on. Since the interest is the later time electron density, the delay time was 3.5 μs or larger. Electron density was estimated using the method for treating non-collective Thomson scattering.

⁸² [1] S.Y. Moon, W. Choe, H.S. Uhm, Y.S. Hwang, J.J. Choi, Characteristics of an atmospheric microwave-induced plasma generated in ambient air by an argon discharge excited in an open-ended dielectric discharge tube, Physics of Plasmas, 9 (2002) 4045-4051.

⁸³ K.M. Green, M.C. Borras, P.P. Woskov, G.J. Flores, III, K. Hadidi, P. Thomas, Electronic excitation temperature profiles in an air microwave plasma torch, Plasma Science, IEEE Transactions on, 29 (2001) 399-406.

⁸⁴ K. Ogura, H. Yamada, Y. Sato, Y. Okamoto, Excitation Temperature in High-Power Nitrogen Microwave-Induced Plasma at Atmospheric Pressure, Appl. Spectrosc., 51 (1997) 1496-1499.

For the air plasma, estimated electron density was shown in Figure 62. For both cases with and without the microwave, after about 4 μ s the electron density was in the similar range (10^{15} cm^{-3}) but slightly higher when the microwave was on. A linear fit shows that when there is microwave, the delay of electron density was a little slower than without the microwave. This result indicates the microwave may slow down the electron-ion recombination process. For larger delays, Thomson scattering signal became undetectable.

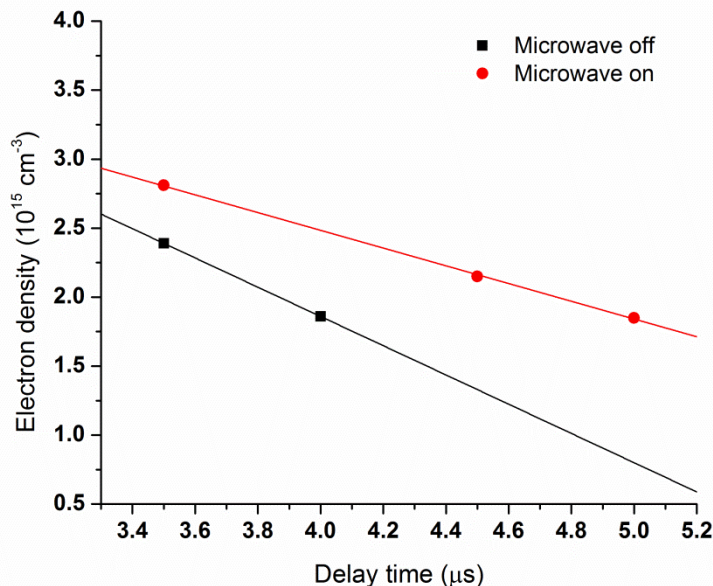


Figure 62. Electron density estimate of MA-LIBS plasma using non-collective Thomson scattering method, and a comparison with normal LIBS plasma.

For the aluminum sample, no non-collective Thomson scattering signal can be measured after 3 μ s. This is because the surface reflection significantly increased the Rayleigh scattering signal, and distorted the weak Thomson scattering spectrum in region close to 532 nm. To perform non-collective Thomson scattering measurements for solid samples, much better filtering techniques have to be applied.

These results infer the late time Ne should be much lower than the typical LIBS plasma density that is often considered to be above 10^{16} cm^{-3} . Our measurements stopped in the transition regime when the electron density was below 10^{16} cm^{-3} . According to the results on microwave sustained gas plasmas⁸²⁻⁸⁵, the electron density could range from 10^{12} to 10^{15} cm^{-3} . Since the lowest electron density measured by our Thomson scattering setup was higher than 10^{15} cm^{-3} , these reported data could explain the difficulty of density measurement in the microwave plasma regime. However, in the microwave plasma regime, the electron density of the MA-LIBS plasma is very likely kept at a level close to the typical densities of microwave plasmas. Therefore the microwave prevents the fast electron-ion recombination so that

⁸⁵ [4] S. Jovićević, M. Ivković, Z. Pavlović, N. Konjević, Parametric study of an atmospheric pressure microwave-induced plasma of the mini MIP torch — I. Two-dimensional spatially resolved electron-number density measurements, *Spectrochimica Acta Part B: Atomic Spectroscopy*, 55 (2000) 1879-1893.

collisional excitation and emission process can still keep going even milliseconds after the plasma was created.

4.4 Performance of MA-LIBS

The performances of MA-LIBS were studied and compared with conventional LIBS in several different experiments. The goals were to find the optimized conditions to obtain maximum enhancement and also characterize the performances in real-world applications. Analytical benefits such as signal enhancement, improvement of sensitivity, and selective enhancement of lines will be shown in the following sections. Some features like enhanced molecular emission, air operation, and enhancement dependence on laser irradiance will also be discussed.

4.4.1 Signal enhancement

Besides the 17-fold enhancement of the 405.8 nm line showed in Figure 4.3, signal enhancement was observed in several studies on different samples. In this section, two examples (studies on alumina ceramics and NIST soil standard reference material (SRM)) will be given to show the enhancement effect in MA-LIBS.

In an experiment on alumina ceramics, signal enhancement from Na, Ca, Al, Mg, Ba, and K was detected. In this experiment 0.42 GW/cm^2 irradiance from a Nd:YAG laser was used to initiate the laser plasma. The acquisition by the ICCD camera was delayed by $1 \mu\text{s}$ after the ablation by the laser and last $30 \mu\text{s}$ when the microwave cavity was not activated, and as long as the microwave pulse duration when it was activated. Each spectrum was obtained by averaging ten single shot spectra on a fresh surface.

The spectra of these elements from both LIBS and MA-LIBS were shown in Figure 63. Although enhancement was observed, the enhancement factor was different from one element to another. A comparison of the enhancement factor was listed in Table 10. Some elements may have multiple emission lines such as Mg. However the enhancement for different lines was also different. Such selective enhancement of lines will be discussed later.

Table 10. Emission line enhancement summary

Element	Wavelength (nm)	Enhancement (times)
Na I	589.6	33
Ca I	422.7	22
Mg I	285.2	16
Al I	396.2	11
Ba II	455.5	5
K I	766.5	5

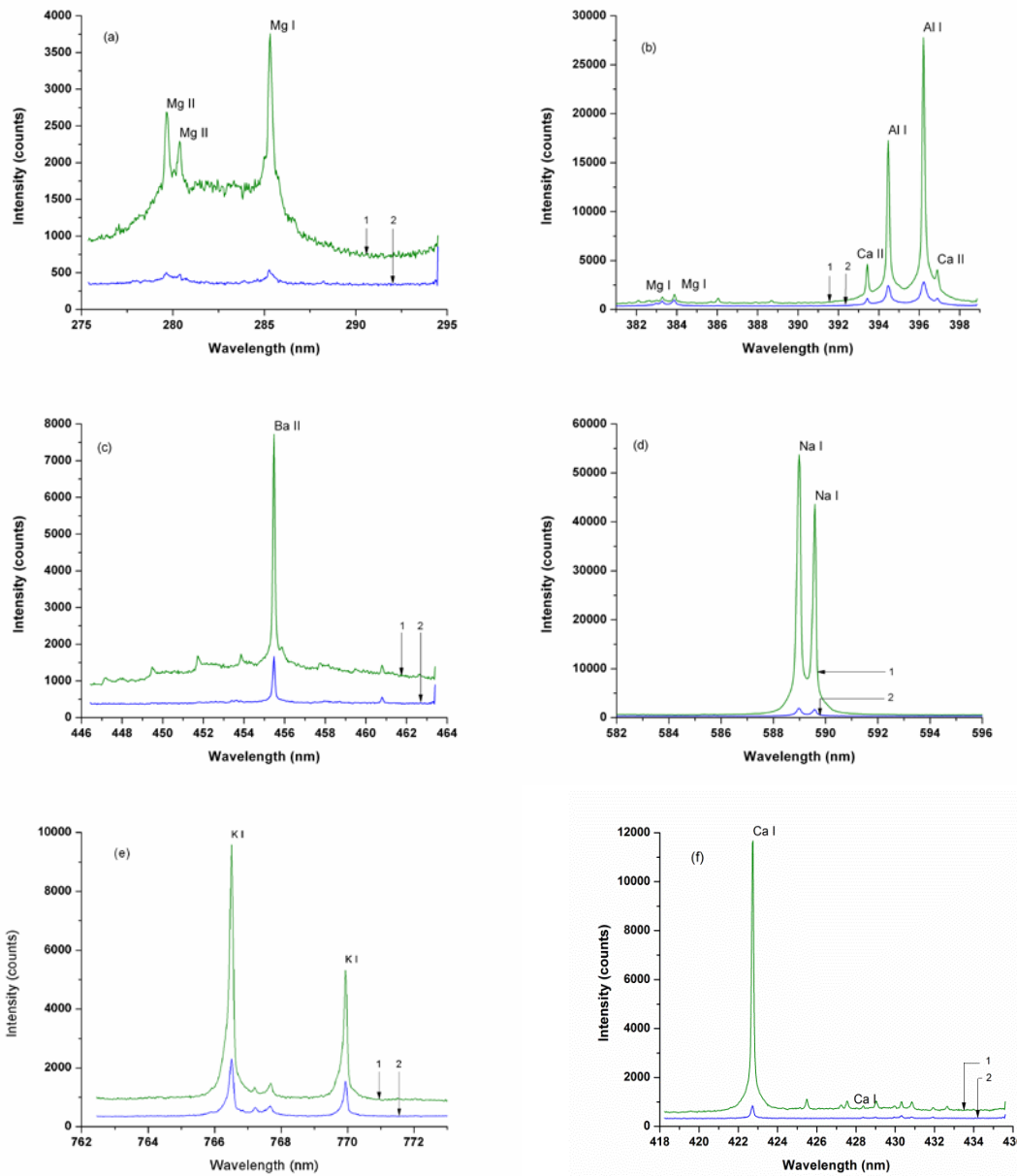


Figure 63. Spectra for (a) Mg; (b) Al; (c) Ba; (d) Na; (e) K and (f) Ca. (1: MA-LIBS, 2: LIBS)

In another experiment on soil pellet samples (NIST SRM 2711a Montana II soil with polyvinyl alcohol as binder material⁸⁶), eight elements (Al, Ca, Ti, Mn, K, Pb, Fe, and Sr) were detected from the NIST soil sample in the spectral range between 395 nm and 413 nm. In Figure 64, the bottom curve indicates the spectrum taken with traditional LIBS method with 15 mJ laser energy (15 GW/cm^2 irradiance), 1 μs delay and 20 μs gate width, and the top curve is the MA-LIBS spectrum with the same experimental parameters but 20 ms gate width.

⁸⁶ B. Lal, H. Zheng, F. Yueh, J. Singh, Parametric study of pellets for elemental analysis with laser-induced breakdown spectroscopy, *Applied Optics*, 43 (2004) 2792-2797.

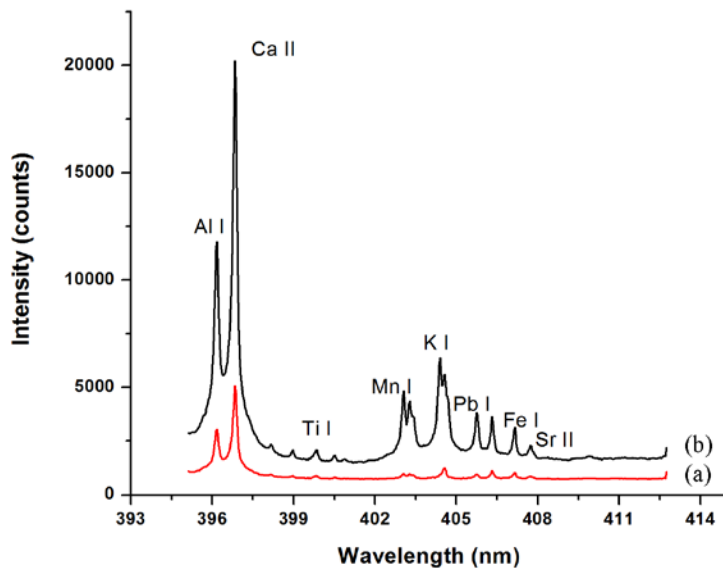


Figure 64. Spectra of Montana soil NIST standard reference material using (a) traditional LIBS and (b) MA-LIBS.

The emission enhancement was clearly shown in Figure 64. According to the NIST sample concentration in mass fraction indicated in Table 11, the enhancement was effective for both major elements such as Al, Fe, and Ca, and trace species like Mn and Sr.

Table 11. Certified Values for Selected Elements in SRM 2711a⁸⁷

Element	Al	Fe	K	Ca	Ti	Pb	Mn	Sr
Mass fraction	6.72%	2.82%	2.53%	2.42%	0.317%	0.140%	675 ppm	242 ppm
Standard deviation	0.06%	0.04%	0.10%	0.06%	0.01%	0.00%	18 ppm	10 ppm

From these examples, one can notice the microwave enhancement is effective for multiple elements and no matter at what concentration of the element is. However, the enhancement effect can be different from one line to another. The reason of this selective enhancement of lines should be understood, and discussion on this topic will be given later. Besides that, in the analytical point of view people would like to know the benefits due to the signal enhancement. Since decent signal enhancement was observed from soil samples, we performed a study on real world soil samples with focus on copper. Through this experiment, we

⁸⁷ NIST, Certificate of Analysis: Standard Reference Material 2711, Montana Soil (Moderately Elevated Trace Element Concentrations), in, Gaithersburg, MD, 2003.

observed clear improvement of sensitivity using MA-LIBS compared with traditional LIBS method.

4.4.2 Improvement of sensitivity: example of copper in soil

The monitoring of concentrations of metallic elements in soil is of great importance to environmental research, agriculture, and public health. An element of interest is copper. The copper concentration in soil determines if it should be considered as a nutrient for plants or a toxic metallic pollutant. As a nutrient, copper is absorbed by plants and involved in photosynthesis and respiration. However, high concentration of copper can lead to growth reduction and other issues. For human beings, both copper deficiency and excess can cause health problems. For ecological preservation, 61 mg kg^{-1} is set as the soil screening level (SSL) for copper by the Environmental Protection Agency (EPA), which is the level that triggers further ecological risk assessment.

To measure the concentration of metals in soil, calibration curves are usually used. The slope of this curve defines the sensitivity of the analytical method according to the IUPAC definition. Assuming similar precision, higher sensitivity would allow for better discrimination between two close values of concentration and helps regulators to achieve conclusive and accurate decision-making. This study presents the improvement of the sensitivity of LIBS for the determination of copper in soil samples using MA-LIBS as well as the detection of silver and copper at concentrations not detected with our conventional LIBS system.

The experimental setup of LIBS and MA-LIBS was similar to the previous experiments. The nanosecond laser (Brilliant, Quantel), the microwave system (Envimetrics), the spectrometer (2300i, Princeton Instruments – Acton) and the ICCD camera (PIMAX, Princeton Instruments) were used as the basic components of the LIBS and MA-LIBS setups. Laser pulses with 10 mJ energy were focused inside the sample, forming a 160- μm -diameter spot on the sample surface. This spot size was optimized for the maximum LIBS signal and minimum signal fluctuation. For MA-LIBS, the same ablation condition was used. The plasma emission was collected from the side by a UV-transmissive fiber at about 70 degree from the laser direction without additional focusing lenses. The position of the fiber was optimized to obtain the maximum LIBS signal. The gate delay was set at 500 ns to eliminate the initial continuum emission, and a 20 ms or 10 μs gate width was applied respectively when the microwave generator was either activated or not. Each spectrum was obtained by adding ten accumulations at the same spot, and 5 spectra from different locations were averaged to obtain the final spectra.

The four soil samples were a subset of the samples used in a previous study⁸⁸. The copper concentrations, measured by ICP-OES, were evaluated at 1232, 738, 544, and 30 mg kg^{-1} in order to measure the sensitivity over a wide range. In the following discussions the samples are labeled as S1 - S4 with S1 having the highest concentration and S4 the lowest. These samples were natural soil samples from different locations rather than matrix-matched soils made in the laboratory, considering a linear calibration curve may have been difficult to obtain due to matrix effects in the latter case^{88,89}. In order to reduce these effects, the above samples were chosen to contain relatively similar concentrations of major elements like Fe, Si, and Al (Table 12). The soils samples were prepared in the pellet form.

⁸⁸ A. Ismaël, B. Bousquet, K. Michel-Le Pierrès, G. Travailé, L. Canioni, S. Roy, In Situ Semi-Quantitative Analysis of Polluted Soils by Laser-Induced Breakdown Spectroscopy (LIBS), *Appl. Spectrosc.*, 65 (2011) 467-473.

⁸⁹ B. Bousquet, J. Sirven, L. Canioni, Towards quantitative laser-induced breakdown spectroscopy analysis of soil samples, *Spectrochimica Acta Part B: Atomic Spectroscopy*, 62 (2007) 1582-1589.

Table 12. Concentration of Cu and major elements in soil samples referred to as S1-S4.

	Cu (mg kg ⁻¹)	Al ₂ O ₃ (%)	Fe ₂ O ₃ (%)	SiO ₂ (%)
S1	1232	16.3	11	55.5
S2	738	12.4	6.8	60.3
S3	544	16.5	10.7	52.3
S4	30	11.2	6.5	68.9

For the detection of copper as a trace element in the soil matrices, the 324.75 nm line from the $4s^2S_{1/2} - 4p^2P_{1/2}^0$ doublet was used. The spectra of S1 from both MA-LIBS and LIBS measurements are shown in Figure 4.10 respectively on the left and the right. The intensity of the line was measured, after background subtraction, by fitting the peak by a Lorentzian profile and integrating its area. In the LIBS spectrum, the Cu line was on a broad background structure in the spectrum. Due to the high level of noise, precise identification of each individual peak was not achieved. The Cu peaks in the MA-LIBS spectrum are much more defined than those in the LIBS spectrum due to the signal and signal-to-noise enhancement. In Figure 65, the integrated line intensity of the 324.75 nm Cu line from the MA-LIBS spectrum was 14 times higher than that of the LIBS spectrum, with a 10-fold improvement of the signal to noise ratio (SNR). Additionally, a few lines from other elements were observed, thanks to the improved SNR. Among them, the line at 328.07 nm was identified as the resonant Ag I emission line from the $5s^2S_{1/2} - 5p^2P_{3/2}$ transition. It should be emphasized that the concentration of silver was reported to be 23.3 mg kg⁻¹ in S1 according to the ICP-OES measurement and was not detected with our LIBS measurement. Consequently, MA-LIBS offered in this case better performances than LIBS for the detection of these specific trace elements. It has to be noted that each LIBS experiment has its own performance depending on the experimental conditions and consequently these values comparing MA-LIBS to LIBS are not to be considered absolute ones.

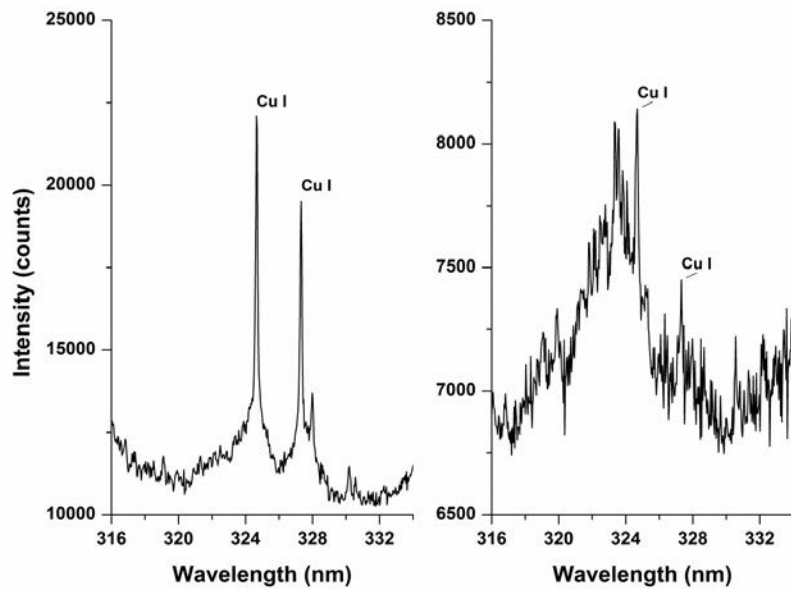


Figure 65. Spectra of the soil sample S1 containing 1232 mg kg⁻¹ of Cu with MA-LIBS (left) and LIBS (right).

The calibration curves for copper are plotted in Figure 66 for both LIBS (circles) and MA-LIBS (squares). The data for each concentration consisted of five single spectra acquired at five different locations on the pellet. The mean values of the intensities were linearly correlated with the concentration of copper. The fitting results are listed in Table 13. In the case of our LIBS experiment, the sensitivity was 0.048 counts/ mg kg⁻¹, while in MA-LIBS, it increased to 1.12 counts/ mg kg⁻¹, which represents a 23-fold increase. The improvement of the sensitivity is by definition beneficial for an analytical method since it is one of the most important factors for discriminating between two close values of concentration. MA-LIBS can thus potentially offer advantages over LIBS in deciding if a soil sample has a concentration of a given pollutant below or above a fixed threshold.

Table 13. Summary of the fitting results for two sets of experiments.

	Experiment 1		Experiment 2	
	Slope	R ²	Slope	R ²
LIBS	0.04823	0.99232	0.05997	0.99872
MA-LIBS	1.1248	0.99296	1.2206	0.99804

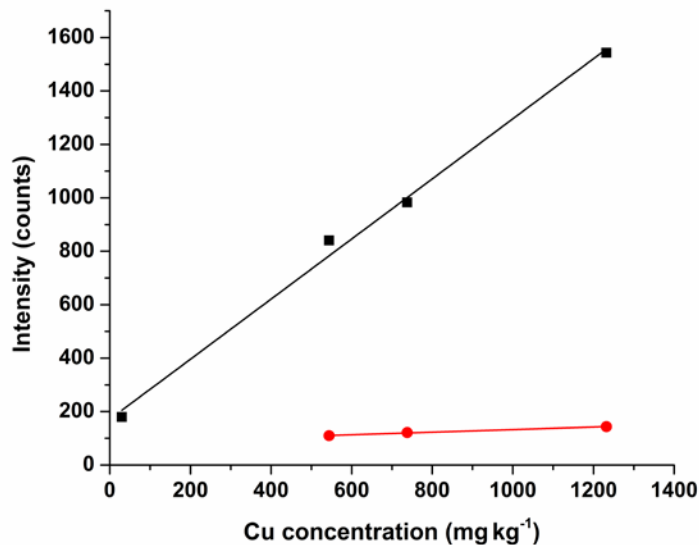


Figure 66. Calibration curves of Cu for MA-LIBS (black squares) and the traditional LIBS (red circles).

Due to intrinsic large sample inhomogeneity of the soil samples, signal fluctuations (in the range of several tens of percent) were observed from one spot to another, for both LIBS and MA-LIBS data. Such signal fluctuation is not specific to LIBS or MA-LIBS but is common for any micro-analysis method on inhomogeneous samples. Indeed, even if the soil samples were prepared and homogenized as much as possible, they are still heterogeneous at the scale of the laser beam size and the observed variations are really related to local composition of the samples. Without going deeper in this discussion of sampling, one can understand that in this case of heterogeneous sample, the variance from point to point has no statistical meaning and that only the average value is representative of the macroscopic sample. That's why error bars are not displayed in Figure 66. Nevertheless, a second set of measurements was performed in this study to confirm the reproducibility of the previous result. Similar fluctuations due to the sample heterogeneity were observed, but again, the mean values of the intensity obtained for each concentration were linearly correlated with the concentrations (Table 13). The experimental points (average values) obtained during this second experiment were overlapped with the previous ones and consequently not displayed on Figure 66 for clarity. Sensitivity improved by 20x for the second set of data, comparable to the 23x obtained with the first set. This confirms that, despite of the high heterogeneity of the soil samples, not discussed here, the results about the sensitivity enhancement by MA-LIBS were found to be reproducible, based on the analysis of the mean values.

In addition to the enhancement of the sensitivity, MA-LIBS extended the range of analysis for copper, for the experimental conditions reported here. The calibration curve built with our LIBS system covered the range from 544 to 1232 mg kg^{-1} , while MA-LIBS extended this range down to 30 mg kg^{-1} . For the same series of soil samples, the lowest detected copper concentration reported in the ICP-OES study⁸⁸ was 80 mg kg^{-1} using another typical LIBS setup.

Moreover, under our experimental conditions, silver has been detected only by MA-LIBS, which makes this technique very promising for the detection of trace elements in soil.

To sum up, calibration curves of copper in soil samples were built by both LIBS and Microwave-Assisted Laser-Induced Breakdown Spectroscopy (MA-LIBS). The MA-LIBS signal for copper at 324.75 nm in soil samples was found to be linearly correlated to the concentration. A comparison with our LIBS data was conducted and an enhancement of sensitivity of more than 20 times was observed with MA-LIBS. This improvement of sensitivity could have a significant positive impact on the monitoring of soil samples. Indeed, the ability of sorting soil samples based on their concentration of a pollutant with respect to a given threshold value could be highly enhanced. As a consequence, quick decision could potentially be taken with a higher level of confidence by MA-LIBS than LIBS. However, this promising result will hold only if the signal fluctuations with MA-LIBS are in the same order of magnitude as the one observed with LIBS. Future work should consequently be focused on the study of the precision in both LIBS and MA-LIBS.

In addition, for soil samples, concentrations as low as 30 mg kg^{-1} of Cu and 23.3 mg kg^{-1} of Ag were detected by MA-LIBS while not by LIBS, under the experimental condition reported here. Consequently, MA-LIBS can potentially give access to spectral lines not detected by LIBS, which can be one of the major ways for detecting trace elements. Future work should address this important topic of improving the detection of trace elements with MA-LIBS.

4.4.3 Selective enhancement of lines

Besides the improvement of sensitivity and the capability to detect low concentration elements, MA-LIBS shows another interesting feature in Figure 65. Without the microwave the SNR of the spectrum was very poor due to the bumpy background signal. However, with the help of the microwave the SNR was improved due to the fact that the Cu and Ag peaks experienced much stronger signal enhancement than the background signal. Because of the limited spectral resolution the background signals were not identified, but clearly one can see from Figure 65 that some properties of three lines (324.8 nm, 327.4 nm from Cu and 328.1 nm from Ag) made the microwave preferably enhance their signal.

The transition properties are the key to understand the selective enhancement of lines. Table 14 listed the major transition parameters of the three lines mentioned above. All the three lines are resonance lines which involve the ground state. The upper levels are low energy levels so that electrons can be excited to these levels easily. Even more, the transition strength, which characterizes the probability of the transition, is also large for the three lines.

Table 14. Transition parameters of two Cu lines and one Ag line.

	Wavelength (nm)	E_i (eV)	E_k (eV)	Transition strength (s^{-1})
Cu I	324.8	0	3.82	5.56E+08
Cu I	327.4	0	3.79	2.74E+08
Ag I	328.1	0	3.78	5.60E+08

In Figure 58, the three lines from Pb (405.8 nm, 368.4 nm, 364.0 nm) which demonstrated highest enhancement showed almost the same properties. Transition parameters are listed in Table 15. The three transitions start at the lowest excited state of Pb. The lower levels are meta-stable levels which can hold a large population like the ground state. The transition strength for the three lines is large. Among them, the 405.78 nm line that experienced

the largest signal enhancement also has the highest transition strength. Just like the Cu and Ag lines, these transition parameters guarantee such transitions to happen easily.

Table 15. Transition parameters of three Pb lines.

	Wavelength (nm)	E_i (eV)	E_k (eV)	Transition strength (s^{-1})
Pb I	364.0	0.97	4.38	1.0E+08
Pb I	368.4	0.97	4.33	1.5E+08
Pb I	405.8	1.32	4.38	2.7E+08

For transitions that start from different energy levels, enhancement is more favorable to those initially at a lower energy level. Take Ca as an example. Figure 67 shows the spectra of an alumina sample with Ca in it. The seven atomic calcium lines in the spectra can be divided into two groups: the $3p^64s^2$ - $3p^64s4p$ transition ($E_{up} = 2.9$ eV) at 422.7 nm and the $3p^64s4p$ - $3p^64p^2$ multiplet ($E_{up} = 4.8$ eV). The 422.7 nm line experienced about 22 times enhancement, much stronger enhancement than the neighboring 428.9 nm calcium line (about 5 times).

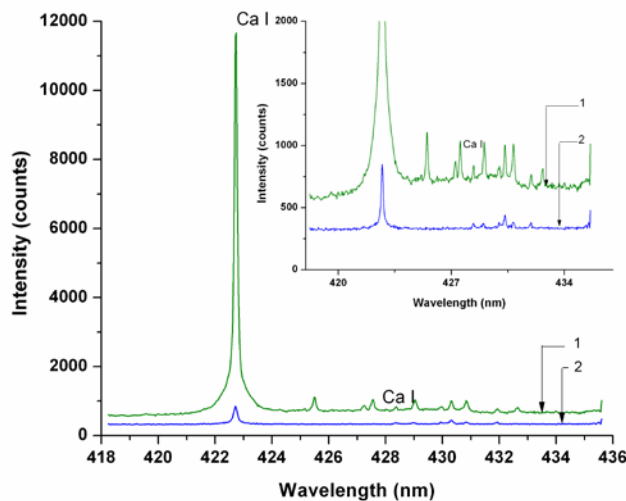


Figure 67. Enhancement difference between different Ca lines.

Similarly most of the lines showing strong enhancement were transitions with large transition strength and low excitation energy levels, especially resonant lines involving the ground states. Figure 63 showed the spectra of Al, Mg, Ba, Na, K, and Ca lines with clear intensity enhancement. Across the spectrum, most of the lines were atomic transitions. Only ionic lines from Mg, Ca, and Ba (elements of the group II) can be observed due to the combination of low ionization potential (respectively 7.6 eV, 6.1 eV and 5.2 eV) and low ionic excitation energy (respectively 4.4 eV, 3.1 eV and 2.5 eV) as opposed to Na and K (elements of the group I) that have low ionization potential but have high ionic excitation energy (above 30 eV). All these results lead to a conclusion that microwave enhancement favors transitions with low upper level energy and high transition strength.

The enhancement preference can be understood if people are aware that the critical electron density of the 2.45 GHz microwave is only $7 \times 10^{10} \text{ cm}^{-3}$. Due to the low critical electron density, the microwave and the plasma coupling is not efficient until the electron density of the

plasma decreased to a relatively low level. This explains why enhancement was often observed for atomic species. Only the easily ionized species are in their ionic states. At the meanwhile, the plasma temperature also decreases. For the Ca lines mentioned above, higher temperature (reached at early times in the plasma) is needed to support the 428.9 nm transition, but in a low temperature plasma it is much more difficult to excite electrons to the high energy level for example 4.8 eV for the 428.9 nm line comparing with a much lower level at 2.9 eV for the 422.7 nm line. As a result, the lifetime of the 428.9 nm radiation is shorter than the one at 422.7 nm, which leads to weaker enhancement.

This selectively enhancement can be beneficial for analytical chemistry applications because the MA-LIBS spectra can be much simpler than LIBS spectra and therefore easier for spectral analysis. A typical example is shown in Figure 65 for copper analysis in soil samples. Only the resonance lines were observed to have significant enhancement in this application. As a result, better SNR was obtained. For general MA-LIBS applications, to reach the best condition for microwave enhancement, transitions have to satisfy the two conditions, namely low upper level energy and large transition strength. For each element, there are only a few lines can meet such requirements. Therefore this advantage can reduce the number of lines that people have to consider during the identification process, and lead to more accurate line identification based on the central wavelength of the peaks.

4.4.4 Enhancement of molecular emission

Besides signal enhancement of line emissions, stronger molecular emission from MA-LIBS plasma was detected. In the analysis of alumina ceramic samples, strong emission from AlO, NO, and OH diatomic radicals was observed (Figure 68). In soil analysis, emission from CaO and CaOH was very intense as shown in Figure 69.

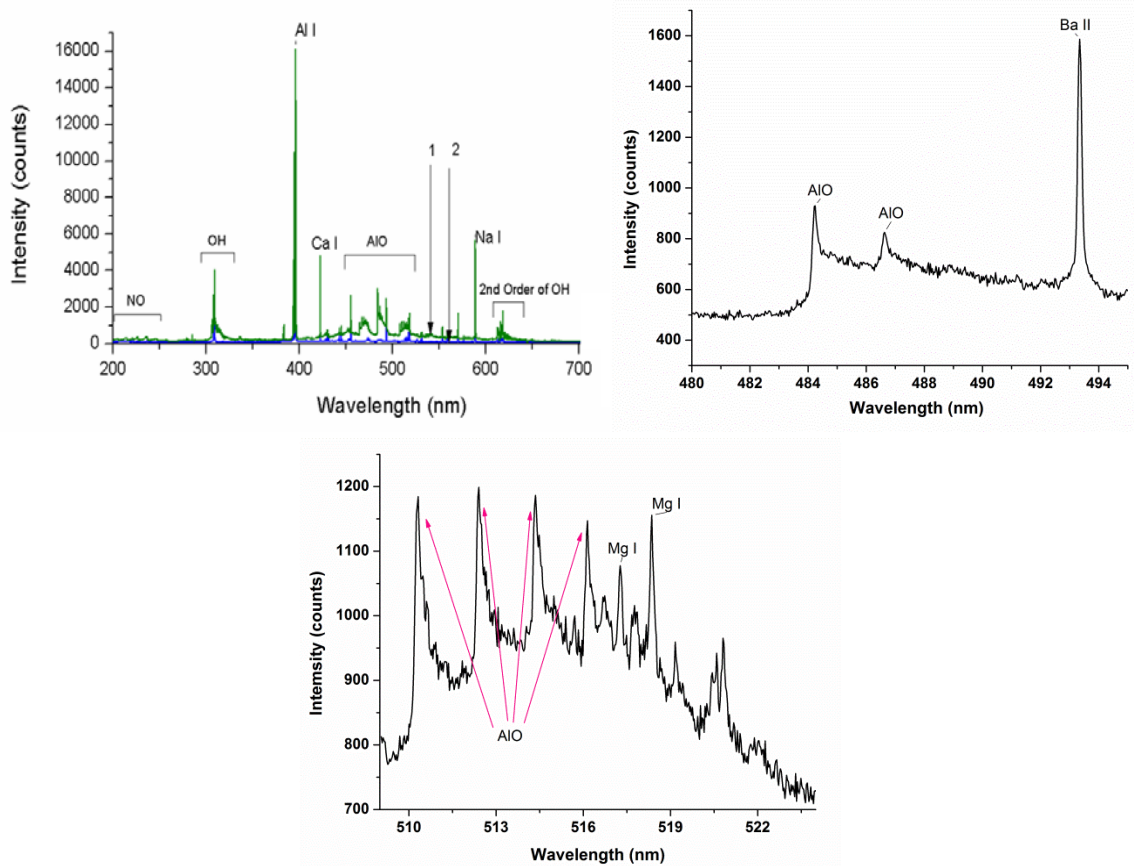


Figure 68. MA-LIBS spectra from (a) alumina samples with emphasis on (b) and (c) AlO radical bands

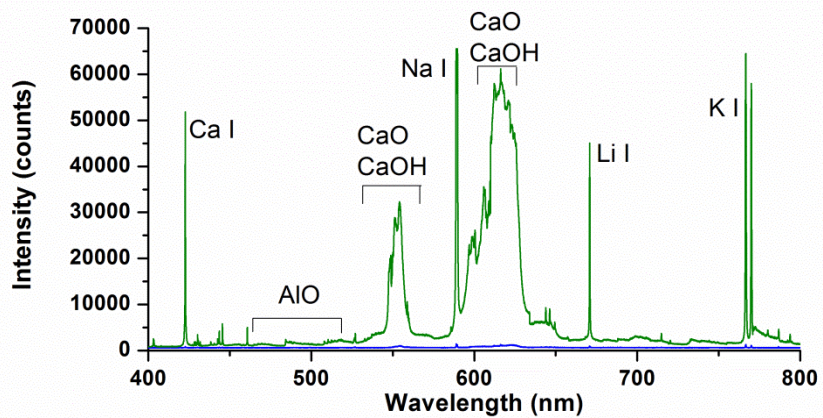


Figure 69. Molecular emission from soil samples.

The emitters of these molecular bands may come from the native matrix due to incomplete atomization. However more likely they are formed during the microwave plasma regime due to the interaction of the plasma with oxygen in the air. Thanks to the long lifetime and low temperature of the microwave sustained plasma, atoms from the sample material and excited oxygen from the air can have much higher possibility to associate together than in

normal LIBS plasma in which many radicals are broken down into atoms by collisions with high energy particles. In another experiment where GaAs wafer was analysed, GaO emission can be observed (Figure 70), even though there was no oxygen in the sample. This can be a proof of the formation hypothesis at low temperature condition.

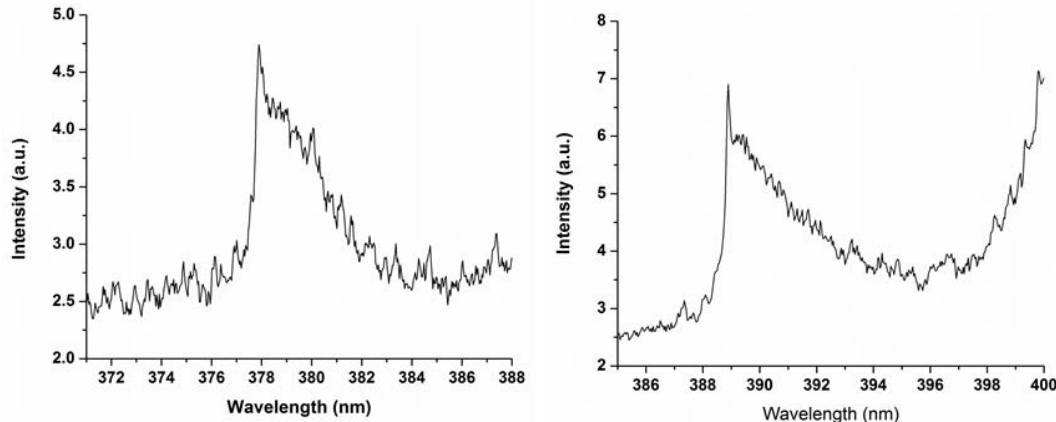


Figure 70. *GaO emission in MA-LIBS spectra from GaAs samples.*

The molecular emission can potentially bring both troubles and benefits. As one can see from Figure 68 (a) and Figure 69, the molecular bands are much broader than atomic and ionic lines, and as a result a wide spectral region can be covered by the molecular bands. The molecular emission causes spectral interference if elements of interests generate emission lines overlapping with the band emission. However, people may be able to take advantage of the molecular emission for isotope detection. Recent studies on laser ablation molecular isotopic spectrometry (LAMIS) showed that isotope detection with LIBS is possible thanks to the larger isotopic shift from molecular emission compared with line mission⁹⁰. Normal LIBS plasma usually has a much shorter lifetime and much weaker molecular emission than MA-LIBS plasma. The enhanced molecular emission in MA-LIBS can be very useful for techniques that utilize molecular emission like LAMIS.

4.4.5 Enhancement dependence on laser irradiance

We defined the enhancement as the ratio between the MA-LIBS intensity and LIBS intensity after baseline removal. In several experiments, the enhancement was found to be related to the laser irradiance. The enhancement dependence on laser irradiance was systematically studied with the alumina sample.

The irradiance was controlled in two ways: either by changing the laser energy at the sample surface at a fixed working distance or by changing the diameter of the laser spot size by defocusing the laser beam. Among all the lines from the alumina sample, the Ca I line at 422.7 nm was chosen for this study, because calcium could be a representative of minor constituent of the sample (0.18% wt), and this particular line didn't interfere with other transition lines in the spectrum and it was subject to significant enhancement by the microwave radiation.

Figure 71 shows the intensity of the Ca I line at 422.7 nm as a function of the laser irradiance with the sample surface at focus without microwave radiation. Two regions can be

⁹⁰ R.E. Russo, A.A. Bol'shakov, X. Mao, C.P. McKay, D.L. Perry, O. Sorkhabi, Laser Ablation Molecular Isotopic Spectrometry, *Spectrochimica Acta Part B: Atomic Spectroscopy*, 66 (2011) 99-104.

outlined: below and above 50 GW.cm^{-2} . The first region shows an efficient ablation (increase of the signal with the laser irradiance). The second region shows a screening effect, where the tail of the laser pulse is reflected by the high electron density plasma at early times (first nanoseconds) created by the high irradiance ablation⁹¹. The uncontrolled interaction between the tail of the laser pulse and the expanding plasma increases the fluctuations from shot to shot, depicted by the large standard deviations on the figure. Laser energies of 1.5, 6, 14, 25, and 47 mJ were used as test values to characterize the effect of the laser pulse irradiance across the behavior shown in Figure 71.

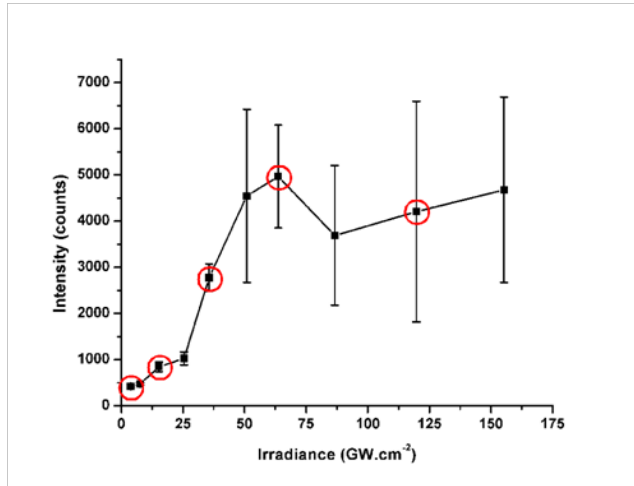


Figure 71. *Ca I* line at 422.7 nm intensity vs laser irradiance.

Figure 72 shows the enhancement factor as a function of the area of the ablation spot (negative spot size means that the laser is focused inside the sample) for different laser peak powers. The enhancement was defined as the ratio between the MA-LIBS intensity and LIBS intensity after baseline removal. To vary the area of the ablation spot, the laser beam was focused down to 2.2 cm, 1.4 cm, 1cm, 0.1 cm inside the sample and 0.7 cm above the sample surface. After defocusing, the plasma emission was either undetectably weak or very unstable if the laser energy was 1.5 mJ or 6 mJ. This corresponded to an irradiance smaller than 250 MW.cm^{-2} , which is approximately the plasma threshold for alumina⁹². Low energy and large defocusing, leading to low irradiance ablation, benefited MA-LIBS enhancement, as it can be seen clearly from the enhancement graph shown in Figure 72. These characteristics result from three aspects. First, the higher irradiance increases the LIBS emission, and the MA-LIBS emission mainly in the LIBS regime. However during the microwave plasma regime, the effect of the initial laser irradiance becomes weak. Although the amount of ablated mass is slightly higher with higher laser irradiance, the microwave power and duration is not changed. As seen from Figure 59, the enhancement is mainly due to the emission from the microwave plasma regime. Since this part of emission does not change much when laser irradiance is increased, while the LIBS emission without microwave increases significantly, the enhancement factor becomes lower. Second, high irradiance laser ablation generates plasma with high electron density. Thus, when the plasma

⁹¹ J.A. Aguilera, C. Aragón, F. Peñalba, Plasma shielding effect in laser ablation of metallic samples and its influence on LIBS analysis, *Applied Surface Science*, 127–129 (1998) 309-314.

⁹² D.K. Killinger, S.D. Allen, R.D. Waterbury, C. Stefano, E.L. Dottery, Enhancement of Nd:YAG LIBS emission of a remote target using a simultaneous CO₂ laser pulse, *Opt. Express*, 15 (2007) 12905-12915.

expands into the microwave cavity, the impedance of the cavity is modified. Impedance mismatch leads to more microwave reflection, and hence lower the energy coupled to the plasma. Third, a corollary to the second explanation is that low irradiance ablation produces low electronic density plasma that reaches the critical electronic density for coupling faster than that created at high irradiance. Therefore the enhancement went up when laser energy dropped.

From Figure 72 we can see that for the alumina sample the enhancement was very weak at the focus whatever the laser irradiance. This is because defocusing helps to create large and uniform laser plasma with relatively low electron density, which can couple more efficiently with the microwave radiation. However, focusing the laser beam in front of the sample surface is likely to cause air plasma, and hence degrade the quality of the spectrum. As a consequence, besides tuning the laser energy, adjusting the defocusing condition is important in order to achieve good enhancement factors. This feature indicates the possibility to use compact low peak power lasers in MA-LIBS systems without losing plasma emission.

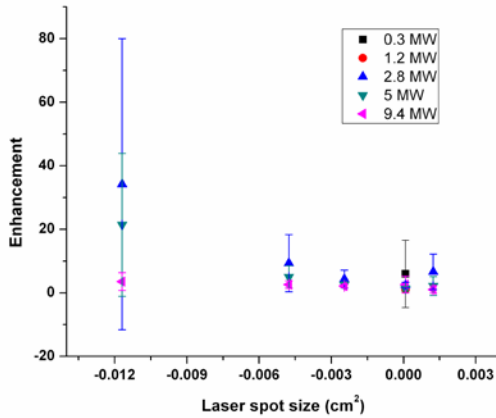


Figure 72. Enhancement dependence on laser power and laser spot size in air.

4.4.6 Influence of atmosphere condition

All experiments discussed above are done in air, so what happens if the air is replaced with other gas background, such as Ar which is often used in LIBS experiments to remove air influence and enhance plasma emission? As mentioned in earlier, the presence of air and its interaction with the plasma led to molecular formation (AlO, NO, OH). Molecular band emission produced background signal that overlapped with the atomic emission and introduces its own fluctuation to the noise in the emission spectrum.

To study the effect of the atmosphere, an enclosure was made around the microwave cavity and argon gas was constantly purged into the microwave cavity so that a localized argon environment can be created. Similar to Figure 72, an “enhancement vs irradiance” map was obtained and illustrated in Figure 73. In an argon environment, the microwave enhancement effect behaved differently from in the air. Weak enhancement can be observed at focus, but no enhancement with optimized experimental parameter found in the air for the alumina sample (laser power below 5 MW, large ablation spot area – 0.012 cm^2 – and long microwave pulse – 20 ms). With all the parameters tested, the enhancement is negligible (up to 4) compared with the results in the air. Figure 74a shows the spectrum for the calcium emission in the argon with and without microwave and a laser irradiance of 330 MW.cm^{-2} . No effect of the microwave radiation

could be detected. Figure 74b shows the same spectral region but with laser irradiation of 15 GW.cm^{-2} at focus. Enhancement of the signal was detected but emission from Ar lines was predominant causing serious spectral interferences. On the other side, the enhancement of the calcium line was weak (3-fold), as expected based on the study above.

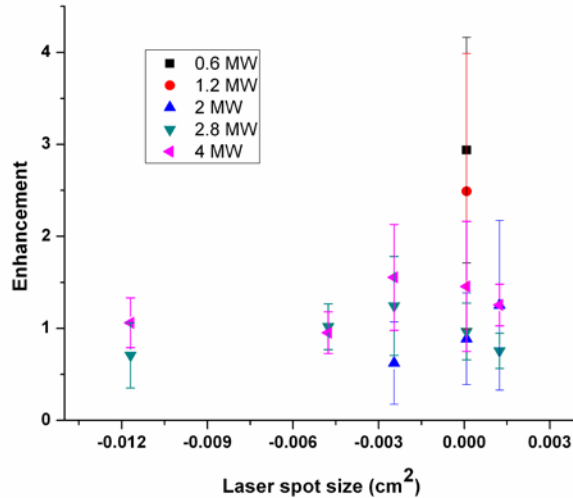


Figure 73. Microwave enhancement vs laser power and spot size in Ar.

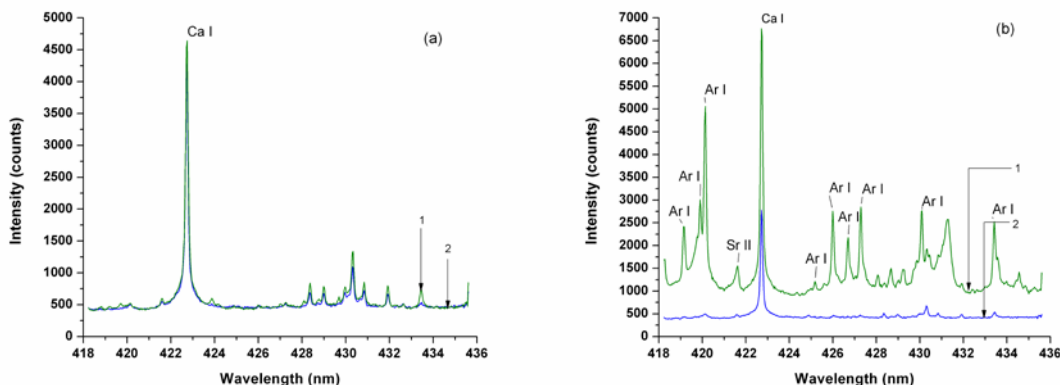


Figure 74. Alumina spectra in Ar environment: a) 330 MW.cm^{-2} on a 0.012 cm^2 spot, b) 15 GW.cm^{-2} at focus. (1: microwave ON, 2: microwave OFF)

The disappearance of the enhancement effect can be explained in several aspects. In the LIBS regime, the microwave power is reduced because of ineffective coupling between the microwave and the plasma. Previous works show that laser-induced plasmas produced in the argon at atmospheric pressure lead to higher electron density than in the air^{93,94}. This causes the

⁹³ L. St-Onge, E. Kwong, M. Sabsabi, E.B. Vadas, Quantitative analysis of pharmaceutical products by laser-induced breakdown spectroscopy, *Spectrochimica Acta Part B: Atomic Spectroscopy*, 57 (2002) 1131-1140.

⁹⁴ J.A. Aguilera, C. Aragón, A comparison of the temperatures and electron densities of laser-produced plasmas obtained in air, argon, and helium at atmospheric pressure, *Appl Phys A*, 69 (1999) S475-S478.

detuning of the microwave cavity and higher reflection, similar to the high irradiance case in the air.

The background gas plays an important role in the microwave enhancement, as can be seen in the strong molecular emission due to the oxide formation. Very likely oxygen in the air is a very important electron provider in the microwave plasma due to its lower ionization potential (13.62 eV) compared with nitrogen (14.53 eV) and argon (15.76 eV). In the microwave plasma regime, the microwave can produce the amount of power just enough to slightly ionize the oxygen in air with the help from initial free electrons from LIBS plasma. Once air is replaced with argon, which has a higher ionization potential, the microwave power is not enough to free electrons in the argon environment. Because of the fast decrease of the electron density, the collisional excitation and emission stops quickly and as a result no enhanced plasma emission can be observed.

For the high laser irradiance case, the high electron density lowers the breakdown threshold of the argon gas by multiple electron-atom collisions. With the help of large amount of electrons, the microwave is able to temporarily breakdown argon and increases the collisions between electrons and argon atoms, which give strong emission enhancement of the Ar lines. However, due to the high electron density, the microwave is not able to couple with the plasma efficiently. Although the microwave was able to enhance the emission of the argon lines, it is not able to sustain the argon plasma due to the higher ionization potential of argon gas and insufficient microwave power. Therefore the plasma lifetime is short, and the enhancement is weaker than in the air.

4.5 Conclusion

This chapter discussed the idea of using microwave to enhance LIBS plasma emission. The idea was realized via a modification of the conventional LIBS system by the addition of a commercialized microwave system. Through the characterization of the MA-LIBS plasma, the enhancement is proved to be from the extended plasma lifetime. The plasma temperature and density in the microwave plasma regime are low (5000-6000 K, less than 10^{15} cm^{-3}) compared with LIBS plasma in the first 1 to 2 μs (around 10000K, above 10^{16} cm^{-3}). Applying the McWhirter Criterion, the LTE assumption is very likely to fail for the MA-LIBS plasma in the microwave plasma regime. However, this does not prevent MA-LIBS from providing good analytical performances. Up to several tens of times signal enhancement was observed from multiple elements in different samples. With the help of the signal enhancement, MA-LIBS provides sensitivity improvement and helps the detection of low concentration elements. In addition, MA-LIBS generates simpler spectra featured with low upper level transitions with large transition strength. This property of MA-LIBS potentially makes the line identification less complicated.

Besides the obvious benefits, some other properties of MA-LIBS can be both beneficial and problematic. The molecular emission due to plasma-air interaction may cause spectral interferences. Meanwhile, the strong molecular can be useful for applications that rely on molecular emission. The good enhancement obtained with low irradiance ablation in normal air condition indicates the possibility to build a MA-LIBS system that does not require energetic lasers or support gas, which are very convenient. However, modifications of the microwave system are needed in order to make the microwave enhancement applicable to broader range of LIBS systems.

USE OF FILAMENTS TOWARDS VERY LARGE DISTANCE SENSING

Filament-induced LIBS of organic thin films

Laser system

High peak power femtosecond pulses are generated using chirped pulse amplification (CPA) based on a titanium sapphire oscillator. The oscillator (Tsunami - Spectra Physics) generates sub-35 femtosecond pulses with a spectrum centered at 800 nm. These pulses are sent through an acousto-optic programmable dispersion filter (Dazzler - Fastlite) and then stretched in time using a grating stretcher. These chirped pulses are used to seed a regenerative amplifier at either 10 Hz or 1 kHz, depending on the application. When the system is run at 10 Hz, a double pass amplifier can also be used to increase the pulse energy. The amplified pulses are then recompressed using a grating compressor. This system yields sub-45 femtosecond pulses with approximately 2 mJ or 25 mJ when run at 1 kHz 10 Hz respectively. The spatial beam profile is obtained using a beam camera (Spiricon) and the pulse duration is measured by frequency resolved optical gating (Grenouille - Swamp Optics). For the experiments reported here, the laser system was operated at 10 Hz with pulse energies of 25 mJ. Self-channeling occurred approximately 2 meters from the laser output and the beam continued to propagate as a stable filament for several meters before irradiating the sample.

Spectroscopic detection analysis

Light emitted by the plasma is collected using an f/1.2 UV grade collection system, positioned approximately 1.5 cm from the sample, and is f-matched to a 1 meter round-to-line UV imaging fiber bundle. A Low effective f-number insures maximum light collection while also limiting the field-of-view; however, because the filament induced plasma is significantly smaller than most nanosecond LIBS plasma this limited field of view is acceptable. All optics must transmit UV light because the emission from organic materials is in the UV as well as visible and infrared spectral regions. A 0.3 m Czerny-Turner spectrometer (2300i - Princeton Instruments) with 150 lines/mm and 1800 lines/ mm gratings is used with a 1024 x 256 pixels Gen II ICCD camera (iStar – Andor Technologies).

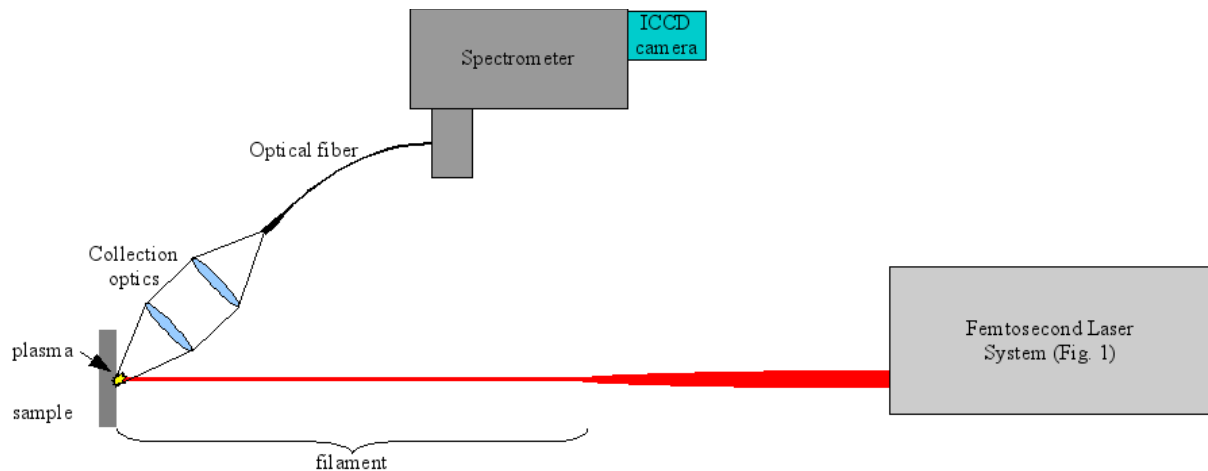


Figure 75. System layout showing laser system, self-channeled beam, sample, collection system, spectrometer and ICCD camera

Samples

For the characterization of spectral emission resulting filament induced breakdown of organic films, this study has focused primarily on two different polymers: Polymethyl methacrylate (PMMA) and a negative photoresist (NR7-1000PY - Futurex). The chemical composition of PMMA (Fig. 76) shows this molecule doesn't contain nitrogen.

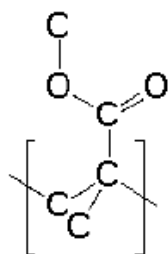


Figure 76.

Chemical composition of PMMA

Although the exact composition of NR7-1000PY is proprietary, Futurex confirmed that nitrogen is used as a cross linker in this photosensitive polymer. Of the two polymers chosen for samples, one contains nitrogen and the other does not contain nitrogen.

The samples are spin coated on a silicon substrate to provide a reproducible means of creating a smooth consistent organic layer with controllable thickness between 500 nm and 1 μ m. Silicon was chosen rather than metal as the substrate material because of the roughness associated with readily available metal substrates.

Results

Figure 77 shows the spectral region for each of the three emitters we are interested in: atomic Carbon (247.86 nm), molecular CN (band head (0-0) of the Violet system at 388.55 nm) and molecular C2 (band head (0-0) of the Swan system at 516.41 nm). Although the spectra shown is the average of 50 shots, since the sample is translated in-between each shot, the spectra is representative of single shot spectra.

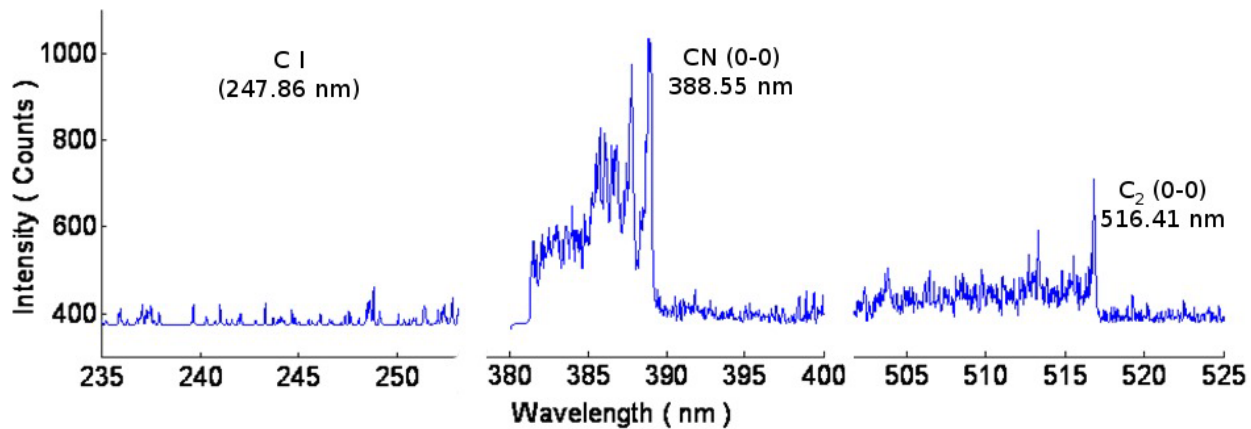


Figure 77. Typical spectrum of PMMA using filament induced breakdown spectroscopy

The intensity of the emission lines shown in Figure 77, are relatively constant—within the error bars—for different film thicknesses between 500 nm and 1 μm (Figure 78).

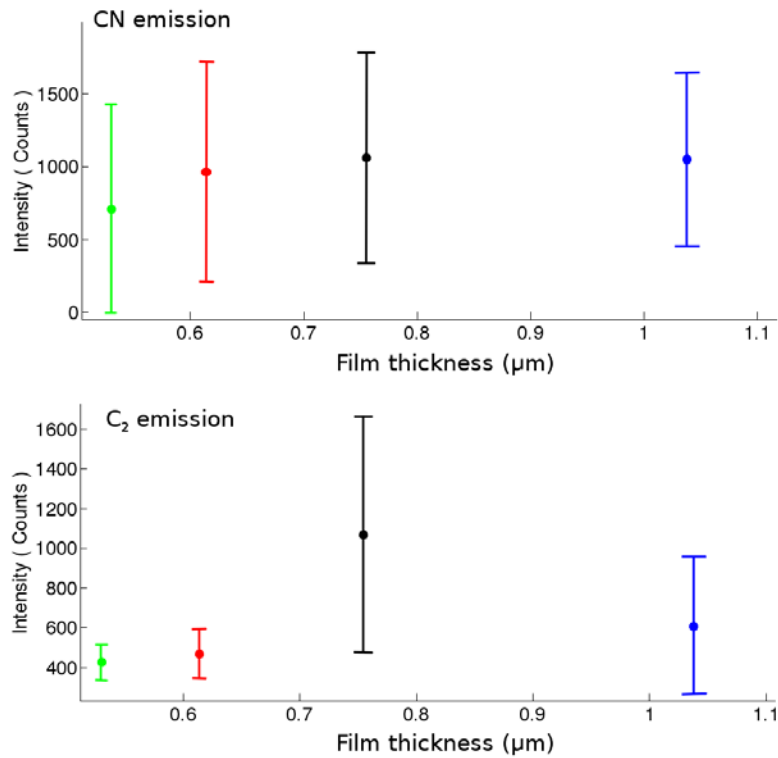
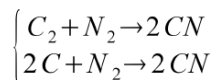


Figure 78. Intensity of CN molecular emission (a) and molecular carbon (b) as a function of film thickness

The spectrum in Figure 4 shows no observable atomic carbon emission at 247.86 nm; however, strong molecular CN radical and C₂ swan band emission. The formation of CN molecules and

subsequent emission from materials without native nitrogen has been observed by others⁹⁵. This emission can possibly be attributed to recombination between nitrogen in the surrounding atmosphere with atomic or molecular carbon present in the filament induced plasma. Of the two possible reactions:



the recombination of two carbon atoms with diatomic nitrogen to produce two CN molecules seems more probable. Others have shown that evidence of molecular recombination is usually present in the kinetics of this CN emission⁹⁶. The emission profile for native emitters is generally

a decreasing exponential function with molecular signal decaying over a longer time compared to atomic emission. When a recombination reaction is occurring within the plasma, there is a finite time for the emission profile to reach a maximum before decreasing.

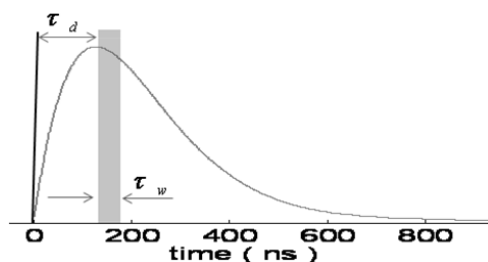


Figure 79. Time gating of ICCD camera to map kinetic profile of emission

To study the kinetic profile of both atomic and molecular signals, the acquisition window (τ_w) of the ICCD camera was decreased to 50 ns and the delay (τ_d) between the laser pulse and beginning of the acquisition was swept in time as illustrated in Figure 79.

To increase the signal-to-noise ratio, the experimental

setup was changed from filament induced breakdown spectroscopy. Atomic carbon and silicon are now present in the focused case. Spectra for atomic carbon, CN radial and molecular carbon are shown below in Figure 80(a) for three different acquisition delay times.

The integrated line intensity as function of time is plotted for each of these three emission lines (the 0-0 transition for the molecular bands) for both samples—PMMA with no native nitrogen and NR-71000PY photoresist with native nitrogen. For both samples, the kinetic profile of atomic carbon is decaying exponentially as expected. The CN molecular signal for PMMA takes a finite time to reach its maximum before decaying exponentially. Comparatively the emission from the nitrogen containing photoresist is always decreasing.

Therefore, the kinetics of molecular CN emission allows us to differentiate between the two samples – one containing nitrogen and the other without nitrogen – showing respectively a decreasing emission from emitters native in the sample or a recombination behavior.

Conclusion

We showed that detection of organic films is possible using filament induced breakdown spectroscopy; however, the spectral signature of these organics is primarily molecular in nature.

⁹⁵ Baudelet M., Guyon L., Yu J., Wolf J.P., Amodeo T., Fréjafon E., Laloi P., "Femtosecond time-resolved laserinduced breakdown spectroscopy for detection and identification of bacteria: a comparison to the nanosecond regime," *Journal of Applied Physics* 99, 084701(2006)

⁹⁶ Baudelet M., Guyon L., Yu J., Wolf J.P., Amodeo T., Fréjafon E., Laloi P., "Spectral signature of native CN bonds for bacterium detection and identification using femtosecond laser-induced breakdown spectroscopy," *Applied Physics Letters* 88, 063901 (2006)

Molecular CN signal is present in the spectrum even if the sample doesn't contain nitrogen. In this case, the emission is likely caused by molecular recombination between the carbon atoms in the filament induced plasma and nitrogen in the surrounding atmosphere. Therefore, CN signal is not a good discriminant between organic materials and explosives, which contain native CN bonds.

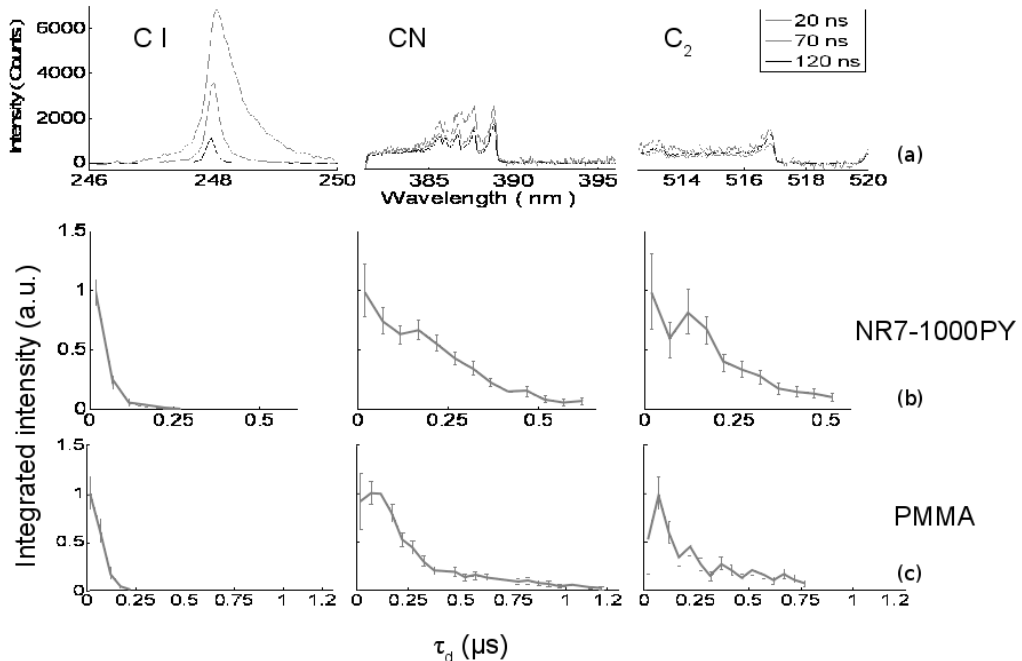


Figure 80. (a) Spectral emission of atomic carbon, molecular CN and C₂ for several acquisition delays and their kinetic for (b) NR7-1000PY and (c) PMMA

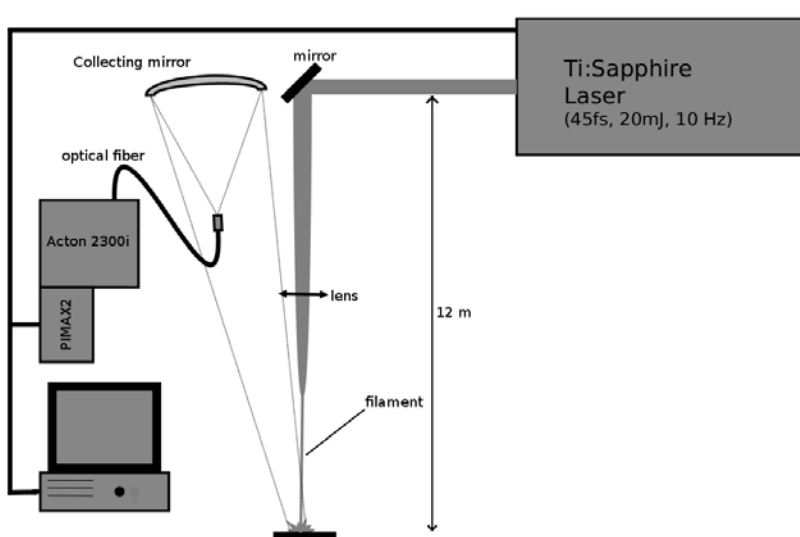


Figure 81. Experimental setup.

Stand-off detection of organic samples using filament-induced breakdown spectroscopy

Experimental section

Laser

The laser used for this project was the same as described above. The filamentation process is forced by a 1 meter focal length lens in order to stabilize the spatial position of the filament inside the beam. The plasma is created on the target 2 meters away from the lens, 12 meters from the

detection optics.

Detection

The emission signal from the stand-off plasma is collected by a 316 mm diameter, 1900 mm focal length parabolic mirror mounted on homemade support. This mirror was extracted from a Newtonian designed telescope to decrease the obstruction due to the secondary mirror in the tube assembly. The mirror is coated with UV-aluminum in order to detect signal down to 200 nm.

The signal is then focused on a round-to-line UV-transmissive fiber bundle connected to a 0.3-meter spectrometer (2300i – Acton Princeton Instruments). The spectrum is then recorded on

an iCCD camera (PIMAX2 – Princeton Instruments) to allow fast triggering of the detection time after the laser pulse. In Figure 81, our typical stand-off LIBS experimental setup is shown.

Results and discussion

The main purpose of this study is to test our facility and show the possibility of detecting an organic film in a single-shot configuration. The samples we decided to analyze in this experiment were a copper sheet, a graphite disk, and a polyisobutylene thin film.

Trace surface detection on copper

Initially, we tested our system by analyzing a sheet of copper. The spectrum obtained by a single shot analysis (delay time = 94 ns, integration time = 1 μ s) is shown in Figure 82. We observed the expected atomic copper lines at 510.6 nm, 515.3 nm, 521.8 nm, 570 nm and 578.2 nm, in addition to atomic sodium at 589 nm and atomic calcium line at 560.2 nm. Sodium and calcium are known to be common pollutants that are adsorbed onto the surface.

By ablating the sample without moving it and so drilling into it, we are able to visualize one shot after another the spectrum for each ablated depth. Figure 83 shows a spectral depth map of an hole we drilled in the copper sample with the filament. We can see that copper lines remain at a relatively stable intensity throughout the drilling after the first shot where the sodium signal is prominent; however, the surface pollutants disappeared after the initial two shots. This observation proved that Filament-induced breakdown spectroscopy is able to give a

Figure 82. Single shot spectrum of the surface of a copper sample

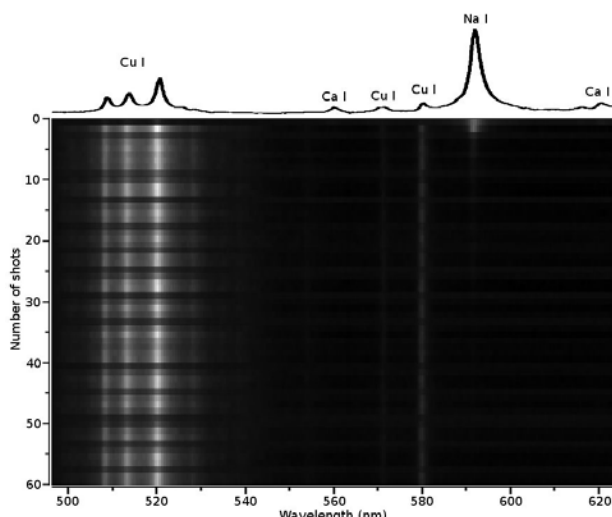


Figure 83. Spectral depth map of copper resulting from drilling the sample on the same spot

spectral signature in a single shot basis of an adsorbed compound at the surface of a metallic sample.

Molecular signal from graphite

As previously mentioned, the purpose of this study is to provide a means to detect trace organic materials. Moving towards that goal, we decide to analyze graphite as it is a carbon-based sample. Figure 84 shows two parts of the spectrum from graphite: (a) the ultraviolet region centered on the emission of atomic carbon at 247.9 nm and (b) the visible region where emission of molecules C₂ (Swan System) and CN (Violet System) occurs.

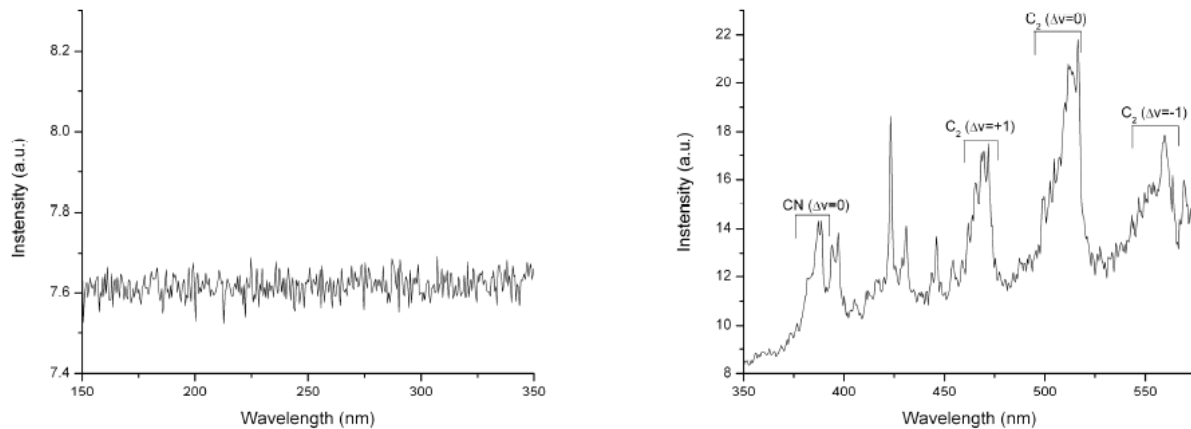


Figure 84. Single shot spectrum of graphite showing (a) no emission from atomic carbon and (b) molecular emission from CN and C₂ radicals

We were unable to observe any atomic carbon at 247.9 nm in our spectra, however, we were able to detect molecular signals from CN and C₂. C₂ is expected from the graphite sample, since this material is composed of carbon only. But CN comes from recombination between the carbon (atomic and molecular) ablated from the sample and the nitrogen in the surrounding atmosphere (air in our experiment). Furthermore, this examination shows the molecular signal can be a signature for carbon-based samples, with the precaution of the interpretation of the CN molecular bands.

Organic film detection

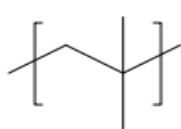


Figure 85. Chemical composition of PIB

In the third part of this study, we analyze an organic thin film. Polyisobutylene (PIB) was chosen as it is a common polymer as well as a prime example of an organic material. Its chemical composition (Fig.85) shows that there is only carbon and hydrogen in its structure, which tells us there is no CN bonds that can emit as a signature of the sample. The sample is prepared by spin-coating a PIB solution on a silicon wafer to approximately 3 μ m thickness. This method of preparation provides us with a uniform sample in order to conduct systematic and reproducible experiments. In addition, the thickness of the PIB moves us towards more realistic samples which are sub-micron in scale.

By ablating the PIB, we obtain the spectrum shown in Figure 86. Once again, we observe molecular carbon signal centered at 516.5 nm from our sample, but we also see the singly-ionized silicon signal around 462 nm and an atomic silicon signal around 505 nm ablated from the substrate. This shows the pulse passes through the film on the first shot. As in the case of graphite, the atomic carbon is not present in the spectrum. However, this also shows we are able to detect the signature of an organic sample on the first shot with the molecular signal.

This situation is very similar to the circumstances we experienced earlier with sodium on the copper sample. In this instance, however, we are instead detecting an organic film on a silicon substrate. By drilling into the sample, we are able to determine the initial shots are ablating polyisobutylene, while subsequent shots are hitting only silicon.

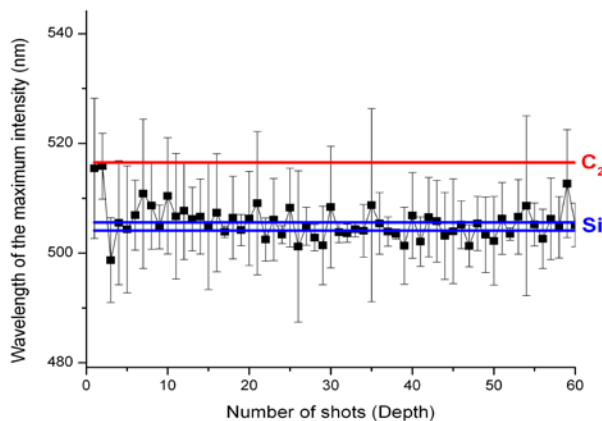


Figure 87. Wavelength of the maximum intensity in a single shot spectrum of a $3\mu\text{m}$ film of PIB on a silicon wafer as a function of depth

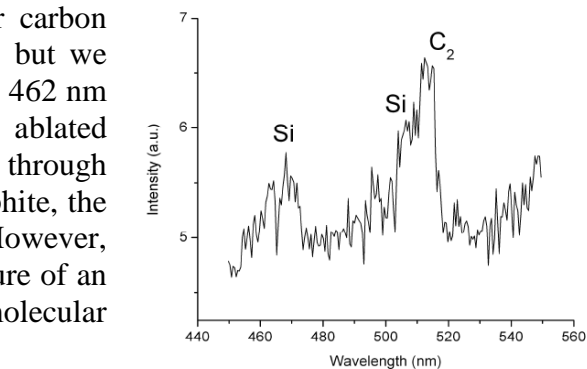


Figure 86. Single shot spectrum of PIB film on a Silicon substrate

A simple way of showing this phenomenon is to compare the wavelength of the maximum intensity in the spectral range from 480 nm to 540 nm that contains the atomic Si lines (504.1 nm and 505.6 nm) and the band head of the $\Delta v=0$ transitions of the C_2 Swan system (516.5 nm) by the number of shots. Figure 87 shows that it is clearly evident the initial shots are centered about the molecular carbon signal from the organic film but then the signal is dominated by the atomic silicon emission from the substrate. This behavior proves that the detection of trace organic materials in a single shot basis is possible by filament-induced breakdown spectroscopy when the drilling is monitored spectrally.

Conclusion

In conclusion, our results support the concept of stand-off detection of trace organic materials. In our experiment, we were able to prove surface analysis of trace materials is possible using filament-induced breakdown spectroscopy by detecting sodium on our copper sample. We determined that molecular C_2 and CN signals are spectral signatures for carbon-based samples and not atomic carbon emission. By using a spectrally monitored drilling method with a filament, it is possible to detect organic thin films based on the C_2 molecular signal. This provides a systematic method for trace materials detection on micron-scale samples

Towards larger distances

Experiments have been performed to evaluate the feasibility of FIBS at large distances: 60 meters and 400 meters.

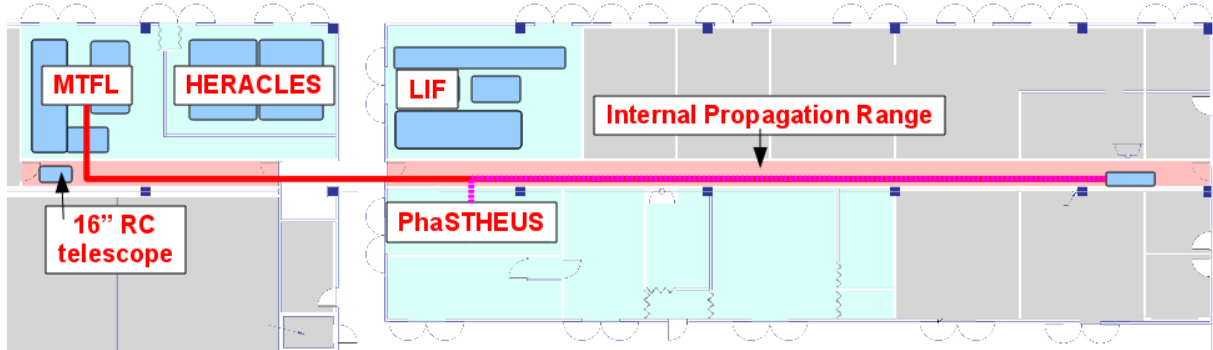


Figure 88. Laser facilities and internal propagation range of the Townes Institute in CREOL

Experiments at 60 meters were performed in the internal laser propagation range of the CREOL building (Figure 88), the laser for filamentation being MTFL. Single shot detection of calcium lines from fingerprints on graphite samples was demonstrated.

Experiments demonstrating the feasibility of large distance stand-off sensing was performed in a different scheme than FIBS, the possibility of filamentating laser pulses at longer distances than the internal propagation range being not possible for the moment. The main question remains “is a laser-induced plasma detectable at large distance?” To that purpose, the laser-induced plasma was created by a nanosecond laser (Nd:YAG, 6 ns, 1064 nm, 100 mJ) on a breadboard positioned 400 meters away from the detection and spectral analysis (Figure 89).

The detection was done by a f/8.4 16" Ritchey-Chretien telescope (Optical Guidance Systems) feeding a 0.5-meter spectrometer (Acton SP500i) equipped with an iCCD camera (Andor iStar). Single-shot spectra were obtained for graphite and showed the signature for atomic carbon (247.8 nm line) and the CN (1 - 0) band of CN Violet system (359 nm) (Figure 90). This demonstration shows the ability of single shot analysis at very large distance (larger than the LIBS record of 120 meters⁹⁷). Nevertheless, the difference in plasma dynamics between nanosecond and femtosecond plasmas have to be considered before directly transposing the application to FIBS.



Figure 89. Localisation of the large distance LIBS experiment

⁹⁷ R. Gronlund, M. Lundqvist, S. Svanberg, “Remote Imaging Laser-induced Breakdown spectroscopy and Laser-Induced Fluorescence Spectroscopy Using Nanosecond Pulses from a Mobile Lidar System”, Applied Spectroscopy 60(8), 853 – 859 (2006).

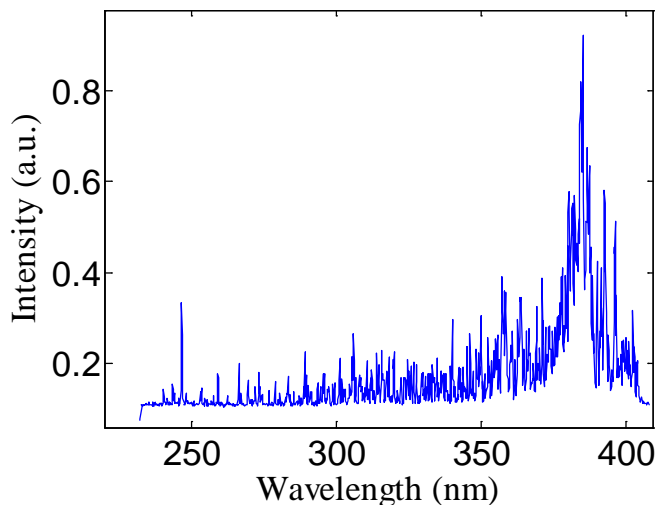


Figure 90. Single-shot. LIBS spectrum from graphite at 400 meters.

Classification procedures that have been optimized using class examples, without including interferences in the examples, may fail to perform well on real samples that contain impurities. However, recent results have shown some success in performing discriminant analysis in the presence of interfering factors. For example, >97% correct classification of the maximum temperature reached by burning soils has been accomplished by partial least squares discriminant analysis in the presence of up to 20% ash interference¹⁰⁰. It is often the case that the number of analyte classes of interest in a particular problem is greatly exceeded by the number of potentially interfering species, thereby complicating the task of securing training sets that contain all possible interferences.

This paper examines a novel approach to analyte classification in the presence of a complex and undetermined interference. The method explored here makes use of target factor analysis, as described by Malinowski¹⁰¹, to determine the presence of an analyte in a mixture without requiring that every component of the mixture be identified. The method introduced here differs from previously reported use of target factor analysis (TFA) for discriminant analysis (also referred to as procrustes discriminant analysis), which has been shown to be mathematically equivalent to partial least squares discriminant analysis (PLS-DA)^{102,103}. In

QUANTITATIVE LIBS FOR DECISION MAKING VIA CHEMOMETRICS

An important problem in chemical analysis is the assignment of object membership among a set of defined classes. Current literature provides examples of the use of discriminant analysis in homeland security applications^{98,99}. Most classification methods are not particularly well adapted to classifying an unknown in the presence of a significant background signal that is independent of the class and highly variable from sample to sample.

⁹⁸ Gottfried, L.; De Lucia, FC., Munson, CA.; Mizolek, AW. "Strategies for residue explosives detection using laser-induced breakdown spectroscopy," *Journal of Analytical Atomic Spectrometry* (2008), 23(2), 205-216.

⁹⁹ Primera-Pedrozo, OM.; Pacheco-Londono, LC.; De la Torre-Quintana, LF.; Hernandez-Rivera, SP.; Chamberlain, RT; Lareau, RT "Use of fiber optic coupled FT-IR in detection of explosives on surfaces," *Proceedings of SPIE-The International Society for Optical Engineering* (2004), 5403(Pt. 1, Sensors, and Command, Control Communications, and Intelligence (C3I) Technologies for Homeland Security and Homeland Defense III), 237-245

¹⁰⁰ Arcenegui, V.; Guerrero, C.; Mataix-Solera, J.; Mataix-Beneyto, J.; Zornoza, R.; Morales, J.; Mayoral, A. M. "The presence of ash as an interference factor in the estimation of the maximum temperature reached in burned soils using near-infrared spectroscopy (NIR)," *Catena*, 2008, 74, 177 – 184.

¹⁰¹ Malinowski, E. R. and Howery, D. G. "Factor Analysis in Chemistry", John Wiley & Sons, New York, USA, 1980.

¹⁰² González-Arjona, D.; López-Pérez, G.; González, A. G. "Performing procrustes discriminant analysis with HOLMES," *Talanta* 1999, 49, 189 – 197.

contrast, the method discussed here relies on testing a library of spectra from representative classes to identify the class or classes that contribute to the data set. The data examined in this paper are taken from spectra obtained by laser-induced breakdown spectroscopy (LIBS) from steel plates that had been penetrated by 9 mm bullets with either copper jackets (CJ), metal alloy jackets (MJ) or non-jacketed lead (NJ) projectiles. The bullet jacketing materials constitute the analyte classes. The objective is to test the TFA method to identify the class of bullet that penetrated a steel plate based on LIBS spectra collected at the edges of the hole where trace residues of jacket materials are deposited. The LIBS spectra reflect contributions from the steel and the jacket material. The class of bullet with the highest probability of contributing to the spectral set is identified by combining a Bayesian classifier with the results of the TFA.

Experimental:

Instrumentation

The LIBS instrument used in this research (LIBS2000+, Ocean Optics, Dunedin, FL, USA) was equipped with a Q-switched Nd:YAG nanosecond pulsed laser (CFR200, Big Sky Lasers, Bozeman, MT, USA). Fundamental (1064 nm) laser output (pulse width of 9 ns and 45 mJ/pulse) was used to generate laser-induced plasmas. The spectrometer delay for spectral collection was optimized at 2.5 μ s, giving maximum signal intensity and signal-to-noise ratio and an integration time of 1 ms. The plasma emission between 200 and 900 nm was collected by a fiber optic bundle connected to seven sequential CCD spectrometers, providing a spectral resolution of 0.06 nm per channel. The sample was placed in a chamber consisting of a plastic box equipped with an X-Y-adjustable sample stage, as previously reported^{104,105}. Data acquisitions were performed using the Ocean Optics OOILIBS software.

Samples

The six 9 mm cartridges used in the tests comprised three classes of bullets. The classes consisted of 15 copper jacketed (CJ), 4 metal jacketed (MJ) and 4 non-jacketed (NJ) bullets. The 15 copper jacketed bullets were of different manufacturers and types, including Remington/UMC, CCI/Blazer, Independence, and Hornady/'Tap'. The 4 metal jacketed bullets were all Winchester/Silver-Tip and the 4 non-jacketed bullets were all "hand loads". The Hornady/'TAP' and the Winchester/Silver-Tip were hollow-point bullets. Five bullets of each manufacturer/type were obtained courtesy of (East Orange Shooting Sports, Orlando, FL). Four bullets of each manufacturer/type were fired to penetrate steel plates and the projectile from one bullet of each manufacturer/type was removed and used to establish the LIBS spectral library. While the bullet jacketing materials constitute the analyte classes, the variation typically observed between LIBS spectra produced a range of spectral profiles that were representative of each class. The plates were 1 mm steel sheeting obtained from Home Depot, Orlando, FL.

The firing of the bullets through the steel plates was performed at the Seminole County Shooting Range by Lt. Jerry Emert, University of Central Florida Police Department. The rounds were fired through the sheet metal positioned approximately seven feet from the shooter.

¹⁰³ González-Arjona, D.; López-Pérez, G.; González, A. G. "Holmes, a program for performing Procrustes Transformations," *Chemometrics and Intell. Lab. Sys.* 2001, 57, 133 – 137.

¹⁰⁴ Bridge, C. M., Powell, J., Steele, K. L., Williams, M., MacInnis, J. M., Sigman, M. E., Characterization of automobile float glass with laser-induced breakdown spectroscopy and laser ablation inductively coupled plasma mass spectrometry. *Appl. Spectros.* 2006, 60(10), 1181-1187.

¹⁰⁵ Bridge, C. M., Powell, J., Steele, K. L., Sigman, M. E., Forensic Comparative Glass Analysis by Laser-Induced Breakdown Spectroscopy. *Spectrochimica Acta Part B: Atomic Spectroscopy* 2007, 62, 1419-1425

A total of three plates were used in the experiments, with each being used for two bullet manufacturer/types. The first two plates were shot with the four CJ class bullets and the last plate was shot with the SJ and then NJ classes. Two clusters of bullet holes were positioned on opposite ends of each plate and labeled at the time of testing. Each cluster consisted of four bullet holes, except for the first set of CJ bullets, wherein one cartridge misfired giving on three bullet holes. Plates were wrapped individually in plastic bags to prevent possible contamination on transportation back to the laboratory for analysis.

The remaining five bullets, one of each manufacturer/type, were taken to the Orlando field office of the Florida Department of Law Enforcement where a firearms crime laboratory analyst, Christine Murphy, safely removed the projectiles with a “bullet puller hammer” to allow for safe LIBS analysis of the jacketing materials.

Sample Analysis

A library of spectra corresponding to each class was generated by collecting LIBS spectra from the unused projectiles. The library was made up of six spectra from each manufacturer/type, with each spectrum comprised of an average of ten single shot spectra. Each bullet projectile was placed on the sampling stage and rotated until six averaged spectra were collected. Similarly, spectra of the steel plates were also collected; however, the plate spectra were not included in the library since they constitute the background interference against which the projectile class is to be determined. The plates containing the bullet holes were cut to obtain individual bullet holes and surrounding plate from each bullet cluster. Each bullet hole was positioned on the LIBS sample stage so the laser would hit the edge of the bullet hole in an area where material transfer from physical contact would be expected to occur. Twelve single shot spectra were collect from around each bullet hole. All spectra in the library and the spectra taken from the holes in the steel plated were collected at an average laser power of 8.5 mJ. Data collection was initiated 4.5 μ s after the laser was fired and the signal was integrated for 1 ms.

Data Analysis

Data analyzed for the TFA tests was restricted to 5636 points in the spectral range of 200-500nm. The emissions comprising each spectrum were normalized to a summed intensity of one and the twelve spectra from each bullet hole were concatenated into a single data matrix for target factor analysis (TFA), as described below. The data manipulation and analysis was performed using Microsoft Excel (Microsoft Corp. Seattle, WA, USA) to compile the data, MatLab (MathWorks, Natick, MA, USA) to perform the TFA, and R (The R Project for Statistical Computing, <http://www.r-project.org>) to perform the classifications and graph the data.

Target Factor Analysis (TFA)

The TFA method involves analyzing spectra from a set of samples where the spectra may have contributions from both the analyte of interest and interferences. The first step is to reduce the dimensionality of the data to obtain a set of latent variables through a process which is equivalent to principal components analysis (PCA). The data matrix is factored into a product of two matrices, equation 1, where $[R^{\ddagger}]$ and $[C^{\ddagger}]$ are commonly referred to as the scores and loadings matrices, respectively, and are designated here by the \ddagger superscript to retain only the number of principal components required to reproduce the desired fraction of the variance in the

data. The number of principal components to retain is estimated in this work using the determination of rank by median absolute deviation (DRMAD) method¹⁰⁶.

$$[D] = [R^\ddagger] [C^\ddagger] \quad (1)$$

The data matrix $[D]$ is an $(n \times m)$ matrix consisting of n spectra measured at m wavelengths. The factors in matrix $[C^\ddagger]$ are comprised of an ortho-normal set of eigenvectors that represent abstract mathematical solutions to the problem and do not represent physically meaningful spectra of the chemical species that contribute to $[D]$. In order to find meaningful spectra that can regenerate the original data without introducing significant error, the factors are transformed through oblique rotations. This can be expressed mathematically as in equation 2, where $[T]$ is the transformation matrix that brings about the oblique rotations.

$$[D] = [R^\ddagger] [T] [T]^{-1} [C^\ddagger] \quad (2)$$

$$\bar{R}_l = [R^\ddagger] T_l \quad \text{or} \quad \bar{C}_l = T_l^\top [C^\ddagger] \quad (3)$$

$$T_l = [\lambda^\ddagger]^{-1} [R^\ddagger]^\top \bar{R}_l \quad \text{or} \quad T_l^\top = \bar{C}_l [C^\ddagger]^\top \quad (4)$$

A key point in this method is that it is not necessary to identify the entire transformation matrix, because individual vectors can be identified one at a time, as shown in equation 3, where \bar{R}_l or \bar{C}_l are *predicted vectors* and T_l and T_l^\top are 1th column and row transformation vectors of $[T]$ and $[T]^{-1}$ respectively. The transformation vectors can be found by either of the equations given designated as 4, where $[\lambda^\ddagger]$ is the diagonal matrix of eigenvalues corresponding to the retained principal components and \bar{R}_l or \bar{C}_l are the *test vectors*. The test vectors may come from theoretical considerations, empirical knowledge, intuition, or in the case described here, from a library of spectra. It is common practice to organize $[D]$ such that each row corresponds to an object (i.e., spectrum) and each column corresponds to a variable (i.e., wavelength). The test vectors will be spectra and the second equations in lines (3) and (4) are preferred in this application.

The test vector \bar{C}_l and predicted vector \bar{C}_l will show a high degree of similarity (i.e., Pearson product moment correlation approaching 1) if the test vector is a potentially significant contributor to the data set. Furthermore, when a given class of analyte contributes to a sample set, tested and predicted vectors from that class should show higher similarities in general than those from non-contributing classes. The property of target factor analysis that allows the search for one transformation vector at a time can then be utilized to identify a class of analyte that may contribute to a data set, even in the presence of interferences.

Assigning Class Membership

In a multiclass classification problem, it is common for each class (ω_i) to be defined by one or more measurable parameters (i.e., x in a single parameter case). Following Bayesian decision theory, the posterior probability, $P(\omega_i|x)$ in equation (5), that an object belongs to a given class can be assessed by the value of the measurable parameter x for that object, a probability density function, $p(x|\omega_i)$, and the prior probabilities for encountering each class,

¹⁰⁶ Malinowski, E. R. "Determination of rank by median absolute deviation (DRMAD): a simple method for determining the number of principal factors responsible for a data matrix," *J. Chemometrics* 2009, 29, 1 – 6.

$P(\omega_i)$. The probability density function can be approximated in different ways, with assumptions of normality and the use of kernel functions constituting common approaches. If the prior probabilities are not known, it is common to assign them equal values or values proportional to the relative populations of each class. The posterior probability for membership in each class is calculated at x and class membership is assigned based on the largest probability.

$$P(\omega_i | x) = \frac{p(x | \omega_i)P(\omega_i)}{\sum_i p(x | \omega_i)P(\omega_i)} \quad (5)$$

In the application examined here, the probability density functions $p(r|\omega_i)$ change for each set of TFA results where a library of spectra that may potentially contribute to a spectral set has been examined and the correlation between \bar{C}_i and \bar{C}_l has been determined for all members of each class. For example, if there are n classes, $\omega_1 - \omega_n$, under consideration in a problem where ω_l contributes to the samples, the distribution of r values for ω_l will tend to be larger than those for the remaining $n-1$ classes. However, in a problem where a different class contributes to the sample set, the distribution of r values for the contributing class will tend to be larger and the relative ordering of the distributions for the remaining classes will also change from one problem to the next. It is therefore necessary to evaluate $p(r|\omega_i)$ following TFA analysis of each sample set. Two methods of estimating $p(r|\omega_i)$ are evaluated in this work. One method involves using a normal approximation based on the average r and variance in r for each class. The second approach uses a kernel approximation given in equation (6), which simulates each distribution by a superposition of normal distribution functions centered at each of the n_i correlation values for each class ω_i ¹⁰⁷. In equation (6), the value h_i is equivalent to the standard deviation in the normal distribution.

$$p(r, \omega_i) = \frac{1}{n_i} \sum_{j=1}^{n_i} \frac{1}{h_i \sqrt{2\pi}} e^{-\frac{1}{2h_i^2} (r - \bar{r}_j)^2} \quad (6)$$

Two further considerations are important to interpreting the results from the combined TFA and Bayesian decision theory: (1) there may be cases where an analyte of interest is not present and a data set should not be classified and (2) it is important to determine the value of r where the posterior probability, $P(\omega_i|r)$, will be calculated.

The coefficient of determination, r^2 , can be interpreted as the percentage of the variation in the *predicted vector* that is associated with variability in the *test vector*. Although an r (or r^2) of 1.0 is ideal, the result may not be practical for real-world data. Can the value of r serve as a criterion for determining if classification is appropriate, and if so, how should the low classification limit for r be chosen? Two approaches are examined in this paper. One highly conservative approach is to only calculate posterior probability for classes which have a median correlation, r_M which is close to unity, i.e., within five times the median absolute deviation for the class, r_{MAD} . This approach would only allow calculation of posterior probabilities for classes where there was greater than approximately 1% chance of observing $r=1$. In this approach, evaluation of $P(\omega_i|r)$ would be made at $r=1$, which represents a perfect correlation between the test and predicted vectors. The posterior probability would be set to zero for classes where $|1-r_M|/r_{MAD} > 5$. In the event that $|1-r_M|/r_{MAD} > 5$ for all classes, the sample would not be classified.

¹⁰⁷ Wilcoxon, F. "Individual Comparisons by Ranking Methods," *Biometrics Bulletin* (1945), 1(6), 80-83.

In a second approach, the posterior probability would ideally be calculated only for classes where a one-sided (directional) test of r_M showed it to be statistically different from $r_{M,blank}$ at a specified significance level. The term $r_{M,blank}$ is the highest median correlation determined for any class as the result of analyzing a sample set which is known to not contain any analyte of interest (a blank). The statistical comparison of the medians for two distributions is conveniently accomplished with the Wilcoxon rank sum test.ⁱ This approach may be considered impractical in cases where the background interference signal is highly variable and $r_{M,blank}$ cannot be determined accurately. In those cases where $r_{M,blank}$ cannot be determined experimentally, the value can be set equal to a cutoff for classification which is determined experimentally from a “training” data set. In this approach, it could be inappropriate to calculate $P(\omega_i|r)$ at $r=1$ in some cases, since there is no guarantee of a significant probability $p(r|\omega_i)$ at $r=1$. An alternative is to calculate $P(\omega_i|r)$ at $r=r_M$ determined for the class having the largest median correlation. The median correlation, r_M , is preferred over the mean r because r_M is more robust and less significantly influenced by outliers.

Results:

LIBS Spectra

Figure 91 shows one LIBS spectrum from each of the manufacturer/type projectile in the library and a spectrum from the steel plate. The similarity between the four CJ spectra (Figure 91a-d) is obvious, however some differences are observed in the 200 – 250 nm and 450 – 500 nm ranges. The two strong peaks at 324.754 nm and 327.396 nm are attributed to Cu I transitions. The representative spectrum of the one MJ projectile (Figure 91e) also contains emissions attributed to the Cu I transitions along with emissions in the c.a. 330 – 360 nm region that are not present in the CJ projectiles. The representative spectrum from the NJ class projectile (Figure 91f) contains multiple lines attributed to lead, including the 363.958 nm and 368.347 nm Pb I lead transitions. The spectrum from the metal plate (Figure 91g) does not contain excessively strong lines for the Cu I or Pb I transitions but does contain approximately 15 lines in common with the three projectile classes.

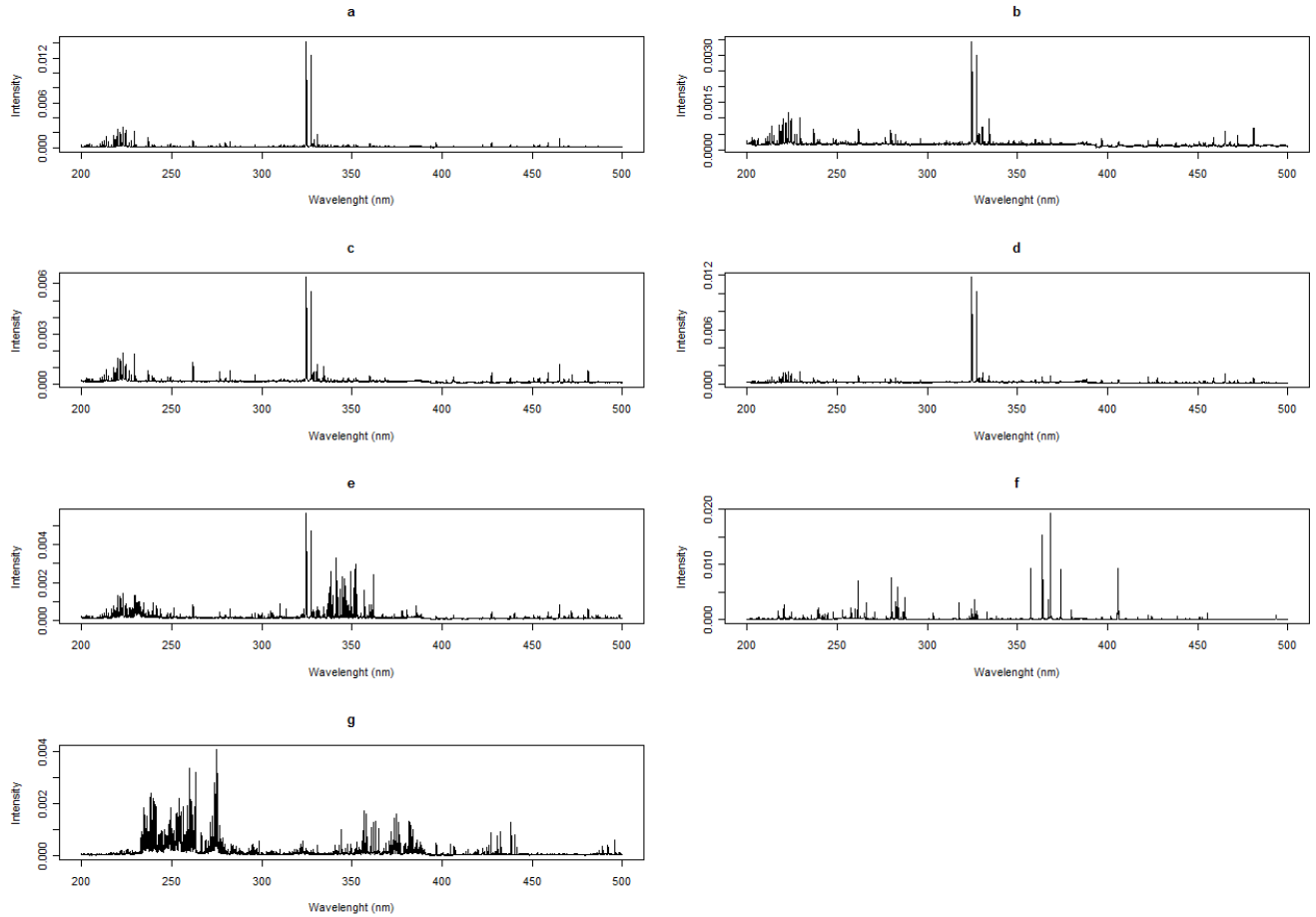


Figure 91. LIBS spectra from each of the manufacturer/type projectile in the library and a spectrum from the steel plate.

Figure 92 shows a set of six spectra taken from the edge of a bullet hole made with a CJ class projectile. The two Cu I emissions seen in both the CJ and MJ projectile classes are seen in all of the spectra; however, each spectrum also contains a very strong contribution from the plate which servers to interfere with facile assignment of the class of projectile that penetrated the plate. In addition, there are two strong emissions at 455.404 nm and 493.409 nm that were not present in the library.

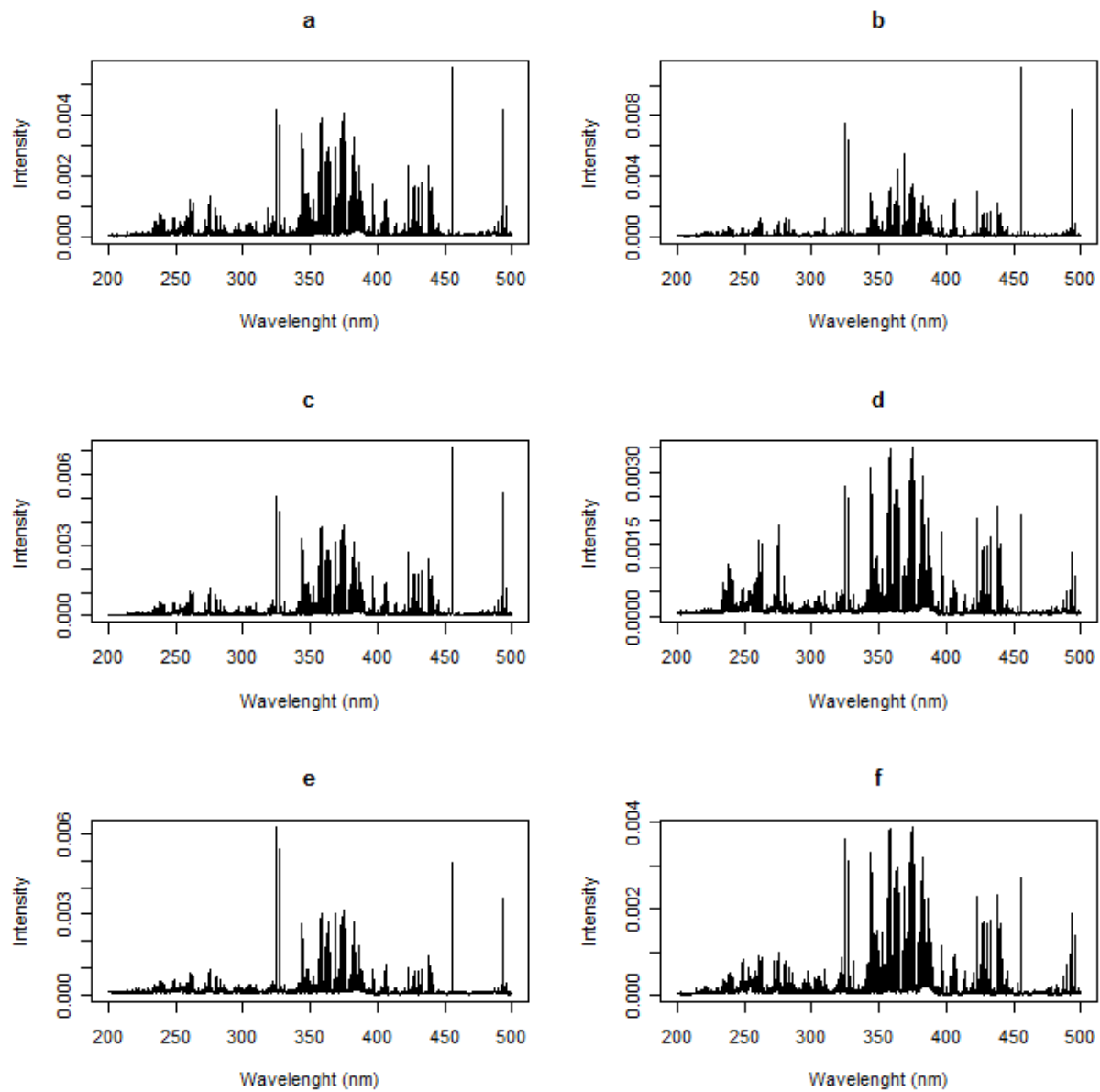


Figure 92. Spectra taken from the edge of a bullet hole made with a CJ class projectile.

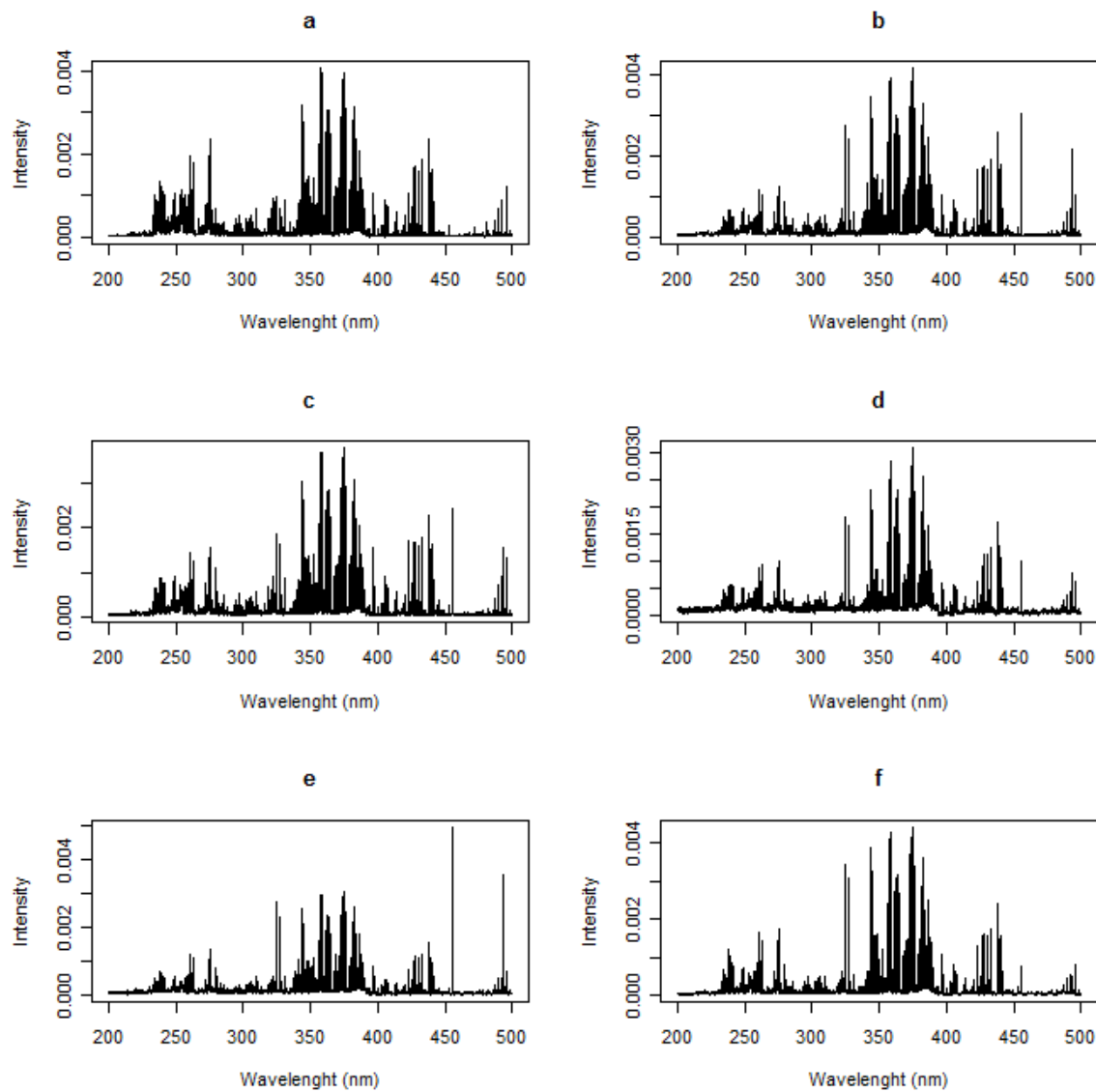


Figure 93. Spectra taken from the edge of a bullet hole made with a MJ class projectile.

The harder nature of the metal jacket, relative to Cu, may have resulted in less transfer of jacket material to the metal. Again, the Ba II transitions are seen strongly in spectra 93b, 93c and 93e. Figure 94 shows a set of LIBS spectra collected from the edge of a bullet hole made with a NJ class projectile. The two Pb I transitions are readily observed in most of the spectra and the Ba II transitions are also observed in some spectra.

These transitions are both tentatively assigned Ba II and likely arise from gunshot residue deposited as a result of the proximity of the firearm to the steel plate. The gunshot residue in these samples contributes to the background interference.

A set of six LIBS spectra collected from the edge of a bullet hole made with a MJ class projectile is shown in Figure 93. The Cu I transitions are seen prominently in some, but not all, of the spectra in Figure 93.

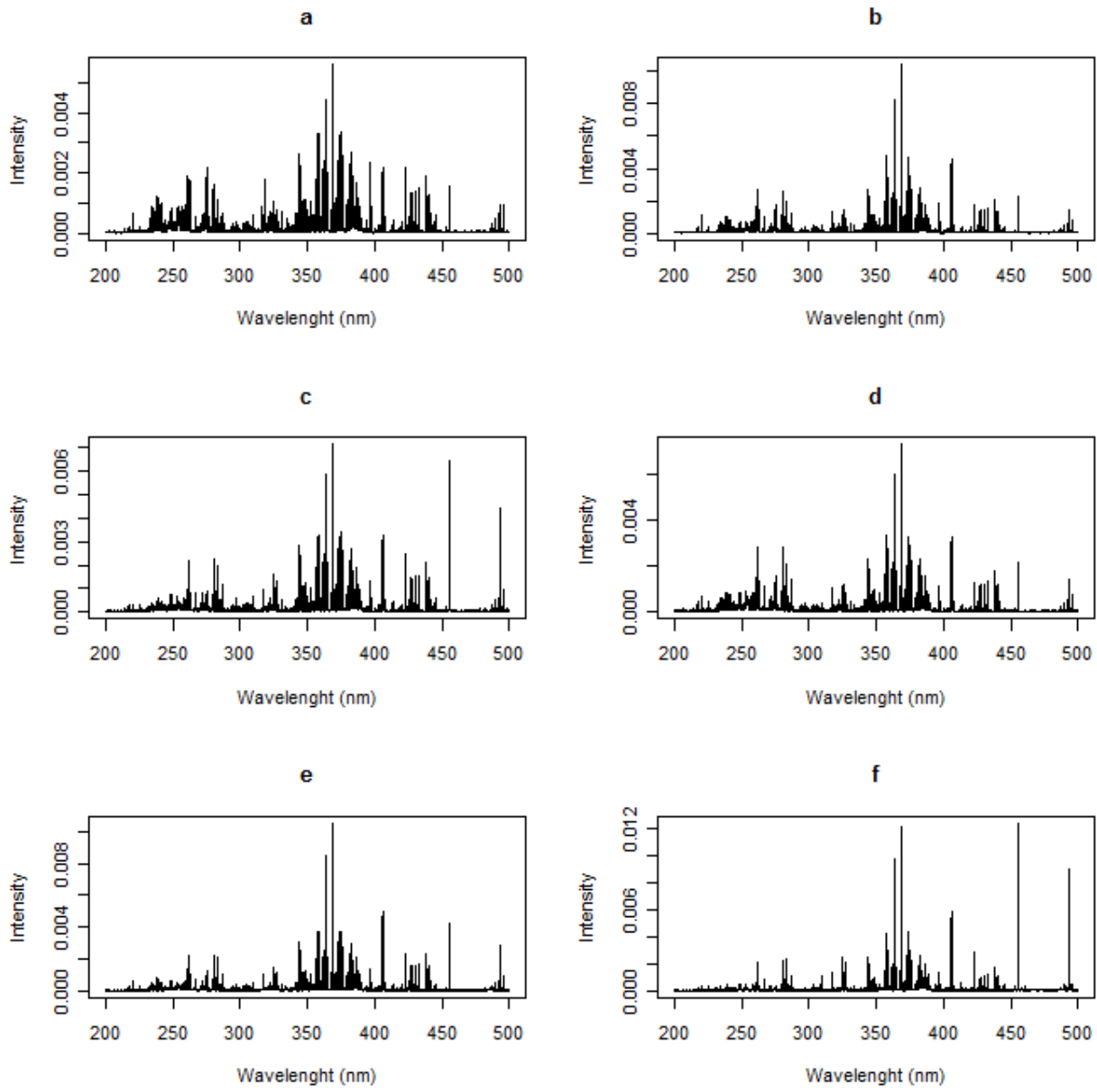


Figure 94. Spectra taken from the edge of a bullet hole made with a NJ class projectile.

Class Examples of TFA Classification

A set of 12 LIBS spectra taken from the edges of a bullet hole made with a copper jacketed bullet was analyzed as described in the Experimental section. Principal components analysis of the data with subsequent DRMAD analysis of the eigenvalues found that three principal components were making significant contributions to the data and accounted for c.a. 95% of the variance in the spectra. Results from the oblique rotations of the three principal component eigenvectors using the library of LIBS spectra as test vectors are shown in Figure 95. Figure 95b shows box plots of the distribution of correlations between test and predicted vectors for the three classes of projectiles.

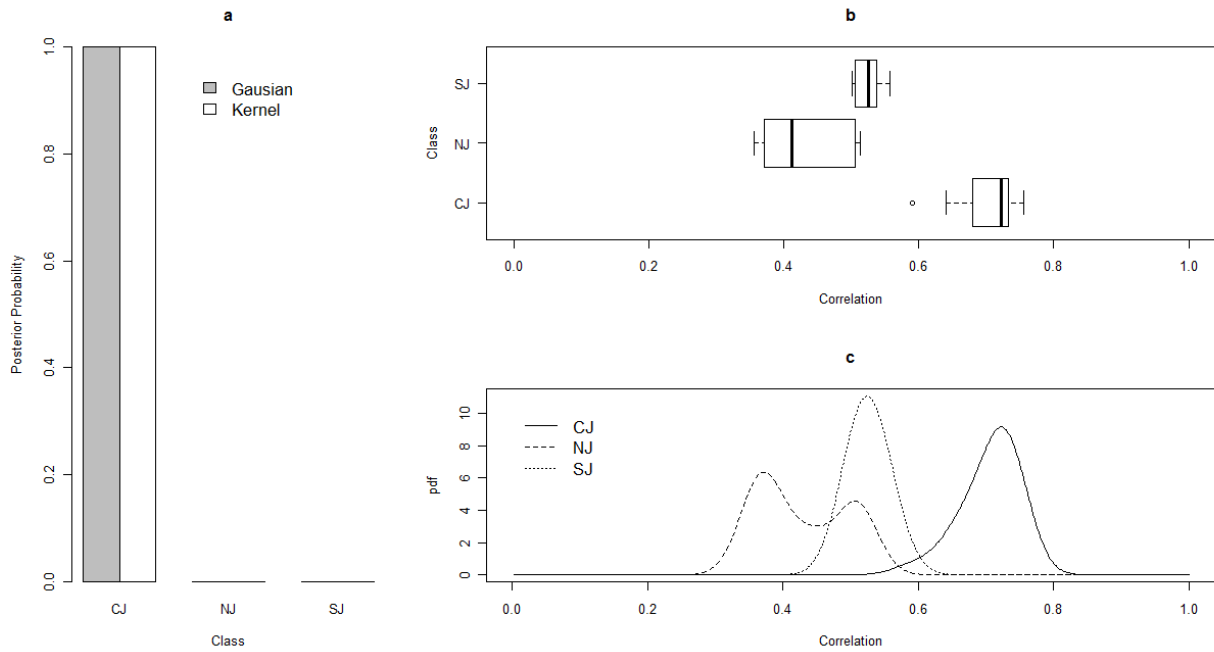


Figure 95. TFA classification results for LIBS spectral data from jacket residue deposited by a CJ class projectile passing through a steel plate: (a) posterior probabilities calculated by Gaussian and kernel probability density functions, (b) boxplot of correlation coefficient distributions for each projectile class and (c) kernel probability density distribution functions for each projectile class.

Figure 95c shows the kernel density plots for the three classes. In this example, the correlations for the CJ class are in the range of c.a. 0.6 – 0.8 with a median r of 0.72. The kernel density graphs in Figure 95c, along with the boxplots in 95b reflect no significant contributions to the correlation distributions at r values approaching 1; however, the CJ class gave significantly higher correlations than the other two classes. The value of $|1-r_M|/r_{MAD}$ for all three classes exceeds 5 and under the MAD classification method, the sample would go unclassified.

The CJ class posterior probability evaluated at $r_M = 0.72$, using either the Gaussian estimates of the probability densities or the kernel functions, is approximately 1, as shown by the bar graph in Figure 95a. The value of $r_{M,blank}$ was determined for a set of spectra from the metal plates used in this project. The r_M values obtained from comparing the blank spectra with the library are shown in Figure 96. The MJ class was most similar to the plates, $r_M = 0.13$, and is significantly below the r_M values determined for each class from analysis of the bullet hole data. Classification based on $P(\omega_i|r)$ calculated at $r_M=0.72$ clearly predicts correct class membership.

Similar analysis of spectral data collected from around a hole prepared from penetration of a MJ class projectile through steel gives results shown in Figure 97. The graphs in Figure 97 reveal an overall higher distribution of correlation values for the MJ class. Calculation of $P(\omega_i|r)$ at $r_M=0.60$ gives a poster probability for the MJ class of approximately 1 using Gaussian estimates for the density function and 0.91 using the kernel density estimation. The kernel density estimation results in a posterior probability of 0.09 for the CJ class. Either approximation results in the correct class assignment.

Once again the value of $|1-rM|/rMAD$ for all classes exceeds 5 and under the MAD classification method, the sample would go unclassified.

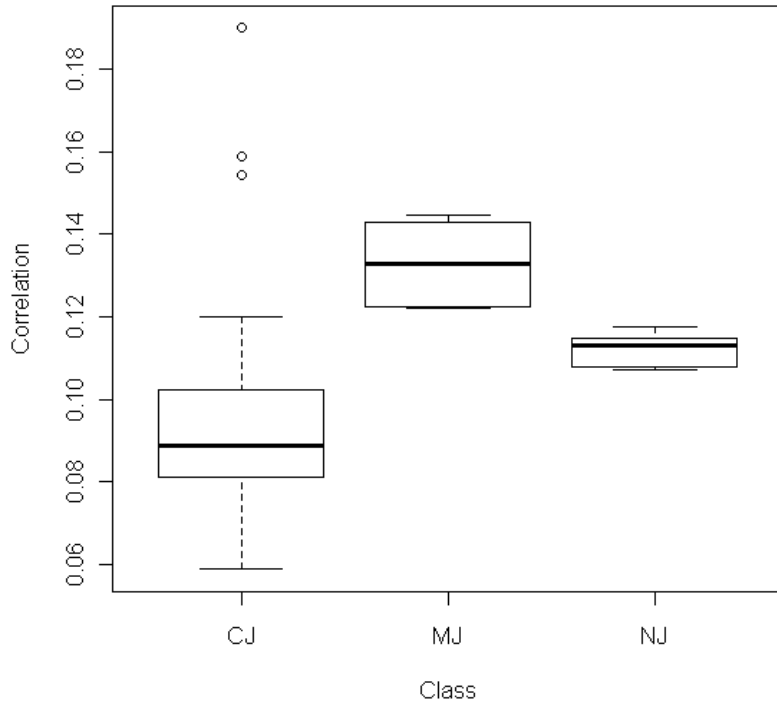


Figure 96. Boxplot of the rM values obtained from comparing LIBS spectra with the library.

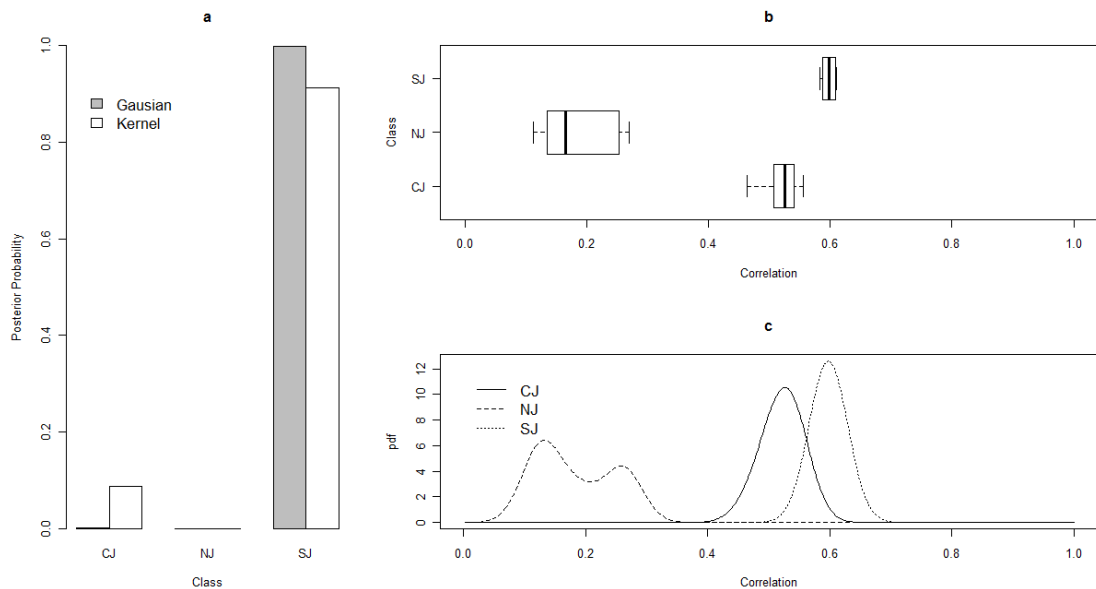


Figure 97. TFA classification results for LIBS spectral data from jacket residue deposited by a MJ class projectile passing through a steel plate: (a) posterior probabilities calculated by Gaussian and kernel probability density functions, (b) boxplot of correlation coefficient distributions for each projectile class and (c) kernel probability density distribution functions for each projectile class.

Results for the analysis of spectra taken from the edge of a bullet hole made with a projectile of the NJ class are shown in Figure 98. The value of $|1-r_M|/r_{MAD}$ exceeds 5 for the CJ and MJ classes, but not for the NJ class. Under the MAD classification method, the posterior probability for the NJ class, calculated at $r=1$, would be 1.0 and the sample would be correctly classified as NJ. Similarly, the posterior probability for the NJ class would be 1.0 when calculated at $r_M=0.95$ for the NJ class. The r_M values for the CJ and MJ classes are significantly lower; however the distributions of r_M for both the CJ and MJ classes are statistically different from the $r_{M,blank}$ value determined from TFA analysis of the steel plate spectra.

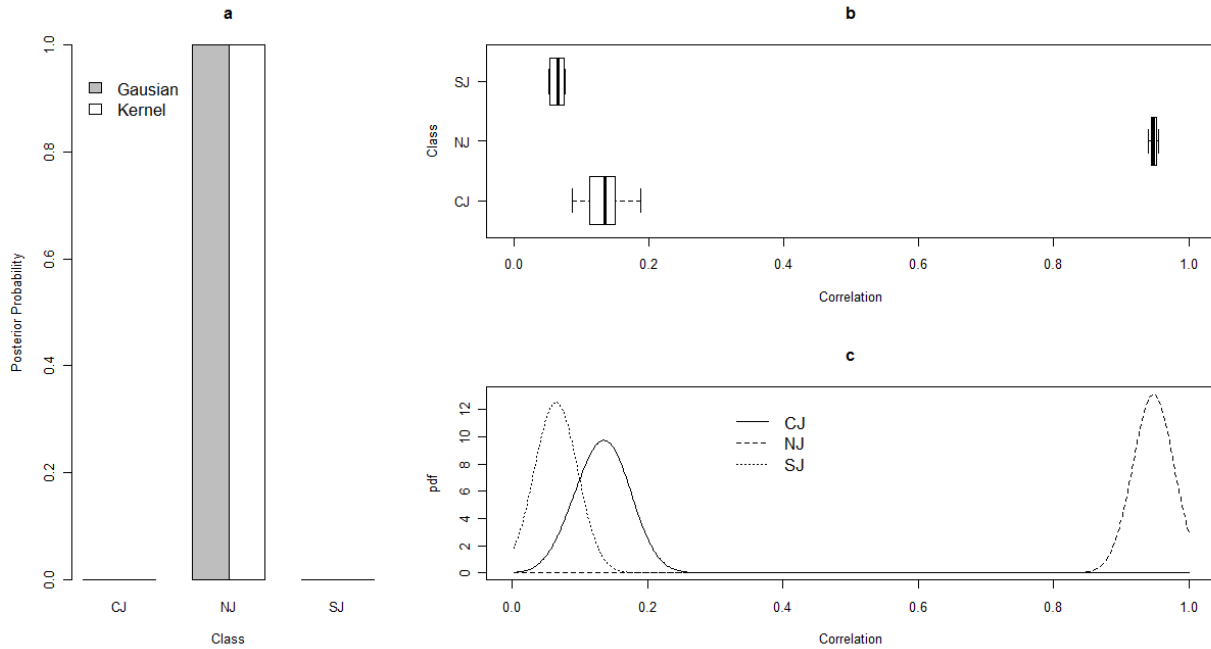


Figure 98. TFA classification results for LIBS spectral data from jacket residue deposited by a NJ class projectile passing through a steel plate: (a) posterior probabilities calculated by Gaussian and kernel probability density functions, (b) boxplot of correlation coefficient distributions for each projectile class and (c) kernel probability density distribution functions for each projectile class.

Correct Classification rates

A total of 23 bullet holes (15 CJ, 4 MJ and 4 NJ) were analyzed and the bullet class assigned by the highest calculated posterior probability. The posterior probabilities were calculated by two methods: (1) at $r=1$ for classes with $|1-r_M|/r_{MAD} < 5$ and (2) at $r=r_M$ determined for the class having the largest median correlation. The class assignments were the same for posterior probabilities calculated from an assumed Gaussian probability distributions or from the kernel distributions calculated by equation (6) with $h=0.03$ for all classes.

The classification results based on $r=1$ for classes with $|1-r_M|/r_{MAD} < 5$ are given in Table 16. This method is very conservative, resulting in 40%, 0% and 100% classification for the CJ, MJ and NJ classes respectively; however, for those samples that were classified, the correct classification rate was 100%. Samples were not classified if all classes failed to meet the criterion given by $|1-r_M|/r_{MAD} < 5$. For example, in nine of the 15 data sets from bullet holes formed by CJ bullets, the median correlation, r_M , for all classes failed to meet the criterion

$|1-r_M|/r_{MAD} < 5$, and the bullet holes were not classified. The data for the remaining six bullet holes met the criterion for classification and the bullets producing the holes were correctly classified. None of the data from bullet holes formed by MJ bullets met the classification criterion; however, all of the data from bullet holes formed by NJ bullets met the classification criterion and the bullets making the holes were correctly classified. It is interesting to note that the percent of the samples classified by this method is highest for the NJ bullets which are composed of lead, a soft metal that would be expected to leave significant amounts of trace residue. Similarly, the bullets with the jackets composed of harder materials gave lower percent classifications and would be expected to transfer smaller amounts of residue to the steel plate.

Table 16. Classification results for Gaussian and kernel probability distribution function estimations with posterior probabilities calculated at $r=1$ for classes with $|1-r_M|/r_{MAD} < 5$.

Test Class	Assigned Class			Not Classified	Total	% Classified	% Correct Classification
	CJ	MJ	NJ				
CJ	6	0	0	9	15	40	100
MJ	0	0	0	4	4	0	NA
NJ	0	0	4	0	4	100	100
Total	6	0	4	13	23	43	100

The criteria for classification based on posterior probabilities calculated at r_M for the one class having the largest median correlation are far less conservative. The only restrictions imposed are that r_M for a class exceed either an experimentally established cutoff r , or the r_M differ from $r_{M,blank}$ at a pre-determined significance level. In the data examined here, $r_{M,blank}$ was determined by TFA of a set of LIBS spectra collected from the steel plates used in the experiments, see Figure 96. The comparisons between r_M and $r_{M,blank}$ for each class was made by the Wilcoxon rank sum test at a significance level of 0.05, and in each case, the distributions were found to be significantly different from the blank. Therefore, none of the distributions were exempted from the posterior probability calculations. Classification results are given in Table 17; none of the samples were unclassified and the overall correct classification rate was 87%.

Table 17. Classification results for Gaussian and kernel probability distribution function estimations with posterior probabilities calculated at the highest median r in each test as calculated for all bullet classes.

Test Class	Assigned Class			Total	% Correct Classification
	CJ	MJ	NJ		
CJ	13	0	2	15	87
MJ	1	3	0	4	75
NJ	0	0	4	4	100
Total	14	3	6	23	87

Two of the 15 CJ bullets were incorrectly classified. Both of these bullets were “hollow point” bullets, which undergo larger amounts of fragmentation on impact. The jacketing material on each of the CJ and MJ bullets surrounds a lead core. Examination of the LIBS spectra from

the “misclassified” bullet holes revealed significant lead lines in several of the spectra, which led to the misclassification as NJ (lead) bullets for two of the highly fragmenting hollow point projectiles. On this basis, while the classification was incorrect (strictly speaking), the analysis provided important insight into the behavior of the bullet.

COLLABORATIONS WITH DOD AND NATIONAL LABORATORIES

- Drs. Andrzej Mizolek, Kevin Mc Nesby, and co-workers (Army Research Laboratory, Aberdeen Proving Ground, MD)
- Dr. Richard E. Russo and co-workers (Lawrence Berkeley National Laboratory, Berkeley, CA)

COLLABORATIONS WITH COMPANIES

- Dr. Pat Treado (ChemImage Inc., Pittsburgh, PA)
- Dr. Jason Eichenholtz (Ocean Optics, Winter Park, FL)
- Dr. Steven Grantham (NIST, Gaithersburg, MD)
- Dr. Richard E. Russo (Applied Spectra, Inc., Fremont, CA)
- Dr. Philip Efthimion (Envimetrics, NJ)

FACULTY

Martin Richardson

Pegasus Professor and University Trustee Chair, Northrop Grumman Prof of X-ray Photonics; Prof of Optics; Director Townes Laser Institute

Michael E. Sigman

Associate Professor of Chemistry

PUBLICATIONS

"Improvement of the sensitivity for the measurement of copper concentrations in soil by Microwave-Assisted Laser-Induced Breakdown Spectroscopy"; Y. Liu, B. Bousquet, M. Baudelet, and M. C. Richardson; Spectrochimica Acta Part B-Atomic Spectroscopy 73 pp. 89-92

"Moisture Measurement Using LIBS"; Y. Liu, M. Baudelet, and M. C. Richardson; G.I.T. Laboratory Journal Europe (June 2012); <http://www.laboratory-journal.com/science/chemistry-physics/moisture-measurement-using-libs>

"Discriminant analysis in the presence of interferences: Combined application of target factor analysis and a Bayesian soft-classifier"; C. N. Rinke, M. R. Williams, C. G. Brown, M. Baudelet, M. C. Richardson, and M. E. Sigman; Analytica Chimica Acta 753 (2012) 19 – 26

"Correlation between laser-induced breakdown spectroscopy signal and moisture content"; Y. Liu, L. Gigant, M. Baudelet, and M. C. Richardson; Spectrochimica Acta Part B-Atomic Spectroscopy 73 pp.71-74 (2012)

"Microwave-Assisted LIBS: Towards a New Tool for Trace Element Detection and Molecular Plasma Spectrochemistry"; M. Baudelet, Y. Liu, and M. Richardson; Laser Applications to

Chemical, Security and Environmental Analysis, OSA Technical Digest Series (CD) (Optical Society of America, 2010), paper LWC3P

"Tm-Fiber 2 μm Laser for Laser-Induced Plasma Spectroscopy of Organic and Biological Materials"; M. Baudelet, C. Willis, L. Shah, and M. Richardson; in Laser Applications to Chemical, Security and Environmental Analysis, OSA Technical Digest Series (CD) (Optical Society of America, 2010), paper LWC2.

"Nd:YAG-CO2 Double-Pulse Laser Induced Breakdown Spectroscopy for Explosive Detection"; M. Weidman, M. Baudelet, M. E. Sigman, P. J. Dagdigan, and M. Richardson; in Laser Applications to Chemical, Security and Environmental Analysis, OSA Technical Digest Series (CD) (Optical Society of America, 2010), paper LWD3

"Optics and Lasers"; Andy Whitehouse, Ken Kaufman, Matthieu Baudelet and Rob Morris; Discussion hosted by Spectroscopy Online (10/08, 2010)

<http://spectroscopyonline.findanalyticchem.com/spectroscopy/article/articleDetail.jsp?id=690503>

"Laser-Induced Breakdown Spectroscopy of Copper with a 2 μm Thulium Fiber Laser"; M. Baudelet, C. Willis, L. Shah, and M. Richardson; Optics Express vol. 18, 7905-7910

"Elemental Analysis by Microwave-Assisted Laser-Induced Breakdown Spectroscopy: Evaluation on Ceramics"; Y. Liu, M. Baudelet and M. Richardson; J. Anal. At. Spectrom., 2010, 25, pp. 1316–1323

"Thermodynamic and spectroscopic properties of Nd:YAG-CO2 Double-Pulse Laser-induced Iron Plasmas "; Matthew Weidman, Santiago Palanco, Matthieu Baudelet, Martin Richardson; Spectrochimica Acta Part B: Atomic Spectroscopy, Volume 64, Issue 10, October 2009, Pages 961–967

"Self-channeling of Femtosecond Laser Pulses for Rapid and Efficient Standoff Detection of Energetic Materials"; Matthieu Baudelet, Martin Richardson, Michael Sigman; IEEE Conference on Technologies for Homeland Security, 2009, IEEE (Waltham, MA, USA), pages 472-476

"Nd:YAG-CO2 Dual-Pulse Laser-Induced Breakdown Spectroscopy of Organic Films"; Matthew Weidman, Matthieu Baudelet, Santiago Palanco, Michael Sigman, Paul J Dagdigan, Martin C. Richardson; Optics Express, Vol. 18, No. 1, pp.259 (2010)

"Atmosphere Issues in Detection of Explosives and Organic Residues" ; Christopher G. Brown, Matthieu Baudelet, Candice Bridge, Matthew Fisher, Michael Sigman, Paul J. Dagdigan, Martin C. Richardson; Proceedings of SPIE, volume 7304, pages 73041D-1 (2009)

Molecular signal as a signature for detection of energetic materials in filament-induced breakdown spectroscopy ; Matthew Weidman, Matthieu Baudelet, S. Fischer, Candice Bridge, Christopher G. Brown, Michael Sigman, Paul J Dagdigan, Martin C. Richardson, " Proceedings of SPIE, volume 7304, pages 73041G-1 (2009)

"Stand-off detection of organic samples using filament-induced breakdown spectroscopy"; James Martin, Matthieu Baudelet, Matthew Weidman, Matthew Fisher, Candice Bridge, Christopher G. Brown, Michael Sigman, Paul J Dagdigian, Martin C. Richardson; Proceedings of SPIE, volume 7306, pages 73060Z-1 (2009)

Remote Femtosecond Laser Induced Breakdown Spectroscopy (LIBS) in a Standoff Detection Regime"; Christopher G. Brown, Robert Bernath, Matthew Fisher, Martin C. Richardson, Michael Sigman, R.A. Walters, A Mizolek, H. Bereket, Lewis E. Johnson; Proceedings of SPIE. SPIE Defense and Security Symposium , SPIE (Orlando, FL, USA, 2006), volume 6219, pages B1-B7, May 2006

"Femtosecond LIBS at 300 kHz "; Matthew Fisher, Martin Richardson, L. Shah and M. E. Fermann; Laser Induced Breakdown Spectroscopy 2006 (Montreal, Canada, 2006) 5-8 September 2006

"Double pulse UV laser induced breakdown spectroscopy of stainless steel"; Ahmed Khalil, Martin C. Richardson, Cleon Barnett, Lewis E. Johnson; Journal of Applied Spectroscopy, volume 73, number 5, pages 654-660

"Control of Filamentation for Enhancing Remote Detection with Laser Induced Breakdown Spectroscopy"; Matthew Fisher, Craig W. Siders, Eric Johnson, Oleksiy Andrusyak, Christopher G. Brown, Martin C. Richardson; Proceedings of SPIE Defense and Security Symposium , SPIE (Orlando, FL, USA, 2006), volume 6219, number 07, pages 1-5, May 2006

PRESENTATIONS

6. Matthew Weidman, Khan Lim, Nicholas Barbieri, Erik McKee, Magali Durand, Matthieu Baudelet, Martin Richardson, "Quantitative studies of filament interaction with matter for spectroscopic applications", seminar at GAP Biophotonics group, University of Geneva; Geneva, Switzerland; 11/30, 2012. *Seminar*
7. Yuan Liu, Matthew Weidman, Christopher Brown, Corey Butler, Marie Vangheluwe, Shima Fardad, Andreas Knebl, Lionel Gigant, Martin Richardson, Matthieu Baudelet, "New Perspectives in Laser Spectroscopy as a Science for Sensing, Monitoring and Diagnostics", seminar at Center of Excellence "Laser & Photonique en Aquitaine", University of Bordeaux; Bordeaux, France; 11/13, 2012. *Seminar*
8. Martin Richardson, Matthieu Baudelet, Michael Sigman and Andrzej Mizolek, "Stand-off chemical and biological sensing", Frontiers in Optics 2012, Laser Science XXVIII; Rochester, NY, USA; 10/14-18, 2012; *Invited talk*
9. Martin Richardson, Matthieu Baudelet, Michael Sigman and Andrzej Mizolek, "Stand-off LIBS – The status today and the future", LIBS 2012; Luxor, Egypt; 09/29 – 10/04, 2012; *Invited talk*
10. Yuan Liu, Matthieu Baudelet, Martin Richardson, "Microwave-assisted LIBS: Signal enhancement and beyond", SciX 2012; Kansas City, MO, USA; 10/02, 2012. *Invited talk*

11. Matthieu Baudelet, “Fifty years of LIBS and no limits for analysis”, SciX 2012; Kansas City, MO, USA; 10/02, 2012. *Invited talk*
12. Yuan Liu, Matthieu Baudelet, Martin Richardson, “Laser-Induced Breakdown Spectroscopy for Moisture Monitoring in Food”; Pittcon 2012, Orlando, FL, USA; 03/11, 2012
13. Yuan Liu, Mark Koehler, Matthieu Baudelet, Martin Richardson, “Fusion of infrared and Raman spectroscopy for carotenoid analysis”; Pittcon 2012, Orlando, FL, USA; 03/11, 2012.
14. Yuan Liu, Matthieu Baudelet, Martin Richardson, “Advanced LIBS Methodology for Food and Environment Monitoring”; 2012 Winter Conference on Plasma Spectrochemistry; Tucson, AZ, USA; 01/10, 2012. *Poster presentation*
15. Cheonha Jeon, Matthieu Baudelet, Martin Richardson, “Fundamental Time-Resolved Mass Spectrometry of Laser-Induced Plasmas for Organic Analysis”; 2012 Winter Conference on Plasma Spectrochemistry; Tucson, AZ, USA; 01/10, 2012.
16. Matthieu Baudelet, Michael Sigman, Martin Richardson, “Laser-induced breakdown spectroscopy in complex situations”; FACSS 2011; Reno, NV, USA; 10/06, 2011. *Invited talk*
17. Yuan Liu, Matthieu Baudelet, Martin Richardson, Richard Russo “Advanced LIBS Methodologies for Food and Environment Monitoring”; Euro-Mediterranean Symposium on Laser-Induced Breakdown Spectroscopy 2011; Izmir, Turkey; 09/13, 2011
18. Matthieu Baudelet, Martin Richardson, Michael Sigman, “Laser spectroscopy and sensing at the Townes Laser Institute”; ATLANTIS-MILMI Summer School; Orlando, FL, USA; 07/21, 2011. *Invited talk*
19. Yuan Liu, Lionel Gigant, Matthieu Baudelet, Martin Richardson, “Combination of LIBS and Raman for Food Quality Monitoring”; North-American Symposium on Laser-Induced Breakdown Spectroscopy 2011; Clearwater, FL, USA; 07/20, 2011.
20. Yuan Liu, Matthieu Baudelet, Martin Richardson, “Laser Material Analysis using Calibration Free Laser-Induced Breakdown Spectroscopy”; North-American Symposium on Laser-Induced Breakdown Spectroscopy 2011; Clearwater, FL, USA; 07/19, 2011. *Poster presentation*
21. Matthew Weidman, Matthieu Baudelet, Martin Richardson, “Time-Resolved Goniometric Measurement of the Filament-Induced Plasma Emission for Stand-Off LIBS Applications”; North-American Symposium on Laser-Induced Breakdown Spectroscopy 2011; Clearwater, FL, USA; 07/19, 2011. *Poster presentation*
22. Santiago Palanco, Jose Ramos-Barrado, Matthew Weidman, Matthieu Baudelet, Martin Richardson, “Correlation Between Spectral Emission and Nanoparticle Generation During Nano- and Femtosecond Laser-induced Breakdown”; North-American Symposium on Laser-Induced Breakdown Spectroscopy 2011; Clearwater, FL, USA; 07/18, 2011.
23. Caitlin Rinke, Christopher Brown, Martin Richardson, Matthieu Baudelet, Michael Sigman, “LIBS signature recognition of trace materials in complex background

environments"; North-American Symposium on Laser-Induced Breakdown Spectroscopy 2011; Clearwater, FL, USA; 07/18, 2011. *Invited talk*

24. Yuan Liu, Lionel Gigant, Matthieu Baudelet, Martin C. Richardson, "Combination of LIBS and Raman for food quality monitoring"; SPIE Defense, Security, Sensing; Orlando, FL, USA; 04/26, 2011.
25. Khan Lim, Jason M. Eichenholz, Matthieu Baudelet, Martin C. Richardson, "Far-UV LIBS for biological and organic samples"; SPIE Defense, Security, Sensing; Orlando, FL, USA; 04/25, 2011.
26. Khan Lim, Yuan Liu, Matthieu Baudelet, Evgeni Slobodtchikov, Peter Moulton, Andrzej W. Mizolek, Martin C. Richardson, "New generation of compact femtosecond system for laser-based detection and identification of biological materials"; SPIE Defense, Security, Sensing; Orlando, FL, USA; 04/25, 2011.
27. Matthew Weidman, Matthieu Baudelet, Christina C. C. Willis, Lawrence Shah, Martin C. Richardson, "Novel laser sources for LIBS: From fiber lasers, self-channeled laser to dual pulse configuration,"; Pacificchem 2010; Honolulu, HI, USA; 12/18, 2010.
28. Yuan Liu, Matthieu Baudelet, Martin C. Richardson, "Microwave-assisted LIBS: Extending the laser induced plasma lifetime for trace detection" Pacificchem 2010; Honolulu, HI, USA; 12/18, 2010. *Poster presentation*
29. Matthew Weidman, Matthieu Baudelet, Martin C. Richardson, Paul J Dagdigian, "Spatial and temporal spectral imaging of self-channeled laser-induced breakdown spectroscopy on carbon-based samples: Molecular chemistry in air"; Pacificchem 2010; Honolulu, HI, USA; 12/18, 2010. *Poster presentation*
30. Martin Richardson, Michael Sigman, Matthieu Baudelet, "Standoff Detection of Trace Radio-Nuclides using New Laser Spectroscopy Techniques"; NNSA, University and Industry Technical Interchange (UITI2010) Review Meeting; Knoxville, TN, USA; 12/08, 2010
31. Matthew Weidman, Matthew Fisher, Khan Lim, Christopher Brown, Caitlin Rinke, Matthieu Baudelet, Michael Sigman, Martin Richardson, "Advanced LIBS Modalities for Stand-Off Detection of Explosive and Biological Threats"; 27th Army Science Conference; Orlando, FL, USA; 11/30, 2010.
32. Caitlin Rinke, Christopher G. Brown, Matthieu Baudelet, Martin C. Richardson, Michael Sigman, "A New Paradigm for Substrate Independent Discrimination of Organic and Explosive Materials by Target Factor Analysis of Molecular Optical Signatures"; 2010 Chemical and Biological Defense Science and Technology Conference; Orlando, FL, USA; 11/16, 2010. *Poster Presentation*
33. Yuan Liu, Matthieu Baudelet, Martin C. Richardson, "Compact Laser-based Spectroscopic Systems for Biological Analysis"; 2010 Chemical and Biological Defense Science and Technology Conference; Orlando, FL, USA; 11/16, 2010. *Poster Presentation*
34. Matthew Weidman, Matthieu Baudelet, Martin C. Richardson, "Stand-off Laser Sensing for Chemical and Biological Traces Detection"; 2010 Chemical and Biological Defense Science and Technology Conference; Orlando, FL, USA; 11/16, 2010. *Poster*

Presentation

35. Danielle Simmons, Nathan Bodnar, Matthieu Baudelet, Martin Richardson, "Fourier Transform Infrared Spectroscopy"; Symposium on undergraduate research, Division of Laser Science of A.P.S - LS XXVI; Rochester, NY, USA; 10/25, 2010. *Poster Presentation*
36. Khan Lim, Matthieu Baudelet, Jason Eichenholz, Martin C. Richardson, "Far-UV LIBS for Biological and Organic Samples"; 6th International Conference on Laser-Induced Breakdown Spectroscopy; Memphis, TN, USA; 09/16, 2010.
37. Yuan Liu, Matthieu Baudelet, Martin C. Richardson, "Elemental Analysis on Ceramic and Soil Samples Using Microwave-Assisted Laser-Induced Breakdown Spectroscopy"; 6th International Conference on Laser-Induced Breakdown Spectroscopy; Memphis, TN, USA; 09/16, 2010. *Poster Presentation*
38. Matthew Weidman, Matthieu Baudelet, Paul J Dagdigan, Martin C. Richardson, "Temporally and Spatially Resolved Filament Induced Breakdown Spectroscopy of Carbon Based Samples"; 6th International Conference on Laser-Induced Breakdown Spectroscopy; Memphis, TN, USA; 09/15, 2010. *Poster Presentation*
39. Khan Lim, Yuan Liu, Matthieu Baudelet, Evgeni Slobodtchikov, Peter Moulton, A Mizolek, Martin C. Richardson, "LIBS of Biological Materials with a Compact Femtosecond System"; 6th International Conference on Laser-Induced Breakdown Spectroscopy; Memphis, TN, USA; 09/15, 2010. *Poster Presentation*
40. Yuan Liu, Matthieu Baudelet, Paul J Dagdigan, Martin C. Richardson, "Molecular Emission Enhancement from Microwave-Assisted Laser-Induced Breakdown Spectroscopy"; 6th International Conference on Laser-Induced Breakdown Spectroscopy; Memphis, TN, USA; 09/15, 2010. *Poster Presentation*
41. Christopher G. Brown, Reuvani Devi Kamtaprasad, Matthieu Baudelet, Michael Sigman, Martin C. Richardson, "Stoichiometric Study of Organic Mass Limited Droplets"; 6th International Conference on Laser-Induced Breakdown Spectroscopy; Memphis, TN, USA; 09/15, 2010. *Poster Presentation*
42. Martin C. Richardson, Matthieu Baudelet, Michael Sigman, "Fundamental Considerations for an Efficient Application of LIBS in Forensics and Security"; 6th International Conference on Laser-Induced Breakdown Spectroscopy; Memphis, TN, USA; 09/14, 2010. *Invited paper*
43. Matthew Weidman, Matthieu Baudelet, Michael Sigman, Martin C. Richardson, "Nd:YAG-CO₂ double-pulse laser-induced breakdown spectroscopy for explosive residues detection"; SPIE Defense, Security, Sensing; Orlando, FL, USA; 04/07, 2010.
44. Matthew Weidman, Matthieu Baudelet, Paul J Dagdigan, Michael Sigman, Martin C. Richardson, "Self-channeled laser-induced breakdown spectroscopy for detection of organic compounds in atmosphere via their molecular signature"; SPIE Defense, Security, Sensing; Orlando, FL, USA; 04/07, 2010.
45. Yuan Liu, Matthieu Baudelet, Martin C. Richardson, "Microwave-assisted laser-induced breakdown spectroscopy for trace detection in soil and food"; SPIE Defense, Security, Sensing; Orlando, FL, USA; 04/06, 2010.

46. Matthieu Baudelet, Christina C. C. Willis, Lawrence Shah, Martin Richardson, "Mid-IR Tm-fiber laser for laser-induced plasma spectroscopy of organic and biological materials"; SPIE Defense, Security, Sensing; Orlando, FL, USA; 04/05, 2010.
47. Yuan Liu, Matthieu Baudelet, Martin C. Richardson, "Trace Detection in Ceramics, Organic and Biological Samples by Microwave-assisted Laser-induced Plasma Spectroscopy"; 2010 Pittsburgh Conference on Analytical Chemistry and Applied Spectroscopy; Orlando, FL, USA; 03/04, 2010.
48. Matthieu Baudelet, Christina C. Willis, Pankaj Kadwani, Lawrence Shah, Martin C. Richardson, "Laser-induced Breakdown Spectroscopy of Organic Materials with a Mid-IR Thulium-fiber-laser Nanosecond Pulse at 2 μm "; 2010 Pittsburgh Conference on Analytical Chemistry and Applied Spectroscopy; Orlando, FL, USA; 03/04, 2010. *Poster presentation*
49. Caitlin Rinke, Christopher G. Brown, Douglas Clark, Matthieu Baudelet, Martin C. Richardson, Michael Sigman, "Substrate Independent Discrimination of Organic and Explosive Materials Via Target Factor Analysis of Their Molecular Optical Signature"; 2010 Pittsburgh Conference on Analytical Chemistry and Applied Spectroscopy; Orlando, FL, USA; 03/04, 2010. *Poster presentation*
50. Matthew Weidman, Matthieu Baudelet, Michael Sigman, Paul J Dagdigian, Martin C. Richardson, "Nd:YAG-CO₂ Double-Pulse Laser Induced Breakdown Spectroscopy for Explosive Detection"; OSA Laser Application to Chemical Security and Environmental Analysis; San Diego, CA, USA; 02/03, 2010.
51. Matthieu Baudelet, Yuan Liu, Martin C. Richardson, "Microwave-Assisted LIBS: Towards a New Tool for Trace Element Detection and Molecular Plasma Spectrochemistry"; OSA Laser Application to Chemical Security and Environmental Analysis; San Diego, CA, USA; 02/03, 2010.
52. Matthieu Baudelet, Christina C. C. Willis, Lawrence Shah, Martin C. Richardson, "Tm-Fiber 2 μm Laser for Laser-Induced Plasma Spectroscopy of Organic and Biological Materials"; OSA Laser Application to Chemical Security and Environmental Analysis; San Diego, CA, USA; 02/03, 2010.
53. Matthieu Baudelet, Yuan Liu, Martin Richardson, "Trace Detection in Ceramics, Organics, and Biological Samples by Microwave-Assisted Laser-Induced Breakdown Spectrometry"; 2010 Winter Conference on Plasma Spectrochemistry; Fort Myers, FL, USA; 01/05, 2010.
54. Matthieu Baudelet, Yuan Liu, Paul J. Dagdigian, Martin Richardson, "Molecular Emission Enhancement From Microwave-Assisted Laser-Induced Breakdown Spectroscopy on Alumina"; 2010 Winter Conference on Plasma Spectrochemistry; Fort Myers, FL, USA; 01/05, 2010. *Poster presentation*.
55. Matthew Weidman, Matthieu Baudelet, Paul J. Dagdigian, Martin Richardson, "Spatial and temporal spectral imaging of self-channeled laser-induced breakdown spectroscopy on carbon-based samples: Thermochemistry leading to molecular formation in air"; 2010 Winter Conference on Plasma Spectrochemistry; Fort Myers, FL, USA; 01/05, 2010. *Poster presentation*.

56. Matthieu Baudelet, Matthew Weidman, Christopher G. Brown, Michael Sigman, Paul J. Dagdigian, Martin Richardson, "Enhancement of LIBS signal from metallic, ceramic and organic samples by a Nd:YAG-CO₂ double-pulse scheme"; North-American Symposium on Laser-Induced Breakdown Spectroscopy 2009; New Orleans, LA, USA; 07/15, 2009.

57. Martin Richardson, Dennis Alexander, Matthieu Baudelet, Paul J. Dagdigian, Lewis E. Johnson, Samuel S. Mao, Michael Sigman, "Femtosecond LIBS – Light at the end of the end of the channel: The ARO MURI program on femtosecond LIBS"; North-American Symposium on Laser-Induced Breakdown Spectroscopy 2009; New Orleans, LA, USA; 07/15, 2009.

58. Matthieu Baudelet, Christina Willis Lawrence Shah, Martin Richardson, "Laser-induced breakdown spectroscopy of organic materials with a mid-IR Thulium fiber-laser nanosecond pulse at 2 μ m"; North-American Symposium on Laser-Induced Breakdown Spectroscopy 2009; New Orleans, LA, USA; 07/14, 2009. *Poster presentation*.

59. Yuan Liu, Nicholas Barbieri, Matthew Weidman, Matthieu Baudelet, Martin Richardson, "Plasma heating by microwave radiation: thermodynamic processes and analytical applications"; North-American Symposium on Laser-Induced Breakdown Spectroscopy 2009; New Orleans, LA, USA; 07/14, 2009. *Poster presentation*.

60. Matthew Weidman, Matthieu Baudelet, Christopher G. Brown, Michael Sigman, Paul J. Dagdigian, Martin C. Richardson, "Self-channeled femtosecond LIBS: Molecular processes between the atmosphere and the plasma and their analytical use for detection of organic samples"; North-American Symposium on Laser-Induced Breakdown Spectroscopy 2009; New Orleans, LA, USA; 07/14, 2009. *Poster presentation*.

61. Christopher G. Brown, Caitlin Rinke, Matthieu Baudelet, Martin C. Richardson, Michael Sigman, "Substrate Independent Identification of Organic Analytes with LIBS"; North-American Symposium on Laser-Induced Breakdown Spectroscopy 2009; New Orleans, LA, USA; 07/14 2009. *Poster presentation*.

62. Martin C. Richardson, Matthieu Baudelet, Michael Sigman, Matthew Weidman, Christopher G. Brown, "Ultra-fast lasers for stand-off detection", Ultrashort Pulse Laser Workshop, Directed Energy Professional Society; Newton, MA, USA; 06/29,2009.

63. Martin C. Richardson, Michael Sigman, Matthieu Baudelet, "Self-channeling of Femtosecond Laser Pulses as an Efficient and Rapid Tool for standoff detection of energetic materials", IEEE 2009 International Conference on Technologies for Homeland Security; Waltham, MA, USA; 05/12, 2009.

64. Christopher G. Brown, Matthieu Baudelet, Candice Bridge, Matthew Fisher, Michael Sigman, Martin Richardson, Paul J Dagdigian, "Atmosphere issues in detection of explosives and organic residues"; SPIE Defense, Security, and Sensing; Orlando, FL, USA; 04/16, 2009.

65. Matthieu Baudelet, Matthew Weidman, Matthew Fisher, Christopher G. Brown, Michael Sigman, Martin Richardson, Paul J Dagdigian, "Molecular signal as a signature for detection of energetic materials in filament-induced breakdown spectroscopy"; SPIE Defense, Security, and Sensing; Orlando, FL, USA; 04/16, 2009.

66. James Martin, Matthieu Baudelet, Matthew Weidman, Matthew Fisher, Candice Bridge, Christopher G. Brown, Michael Sigman, Martin C. Richardson, Paul J Dagdigian, "Stand-off detection of organic samples using filament-induced breakdown spectroscopy"; SPIE Defense, Security, and Sensing; Orlando, FL, USA; 04/15, 2009.
67. Matthieu Baudelet, Christopher G. Brown, Candice Bridge, Matthew Weidman, Matthew Fisher, Michael Sigman, Martin C. Richardson, Paul J Dagdigian, "Influence of atmosphere and laser parameters on LIBS detection and analysis of explosives and organic thin films"; SPIE Defense, Security, and Sensing; Orlando, FL, USA; 04/13, 2009.
68. Matthieu Baudelet, Matthew Fisher, Matthew Weidman, Candice Bridge, Christopher G. Brown, Michael Sigman, Martin C. Richardson, Paul J Dagdigian, "LIBS Detection of Explosives with Self-Channeled Laser Light"; GOMACTech Conference; Orlando, FL, USA; 03/19, 2009.
69. Christopher G. Brown, Matthieu Baudelet, Candice Bridge, Matthew Fisher, Michael Sigman, Martin Richardson, Paul J Dagdigian, "Femtosecond LIBS: a better regime to analyze organic samples"; Southeast Ultrafast Conference; Orlando, FL, USA; 01/16, 2009. *Poster presentation.*
70. Matthieu Baudelet, Matthew Weidman, Matthew Fisher, Candice Bridge, Christopher G. Brown, Michael Sigman, Martin C. Richardson, Paul J Dagdigian, "Filament-Induced Breakdown Spectroscopy on Organic Thin Films: Towards an Efficient Detection of Energetic Materials"; Southeast Ultrafast Conference; Orlando, FL, USA; 01/16, 2009. *Poster presentation.*
71. James Martin, Matthew Weidman, Christopher Brown, Candice Bridge, Matthieu Baudelet, Martin Richardson, "Light Detection for Laser Induced Breakdown Spectroscopy"; Symposium on undergraduate research, Division of Laser Science of A.P.S; Rochester, NY, USA; 10/28, 2008. *Poster presentation.*
72. James Martin, Matthew Weidman, Matthieu Baudelet, Matthew Fisher, Martin C. Richardson, Paul J. Dagdigian, "Towards an efficient remote LIBS detection of organic materials"; 5th International Conference on Laser-Induced Breakdown Spectroscopy; Berlin, Germany; 09/25, 2008. *Poster presentation.*
73. Christopher G. Brown, Candice Bridge, Matthew Fisher, Matthieu Baudelet, Michael Sigman, Martin Richardson, Paul J Dagdigian, "Comparison of nanosecond and femtosecond Laser Regimes for LIBS Analysis of Organic Thin Films"; 5th International Conference on Laser-Induced Breakdown Spectroscopy; Berlin, Germany; 09/24, 2008. *Poster presentation.*
74. Matthew Weidman, Santiago Palanco, Matthieu Baudelet, Michael Sigman, Martin Richardson, "Thermodynamic properties of Nd:YAG-CO₂ Double-Pulse Laser-Induced Plasma: Applications Under Stand-Off Conditions,"; 5th International Conference on Laser-Induced Breakdown Spectroscopy; Berlin, Germany; 09/24, 2008. *Poster presentation.*
75. Matthew Weidman, Matthieu Baudelet, Matthew Fisher, Candice Bridge, Christopher G. Brown, Michael Sigman, Martin C. Richardson, Paul J Dagdigian, "Filament-Induced Breakdown Spectroscopy on Organic Thin Films: Towards an

Efficient Detection of Energetic Materials"; 5th International Conference on Laser-Induced Breakdown Spectroscopy; Berlin, Germany; 09/24, 2008.

76. *"Laser-Induced Breakdown Spectroscopy and Related Stand-off Detection"*; Santiago Palanco, Martin Richardson; Laser Application to Chemical Security and Environmental Analysis, OSA (St. Petersburg, FL, USA) 17-20 March 2008

77. *"Thermodynamic Properties of a Nd:YAG-CO₂ Double Pulse Laser-Induced Plasma and Its Applications Under Stand-off Conditions"*; Matthew Weidman, Santiago Palanco, Martin Richardson; Laser Application to Chemical Security and Environmental Analysis, OSA (St. Petersburg, FL, USA) 17-20 March 2008

78. *"Experimental and Kinetic Modeling Study of the Emission Spectrum from Laser-Induced Plasma in Air"*; Paul Dagdigian, Valeri Babushok, Christopher Brown, Matthew Fisher, Santiago Palanco, Martin Richardson; North American Symposium on Laser Induced Breakdown Spectroscopy 2007 (New Orleans, LA, USA, 2007) 8-10 October 2007

79. *"Modeling of the Development of Carbon and Polyethylene LIBS Plasmas- Study of Chemical Processing in the Plume"*; Christopher Brown, Valeri Babushok, Paul Dagdigian, Santiago Palanco, Martin Richardson; North American Symposium on Laser Induced Breakdown Spectroscopy 2007 (New Orleans, LA, USA, 2007) 8-10 October 2007

80. *"Stand-off Detection Technologies"*; Santiago Palanco; North American Symposium on Laser Induced Breakdown Spectroscopy 2007 (New Orleans, LA, USA, 2007) 8-10 October 2007 Invited paper.

81. *"Use of a Hyper Michelson Interferometer for Multiple Pulse Femtosecond Laser-Induced Breakdown Spectroscopy in the Self-Channeled Mode"*; Matthew Fisher, Santiago Palanco, Martin Richardson; North American Symposium on Laser Induced Breakdown Spectroscopy 2007 (New Orleans, LA, USA, 2007) 8-10 October 2007

82. *"A Spectroscopic Analysis Study of Graphite Using LIBS and Semiempirical Calculations"*; Ahmed Khalil, M. Ibrahim, Martin Richardson, Lewis Johnson; Laser Induced Breakdown Spectroscopy 2006 (Montreal, Canada, 2006) 5-8 September 2006

83. *"Control of Filamentation for Enhancing Remote Detection with Laser Induced Breakdown Spectroscopy "*; Matthew Fisher, Craig Siders, Eric Johnson, Oleksiy Andrusyak, Christopher Brown, Martin Richardson; SPIE Defense and Security Symposium , SPIE (Orlando, FL, USA, 2006) May 2006

84. *"Femtosecond Interaction Studies for Stand-off LIBS"*; Martin Richardson, Christopher Brown, Matthew Fisher, Robert Bernath; Laser Induced Breakdown Spectroscopy 2006 (Montreal, PQ, Canada) 5-8 September 2006

85. *"New plasma regimes for stand-off LIBS"*; Martin Richardson, Christopher Brown, Matthew Fisher, Robert Bernath, Simi George, Michael Sigman, Cleon Barnett, H. Bereket, Lewis Johnson, A Mizolek, Frank DeLucia; Laser Application to Chemical Security and Environmental Analysis, OSA (Incline Village, UT, USA) (2006)

86. *"Remote Femtosecond Laser Induced Breakdown Spectroscopy (LIBS) in a Standoff Detection Regime."*; Christopher Brown, Robert Bernath, Matthew Fisher, Martin Richardson, Michael Sigman, R.A. Walters, A Mizolek, H. Bereket, Lewis Johnson;

SPIE Defense and Security Symposium , SPIE (Orlando, FL, USA) May 2006

87. "UV-Visible Spectra of Double pulse LIBS in Metals"; Ahmed Khalil, Martin Richardson, C. Barnett, Lewis Johnson; Laser Induced Breakdown Spectroscopy 2006 (Montreal, Canada, 2006) 5-8 September 2006

PATENTS AND IP GENERATED

M. C. Richardson, Y. Liu, M. Baudelet, "LIBS Moisture Monitoring System." (2011) *Patent disclosure*

UNDERGRADUATE STUDENTS INVOLVED IN THE PROJECT

Lionel Gigant, France, Physics

Danielle Simmons, US, Physics

Mark Koehler, US, Physics

James Martin, US, Physics

Alex Sincore, US, Physics

Dorian Gomez, France

Matthew Chun, US, High School

GRADUATE STUDENTS INVOLVED IN THE PROJECT

Matthew Fisher, US, Optics

Christopher Brown, US, Physics

Matthew Weidman, US, Optics

Yuan Liu, China, Optics

Caitlin Rinke, US, Chemistry

Cheonha Jeon, South Korea, Optics

Khan Lim, Singapore, Optics

Gregory Katona, US, Physics

Julien Cheiroux, France, Physics

Marie Vangheluwe, France, Physics

Shima Fardad, Iran, Optics

POCT-DICTORAL STUDENTS INVOLVED IN THE PROJECT

Funded:

Santiago Palanco, Spain, Physics

Candice Bridge, US, Chemistry

Matthieu Baudelet, France, Physics

VISITORS INVOLVED IN THE PROJECT

Ahmed Khalil, Egypt

Bruno Bousquet, France

UNDERGRADUATE STUDENTS WHO GRADUATED DURING THE PROJECT

GRADUATE STUDENTS WHO GRADUATED DURING THE PROJECT

Matthew Fisher, US, Optics

MS in Optics

Christopher Brown, US, Physics

PhD in Physics *"Laser induced breakdown spectroscopy for detection of organic residues: impact of ambient atmosphere and laser parameters"*

Matthew Weidman, US, Optics

PhD in Optics *"Laser Filamentation Interaction with Materials for Spectroscopic Applications"*

Caitlin Rinke, US, Chemistry

PhD in Chemistry *"Selective Multivariate Applications In Forensic Science"*

AWARDS, PRIZES, INVITED COMMUNICATIONS

- Invited talk by M. Richardson entitled “Stand-off chemical and biological sensing”, at Frontiers in Optics 2012 in Rochester, NY (October 2012), Laser Science XXVIII; Rochester, NY, USA; 10/14-18, 2012;
- Invited talk by M. Richardson entitled “Stand-off LIBS – The status today and the future”, LIBS 2012; Luxor, Egypt; 09/29 – 10/04, 2012;
- Invited talk by Y. Liu entitled “Microwave-assisted LIBS: Signal enhancement and beyond”, SciX 2012; Kansas City, MO, USA; 10/02, 2012.
- Invited talk by M. Baudelet entitled “Fifty years of LIBS and no limits for analysis”, SciX 2012; Kansas City, MO, USA; 10/02, 2012.
- Invited talk by M. Baudelet entitled “Laser-induced breakdown spectroscopy in complex situations”; FACSS 2011; Reno, NV, USA; 10/06, 2011.
- Invited talk by M. Baudelet entitled “Laser spectroscopy and sensing at the Townes Laser Institute”; ATLANTIS-MILMI Summer School; Orlando, FL, USA; 07/21, 2011.
- Invited talk by M. Richardson entitled “LIBS signature recognition of trace materials in complex background environments”; North-American Symposium on Laser-Induced Breakdown Spectroscopy 2011; Clearwater, FL, USA; 07/18, 2011.
- Invited talk by M. Richardson entitled “Femtosecond LIBS – Light at the End of the Channel : The ARO MURI Program on Femtosecond LIBS” at the NASLIBS Conference in New Orleans July 2009
- 2009 CREOL Affiliates Day Student poster award by Christopher Brown entitled “Principal Component Analysis (PCA) of Femtosecond and Nanosecond Laser Induced Breakdown Spectroscopy (LIBS) for Discrimination of Organic Residues”

Project Summary – Grant #W911NF-06-`-0446 (MURI sub to JHU)
Final Report

Ultrafast Laser Interaction Processes

Paul J. Dagdigian
Department of Chemistry
The Johns Hopkins University, Baltimore, MD 21218

[1] Progress Report

Our main interest has been the development of a full chemical and physical kinetic model to describe the plasma from the interaction of a laser (particularly ultrafast lasers) with matter. This model will need to be tailored for each physical system of interest, because of the likely differing chemistry. Of special interest is the prediction of the time-dependent concentrations of the emitting, excited atomic and molecular states, since the radiative decay of these states is the main observable from the plasma. This will allow us to deduce the important physical and chemical processes leading to the LIBS spectroscopic signatures.

A chemical kinetic model was constructed by considering all chemical and physical processes which affect the concentrations of the various chemical species in the LIBS plume. A literature search was carried out to obtain the best available temperature-dependent rate constants for the expected chemical and ionic reactions. Rate constants for electron-impact processes (electronic excitation, ionization) will be computed by thermal averaging of energy-dependent cross sections available in the literature. Rate constants for the collisional electronic quenching of excited atomic electronic states were estimated from available literature data. The derived matrix of rate constants will be integrated, using the Chemkin suite of programs, to compute predicted time-dependent concentrations of species, including the excited, emitting atomic and molecular states responsible for the spectroscopic signatures from a LIBS plume. The solution of the differential rate equations requires initial concentrations and an assumed temperature profile.

In our first kinetic modeling study, we constructed and applied a kinetic model to the LIBS plume of RDX, in order to understand the processes responsible for the LIBS signature. This model includes processes involving RDX decomposition and air oxidation and ion processes. We conclude from the modeling that the overall reaction can be described with two stages, the first being a fast approach to quasi-equilibrium conditions and the second involving the decay of the plasma temperature. The decomposition of RDX occurs rapidly in the first stage. We find that the production of the emitting states, in the second stage, does not significantly depend upon the detailed mechanism of decomposition. This result has implications for our development of kinetic models for other systems.

We desired to apply our modeling to simple systems, for which comparisons with experimental LIBS spectra would be made. Since LIBS is typically carried out with samples in an air atmosphere, we undertook a computational and experimental study of LIBS in air. The modeling results were compared with experimental observations of 355 nm ns LIBS in air. In our experiments, we have been able to estimate spectroscopically the plasma temperature and electron density as a function of time and have used these data as input in the kinetic modeling. We found that the observed N and O line intensity temporal profile could not be explained

without assuming significant dissociation, and partial ionization, of the constituent N₂ and O₂ by the laser pulse.

We then turned our attention on the development of a complete matrix of temperature-dependent rate constants describing the excitation and decay of the excited, emitting electronic states of the H, C, N, and O atoms, which are the common constituents in organic molecules and the atmosphere. We have developed a matrix of temperature-dependent rate constants describing the excitation and decay of the excited, emitting electronic states of the H, C, N, and O atoms, which are the common constituents in organic molecules and the atmosphere. The model includes a comprehensive set of chemical processes involving both neutral and ionic chemistry and physical excitation and de-excitation of atomic levels affecting the neutral, ionic, and excited-state species concentrations. We have augmented this set of rate constants with those describing the excitation of the Al atom to its lowest excited state (4s ²S) and initial steps of oxidation of Al. This will allow us to consider the ablation of Al substrate

We have tested the applicability of this model by comparison of computed relative populations of excited, emitting atomic levels with laboratory observations of LIBS spectra for 355 nm ns laser irradiation of organic residues on Al substrates in air. We have investigated two organic samples, namely anthracene and 2,4-dinitrotoluene. In order to compute relative excited-state populations from observed emission line intensities, we corrected the spectra for the wavelength response of the spectrometer/ICCD combination. The temperature profile employed in the kinetic modeling was obtained from measured Al 308/394 nm line intensities. Best agreement of observed and computed excited-state populations was obtained with the assumption of complete atomization and partial ionization of the sample. The calculations provided a reasonable description of the relative populations and their time dependence. In the case of anthracene, we were able to estimate the degree of air entrainment from the relative N/O atomic line intensities. From the observed Al line intensity, it appears that only a small amount of Al atoms is entrained in the LIBS plume.

Since emission from CN and C₂ is often observed in the LIBS of organic molecules, we then extended our kinetic model to include excited states of these molecules. The rate constant for excitation of C₂ can be obtained from computed energy-dependent excitation cross sections reported in the literature. No such data are available for CN, and we have assumed that the CN rate constant is equal to that for C₂. The electron-impact de-excitation rate constants are obtained by detailed balance. Other processes involving the excited molecular states included radiative decay and collisional electronic quenching.

We tested the applicability of this extended kinetic model for both atomic and molecular emissions by comparison of the computed relative populations of the excited, emitting levels with laboratory observations of LIBS spectra for ns laser irradiation of organic residues on Al substrates in air. We have investigated a number of different organic compounds, including a polyatomic hydrocarbon (perylene) and molecules containing various kinds of C–N bonds (2,4-dinitrotoluene, imidazole, adenine). We have completed study of LIBS at 355 nm and are currently investigating 1064 nm LIBS of these compounds. In order to compute relative excited-state populations from observed emission line intensities, we corrected the spectra for the wavelength response of the spectrometer/ICCD combination, and have converted intensities to populations. We have been particularly interested in the time dependence of the excited-state populations and have determined these populations as a function of delay time. We find a very different temporal variation of the atomic and molecular excited-state populations. The atomic populations decay approximately exponentially, with a decay lifetime of <~1 μ s. By contrast,

the molecular emission usually initially increases with time and then decays after a maximum in the population at \sim 300 ns and persists for more than 2 μ s. This behavior is nicely reproduced in our kinetic simulations. In our previous study of time-dependence excited atomic populations, we concluded that the observed prompt appearance of atomic emission implied that the compounds were injected into the vapor phase almost exclusively as atoms, which were slightly ionized. We have taken this assumption in our present set of simulations. The long duration of the molecular emission can be understood as a result of the increase in the ground-state CN and C₂ concentrations as a function of time. There has been much speculation as to the source of these molecules in the plasma and the C₂ + N₂ reaction has often been invoked. Analysis of the rate of production of CN from different elementary reactions suggests that this reaction is a negligible source of this molecule

We have also investigated LIBS of polymers with laser irradiation in the mid-IR on fundamental vibrational transitions. Samples investigated include polymers in bulk form and spin coated on Si wafers. Of particular interest is whether the LIBS signals are enhanced when the laser wavelength is resonant with a fundamental vibrational transition of the polymer. Significant increases in the LIBS signals were observed for irradiation on hydride stretch fundamental transitions, and the magnitude of the enhancement showed a strong dependence upon the mode excited (*e.g.* C–H stretch *vs.* N–H or O–H stretch). The role of the substrate was investigated by comparison of results for bulk and spin coated samples. For polymers spin coated on SI wafers, a more complicated dependence upon the laser irradiation wavelength was observed. Finally, the LIBS signals were found to be significantly weaker than for near-infrared laser irradiation.

In collaboration with the UCF group., we have estimated vibrational and rotational temperatures of AlO emitted from the plasma above an aluminum sample exposed simultaneously to microwave and Nd:YAG laser radiation. The temperatures were determined by comparison of experimental spectra with simulations of the AlO *B* – *X* electronic band system. In another project, the UCF group has recorded spatially and temporally resolved LIBS spectra of graphite samples upon irradiation with filamented fs laser radiation. Our group has analyzed CN emission spectra in order to determine the vibrational and rotational temperatures of the emitting molecules

[2] *Names, level and status of faculty involved*

Paul J. Dagdigian, Professor of Chemistry

[3] *Publications resulting from this work over the full 6 year period*

“Kinetic modeling study of the laser-induced plasma plume of the explosive cyclotrimethylenetrinitramine (RDX),” V. I. Babushok, F. C. DeLucia Jr., P. J. Dagdigian, J. L. Gottfried, C. A. Munson, M. J. Nusca, and A. W. Mizolek, Spectrochim. Acta Part B **62**, 1321–1328 (2007).

“Laser-induced breakdown spectroscopy with laser irradiation on mid-infrared hydride stretch transitions: polystyrene,” A. Khachatrian and P. J. Dagdigian, Appl. Phys. B **97**, 243–248 (2009).

“Nd:YAG-CO₂ dual-pulse laser- induced breakdown spectroscopy of organic films,” M. Weidman’ M. Baudelet, S. Palanco, M. Sigman, P. J. Dagdigian, and M. Richardson

Optics Express **18**, 259-266 (2010).

“Laser-induced breakdown spectroscopy with laser irradiation resonant with vibrational transitions,” A. Khachatrian and P. J. Dagdigian, Appl. Optics **49**, C1–C7 (2010).

“Kinetic model of C/H/N/O emissions in laser-induced breakdown spectroscopy of organic compounds,” P. J. Dagdigian , A. Khachatrian, and V. I. Babushok, Appl. Optics **49**, C58–C66 (2010).

“Kinetic model of atomic and molecular emissions in laser-induced spectroscopy of organic compounds,” Q. Ma and P. J. Dagdigian, Anal. Bioanal. Chem. **400**, 3193-3205 (2011).

[4] *Presentations over the same time period (not including presentations with Dagdigian as a co-author, presented by UCF personnel)*

“Experimental and Kinetic Modeling Study of the Emission Spectrum from Laser-Induced Plasmas in Air,” Paul J. Dagdigian, Valeri I. Babushok, Christopher G. Brown, M. Fisher, and Santiago Palanco, contributed oral paper, North American Symposium on Laser-Induced Breakdown Spectroscopy, New Orleans, LA, Oct 8, 2007

“Laser Spectroscopy for Basic and Applied Studies: Investigations of Transient Intermediates and Detection of Explosives,” Paul J. Dagdigian, Maryland Chemist of The Year award talk, Maryland Section of the American Chemical Society meeting, Towson, MD, Dec 12, 2007

“Laser-Induced Breakdown Spectroscopy with Laser Irradiation on Mid-Infrared Stretch Transitions,” Ani Khachatrian and Paul J. Dagdigian, contributed poster paper, North American Symposium on Laser-Induced Breakdown Spectroscopy, New Orleans, LA, July 17, 2009

“Development and Validation of a Kinetic Model to Describe Relative C/H/N/O Emission Intensities in LIBS of Organic Compounds,” Paul J. Dagdigian, contributed oral paper, North American Symposium on Laser-Induced Breakdown Spectroscopy, New Orleans, LA, July 18, 2009

“Detection of Explosives: Spectroscopic Methods,” Paul J. Dagdigian, talk at NSF/DOE sponsored workshop (QUARKNET) for high school physics teachers, JHU Department of Physics and Astronomy, Aug 5, 2010

“Kinetic Model of Atomic and Molecular Emissions in Laser-Induced Breakdown Spectroscopy of Organic Compounds,” Paul J. Dagdigian, invited talk, Laser-Induced Breakdown Spectroscopy 2010, Memphis, TN, Sep 13, 2010

“Kinetic Model of Atomic and Molecular Emissions in Laser-Induced Breakdown Spectroscopy,” Paul J. Dagdigian, invited talk, Pacificchem 2010, Honolulu, HI, Dec 17, 2010

“Using Lasers to Study Transient Intermediates and for Sensitive Detection of Molecules,”
Paul J. Dagdigian, graduate student recruiting visit, Department of Chemistry, Muhlenberg
College, Allentown, PA, Oct 21, 2011

“Kinetic Model of Atomic and Molecular Emissions in Laser-Induced Breakdown
Spectroscopy of Organic Compounds,” Paul J. Dagdigian, invited talk, SCIX 2012,
organized by FACSS (Federation of Analytical Chemistry and Spectroscopy Societies),
Kansas City, MO, Oct 1, 2012

[5] *Patents and IP generated*

None

[6] *Names, citizenship, discipline, of all undergraduates involved in the project (two
categories : those funded : those involved)*

None

[7] *Names, citizenship, discipline of all graduate students involved in the project (two
categories : those funded : those involved)*

Diane M. Wong, USA, Chemistry, funded

Qianli Ma, Chinese, Chemistry, current graduate student, funded

[8] *Names, citizenship, discipline of all post-docs involved in the project (two categories: those
funded : those involved)*

Ani Khachatrian, Armenian, Chemistry, currently working as a postdoc at the Naval Research
Laboratory, Washington, DC, funded

[9] *Names, citizenship, discipline of all undergraduates who graduated in the program (two
categories: those funded : those involved)*

None

[10] *Names, citizenship, discipline of all graduate students who graduated in the (two
categories : those funded : those involved)*

Diane M. Wong, USA, Chemistry, Ph.D. 2008, currently regional sales manager, Quantel Lasers
USA, partially funded

[11] *Awards, prizes etc.*

Paul J. Dagdigian, Maryland Chemist of the Year, Maryland Section of the American Chemical
Society, 2007

Final Progress Report (Due Date: 10/30/2012)
ARO MURI
University of Central Florida
Dr. Martin Richardson

Title: Fundamental Physical & Chemical Processes in Ultrafast Laser Materials Interaction

Submitted to:

Mary B. Stanley, Senior Contract Manager
University of Central Florida
Office of Sponsored Research
12201 Research Parkway, Suite 501
Orlando, FL 32826-0150
Phone: (407) 823-2836
Fax: (407) 823-3299

Date Prepared:
October 30, 2012

Prepared by:

Dr. Dennis R. Alexander
Dr. Troy Anderson
Mr. John Bruce III
Mr. Craig Zuhlke
202 N WSEC Link
Electrical Engineering Department
University of Nebraska-Lincoln
Lincoln, Nebraska 68588-0511
Phone: 402-472-3091
Email: dalexander1@unl.edu

Objective

The role of the UNL team, in the final year of the MURI, is to understand and model the effect of the position of the sample with respect to focus and the effects this has on the enhancing the femtosecond laser induced breakdown spectroscopy (FLIBS) signal observed both for single pulse as well as dual pulse LIBS. During the six year MURI research project, the significance of varying the sample location with respect to focus was first reported by Schiffern, Doerr and Alexander, "Optimization of collinear double-pulse femtosecond laser-induced breakdown spectroscopy of silicon", Spectrochimica Acta Part B 62 1412-1418, (2007). Only during the MURI research project was the significance of this uncovered, and is the major point being emphasized in this final MURI project report.

During the research project, it is well known that the generation of nanoparticles is often a byproduct of femtosecond laser ablation. However, the generation of nanoparticles is generally undesirable for LIBS applications as they do not emit atomic lines and thus represent wasted energy. In the final year of the research project, the efficiency of the LIBS process was investigated from both the fundamental point of view of why sample location played such an important role in the formation of nanoparticles and the production of the FLIBS signal. Of particular interest was the idea that by using nanoparticles ejected from a sample surface during ablation, as a target material for FLIBS signal production, with a second laser pulse. In this way, a higher percentage of the target material is atomized and the strength of the FLIBS signal can be optimized. This research is also fully compatible with the larger goals of the MURI including stand-off detection of biological and chemical explosives at a distance. In addition, the role of the UNL team is to understand the fundamentals of femtosecond LIBS

Approach

The UNL team use a collinear dual-pulse-dual-focus geometry to efficiently generate FLIBS signals from both the target material and nanoparticles ejected from the surface during ablation. In this arrangement, two collinear femtosecond laser pulses illuminate the sample. The two pulses are separated by a variable time delay (dual-pulse) and their focal positions can be varied relative to each other (dual-focus). This configuration provides a large amount of freedom to optimize the FLIBS process while maintaining a geometry suitable for field applications and stand-off detection. Specific to the goal of creating a model of laser interaction with nanoparticles, this geometry permits an experimental basis for the testing and refining of our models by allowing separate interactions with both the sample surface and the ejected particles in both space and time.

Relevance to Army

FLIBS is a potentially effective technique for the detection of a wide variety of potentially hazardous materials at standoff distances. The efficiency of the system determines the requirements on laser size and collection optics. By increasing the efficiency of the FLIBS process, the requirements on laser energy, detector efficiency, cost, reliability, and weight are simultaneously reduced. Our work at UNL is primarily focused on improving the quality and quantity of the FLIBS signal through dual pulse techniques and optimal utilization of ablated

material. In addition, the UNL effort investigates the fundamentals of femtosecond FLIBS and the creation of nanoparticles.

Accomplishments for Reporting Period

Experimental Setup

The laser source used in all of the work done at UNL is a Spectra Physics Spitfire system, which produces 50 fs pulses with a maximum pulse energy of 1 mJ with a center wavelength of 800 nm. A schematic of the beam path is shown in Figure 1.

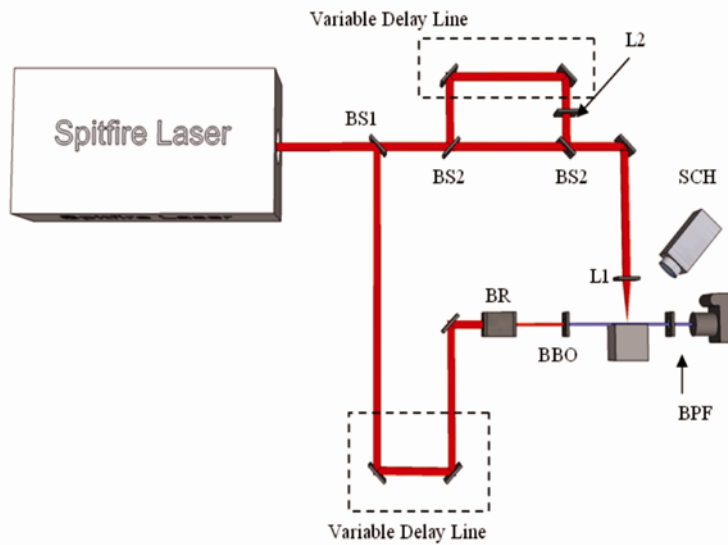


Figure 1: Diagram of the setup used. BS1 = 70/30 beamsplitter, BS2 = 50/50 beamsplitter, BR = beam reducer, BBO = frequency doubling crystal, BPF = 400 nm bandpass filter, SCH = spectrometer collection head, L1 = common focusing lens, L2 = lens used to create dual focus (with or without axicon lens pair)

The first beamsplitter (BS1 in Figure 1) splits 30% of the power to a delay arm that is used as a light source for shadowgraphic imaging. The 70% of the beam that passes through BS1 is split into two pulses of equal energy by a 50% beamsplitter, which is the start of a Mach-Zender interferometer. One branch of the interferometer has a variable delay line to control the time delay between the two pulses. The delay arm also has a long focal length lens and optionally a matched axicon lens pair. This arrangement allows the focal position of the delayed pulse to be different than the first pulse as shown in Figure 2.

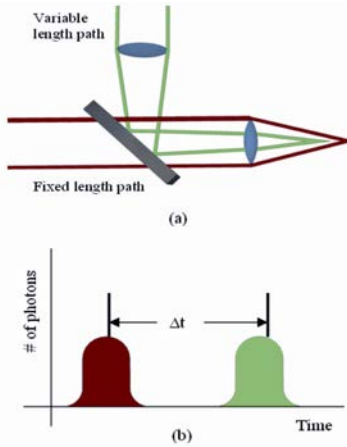


Figure 2: Illustration of the different foci, in both space and time, achieved by inserting a lens in one arm of the delay line.

Understanding the formation of nanoparticles for enhanced dual pulse LIBS and the importance of where the laser beam is focused

The location of the target sample with respect to the focal volume is of critical importance to the proper alignment of and interpretation of results from a LIBS system. Figure 3 shows the regions of importance when a high power femtosecond laser pulse interacts with a material. In many applications, a focusing element such as a lens focuses the beam onto the sample surface in order to achieve a high fluence and achieve efficient ionization. However, the LIBS community as a whole places little importance on the exact location of the sample with respect to the laser focus. Rather, many published accounts of LIBS experiments place the sample either at the laser focus (without mentioning the alignment method) or at the location that maximizes the LIBS signal (without accurate knowledge of the precise location). We have shown that the exact placement of the sample relative to the laser focus critically influences the nature of the laser ablation as well as the intensity of the LIBS signal. In many practical cases, factors such as lens aberrations and the ionization of the atmosphere critically affect the spatial, temporal, and spectral properties of the beam on the sample surface and thus the intensity of the LIBS signal. Furthermore, we have demonstrated that the LIBS signal is maximized when the sample is located prior to the laser focus (~10 Rayleigh lengths prior to focus for a 40 mm focal-length lens) rather than at the laser focus. **These observations help clarify the difficulties associated with directly comparing LIBS data between different experimental setups.**

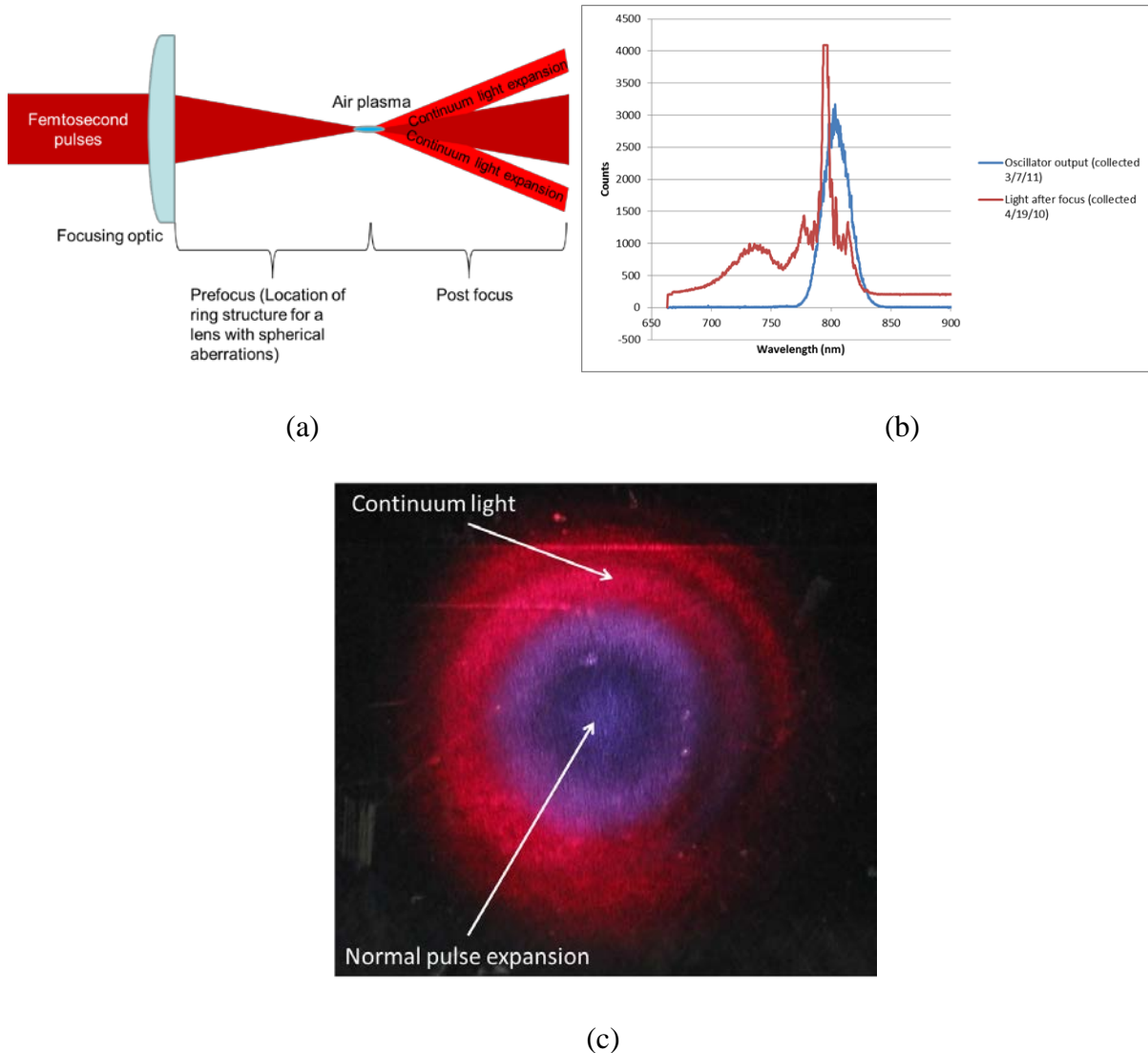


Figure 3: (a) Illustration of the important regions around the focus of a femtosecond pulse. This illustrates how the spectrum of the 800 nm laser light is altered as the continuum is formed around focus. (b) Spectrum of laser pulse before (blue) and after (red) focus. The continuum generation is shown through the increased bandwidth of the light after focus. (c) Image of the laser profile viewed on a black metal target located after the focus showing spatial and spectral variations between the laser pulse and generated continuum light.

There are several phenomena that complicate the identification of an “ideal” sample location for LIBS experiments including ionization of the atmosphere and variations in the electric field profile of the laser pulse. The extent to which these phenomena occur is a function of the exact laser parameters and experimental setup and is thus difficult to quantify. In many practical experiments, the laser fluence is high enough to ionize the atmosphere and generate a plasma at or near to the focal volume. For LIBS analysis, air breakdown is avoided because it robs energy that would otherwise ablate the sample of interest as well as modifies the spatial, temporal, and spectral properties of the beam incident on the sample. One such effect is the production of continuum light that diverges from the beam and forms a halo around the ablation spot on the sample. An example spectrum of continuum light generated by air ionization is shown in Figure 3(b,c). The location at which continuum light begins to be generated will necessarily depend on

the laser fluence and the focusing lens used in the experiment. Figure 4 depicts the development of continuum laser light for the Spitfire laser (parameters described previously) focused with a 40 mm focal-length lens. A silicon wafer was irradiated with 800 mW of laser power at various locations prior to the focus. Analysis of the laser damage craters imaged using a scanning electron microscope revealed the location at which continuum light was observed. In this case, which is typical of femtosecond LIBS experiments reported in the literature, continuum light is generated as early as 400 μm prior to the focal position of the lens, corresponds to 7.4 Rayleigh lengths prior to focus. **Thus, this experiment demonstrates that under typical conditions, the sample must be placed greater than 400 μm prior to focus in order to avoid the adverse effects continuum generation on the sample during a LIBS experiment.**

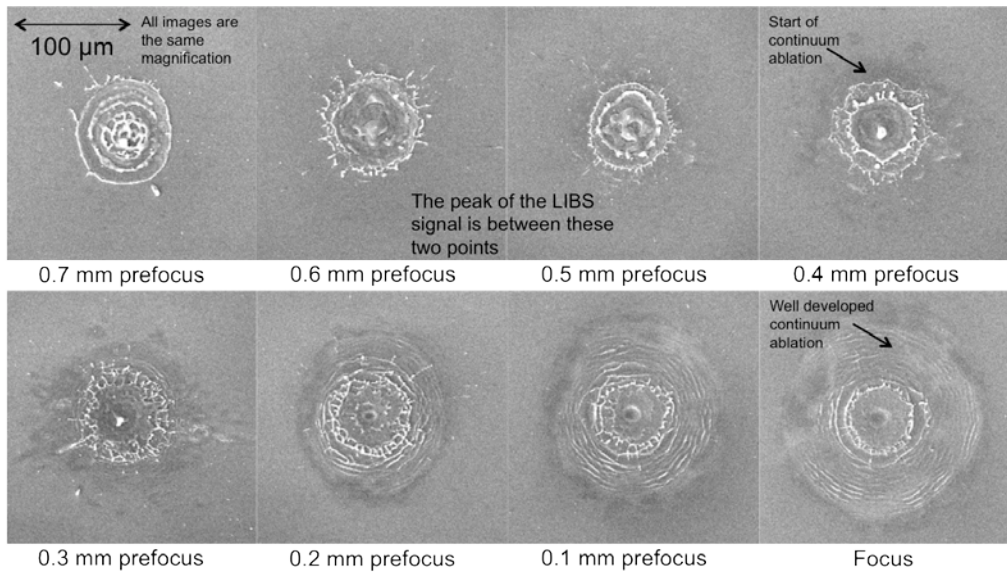


Figure 4: Series of SEM images depicting the evolution of continuum light prior to the focal volume of a femtosecond laser focused by a lens with a 40 mm focal length. The Rayleigh length of the focused beam was 54 μm .

The exact location of the laser focus was determined by irradiating the sample with a laser fluence at the ablation threshold at multiple locations through the focal volume and analyzing the laser damage using a scanning electron microscope. At this fluence, laser damage only occurred when the sample surface was within the confocal length of the lens with the laser focus in the center of the confocal length. Because the sample was located on a computer-controlled translation stage with nanometer precision, the exact location of the sample with respect to the focus could be known for every data point. The analysis of the focal length is shown in Figure 5. **It should be noted that this method to define the sample position relative to the laser focus is significantly more involved than typically performed for traditional LIBS measurements.**

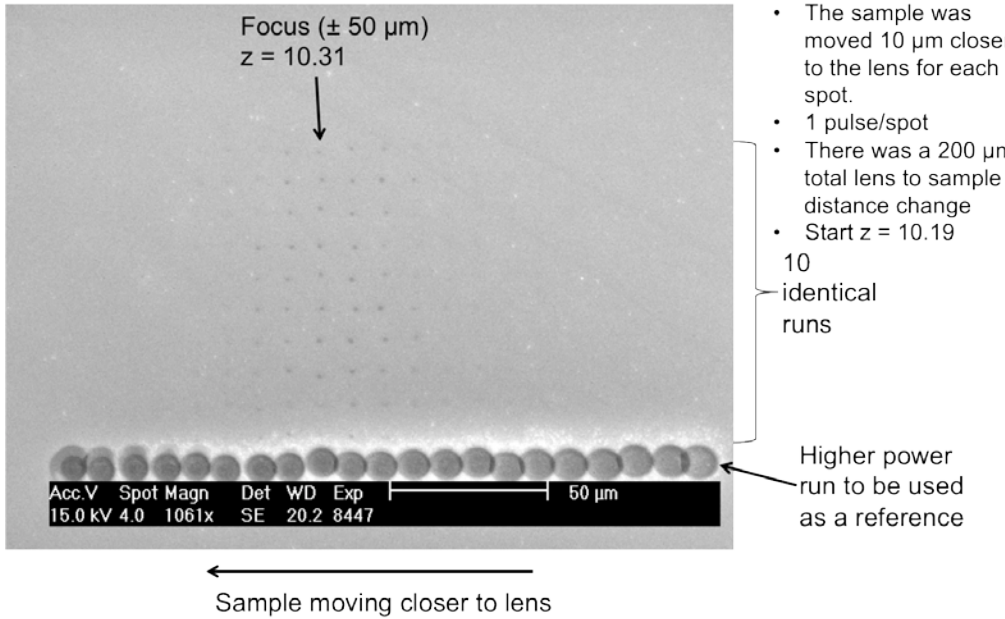


Figure 5: SEM image analysis used to find the exact location of the laser focus. A sample (polished silicon wafer) was irradiated with a laser fluence at the ablation threshold at various locations through the focal volume. Laser damage was induced only in the confocal length (twice the Rayleigh length) with the focus in the center of the confocal length.

Another phenomenon that can influence the intensity of the LIBS signal is localized variations of the electric field across the beam profile. Aberrations induced by the focusing optic are a common example. When a lens with spherical aberrations is used to focus a laser pulse, the electric fields exhibit distortions in the form of concentric rings of varying intensity, which are only present in the spatial region between the focusing lens and the focal volume. Evidence of these concentric ring distortions in focused femtosecond laser pulses have been demonstrated through direct measurement of the electric field of focused femtosecond pulses by Bowlan et al [2] (see Figure 6) as well as through observation of ablation in high-carbon steel (see Figure 7) where the electric field distribution transferred to the surface ablation profile. Thus, a precise understanding of the spatio-temporal electric field profile on the target is critical to the understanding of the LIBS process. Variations of the electric field profile on the sample surface will result in the formation of localized temperature and pressure gradients during ablation and thus variations of the LIBS signal intensity.

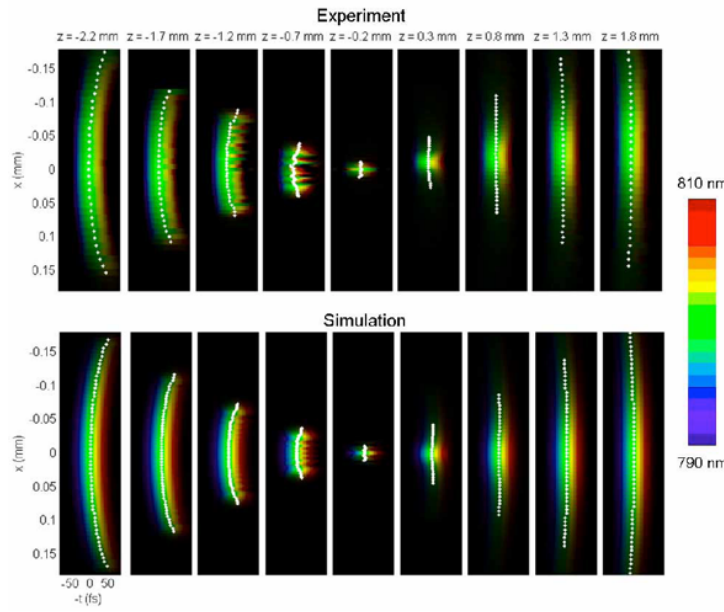


Figure 6: $E(x,z,t)$ in the focal region the spatial profile that are particularly visible at $z = -0.7\text{mm}$.¹ These hot spots in the electric field intensities cause localized nonlinear effects on the target surface since the intensity is the square of these electric fields of a plano-convex lens. The spherical aberrations introduced by this lens result in ripples in the electric field intensities.

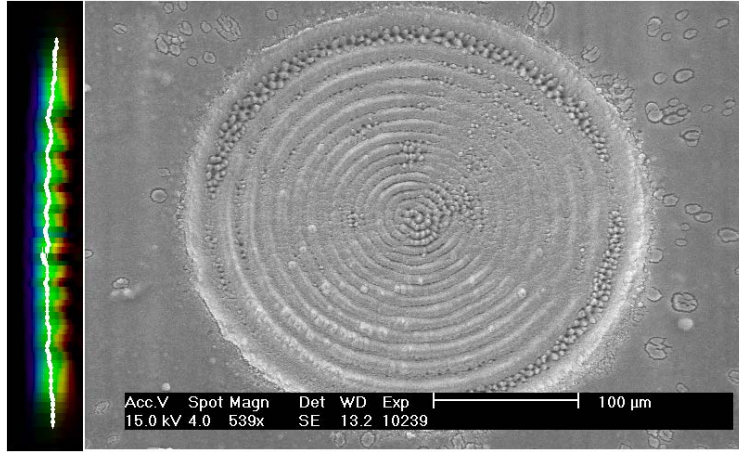


Figure 7: Ring structures are from the laser ablation of a high carbon steel surface freezing the electric field intensity distribution as shown on the left color insert (taken from ref. 1).

Studies of the influence of sample position on LIBS signal intensity

In this section, we demonstrate the necessity of precisely understanding the focusing conditions as well as the spatio-temporal electric field profile on the sample when analyzing a femtosecond LIBS signal. First, consider the FLIBS signal of the 288.16 Si line observed from a silicon wafer target using an 800 nm, 50 fs laser pulse focused by a 40 mm plano-convex lens. The f/# of the focal system is 3.5 and the Rayleigh length is 54 μm . The single-pulse LIBS signal intensity relative to the laser focus is shown in Figure 8. SEM images of the laser damage spots are

shown on the perimeter of the plot. The location of the sample with respect to the laser focus was precisely determined using the method described in Figure 5.

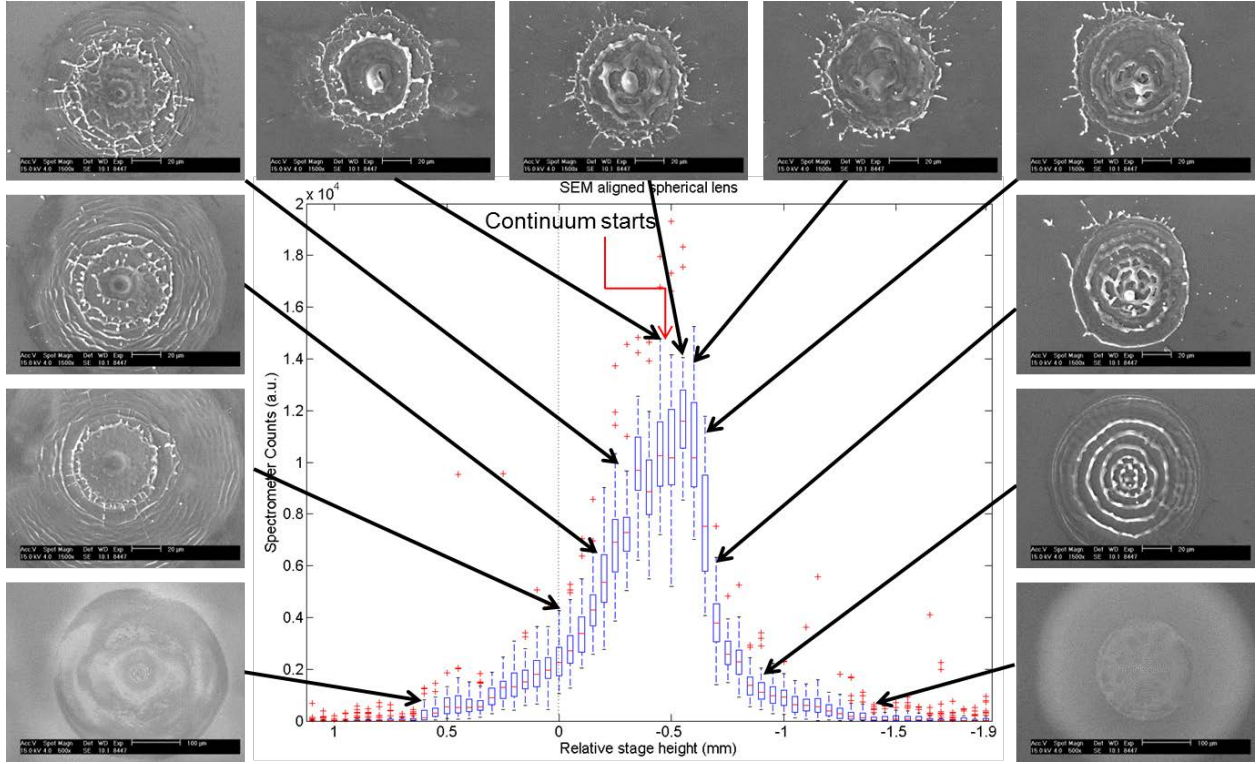


Figure 8: LIBS and ablation SEM images for a spherical lens with a 40 mm focal length for the 288.16 Si line. Negative numbers for the relative stage height correspond to sample locations prior to the laser focus (between the lens and the laser focus).

The maximum LIBS signal intensity is observed at a stage height 400 μ m prior to the laser focus (the sample is located between the lens and the laser focus). This stage height is 7.4 Rayleigh lengths away from focus and is thus well outside the focal volume. In fact, the LIBS signal is roughly 20% of the peak value at the laser focus. Thus, the maximum LIBS signal does not correspond to the largest laser fluence, but rather at a point at which the influences of continuum generation and aberration-induced electric field variations are minimized.

Impact of Electric Field Variations

The series of SEM images in Figure 8 for sample locations prior to the focus (negative stage height in the plot) show evidence of spherical aberration in the focusing optic in the form of concentric rings in the ablation profile. This is most strikingly seen at a stage height of -0.8 mm. These rings are formed by thermocapillary effects induced by the interaction of the periodic electric field profile and the surface melt layer during irradiation. In order to isolate the effect of the spherical aberration, the LIBS analysis was duplicated using a 40 mm achromatic aspheric lens designed to eliminate spherical aberration. The results are shown in Figure 9. Again, the location of the sample with respect to the laser focus was precisely determined using the method described in Figure 5.

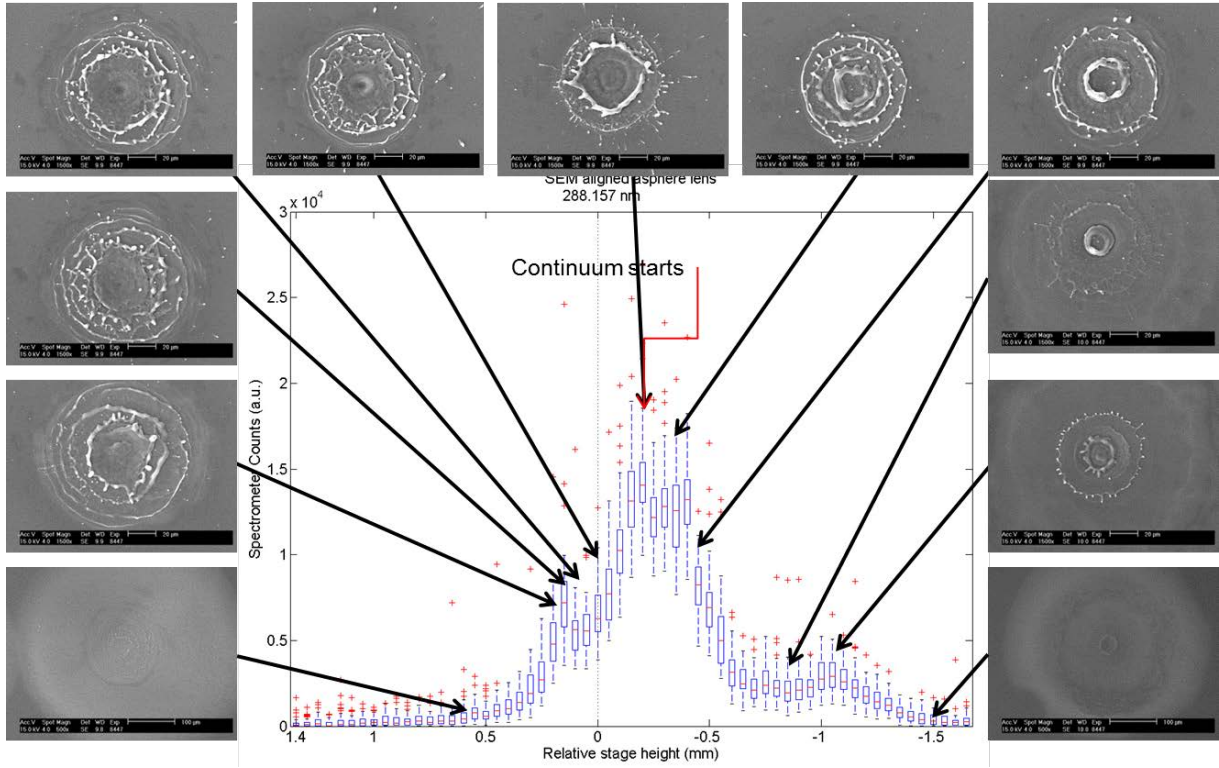


Figure 9: LIBS and ablation SEM images for an achromatic aspheric lens with a 40 mm focal length for the 288.16 Si line. Negative numbers for the relative stage height correspond to sample locations prior to the laser focus (between the lens and the laser focus).

The use of an achromatic aspheric lens had the desired effect of eliminating the concentric rings in the ablation profile when the sample was located prior to focus. However, the use of this lens led to several new observations. First, the location of the maximum LIBS intensity was the same as for the spherical lens, which indicates that the spherical aberration did not directly impact the peak LIBS signal. Second, two additional local maxima in the LIBS signal were observed at stage heights -1.1 mm and +0.2 mm relative to the laser focus. These local maxima have been attributed to opening and closing of a secondary crater observed in the ablation profile. This is demonstrated more clearly in Figure 10, which focuses on the local LIBS maxima between -0.5 and -1.5 mm. This same phenomenon is observed for the local maxima centered at +0.2 mm.

These two experiments clearly demonstrate the impact of the electric field profile on the LIBS signal intensity. Subtle variations of the profile can lead to measurable differences in not only the ablation crater, but also the LIBS signal. Furthermore, steps to control and minimize aberrations (e.g. using an aspheric lens) do not necessarily solve the problem.

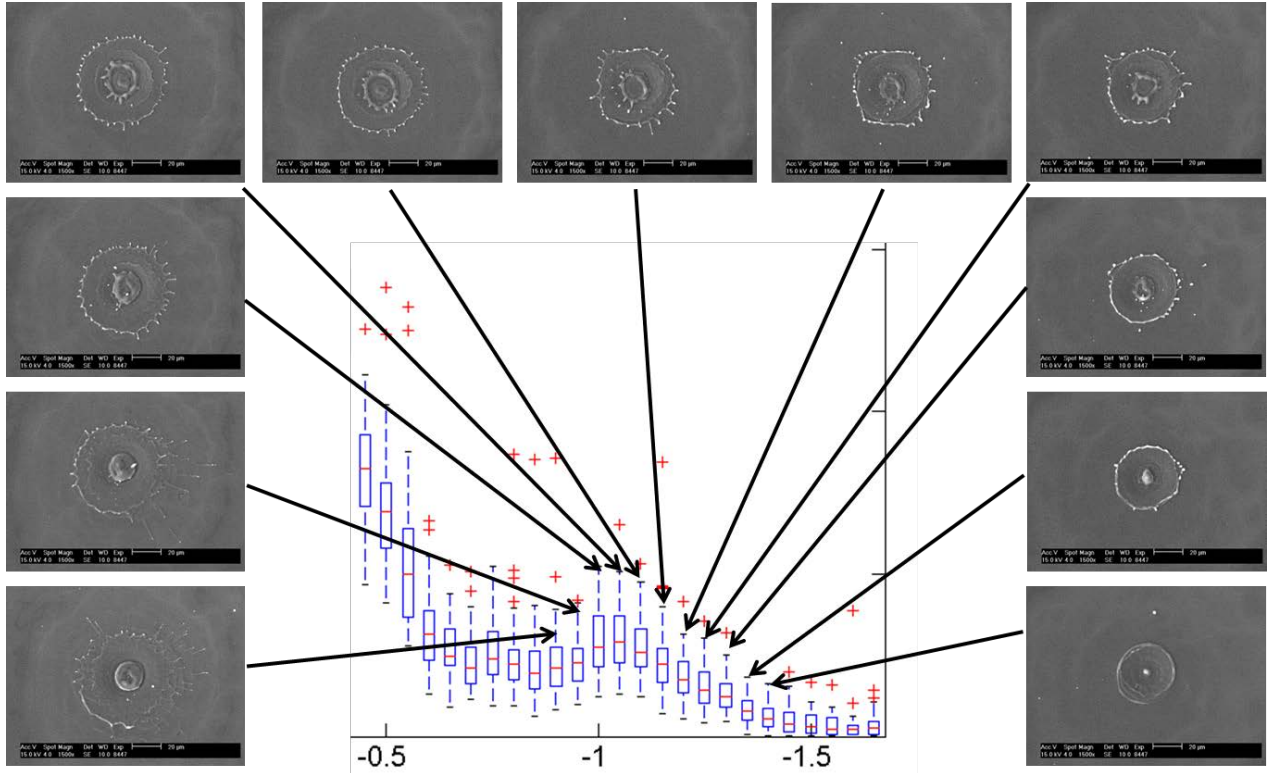


Figure 10: LIBS and ablation SEM images for a 40 mm focal length achromatic aspheric lens showing the correlation between local maximum and minimum and the closing and opening of the local electric magnetic fields as imprinted by the ablation spots.

Impact of Continuum Generation

The SEM images in Figure 8 and Figure 9 indicate that the peak LIBS signal occurs just prior to continuum generation. This is evident when comparing the size of the laser damage craters before and after focus. As depicted schematically in Figure 3, continuum light generated at focus diverges rapidly as a halo around the propagating laser pulse, which leads to increased ablation diameters observed when the sample is located after continuum generation begins. The impact of the continuum generation on the LIBS signal was further investigated by comparing LIBS measurements taken in a vacuum with those taken in open atmosphere using the spherical lens described above. Performing the measurements in a vacuum will prohibit atmospheric ionization and thus the generation of continuum light. The results are shown in Figure 11(a).

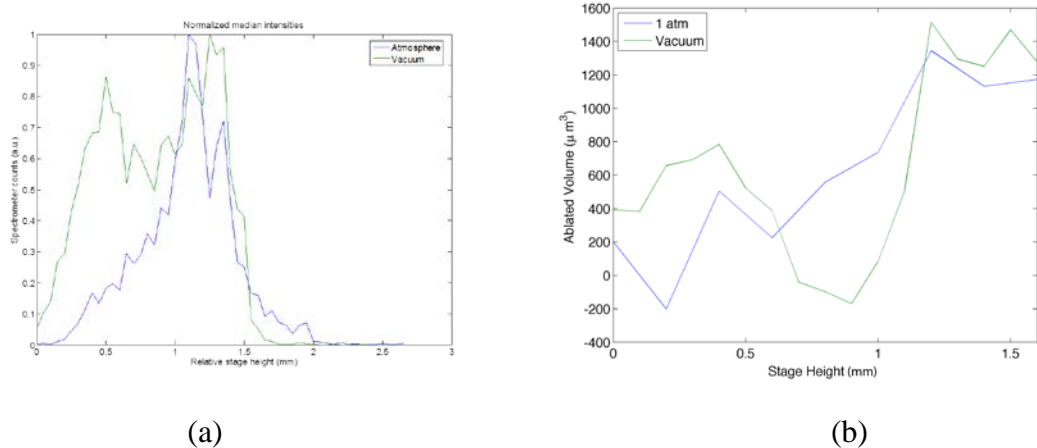


Figure 11: (a) Comparison of LIBS signal intensity of the 288.16 nm Si line in vacuum and open atmosphere as a function of sample location for a spherical lens (laser focus at ~ 0.9 mm). (b) Plot of the ablated volume corresponding to the data in (a).

Regardless of the lens used, prohibiting the generation of continuum light had a substantial impact on the intensity of the LIBS signal after the laser focus. Without the loss of energy associated with continuum generation, the laser beam profile is not significantly modified as it passed through the geometric focus and the LIBS signal is approximately symmetric about the laser focus. This is in sharp contrast to the measurements performed in open atmosphere, where the intensity of the LIBS signal steadily decreases after the laser focus for both lenses.

It is important to note, however, that the LIBS signal intensity at the laser focus is $\sim 50\text{-}60\%$ of the maximum intensity, even when measured in a vacuum environment. In fact, the peak of the LIBS signal can be correlated to the maximum ablated volume as shown in Figure 11(b). The ablated volume of the laser damage crater was measured using a Veeco Wyko Optical Profiler. The negative ablated volume measured at the laser focus is due to the redisposition of lower density material around the ablation crater as has been previously reported [4]. The reason that the peak LIBS signal intensity does not appear at the laser focus (the location at which the laser fluence is maximized) is unclear and is currently under investigation. It is likely due to the redeposition of material near the crater, which detracts from the amount of atomized ejected material observed in LIBS measurements.

Impact of Alignment

In addition to the experimental setup, the way the researchers align the optical system is very important in LIBS research. In Figure 12, we demonstrate three optical methods used to align the optical system. The first method, *aperture aligned*, is the standard way of looking at the back reflection through an aperture. The second method, *SEM aligned*, relies on iteratively adjusting the lens and sample such that the ablation crater is as symmetric as possible. This is simplified by introducing spherical aberration and optimizing the concentric ring pattern visible on the sample after ablation. The third method, *continuum aligned*, is aligning the system by observing the bulls-eye continuum below the focus of the lens. When properly aligned, the continuum light forms a concentric ring around the unaffected laser pulse. The SEM method is the best method

when extreme accuracy is needed in making FLIBS measurements; it is also the most time-consuming and difficult.

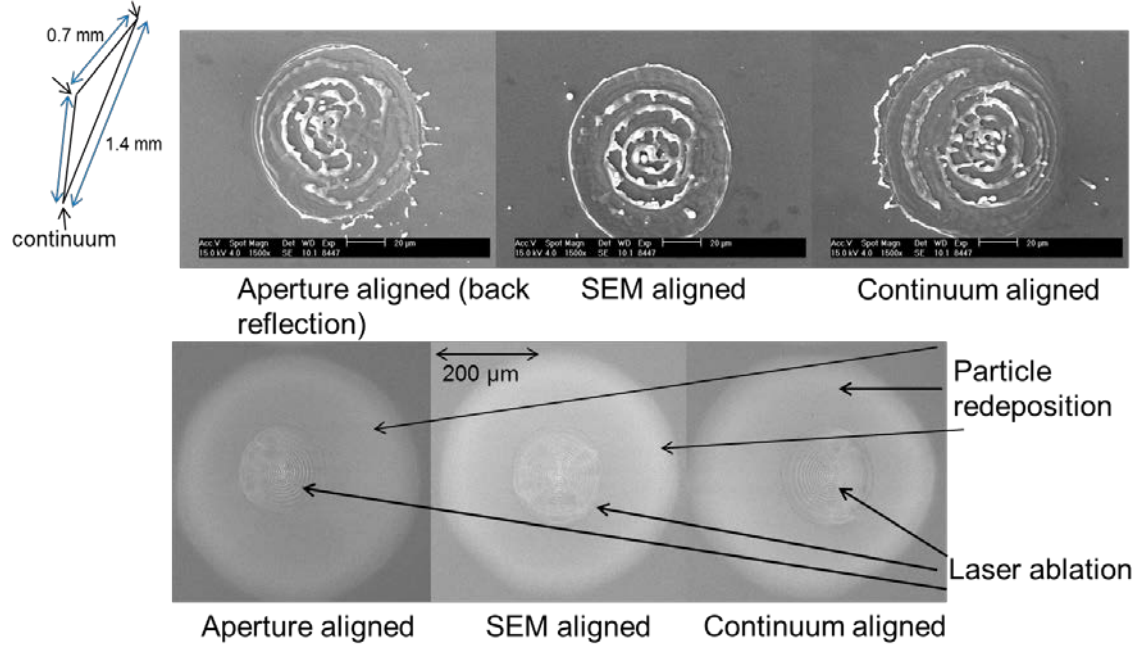


Figure 12: Ablation from different lens alignment methods.

It is clear from the SEM images that the method used to align the experimental setup can impact the quality and symmetry of the beam profile on the sample surface. It is expected that few, if any, researchers in the LIBS community take the time to truly optimize the alignment of the system to the degree possible when using an iterative approach such as the *SEM alignment* method. However, as can be expected based on the results shown in Figure 8 - Figure 10, even subtle variations in the laser pulse profile can lead to measurable differences in the LIBS signal intensity and can practically limit the reproducibility of measurements. This is highlighted in Figure 13, which plots the LIBS signal intensity in open atmosphere using the achromatic aspheric lens as a function of the sample location with respect to the laser focus for the three alignment method. A clear difference between the *continuum aligned* method and the other two methods is observed.

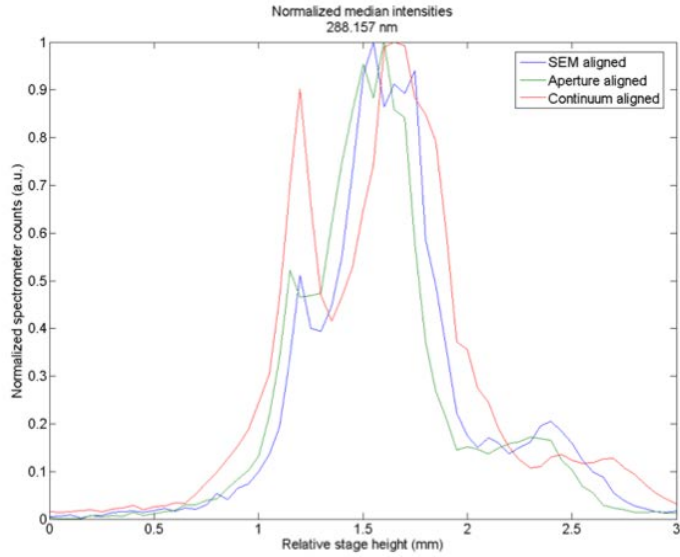


Figure 13: Comparison of LIBS signal intensity of the 288.16 nm Si line in open atmosphere as a function of sample location with respect to laser focus for three different alignment methods highlighting the importance of precise alignment. The lens is a 40 mm focal-length aspheric achromat.

Summary

One of the primary objectives of this MURI was to understand the fundamentals of Laser Induced Breakdown Spectroscopy (LIBS) in order to make it more quantitative and precise. During our investigations of an advanced dual-pulse dual-focus configuration for femtosecond LIBS, we realized the importance, and difficulty, of understanding the complex dynamics of focused femtosecond laser beams. It is now apparent that spatio-temporal variations in the electric field profile have substantial impacts on the laser ablation as well as the LIBS signal intensity. We have demonstrated here that the presence of continuum generation prior to the laser focus, variations in the spatio-temporal electric field of the beam, and even small changes in the alignment procedure lead to significant modifications of the LIBS signal intensity. Furthermore, it is expected that very few, if any, researchers in the LIBS community make the painstaking measurements needed to fully understand the laser electric field profile on the target sample. Future studies are needed to continue this important research to further investigate the ability of using precise spatio-temporal control of a laser beam to achieve the goal of reproducible, quantitative LIBS measurements.

References:

1. D. Scuderi, O. Albert, D. Moreau, P. Pronko, and J. Etchepare, "Interaction of a laser-produced plume with a second time delayed femtosecond pulse," *Applied Physics Letters* **86**, 071502 (2005).
2. Pamela Bowlan, Pablo Gabolde, and Rick Trebino, "Directly measuring the spatio-temporal electric field of focusing ultrashort pulses, *Optics Express*, Vol. 15, No. 16, 10219, August, 2007.
3. Schiffen, Doerr and Alexander, "Optimization of collinear double-pulse femtosecond laser-induced breakdown spectroscopy of silicon", *Spectrochimica Acta Part B* 62 1412-1418, (2007).
4. D. J. Hwang, C. P. Grigoropoulos, and T. Y. Choi, "Efficiency of silicon micromachining by femtosecond laser pulses in ambient air," *Journal of Applied Physics*, vol. 99, no. 8, p. 083101, 2006.

2. Names, Level and Status of Faculty Involved... Funded or Not funded by the MURI

Dr. Dennis R. Alexander, Professor of Electrical Engineering, Kingery Chaired Professor

3. Publications

- David Doerr, John T. Schiffen, Dennis R. Alexander, "Optimization of collinear dual pulse femtosecond laser-induced breakdown spectroscopy of silicon", *Spectrochimica Acta Part B: Atomic* 62 , 1412-1418, 2007.
- Ufuk Parali and Dennis R. Alexander, "Interaction of a single-cycle laser pulse with a bound electron without ionization," *Optics Express*, Vol. 18, No. 14, p. 15155-15168, July 5, 2010.
- Ufuk Parali and Dennis R. Alexander, "Modeling the interaction of a single-cycle laser pulse with a bound electron without ionization," Book Chapter, *Coherence and Ultrashort Laser Emission*, Edited by F. J. Duarte, (IN-TECH), ISBN:978-953-307-242-5. Dec. 2010.
- Craig A. Zuhlke, Dennis R. Alexander, John C. Bruce III, Natale J. Ianno, Chad A. Kamler, and Weiqing Yang, "Self assembled nanoparticle aggregates from line focused femtosecond laser ablation," *Optics Express*, Vol. 18, Issue 5, pp. 4329-4339, 2010.
- E. Manley, J. Deogun, L. Xu, D. Alexander, "All-Optical Network Coding," *Optical Communications and Networking, IEEE/OSA Journal of*, No.99, pp.175-191, 2010.
- Ufuk Parali and Dennis R. Alexander, "Volterra intergral equation solution of the convolutional modifier function approach for ultra short single cycle light pulse

interaction with a bound electron without ionization," Submitted to Journal of Applied Physic, B with revisions, October 2012.

- Cody Raml, Xiangnan He, Ming Han, Dennis R. Alexander, Yongfeng Lu, "Raman spectroscopy based on a single-crystal sapphire fiber", Optics Letters, Vol. 36, Issue 7, pp. 1287-1289, April 1, 2011.
- Amelie Veillere, Thomas Guillemet, Zhi Qiang Xie, Craig A. Zuhlke, Dennis R. Alexander, Jean-Francois Silvain, Jean-Marc Heintz, Namas Chandra, and Yong Feng Lu, "Influence of WC-Co Substrate Pretreatment on Diamond Film Deposition by Laser-Assisted Combustion Synthesis, ACS Appl. Mater. Interfaces, 3, 1134-1139, 2011.
- Lucas Koester, Craig Zuhlke, Joseph A. Turner, Allen J. Fuller, Brent M. Wilson, Dennis Alexander, "Near-Race Ultrasonic Detection of Subsurface Defects in Bearing Components," Accepted for publication in Journal of ASTM International, June 11, 2012.
- M. L. Rohlfs and D. R. Alexander, ``Transient Plane Wave Scattering by a Dielectric Sphere," in preparation to Journal of Optical Society of America, October, 2012.
- J. Bruce III, C. Zuhlke, and D. Alexander, "Thermally related optical hysteresis of semiconductor quantum dots," Optics Letters, under revision, October, 2012.
- T. Anderson, C. Zuhlke, J. Bruce III, "Fundamental Studies of the Femtosecond Electric Fields on Either Side of Focus on the Laser Induced Breakdown Spectroscopy Signal", In preparation, Journal of Applied Physics, September, 2012.
- T. Anderson, C. Zuhlke, J. Bruce III, "Femtosecond Laser Surface Structuring of Superhydrophobic/Superhydrophilic Surfaces", in preparation, Journal of Surface Science, September, 2012.
- C. Zuhlke, T. Anderson, D. Alexander, "Use of Femtosecond Laser Pulses to Produce a Variety of Microstructure Morphologies on Metals", in preparation, Physical Review B.
- T. Anderson, C. Zuhlke, D. Alexander, "Laser Damage Thresholds of Hybrid Micro/Nanostructured Metal Surfaces", in preparation, Optics Express.
- C. Zuhlke, T. Anderson, D. Alexander, "Growth Mechanisms of Pyramidal Micro/Nanostructures Formed on Nickel using Femtosecond Laser Pulses", in preparation, Optics Express.
- C. Zuhlke, T. Anderson, D. Alexander, "Formation of Extruding Spikes on Nickel using Femtosecond Laser Pulses", in preparation, Optics Express.
- T. Anderson, C. Zuhlke, C. Wilson, D. Alexander, "High Efficiency Electrodes for Hydrogen Production Fabricated Using Femtosecond Laser Processing", in preparation, Journal of Hydrogen Energy.

4. Presentations:

- N. Batta, Y. F. Lu, X. W. Wang, J. Shi, D. W. Thompson, D. W. Doerr, D. R. Alexander, "Monitoring of steam laser cleaning using optical-probe techniques", The Sixth International Symposium on Laser Precision Microfabrication (LPM 2005, 4-8

April 2005, Radisson Fort Magruder Hotel and Conference Center Williamsburg, Virginia, USA)

- H. Wang, K. K. Mendu, **Y. F. Lu**, J. Shi, D. R. Alexander, D. W. Doerr, “Laser-assisted fabrication of 3-D structures on polymer film”, The Sixth International Symposium on Laser Precision Microfabrication (LPM 2005, 4-8 April 2005, Radisson Fort Magruder Hotel and Conference Center Williamsburg, Virginia, USA)
- D. Alexander, D. Doerr, N. Singh, Q. Peng, J. Schiffen, “Femtosecond Laser Production of Silicon Nanoparticles and Metal Surfaces having Nanostructures that are Broadband Absorbers.” INVITED PAPER,(ICCE-12) Tenerife, Spain, August 1-6, 2005
- D. Alexander, J.S. Deogun, H.S. Hamza, J. Bruce III, C. Zulke, B. Koch, P. Le, “Quantum Dots Based Technology for multiple wavelength conversion” LEOS IEEE 18th, October 23-27, Sydney, Australia
- Jian Chao Li, Hai Feng Zhang, Dennis R. Alexander, David W. Doerr, “Characteristics of Ultrashort Laser Pulses Illumination of a Fresnel Zone Plate,” Conference on Lasers and Electro-Optics Quantum Electronics and Laser Science Conference, Long Beach Convention Center, Long Beach, California, USA, May 22-25, 2006.
- Dennis Alexander, Jitender S. Deogun2, Haitham S. Hamza2, John Bruce III, Craig Zuhlke1, Brandon Koch, Pong Le “Quantum Dots Based Technology for Multiple Wavelength Conversion”, IEEE, LEOS conference, Oct. 23., Sydney Australia, 2005
- Dennis R. Alexander, John Bruce III, “Femtosecond LIBS for Detection of Biological/Chemical Agents Nanomorphing/Stratigraphy”, Pacificchem 2005 Congress, **INVITED**, Honolulu, Hawaii, December, 2005.
- Jian Chao Li, HaiFeng Zhang, Dennis R. Alexander, David W. Doerr, “Characteristics of Ultrashort Laser Pulses Illumination of a Fresnel Zone Plate,” Conference on Lasers and Electro-Optics Quantum Electronics and Laser Science Conference, Long Beach Convention Center, Long Beach, California, USA, May 22-25, 2006.
- D. Alexander, S. Mao, R. Russo, M. Richardson and R. Fedosejev, “Particle Generation in FS Laser Interactions,” MURI Kickoff Meeting, August 8, 2006.
- D. Alexander, John Schiffen, David Doerr, “Dual Pulse Femtosecond Laser Fundamentals for the Detection of Biological, Chemical, and Explosives,” LIBS 2006, September 4-9, Montreal Canada.

- D.R. Alexander, Jianchao Li, Haifeng Zhang, David W. Doerr, “Optical Communications with Femtosecond Lasers”, SPIE INVITED Paper, Stockholm, Sweden, September 13, 2006.
- D. Alexander, John Schiffen, David Doerr, "Optimization of Collinear Dual Pulse Femtosecond Laser Induced Breakdown Spectroscopy of Silicon, EMLIBS Conference, Paris France, September 11, 2007.
- D. Alexander, John Schiffen, David Doerr, "Optimization of Collinear Dual Pulse Femtosecond Laser Induced Breakdown Spectroscopy of Silicon," NASLIBS, New Orleans, October 8-11, 2007.
- D. Alexander, “All Optical Multicast Devices and Switches Based on Nanotechnology and Micro Ring Cavities,” Verizon, Invited, November 14, 2007.
- Dennis R. Alexadner, John Schiffen, and Victor A. Rivas, “Femtosecond laser Modified Surfaces for Enhanced Broadband Absorbers,” Southeast Ultrafast Conference (SEUFC), January 10th and 11th 2008, University of Arkansas.
- Dennis R. Alexander, “Dual Pulse Femtosecond Spectroscopy for FLIBS and Issues Related to Femtosecond Pulse Propagation,” DARPA working group meeting on Femtosecond Spectroscopy, Dr. Devanand Shenoy, Program Manager DARPA/MTO, February 28, 2008, Washington, DC.
- Dennis R. Alexander and John Bruce, “Collinear Dual Pulse-Dual Focus Enhancement of Femtosecond LIBS,” LIBS 2008, International Conference on Laser Induce Breakdown Spectroscopy, September 22-26, Adlershof, Berlin, Germany, September 23, 2008.
- J. Bruce III, D. R. Alexander, “Fundamentals Associated with Collinear Dual Beam Dual Focus Femtosecond LIBS,” LIBS 2009, New Orleans, July 13-15, 2009.
- E. Jackson, D. Admiraal, D. Alexander, J. Stansbury, J. Guo, D. Rundquist, and M. Drain. "Thermal Imaging for Discharge and Velocity Measurements in Open Channels," Proceedings 33rd Congress of the *International Association of Hydraulic Research*, Vancouver, Canada, 2009.
- J. Bruce III, D. R. Alexander, “Fundamentals Associated with Collinear Dual Beam Dual Focus Femtosecond LIBS,” LIBS 2009, New Orleans, July 13-15, 2009.
- Troy Anderson, John Bruce III, and Dennis Alexander, “The Use of A “Bulls eye” Focal Distribution in a Dual-Pulse Arrangement for Efficient Interaction with Ejected Nanoparticles for Analytical LIBS,” LIBS 2010, Memphis, Tennessee, August, 2010.

- John Bruce III, Troy Anderson, and Dennis Alexander, “Spatial Distribution of LIBS Plasma Emission Using A Dual Pulse Arrangement,” LIBS 2010, Memphis, Tennessee, August, 2010.
- Troy Anderson, John Bruce III, and Dennis Alexander, “The Role of Nanoparticles and Dual Pulse Dual Focus in the Enhancement of LIBS Sensors for Detection ECBN, 27th Army Science Conference, November 28-December 2, Orlando, Florida, 2010.
- Craig Zuhlke, and John Bruce III, “Femtosecond Laser Production of Nanoparticles and Their Subsequent Layered Aggregate Growth Using a Line Focused Beam,” 18th International Conference on Composites or Nano Engineering, Anchorage Alaska, ICCE July 4-10, 2010.
- Dennis R. Alexander, and John Bruce III, “Fundamentals of femtosecond laser induced breakdown spectroscopy: effects of focus location and short time emissions on the entrainment of atmospheric species,” 2010 International Chemical Congress of Pacific Basin Societies, Honolulu, Hawaii, Sept. 15, 20, 2010.
- Dennis R. Alexander, “Modeling the Single-Cycle Laser Pulse Interaction with Matter,” **Invited Lecture**, University of Tennessee Space Institute, March 24, 2011.
- Dennis R. Alexander, “Femtosecond Laser Surface Modification Processes for Producing Super-Hydrophobic/Super-Hydrophilic Material Properties” **Invited Lecture**, University of South Dakota, Chemistry Department, Smart Grid Presentation to All South Dakota Schools, November, 2011.
- T. Anderson, C. Zuhlke, J. Bruce III, D. Alexander, C. Parigger, “Evidence of near-field filaments and how sample location affects femtosecond LIBS,” NASLIBS 2011: 3rd North American Symposium on Laser-Induced Breakdown Spectroscopy, Clearwater, USA, July 18-20, 2011.
- J. Bruce III, T. Anderson, D. Alexander, “An investigation of dual pulse femtosecond LIBS on aluminum”, NASLIBS 2011: 3rd North American Symposium on Laser-Induced Breakdown Spectroscopy. Clearwater, USA. July 18-20, 2011.

5. Patents and IP generated

Patent 6,864,457: Laser Machining of Materials: issued on March 8, 2005.

Patent 7868302: Nano-particle/quantum dot based optical diode: issued on January 11, 2011

Patent 8189190: Remote Chemical and Elemental Analysis by Ultra Fast Spectroscopy; issued 5/29/2012

Patent 8247731: Laser Scribing and Machining of Materials; issued 8/21/2012

Patent Royalties from Advanced Materials, Inc. and Attochron Inc.

Patent 7868302: Nanoparticle/quantum dot based optical diode, January 11, 2011.

Patent Pending, “Wireless Laparoscopy”, UNeMed Managing patenting process, June, 2011.

Provisional Patent Application, “Femtosecond Surface Modification Methods for Increasing Surface Area and the Release of Small Bubbles, Standstill Licensing Agreement with Photonic Solutions, Inc., April 15, 2011.

Provisional Patent Application, “Enhanced Signal to Noise Ration Laser Induced Breakdown Spectroscopy (LIBS)”, Provisional Application, July 17, 2012.

Office Action, “Collinear Dual Pulse and Dual Focus Femtosecond Laser Machining and Enhanced LIBS Spectroscopy,” Filed Response to First Office Action 5/3/12

Patent Pending (waiting for patent to be issued), “Femtosecond Nanomachined High Surface Electrodes for Super Capacitors and Other Applications,” May 17, 2012.

Exclusively Licensed, “Technical Information for a Cell Phone Triggered Animal Trapper”, June, 2007. (UNL receives Royalties).

6. Names, citizenship, discipline, of all undergraduates involved in the project:

Funded: Craig Zuhlke, USA, Electrical Engineering

John Bruce, USA, Electrical Engineering

Unfunded: Cody Raml, USA, Electrical Engineering

Christopher Wilson

Nick Roth

7. Names, citizenship, discipline of all graduate students involved in the project:

Funded:

David Doerr, USA, Electrical Engineering

John Schiffen, USA, Electrical Engineering

John Bruce III, USA, Electrical Engineering

Unfunded: Craig Zuhlke, USA Electrical Engineering

Ufuk Parali, Turkey, Electrical Engineering

Kimberly Bay, USA, Electrical Engineering

8. Names, citizenship, discipline of all post-doc involved in the project:

Funded: Dr. Troy Anderson, USA, Electrical Engineering

9. Names, citizenship, discipline of all undergraduates who graduated in the program

Funded: John Bruce III, USA, Electrical Engineering

Involved: Craig Zuhlke, USA, Electrical Engineering

Christopher Wilson, Electrical Engineering

10. Names, citizenship, discipline of all graduate who graduated in the program

Funded: John Bruce III, USA, Electrical Engineering

John Schifern, USA, Electrical Engineering

Involved: Craig Zuhlke, USA, Electrical Engineering

11: Awards, Prizes, etc.

Dr. Alexander: University of Nebraska Wide Teaching Award, 2011

Dr. Alexander: College of Engineering Holling Family Master Teaching Award, 2011

Project Summary (Sub of Grant # W911NF-06-1-0446)

FUNDAMENTAL PHYSICAL & CHEMICAL PROCESSES IN ULTRAFAST LASER MATERIALS INTERACTIONS (MURI sub)

Samuel S. Mao (U.C.Berkeley PI)
University of California at Berkeley
Berkeley, CA 94720

Objective

The overall objective of this MURI program is to obtain a comprehensive understanding of the interaction of ultrafast femtosecond laser pulses with matter, with specific reference to the detection of trace elements of materials. Based on the guidance provided at the 2009 program review, the objective of the UCB group is focused on the initial and fundamental interaction science, in particular to develop theoretical understanding of early-stage ultrafast laser material interactions expressed in physical models.

Approach

Comprehensive theoretical model integrating laser-material interactions with early-stage laser produced plasma development. In particular, the theoretical model is aimed to provide the first insight of how ions from laser-irradiated materials are ablated to form a plasma for chemical analysis.

Relevance to Army

A full understanding of the interaction of ultrafast laser light with materials, in particular the formation of laser plasma, is critical to achieving LIBS for stand-off explosive sensing technology that can be deployed to the field.

Accomplishments for Reporting Period

The UCB team identified the significant effect of the intrinsic electric field just above laser irradiated target, which was verified by experimental measurements.

Collaborations and Technology Transfer

- The UCB PI visited Nebraska.

Resulting Journal Publications During Reporting Period

- J. Li, X. Wang, Z. Chen, J. Zhou, S. S. Mao, and J. Cao, "Real-time probing of ultrafast residual charge dynamics." *Applied Physics Letters*, V.98, 011501 (2011).
- T. Owens, S. S. Mao, E. K. Canfield, C. P. Grigoropoulos, X. Mao, and R. E. Russo, "Ultrafast thin-film laser-induced breakdown spectroscopy of doped oxides." *Applied Optics*, V.49, 67 (2010).
- J. Li, X. Wang, Z. Chen, R. Clinite, S. S. Mao, P. Zhu, Z. Sheng, J. Zhang, and J. Cao, "Ultrafast electron beam imaging of femtosecond laser-induced plasma dynamics." *Journal of Applied Physics*, 107, 083305 (2010).
- Z. Chen and S. S. Mao, "Ion emission induced by femtosecond laser at metal surface." *Applied Physics Letters*, submitted.
- Z. Chen and S. S. Mao, "Plasma development of femtosecond laser-irradiated metal surface." to be submitted.

Graduate Students Involved During Reporting Period

- Travis Owens (Ph.D., current)

Awards, Honors and Appointments

- In the current report period, the UCB PI gave invited presentations in the following international conferences:

2010 Society of Engineering Science (SES) Technology Conference, *invited*
2010 NSF-MEXT Symposium on the Future of Nanotechnology, *invited*
2010 Julius Springer Applied Physics Forum, *invited*
2011 NSF Workshop on Laser Processing and Energy Applications, *invited*
2011 7th International Conference on Low Dimensional Structures and Devices, *invited*
2011 9th International Meeting of Pacific Rim Ceramic Societies, *invited*
2011 International Workshop on Nanomaterials for Clean Energy Conversion, *invited*
2011 1st Joint Workshop on Advanced Materials for Energy Conversion, *invited/keynote*
2011 2nd International Workshop on Renewable Energy, *invited/keynote*
2011 SPIE Optics and Photonics Conference, *invited*

Detailed Technical Progress Report

Previously we used one-dimensional full multi-species fluid dynamics to simulate the plasma formation and the plume expansion at the early stage. The front of the plasma is determined by the front of the electrons moving away from the target surface. The early stage plasma can expand at a speed on the order of 10 to 1000 km/s and the expansion slows down gradually with time. Due to the emission of electrons, a positively charged surface will build up gradually. Then the early stage plasma can contract due to the induced electric field and also the confinement of ambient gas. Meanwhile, many positive material ions are emitted from the target surface on the time scale of a few tens of picoseconds when the lattice temperature exceeds the boiling temperature. Another core of plasma close to the target surface is formed a little later. The main positive ions in this core are from target. This plasma core moves at a much slower speed compared to the early stage plasma. Fig. 1 presents the two plasma fronts as a function of time for a specific case study (laser pulse with 100 fs FWHM, 800 nm wavelength and peak intensity of 2E14 W/cm², Cu target and He ambient gas).

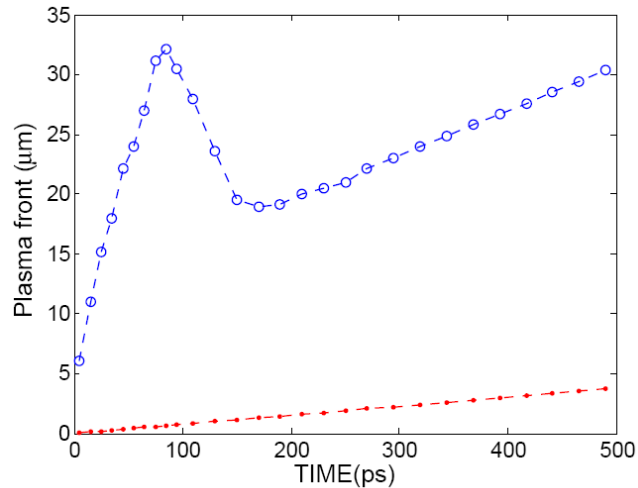


Fig. 1 Two early-stage plasma fronts as a function of time.

At the time scale of nanoseconds, however, the fast plasma front will gradually disappear and all heavy particles in the plume move with the same bulk velocity. Thus, instead of using the full multi-species fluid model for simulating the plasma expansion at this stage, we turn to a simplified two-temperature model (electron temperature and heavy particle temperature). Fig. 2 presents the plasma front as a function of time. On such a long time scale, there is no early stage plasma. The fast electrons corresponding to the early stage plasma front get lost due to diffusion and recombination processes. The front of this plasma is determined by the front of ejected ions and neutral atoms from the target, where the ion density is higher than the ambient ion density. After 50 ns, the plume plasma tends to stop expanding and will finally disappear by diffusing into the

surrounding. Through this two-stage simulation, we developed a basic understand that the formation of the early-stage and the later stage plasma as well as their expansion are very different.

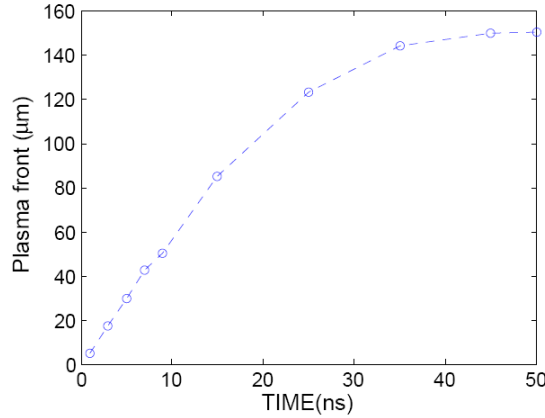


Fig. 2 Later-stage plasma front as a function of time.

We have also studied the temporal behavior of the transient electric field induced by ultrafast laser-excitation of metal and dielectric materials. The results indicate the electric fields are affected by both the emitted electrons and the residual charges. In metals, the residual charges and free carriers will screen inner electric field generated by emitted electron at every moment. This observation suggests that the electric field on the pumped side of a metal target could be modeled as being generated by emitted electrons and their image charges. In dielectric target, the residual charges are confined within the excited area for hundreds of picoseconds and longer timescale, providing the driving force for the coulomb explosion taking place when the residual charge density surpasses the critical value.

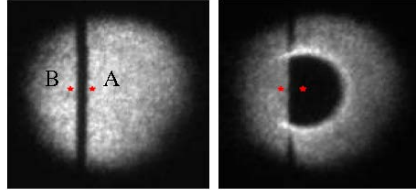


Fig. 3 An electron beam shadow image of a copper slab without pump femtosecond laser pulse and with a femtosecond pump laser pulse at a time delay of 13 ps. Positions A is 70 μm away from the front surface of the slab. Position B is 70 μm away from the back surface.

Project Summary - Grant # W911NF-06-1-0446 (MURI sub)

fs/ns LIBS Spectroscopy (MURI sub)

Lewis Johnson
Department of Physics
Florida A&M University (FAMU)
Tallahassee, FL, 32307

Objective

The objective of this effort is to experimentally study Laser Induced Breakdown Spectroscopy (LIBS) plasmas and emissions generated from multiple combinations of nanosecond gigawatt and femtosecond multi-terawatt lasers. The spectral emissions from reference substrates and explosives materials are to be studied and characterized. Optimizing emission signatures to maximize explosive material detection while minimizing background atmosphere and substrate contributions is the ultimate goal.

Approach

- Experimentally study laser interaction with sample in the multi-pulse fs and ns regimes
- Study the optimum focal position to minimize ambient air contribution since sample oxygen and nitrogen information is critical for the detection of most explosive residues.
- Observe the parameters of the plasma volume at various points of evolution
- Determine suitable imaging and the corresponding focussing point for optimized emission collection
- Investigate the detection of explosive residues.
- Demonstrate remote LIBS detection of explosive residues using self-channelled emissions.

Relevance to Army

The current mode of war has evolved from the use of conventional weapons to the deployment of improvised devices that are extremely hard to detect. The increased insurgent and terrorists threats have lead to a need for the development of capable rapid remote sensing technologies. The Ultimate goal of this effort is to understand the relevant physics and chemistry of the use of femtosecond lasers for the remote detection of trace amounts of hazardous materials to build capable forward deployed sensors for the war-fighter. In addition, this technology has many applications in Port Security, Border Protection, Drug Enforcement, Agriculture, Environmental monitoring, Nuclear proliferation monitoring, and Public health.

Accomplishments for Reporting Period

- We have used the CO₂ laser to look at potential enhancement of Uranium under ns and femtosecond excitation. Some early results are presented below. We are working to quantify the LOD and SNR enhancements for the various modalities.
- Work has been done on applying different multivariate techniques to acquired organic residue data. Contrasting Principle Component Analysis and Discriminant Function Analysis was one of the aims of this study. Residues of several essential oils were probed using nanosecond and

femtosecond single pulsed LIBS. CO₂ enhanced LIBS also was carried out on the prepared samples of oils using both silicon and aluminium substrates.

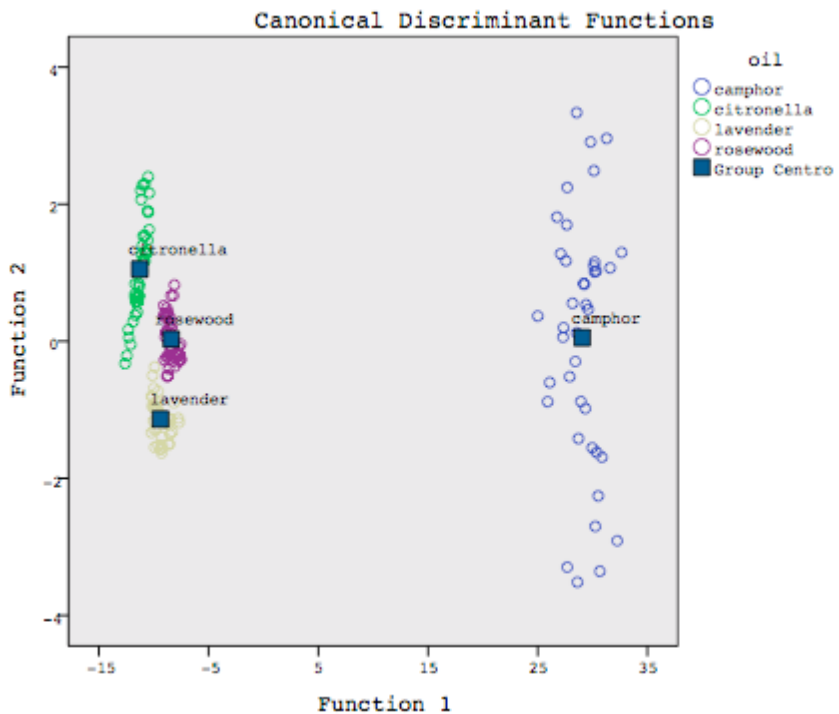


Figure 1. CO₂ with ns normalized (by dividing each spectral line by CN 388 peak) grouped together by oil type (co2 and ns)

- We have finished a majority of the work on the thin film and are working on a publication.
- We are studying the LIBS on thin films of Al Oxide and Iron. We wish to quantify the amount of oxygen and nitrogen rich material that can be ablated from uniform thin films of various thicknesses deposited on silicon substrate. Both single and double pulse LIBS were employed to study the amount of material ablated as a function of trace and bulk material in ambient atmosphere. We wanted to understand the limits of detection of O materials in a normal atmosphere. Samples consisted of thin (5, 10, 50, 100 nm) Al oxide layers over 100nm Fe on a Si Substrate. Sample were transported and stored in N₂ atmosphere to control native Oxide Growth. (Previous)

Early Results indicate that:

- Femtosecond Self-Channelled Beams are best at removing surface residue and reducing substrate contribution
- Early Results indicates, there appears to be limits of detection for oxygen rich (~ 10 nanogams/cm²) materials in ambient atmosphere
- Early results yields an range of energy (~20 – 40mJ/pulse) for optimal thin film removal

- Begin Study of explosive detection in various regimes. Single Nanosecond and Femtosecond pulses and combination of nanosecond and femtosecond pulses were applied to thin films of energetic materials and hydrocarbons on a silicon substrate. Single Femtosecond pulses produced the worst system response with very little differentiation between energetic materials and other hydrocarbons. The combination of femtosecond pulse followed by a nanosecond pulse produced the best differentiation among the samples. The nanosecond system is better at producing a plasma, while the femtosecond is better at producing nanoscale material fuel the nanosecond produced plasma. (*Previous*)

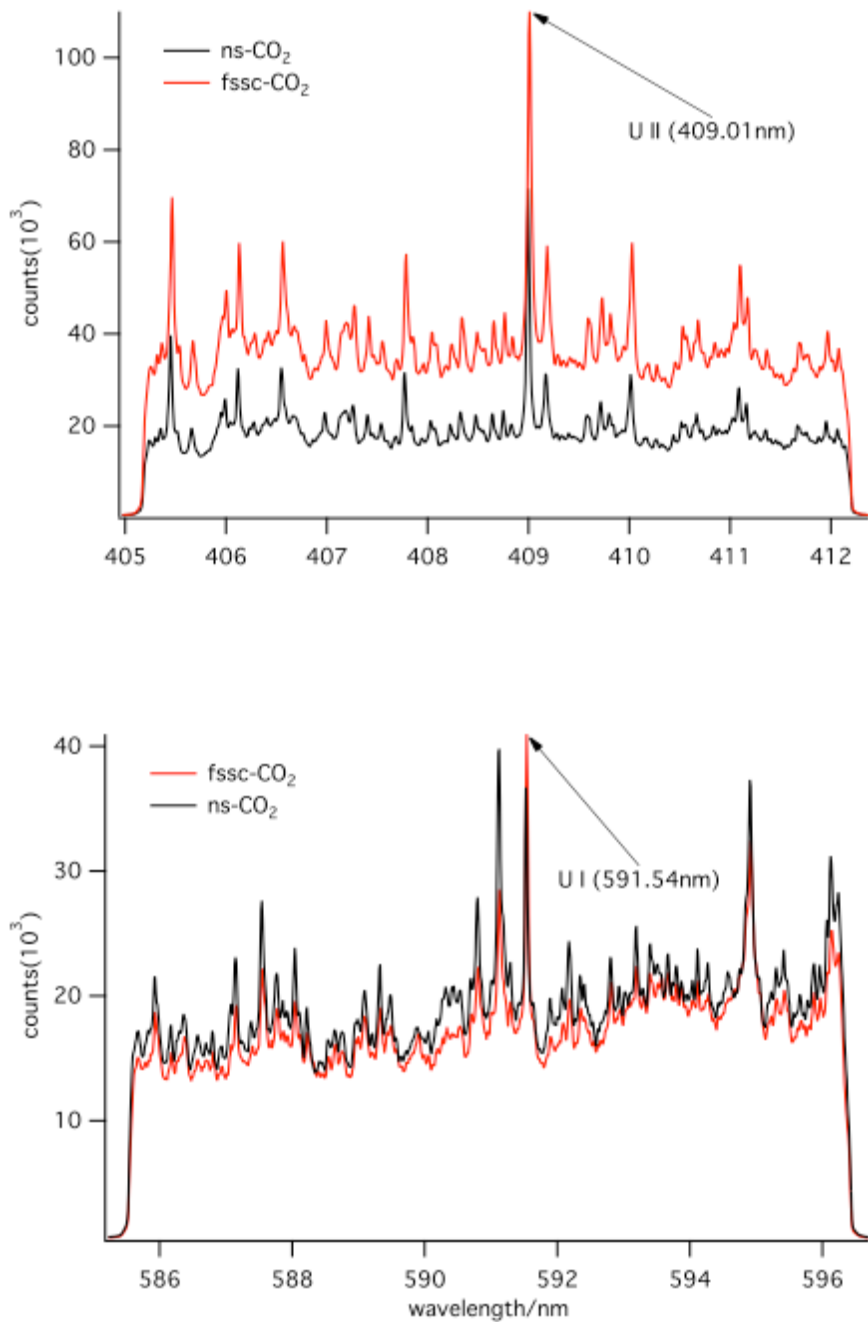


Figure 2. Comparison of CO₂ enhancement for nanosecond and femtosecond produced plasma for U II (409.01nm) and U I (591.54nm) emissions

- Initiated a study of effects of LIBS emission signals from nanosecond or femtosecond pulse initiation followed by below threshold CO₂ illumination. Nanosecond pulse produced the highest emission signals over the femtosecond system.
- Implemented principle component and PLSDA analysis

- Nanosecond LIBS system has been reconfigured for inline – Horizontal sample illumination.
- Reconfigured LIBS system for inline illumination and detection (*Previous*)
- Enhanced throughput of remote detection optics (*Previous*)
- Begin Study of atmospheric oxygen/nitrogen suppression for femtosecond (fs), nanosecond (ns), femtosecond self channelled (fs-sc), Dual ns, ns-fs, fs-ns, ns-fs-sc, fs-sc,ns modes of excitation. (*Previous*)
- Demonstrated Single Shot Self-Channelled LIBS Detection of Substrate material at ~50ft Outdoors. (*Previous*)
- Determined optimal conditions for substrate emission signal enhancement and atmospheric contribution minimization for a perpendicular detector configuration. (*Previous*)
- Attempted explosive detection by observing the Oxygen to Nitrogen ratios in TNT, RDX and PETN. (*Previous*)

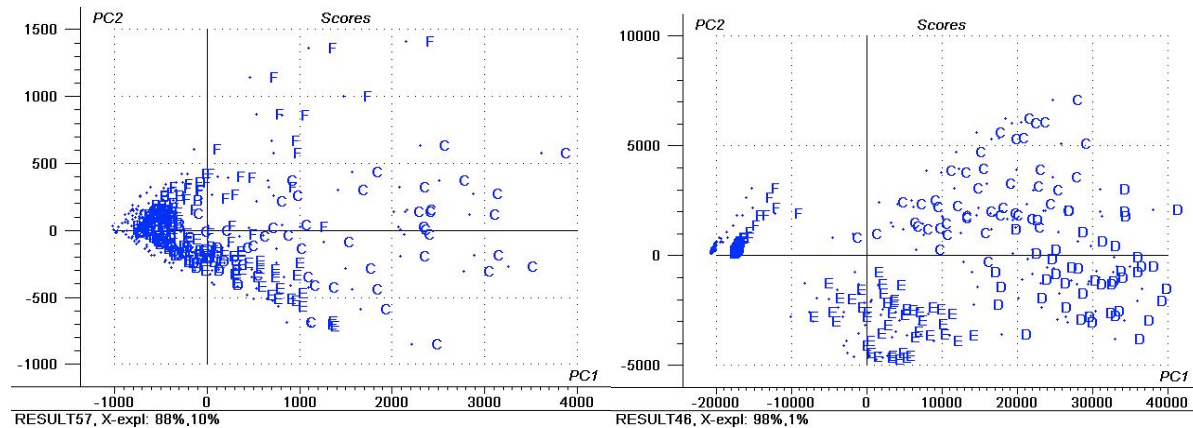


Figure 3. femtosecond (fs) vs fs/ns illumination of thin film of material on silicon substrate. PCA analysis based on 1 Hydrogen, 2 Nitrogen and 2 Oxygen lines. (B = Diesel C = TNT D = RDX E = DNT F = WD40)

Collaborations and Technology Transfer

NONE

Resulting Journal Publications During Reporting Period

LIBS on Aluminium Oxide and Iron Thin Films, publication in progress

CO2 Enhanced Detection of Uranium with LIBS, Publication in progress

Graduate Students Involved During Reporting Period

- Jorge Martinez (Ph.D Physics, current)

Awards, Honors and Appointments

NONE